Synthesis and Characterisation of Barium Strontium Cobalt Iron Oxide Mixed Ionic and Electronic Conductors

A thesis submitted to the University of Manchester for the
degree of Doctor of Philosophy in the Faculty of Engineering
and Physical Sciences

2013

Colin John Norman

School of Materials

Table of Contents

Word count 47289

Abstract

Oxygen separation membrane technology is an alternative to cryogenic distillation for the production of oxygen. Barium strontium cobalt iron oxide (BSCF, $Ba_{0.5}Sr_{0.5}Co_{0.8}Fe_{0.2}O_{3-\delta}$) is one of the candidate membrane materials for this application.

A robust wet-chemical synthetic route for the synthesis of BSCF has been developed. The route comprises reverse precipitation from a mixed metal nitrate solution at pH> 10 and uses a minimum amount of reagents. In particular there are no organic additives which need to be burnt off.

All the metal ions precipitated simultaneously but a single phase was not then formed. The phases formed during precipitation, drying and calcining varied with the experimental conditions used. It was shown that ~80% of the barium and strontium precipitated as their mixed carbonate. However, on sintering, a single cubic phase material was formed. The process was capable of variation in the BSCF composition and the addition of copper to the system.

The electrical and oxygen permeation properties were measured. The relationship between them was found to be dependent on the lattice parameter, tolerance factor and oxygen non-stoichiometry (δ). Values of δ greater than 0.5 at high temperature were found to give poor oxygen permeation and an increase in resistance although they did not decompose to the ordered brownmillerite structure.

The addition of copper to BSCF by substituting it for iron and cobalt enhanced grain growth during sintering. However, except at the lowest addition level of 0.05 on the B-site, it did not show any oxygen permeation.

High temperature x-ray diffraction (HTXRD) and x-ray photoelectron spectroscopy (XPS) studies were carried out. They showed that the thermal expansion coefficient increased at ~400° as loss of oxygen from the material started. As the materials were heated in the XPS surface carbonates were removed and the surface concentration of Ba and Sr ions decreased at 3-500°C although on further heating to 800°C their concentration returned to close to the original values.

The University of Manchester
Colin John Norman
Doctor of Philosophy
Synthesis and Characterisation of Barium Strontium Cobalt Iron Oxide Mixed Ionic and Electronic Conductors
September 2013

Declaration

No portion of the work referred to in the thesis has been submitted in support of an application for another degree or qualification of this or any other university or other institute of learning.

Copyright Statement

i. The author of this thesis (including any appendices and/or schedules to this thesis) owns certain copyright or related rights in it (the "Copyright") and he has given The University of Manchester certain rights to use such Copyright, including for administrative purposes.

ii. Copies of this thesis, either in full or in extracts and whether in hard or electronic copy, may be made only in accordance with the Copyright, Designs and Patents Act 1988 (as amended) and regulations issued under it or, where appropriate, in accordance with licensing agreements which the University has from time to time. This page must form part of any such copies made.

iii. The ownership of certain Copyright, patents, designs, trademarks and other intellectual property (the "Intellectual Property") and any reproductions of copyright works in the thesis, for example graphs and tables ("Reproductions"), which may be described in this thesis, may not be owned by the author and may be owned by third parties. Such Intellectual Property and Reproductions cannot and must not be made available for use without the prior written permission of the owner(s) of the relevant Intellectual Property and/or Reproductions.

iv. Further information on the conditions under which disclosure, publication and commercialisation of this thesis, the Copyright and any Intellectual Property and/or Reproductions described in it may take place is available in the University IP Policy
(see http://documents.manchester.ac.uk/DocuInfo.aspx?DocID=487), in any relevant Thesis restriction declarations deposited in the University Library, The University Library's regulations
(see http://www.manchester.ac.uk/library/aboutus/regulations) and in The University's policy on Presentation of Theses

Acknowledgements

I would like to thank my supervisor Dr Colin Leach for his help, advice and encouragement as I embarked on an exploration of a new field.

I would like to thank the many members of the department who so gladly gave of their time and expertise in setting me on the right route for using the department's facilities. In particular I would like to acknowledge:- Dr Rob Bradley, Ivan Easdon, Mike Faulkner, Andy Forrest, Polly Greensmith, Gary Harrison, Ken Gyves, Dr Fabien Leonard, Dr Tristan Lowe, Judith Shackleton, Dave Strong, Andy Wallwork and Dr Chris Wilkins.

Dr Chris Muryn, Department of Chemistry, is thanked for his help in using the high temperature x-ray diffractometer.

I am grateful for access to the Daresbury NCESS Facility under EPRSC grant EP/E025722/1. Dr Daniel Law is thanked for his assistance in using the NCESS facilities.

Mr William Wiseman, MEL Chemicals, a division of Magnesium Elektron Limited, is thanked for carrying out the nitrogen adsorption experiments.

I am indebted to the members of the functional ceramics team and other residents of E30a who made me very welcome as a mature student in particular; Robert Lowndes, Margaret Wegrzyn, Steph Ryding, Nicola Middleton-Stewart, James Griffiths, Ellyawan Arbintarso, Poonsuk Poosimma, Huanghai Lu, Zijing Wang, Guannan Chen and Sam Jackson. This is not to forget the ever present Dr Feridoon Azough.

I would like to thank Mark Sellers, Gareth Daniel and Alan Barbour for regularly reminding me of the real world and who, despite my researching into ceramics, won't be getting their kitchens and bathrooms retiled!

Finally I would like to thank my wife, Helen, for her encouragement, support and love as I embarked on a late career change.

Sample Nomenclature

The samples used in this study are named as follows.

The designation of the powders is that the numbers correspond in turn to **B**arium **S**trontium **C**obalt Iron(**F**e) within the oxide and represent ten times the value in the empirical formula ie $Ba_{0.3}Sr_{0.7}Co_{0.8}Fe_{0.2}O_{3-\delta}$ is BSCF 3782.

Designation	Ba	Sr	Co	Fe
BSCF 3782	0.3	0.7	0.8	0.2
BSCF 5582	0.5	0.5	0.8	0.2
BSCF 7382	0.7	0.3	0.8	0.2
BSCF 5564	0.5	0.5	0.6	0.4

Synthesis studies were carried out on BSCF 5582 with following variations

	Precipitation @ pH 10	Precipitation @ pH 12
No Boil	✓	✓
Boil at Precipitation pH (High pH before wash) (Hydrothermal 1)	✓	✓
Boil at pH 7 (Low pH after wash) (Hydrothermal 2)	✓	✓

The addition of copper adds **Cu** to the end

Designation	Ba	Sr	Co	Fe	Cu
BSCF 5562Cu2	0.5	0.5	0.6	0.2	0.2
BSCF 5571Cu1	0.5	0.5	0.75	0.15	0.1
BSCF 5582Cu0.5	0.5	0.5	0.775	0.175	0.05

Abbreviations

γ	surface tension
$\Delta\mu_{O_2}$	chemical potential difference
μ	x-ray absorption coefficient
A	area of the pellet
a'_O & a''_O	oxygen activities.
a_m	area of the adsorbed gas molecule
b	instrumental broadening
B	experimental broadening
C	concentration of solution
c	constant which is related to the net heat of adsorption of gas
C_O	oxygen concentration
d	interplanar spacing
d	equivalent particle size
D	thickness of sample
E	activation energy
E_0	amplitude of the applied signal (V)
F	Faraday Constant
f	sweep gas flow rate
h	Planck's constant
I	reduced intensity after a distance t
i	Current
I_o	incident intensity
I_t	current at time t
j	$\sqrt{-1}$
j	total angular momentum number
J_O	oxygen flux
L	membrane thickness
L	crystallite size
L	inductance
l	orbital angular momentum quantum number
L_o	lattice parameter at lower temperature
m	mass
M	relative electric modulus
$M_{BSCFO3-\delta}$.	molecular weight of $Ba_{0.5}Sr_{0.5}Co_{0.8}Fe_{0.2}O_{3-\partial}$.

N_A	Avogadro’s constant
n	number of moles of gas in the system
n	amount of gas adsorbed
n	order of diffraction = 1 for x-ray diffraction
n	principal quantum number
n_m	monolayer capacity
P	pressure
p	partial pressure
p_1 O_2 and p_2 O_2	oxygen partial pressures
p_o	saturation vapour pressure
R	gas constant
R	Resistance
r_m	radius of the meniscus
r_X	ionic radius of the ion in the ABO_3 structure.
s	spin angular momentum quantum number
SA	surface area
T	temperature
t	path length
t	tolerance factor
V	volume of titre
V	volume
V	Voltage
V_L	molar volume of the liquid
V_m	molar volume of an ideal gas
w	weight of sample used
Y	admittance
$Z(\omega)$	impedance
α	exponent and equals 1 for a pure capacitor
α	thermal expansion coefficient
B_s	sample broadening
Δ MW	change in molecular weight
ΔE_a	resolution of analyser.
ΔE_n	electronic transition line width
ΔE_p	energy width of exciting x-rays
ΔL	lattice parameter change

ΔT	temperature difference
ε	relative permittivity
ε_0	electrical permittivity of vacuum
ε_r	dielectric constant
κ	Boltzmann’s constant
θ	diffraction angle
λ	wavelength of x-rays
ρ	theoretical density
ρ_b	bulk density
ρ_L	density of water
ρ_s	apparent solid density
σ	conductivity
T	lifetime
φ	phase shift.
Φ	work function from the sample to free space
ω	radial frequency (radian s^{-1}) and equals $2\pi f$ where f is the frequency (Hz)

1 Introduction

There is a constant demand for energy and, because of the finite resources of fossil fuels, a continuing drive towards the reduction of the use of energy in many applications. This coupled with concerns about climate change and the need to reduce atmospheric carbon dioxide emissions has led to the desire to make oxygen more efficiently than the current cryogenic processes.[1-5] The use of oxygen to burn fuels serves to make carbon capture easier as there is no longer the need to separate nitrogen from the carbon dioxide in the exhaust gases. Also higher temperatures are reached after combustion as there is no heating of the inert nitrogen which in turn leads to better thermal efficiencies on steam (power) generation.

The separation of oxygen from air has traditionally been carried out through cryogenic distillation[3] but more recently the use of ceramic membranes has been advocated.[3] These membranes rely on their ability to be conductors of both electrons and oxygen ions which allows the movement of oxygen through the membrane when exposed to an oxygen pressure gradient. The development of these mixed ionic and electronic membranes has not yet reached commercial operation but a 100 ton per day pilot plant will be operational in late 2013[2], with plans in place to build 2000 ton per day plants for which the building of the ceramic fabrication plant has begun.

The objectives of this study were to develop a synthesis route to produce one of the major candidate materials for oxygen separation membranes, which are in general perovskite structured oxides (ABO_3) and in particular barium strontium cobalt iron oxide (BSCF, $Ba_{0.5}Sr_{0.5}Co_{0.8}Fe_{0.2}O_{3-\delta}$). In particular the aim was to devise a route that uses the minimum amount of reagents especially organic ones which are burnt off during processing and thus create more carbon dioxide. The route also needed to be able to accommodate changes in composition as the ratios of barium to strontium (A site metals) and cobalt to iron (B site metals) were varied and it had to allow the addition of other metals into the system.

A second objective was to investigate the effect on the electrical properties and the oxygen flow of changes in the composition of the BSCF. The compositional changes were varying the ratios of the A and B metals and further to examine the effect of copper additions to the composition. A subsidiary objective was to relate the oxygen flow properties and the measured electrical properties to each other and the other properties of the ceramics.

Finally changes in the structure and surface chemistry would be studied using a combination of high temperature x-ray diffraction and high temperature x-ray photoelectron spectroscopy.

2 Literature Review

Mixed ionic and electronic conductors (MIEC's) are one of the sub sets into which electrically conducting ceramics can be placed. Other types of conducting ceramics include electronic conductors, ionic conductors, resistors (including thermistors and varistors) and superconductors[6]. The combination of electronic and ionic conductivity is in many applications completely undesirable. These applications where mixed conduction is undesirable include oxygen sensors and fuel cells. This is because these applications need a separation of the electronic and ionic charge carriers. When there is no separation short circuits within the component and consequent loss of function occur. Oxide based ionic conductors such as those used in fuel cells and oxygen sensors use an oxygen activity gradient across the component to generate a voltage as the oxygen ions move through the ceramic. The reactions at the two surfaces are: -

High oxygen activity

$$O_2 + 4e^- \rightarrow 2O^{2-} \qquad 2.1$$

Low oxygen activity

$$2O^{2-} \rightarrow O_2 + 4e^- \qquad 2.2$$

The electrons released at the low activity surface are returned to the high activity surface through an external circuit, which gives useful work. The voltage (E) generated is given by the Nernst Equation

$$E = RT/4F\ (\ln\ (a'_O/a''_O) \qquad 2.3$$

Where R is the gas constant (8.314 J K^{-1})

T is temperature (K)

F is the Faraday Constant (9.649x 10^4 $Cmol^{-1}$)

a'_O & a''_O are the oxygen activities at each surface. In most circumstances activity is replaced by partial pressure as oxygen is assumed to be an ideal gas. Therefore equation 2.3 becomes

$$E = RT/4F\ (\ln\ (p_2\ O_2/\ p_1\ O_2) \qquad 2.4$$

Where $p_1\ O_2$ and $p_2\ O_2$ are the oxygen partial pressures at each surface.

A typical circuit is shown below, Figure 1

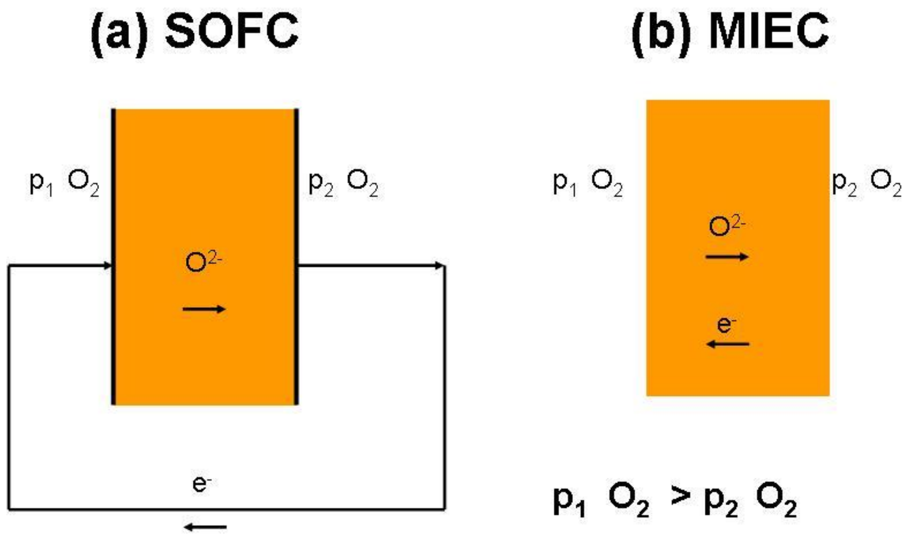

Figure 1 Comparison of solid oxide fuel fell and mixed ionic and electronic conductor (after Sunarso[7])

If there is any short circuit in the oxide conductor then the useful work that can be extracted from the system is reduced.

If all the electrons required for the passage of the oxygen ions flow back through the ceramic then no external electrical work will be available but oxygen will have passed through the ceramic as shown in Fig 1b with an equivalent number of electrons going in the reverse direction to preserve electrical neutrality. This behaviour can be used to produce pure oxygen from air. There are a number of applications for membranes made of such materials, oxygen production, catalytic oxidation and hydrogen production[3, 8, 9].

The mixed ionic and electronic conductors that are used are generally perovskite structured mixed oxides e.g. barium strontium cobalt iron oxide (BSCF, $Ba_{0.5}Sr_{0.5}Co_{0.8}Fe_{0.2}O_{3-\delta}$)[7, 10, 11]. They exhibit significant oxygen ion conductivity over the range 500-800°C.

2.1 Applications

2.1.1 Oxygen production

Pure oxygen is a major industrial raw material; world production is about $100x10^6$ tons/annum[12]. The major applications are steel manufacturing, chemical synthesis and energy production (power stations)[13-15]. The current main processes for oxygen production are cryogenic distillation of liquid air and pressure swing adsorption although the latter is only used for relatively small volumes.[16, 17]

Cryogenic production is done on a large scale with plants typically producing 3000 tonnes/day. The technology is well established however it does have the drawback of requiring large amounts of energy for the compression and cooling required.

The requirement for better processes to produce oxygen is driven by the need to reduce energy consumption and its inherent CO_2 emissions. This is not just a problem at the oxygen production stage.

One of the solutions to the reduction of CO_2 emissions in energy production is carbon capture. This involves collecting the CO_2 generated in the combustion process and then injecting it into suitable rock strata for long-term storage/disposal. In a conventional power station the fuel is burnt in air and the CO_2 in the flue gas is separated from the water, nitrogen and particulate matter. The gas separation of CO_2 and nitrogen is not easy.

If the fuel is burnt with pure oxygen then the difficult separation can be avoided.[1] This can be carried out using either an oxy-fuel burner or gasifying the fuel to form hydrogen, which undergoes clean combustion. Although the operation of membranes is at high temperature, the incorporation of the oxygen production into the power station allows waste heat to be used and reduce the energy requirement compared to a stand-alone unit. Examples of typical plant layouts are given in Figures 2 and 3. The oxygen separation unit which contains the ceramic membrane is the first part of the process in both the oxyfuel combustion and precombustion processes and is to the left of the figure. The mechanical energy input relates to pressurisation of the air to obtain better efficiencies

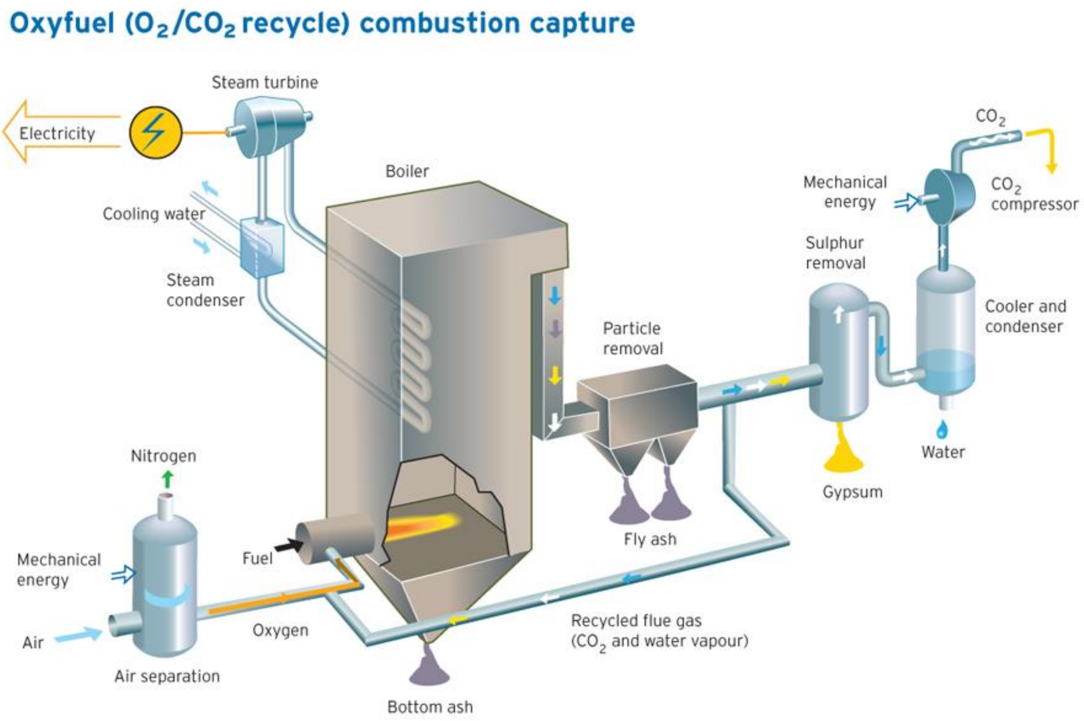

Figure 2 Oxyfuel combustion process plant layout[18]

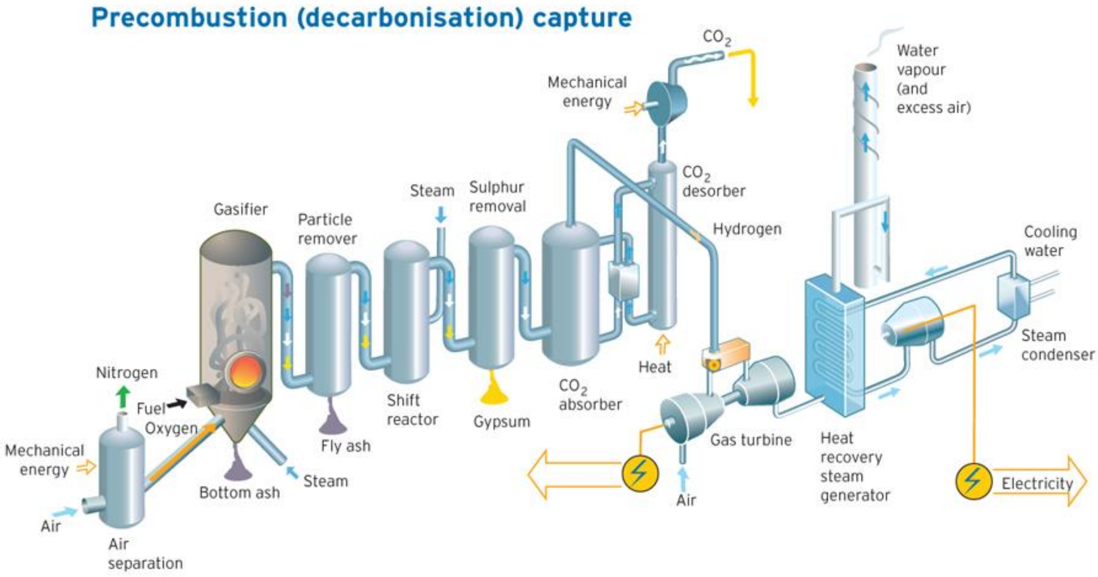

Figure 3 Pre combustion capture plant layout[19]

2.1.2 Catalytic Oxidation

In many chemical processes there is a requirement for an intermediate product to be oxidised[20]. This needs to be controlled to prevent complete oxidation to CO_2 and water. A large number of reagents can be used to effect oxidation but their reduction products need to be separated from the reaction mix. The use of oxygen removes many of these problems though it tends to be less selective towards the partial oxidation reactions[20].

The use of an oxygen membrane to supply the oxygen for the reaction can enable better control of the partial oxidation reactions especially if a suitable catalyst is applied on the reaction side. This approach has been studied for the partial oxidation of methane to produce so called synthesis gas[15].

$$2CH_4 + O_2 \rightarrow 2CO + 4H_2 \qquad 2.5$$

This can be further reacted with steam to produce CO_2 and more hydrogen. These are also examples of the reactions occurring during fuel gasification. Synthesis gas can be used to make many compounds including higher hydrocarbons that make up petrol.

Partial oxidation of methane can also be used to produce methanol, an important chemical intermediate.

$$2CH_4 + O_2 \rightarrow 2CH_3OH \qquad 2.6$$

Through the use of appropriate catalysts and the oxygen partial pressures selectivity to desired reaction can be accomplished.

2.1.3 Hydrogen Production

As part of the need to reduce CO_2 emissions non-carbon containing fuels are being evaluated. The most promising of these is hydrogen as it burns cleanly forming only water. The production of hydrogen is not so easy and despite large amounts being made it is mainly formed through partial oxidation reactions as described above. Electrolysis can also be used but that too relies on electricity from carbon-derived sources.

The use of oxygen separation membranes allows the separation of oxygen and hydrogen produced by the high temperature decomposition of water[21, 22].

$$2H_2O \leftrightarrow O_2 + 2H_2 \qquad 2.7$$

The equilibrium is towards the left but at high temperatures the forward reaction can be forced if the oxygen is continually removed through the membrane. This leaves the hydrogen and steam to be separated.

2.1.4 Fuel Cells

MIEC materials are also of potential use in solid oxide fuel cells as part of the current capture part of the electrodes because their mixed conductivity allows a good electrical contact with both the external circuit (electronic conduction) and the internal circuit (ionic conductivity)[23]. As shown in Figure 1a, the fuel cell electrolyte allows the passage of oxygen ions and the circuit is completed externally. At the interface of the ionic to electronic conduction the oxygen gas must be first adsorbed, dissociated and then take up two electrons to become an oxygen ion. These processes are easier if the substance at the interface is a mixed conductor as both conduction mechanisms can operate in the region of adsorption.

2.2 Materials

The main materials used for oxygen ion conductors are based on the fluorite structure. The conductivity in these systems is optimised by the introduction of aliovalent cations, which generate oxygen vacancies. There has been little success in enhancing the electronic conductivity by introducing cations, which exhibit multiple oxidation states. However the situation is very different in the perovskite based systems where mixed conductivity has been developed extensively.

The perovskite structure (ABO_3) is a cubic structure with a large A cation and a smaller B cation, Figure 4. This structure has been found to be stable over a wide range of compositions. For an ideal cubic perovskite structure the following relation is found[24]: -

$$r_A + r_B = \sqrt{2}(r_B + r_O) \tag{2.8}$$

where r_X represents the ionic radius of the ion in the ABO_3 structure.
For a large number of compounds if

$$r_A + r_B = t\sqrt{2}(r_B + r_O) \tag{2.9}$$

When t is in the approximate range 0.8 to 1 then a perovskite structure is stable although it may be slightly distorted from the ideal cubic one.[25]

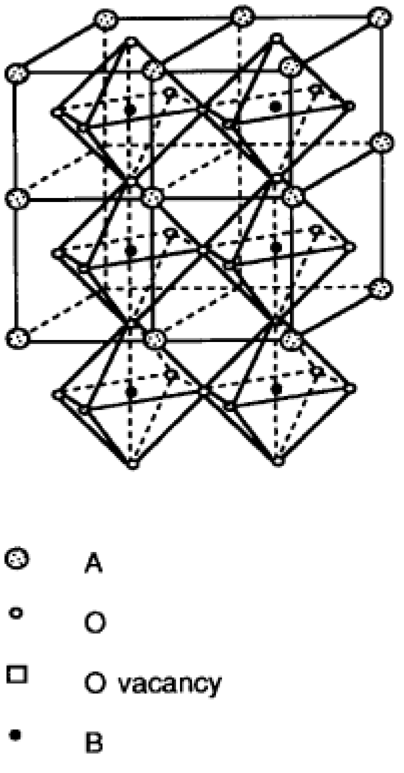

Figure 4 Perovskite structure[20]

In general, for mixed ionic and electronic conductors, the B cations can have multiple oxidation states, these enable charge transfer and electronic conductivity.

$$B^{n+} + B^{(n-1)+} \rightarrow B^{(n-1)+} + B^{n+} \tag{2.10}$$

or

$$B^{n+} + e^{-} \rightarrow B^{n-1} \qquad 2.11$$

$$B^{(n-1)+} \rightarrow B^{n+} + e^{-} \qquad 2.12$$

The larger A cations generally have a single oxidation state and are not involved directly in electronic conductivity.

The oxygen ion conductivity occurs by oxygen ion hopping from a lattice site to a neighbouring vacancy. In an ideal perovskite the charges on the A and B cations add up to 6, this can be any combination of 1-5, 2-4 and 3-3 as long as the tolerance factor is within the normal limits. Vacancies can form if the multivalent cation is present in more than one oxidation state. The formula for the perovskite is then $ABO_{3-\delta,}$ where δ represents non-stoichiometry. The determination of δ and the oxidation state of the cations will be discussed later (Section 3.2.3).

As the value of δ gets larger brownmillerite ($A_2B_2O_5$) structures can be formed. (Figure 5) These structures differ from perovskites in that the oxygen deficiency has increased (δ=0.5) and a stable structure results often with ordering of both the cations and the oxygen vacancies. It is related to the perovskite structure by the removal of oxygen ions along [110] [26-29]. However there have been reported stable structures with δ>0.5, which do not have the Brownmillerite structure, these materials do not have ordered vacancies[30].

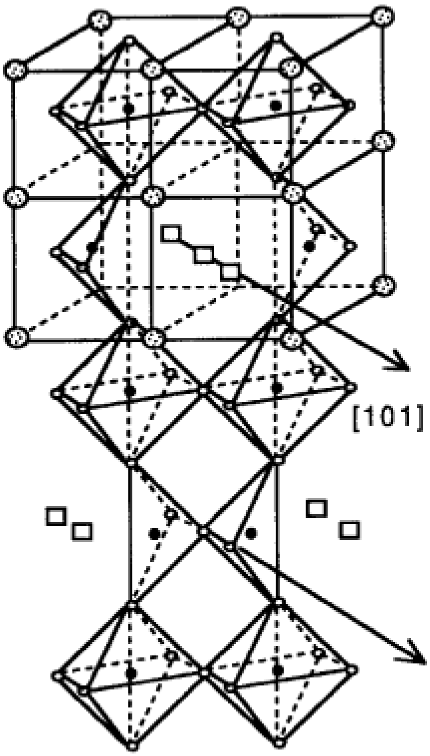

Figure 5 Brownmillerite structure[20]

The most common MIEC compositions were based on $SrCoO_3$[23]. It was found that a number of different phases based on the perovskite structure could be formed but the cubic phase exhibited the best oxygen permeability.[27, 31] However it did not have a good thermal stability and transformed to the other phases with poorer properties. This meant that variants on the composition were sought which gave the required stability. The composition changes were to use lanthanides on the A site and other transition metals on the B site.[32, 33] Some workers were modifying $LaCoO_3$ which was used as a catalyst composition. The result of this work was that $La_{0.6}Sr_{0.4}Co_{0.8}Fe_{.2}O_{3-\delta}$ was found to give the best oxygen permeability.

This structure has 3+ and 2+ ions on the A site, this will reduce the oxygen vacancies as extra oxygen ions will be needed to maintain overall electrical neutrality. This reduction in the oxygen vacancies causes a reduction in the oxygen permeability[11]. Therefore the substitution of La^{3+} with Ba^{2+} would enable the vacancy concentration to be restored without affecting the thermal stability. The composition $Ba_{0.5}Sr_{0.5}Co_{0.8}Fe_{0.2}O_{3-\delta}$ was shown to have both good stability and oxygen permeability.[10] The effect of changing the barium strontium ratio was further studied.[11]

The effect of changing the barium to strontium ratio is to change the tolerance factor for the composition. In order to calculate the tolerance factor, the ionic radius for each ion needs to be known. In the case of non-stoichiometric compounds, such as these, there is also a need to know the oxidation state of each ion. This is not easily determined (see section 2.4.3). One method is to assume the ions have fixed oxidation states and calculate the tolerance factors accordingly. In $Ba_xSr_{1-x}Co_{0.8}Fe_{0.2}O_{3-\delta}$, this has been done[11] (Figure 6) In this figure, **s** represents M^{4+}, **s'** represents M^{3+} and **s"** represents M^{2+}. The line for M^{3+} is the one which shows tolerance factors around 1 and thus could be taken to be the most stable state in terms of the geometry of the perovskite structure. However this corresponds to a delta value of 0.5 which corresponds to the brownmillerite ordered vacancy structure which has poor permeability properties.

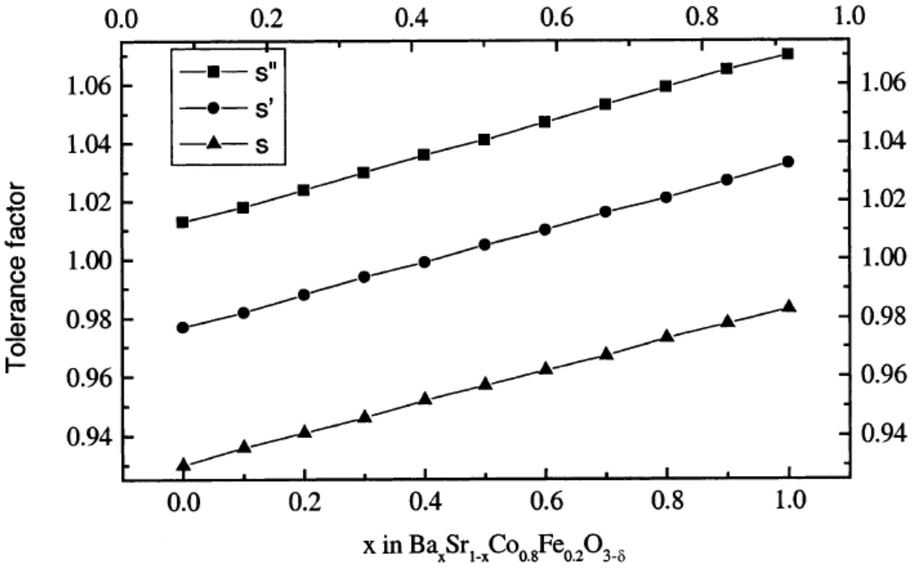

Figure 6 Tolerance factors as a function of oxidation state (from Shao[11])

It was found that except at the extremes of composition the cubic structure was stable.[11] Another study carried also tried to find the optimum composition to give a stable structure but the oxidation states used for iron and cobalt were fixed based on the oxygen content.[34] (Figure 7). It does show the effect of the substitution of lanthanum into the system in that it lowers the tolerance factor.

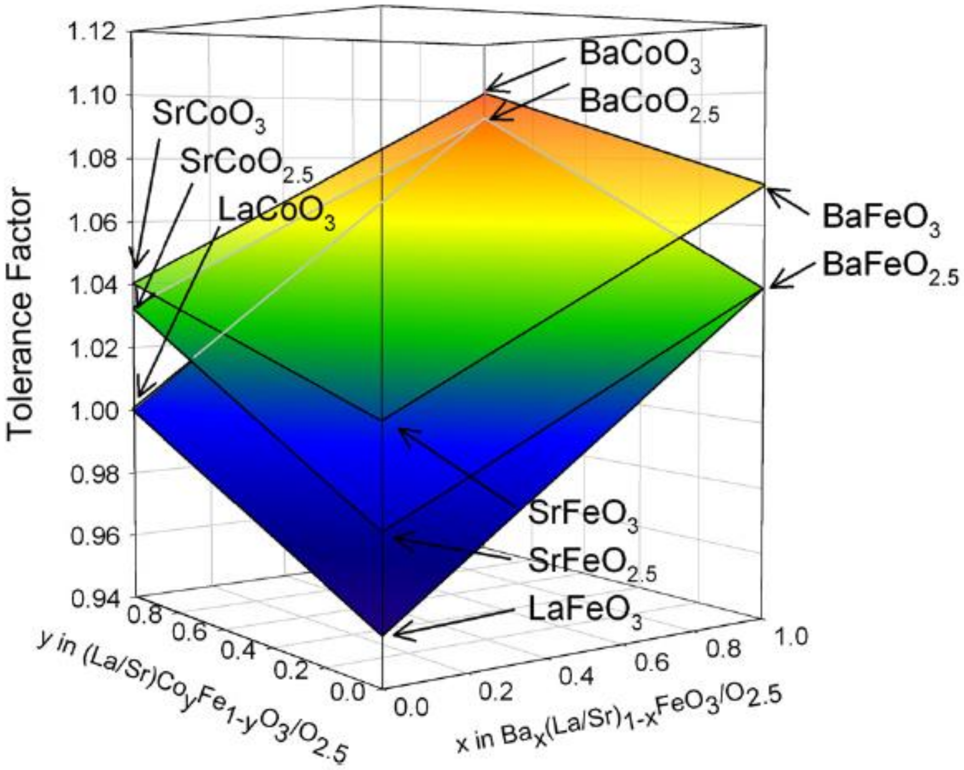

Figure 7 Tolerance factors variation with composition (from Svarcova[34])

There have been many studies on compositional variants of $SrCoO_3$ with the strontium being replaced by lanthanum, barium and other rare earths[7, 32, 33]. Similarly the cobalt has been replaced with other transition metals most notably iron though others including Ga[35, 36] and Zr[9, 37, 38] have been used.

The change in A site cation affects the oxygen conductivity by both introducing vacancies if its oxidation state is less than 3 and altering the lattice parameter. As the lattice parameter is increased the space between the larger ions also increases. This space is the pathway for ion hopping which can therefore become easier. Larger cations thus increase the oxygen ion conductivity, however this is often at the expense of structural stability.

The B site substituents have less effect on the lattice parameter but affect both the electronic charge transfer and the defect concentration as a result of their mean oxidation state.

Although the compositions were originally based on $SrCoO_3$, $Ba_{0.5}Sr_{0.5}Co_{0.8}Fe_{0.2}O_{3-\delta}$ is the leading candidate as it has one of the highest oxygen permeabilities[10].

2.3 Synthesis

The synthesis of MIEC compounds has been carried out using the standard methods[7, 39] used for mixed metal oxides, mixed powder, sol-gel, organic gel (Pechini[40] and variants) and co-precipitation[41]. The object of all the synthesis routes is to produce a chemically homogenous powder, which will sinter at low temperatures to form a fully dense single-phase ceramic. Each of the routes has a number of advantages and disadvantages as will be discussed below with respect to BSCF.

2.3.1 Solid State Reaction

In many ways this is the simplest procedure, the constituent oxides are mixed together and heated until they react and form the desired compound. The oxides can be replaced by hydroxides and carbonates for this process. Also a solution of salts of the metals can be dried and then calcined. The simplicity of the process though its chief advantage does bring some disadvantages. The reactions between the components may take place at different temperature which coupled with grain growth of the initially formed phase may not allow complete homogenisation of the final product. The product is often agglomerated and needs intensive milling prior to forming and sintering. The use of salts may not give a very homogeneous dried product because of their different solubilities. The salt with the lowest solubility crystallises first and then the other salts crystallise in turn. This can lead to crystals with composition gradients from the centre to the outside or a mixture of the various salts. This can be overcome by drying rapidly using processes such as spray or freeze-drying. Overall the mixed powder process has few variables and is therefore not amenable to much optimisation.

2.3.2 Sol-Gel

There are a number of processes that can be called sol-gel they all involve the hydrolysis of a solution to give a sol which then forms a gel which is dried and calcined to give the desired compound. The conditions of the hydrolysis are carefully controlled in order to give a homogeneous sol prior to gelation. The major problem of this process is the difference in reactivity of the components so that a series of sols form which yield an inhomogeneous system. There are however many variables in terms of starting materials, the conditions of hydrolysis and subsequent stages that can be varied which allow good control of the powder properties.

2.3.3 Organic Gel

This is one of the most commonly used methods as it is in some ways a variation on the drying and calcination of salt solutions. In order to prevent the separation of the metal compounds the solution is gelled as a whole prior to drying. Pechini did this by adding ethane-1,2-diol and citric acid to the solution and heating it until gelation. More recent variations are to use EDTA and citric acid[42] with the gelation being controlled at a specific pH by the addition of ammonia. It is a relatively easy route to carry out but does have a number of disadvantages. The gel is quite voluminous relative to the final oxide content and usually contains organic material, nitrate and ammonia. These could combine during the drying and calcination phase to form explosive mixtures.[39] This behaviour has been described in a number of ways e.g. Baumann et al[43], "*Inside a fume hood, this mixture was then heated up until a spontaneous combustion occurred.*", Bi et al[44] "*the solution was heated under stirring to evaporate water until it changed into a viscous gel and finally ignited to flame, resulting in a black ash.*" and Moharil et al[45] "*When the heating was continued further, the gel catched a burning flame itself and charred completely resulting into a light and fragile ash*". In any case the nitrate will decompose giving off noxious fumes.

After gel formation the system is either dried or heated to combustion, this is prior to calcination. The formation of different phases at this stage has given mixtures of $BaCO_3$, $BaFe_2O_4$, CoO, SrO and Fe_2O_3[42]. In another study[46] a different set of phases was found, namely, $Ba_{0.5}Sr_{0.5}Co_{0.2}Fe_{0.8}O_{3-\delta}$, $BaCO_3$ and $CoFe_2O_4$. In a similar preparation of $Ba_{0.5}Sr_{0.5}Co_{0.8}Zn_{0.2}O_{3-\delta}$ no crystalline phases were found until a calcination temperature in excess of 700°C was used[47]. At that temperature the powder comprised barium-strontium carbonate, a zinc-iron spinel and zinc oxide, which at higher temperatures formed a single phase material. A simplification of the method was reported[48] which just used ethylene diamine N,N,N',N' tetra N-acetyl diamine as the complexing agent to replace EDTA, citric acid, nitric acid and ammonia as the earlier system needed careful pH control to prevent precipitation prior to gelation.

The decomposition of the metal compounds occurs at different temperatures, which may give some inhomogeneity as found in the solid state method. However the crystallite size may be much smaller and allow better homogeneity. Oxides may form at low temperatures but then adsorb CO_2 from the combustion of the organics to form less reactive carbonates.

2.3.4 Co-precipitation

The addition of a precipitant to a mixed metal solution is seemingly a simple process. However the different components have to be both soluble at the starting point and ideally all insoluble at the same point during the precipitation process. If the latter cannot be achieved because the precipitation of the solute species occurs in stages as the solubility is reached as either the pH rises or the precipitant concentration increases, then techniques such as continuous and reverse precipitation can be employed. (Forward precipitation is the process whereby the precipitant is added to the mixed metal salt solution.) In these latter methods precipitation occurs under conditions where there is always an excess of precipitant, which ensures simultaneous precipitation of all species. With forward precipitation the least soluble component precipitates first followed sequentially by the others. There are many variables in this process, temperature, anions, concentration, precipitant and pH, which allow variations to be made or control difficult. Drying often leads to leads to the formation of hard agglomerates, which are difficult to break down either before or after calcination.

Pelosato et al[49,50] used ammonium hydroxide solution and ammonium carbonate to prepare $La_{0.8}Sr_{0.2}Ga_{0.8}Mg_{0.2}O_{3-\delta}$ and $LaMnO_3$, $La_{0.7}Sr_{0.3}MnO_{3-\delta}$, $La_{0.8}Sr_{0.2}FeO_{3-\delta}$

and $La_{0.75}Sr_{0.25}Cr_{0.5}Mn_{0.5}O_{3-\delta}$. Their aim was to achieve complete precipitation and only have impurities (nitrates, carbonates and the ammonium ions) which would be readily lost on calcination. In the case of $La_{0.8}Sr_{0.2}Ga_{0.8}Mg_{0.2}O_{3-\delta}$, when ammonium hydroxide solution was used as the precipitant, strontium and magnesium were detected in the filtrate. This was also the case when the mixed nitrates were added directly to an excess of ammonium carbonate. Minor magnesium losses only occurred when the mixed nitrates were added to a stoichiometric amount of carbonate after the starting solution was reduced in pH to 1 by the addition of nitric acid. In the second group of oxides an excess of ammonium carbonate was found to be necessary in order to obtain complete precipitation. It is clear that a generic method e.g. addition of excess ammonium carbonate as the precipitant to an acidified mixed salt solution will not always work. The method chosen must reflect the actual composition being synthesised.

Toprak et al[51] had problems using sol-gel methods used for the synthesis of $Ba_{0.5}Sr_{0.5}Co_{0.2}Fe_{0.8}O_{3-\delta}$, as their active powders reacted with their crucibles and substrates during calcination and sintering, respectively. Their solution was to use a co-precipitation technique using oxalate as the precipitant. Using Medusa software[52] they found that in the pH range of 2-3 all the ions precipitated completely (apart from Fe^{2+}). The addition of oxalic acid to the mixed salt solution only precipitated 80% of the iron present in solution so they added an extra 20% iron nitrate to compensate which enabled the correct stoichiometry to be obtained at the end of the synthetic route. The precipitates were dried at 110°C before carrying out thermogravimetric analysis. This showed 4 decomposition steps starting at ~100°C, 375°C, 420°C and 790°C. Powder was calcined after each of these stages and examined by XRD. At all temperatures a number of different phases were present before the single phase perovskite was formed at 1000°C.

2.3.5 Finishing Processes

There are a number of additional stages that can be included in the 3 wet processes[41]. Hydrothermal or solvothermal treatments can affect the powder properties especially homogeneity and crystallinity prior to drying and calcination.[53]

The drying stage can be varied and includes freeze and spray drying. The temperature used affects the agglomeration and decompositions occurring at this stage. Calcination can be carried out under different atmospheres, which may affect the final product.

The formation of a single phase perovskite after calcination has been described by many authors with a variety of pathways from the initial precipitate or gel. The formation of a single phase in BSCF has been shown to occur through a number of different structurally related phases and after time at temperature may decompose into a relatively stable two phase composition before forming the single cubic phase. These two phases are a cubic and a hexagonal perovskite which differ in their stacking sequences based on the close packing of the A and O ions[54]. However other studies have shown a single stable phase being formed directly on calcination from a mixed carbonate of the A site cations and a spinel formed from the B site cations[55]. Two reaction schemes are shown in Figure 8 and Figure 9. These differences are based on the preparative route and the degree of homogeneity achieved in the production of the powder that is calcined. This starting powder may have ultrafinely dispersed phases present which may not be detectable using x-ray diffraction.

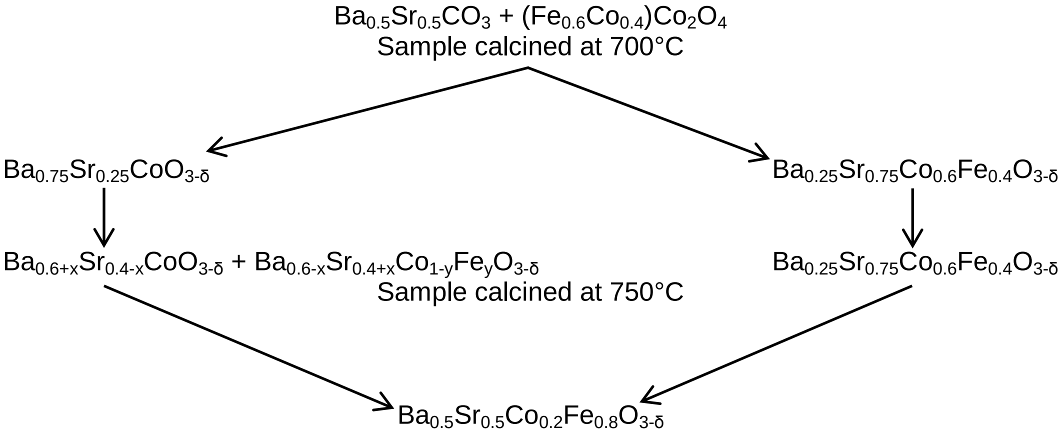

Figure 8 Reaction scheme of the calcination of BSCF (after Arnold[54])

$$BaCO_3 + BaFe_2O_4 + CoO + SrO + Fe_2O_3$$

$$\downarrow 750°C$$

$$BaFe_2O_4 + Ba_6Co_4O_{12} + SrCoO_3 + Sr_2Fe_2O_5 + BaFeO_{3-\delta}$$

$$\downarrow 900°C$$

$$Ba_{0.5}Sr_{0.5}Co_{0.2}Fe_{0.8}O_{3-\delta} + BaFeO_{3-\delta} + BaFe_2O_4 + CoO + BaO$$

$$\downarrow 950°C$$

$$Ba_{0.5}Sr_{0.5}Co_{0.2}Fe_{0.8}O_{3-\delta}$$

Figure 9 Reaction scheme of the calcination of BSCF (after Patra[42])

One of the problems in identifying the reaction sequence during the calcination step is that the phases present have similar structures and have small crystallite sizes. The phases can exist as solid solutions with substitution of Sr by Ba and Fe by Co and vice versa. This means that changes in composition cause a variation in lattice parameter which is manifested by a broadening of the diffraction peaks. This broadening is in addition to that from the small crystallite size. The number of distinct diffraction peaks is often small and identification of phases can be made on less than 3 peaks.[42]

2.4 Properties

2.4.1 Oxygen Permeability

Oxygen permeability is the most important property for MIEC's. For good operation in all applications, a high stable oxygen flow must be obtained over the approximate temperature range 600-1000°C with a preference for lower temperatures. The operating conditions can affect the stability of the ceramic. The driving force for the oxygen flux is an oxygen activity gradient across the ceramic. This gradient can be generated in a number of ways as is shown in Table 1.

High O_2 Activity	Low O_2 Activity	Comment	Ref
Air	Helium	Used in laboratory measurements	10
Air	Vacuum	Oxygen separation	13
Air	Methane	Partial Oxidation	20
Air	Flue gas	Oxygen separation in Oxy-Fuel	1
Steam	Vacuum	Hydrogen generation	22

Table 1 Atmospheres present during permeability measurements

The low activity side of the ceramic is in either a neutral or reducing atmosphere. Both sides may also have carbon dioxide present either from the atmosphere or poor selectivity in systems used for partial oxidation reactions.

The equipment used for oxygen permeability measurement is generally similar. The oxygen flow through the test piece is measured from its concentration in the sweep gas. Techniques for this measurement include mass spectrometry[56], potentiometric cells[57] and gas chromatography[58, 59]. Leakage through the system is compensated for through the measurement of nitrogen concentration in the sweep gas,

2.4.1.1 Mechanism of Permeation

The permeation of oxygen through a mixed ionic electronic conductor membranes occurs because of a difference between the chemical activity (partial pressure) of oxygen on each side of the membrane. The rate of permeation is dependent on a number of different factors. In addition to the chemical potential difference, membrane thickness, ionic and electronic conductivity are also of importance. However the surface exchange properties of oxygen gas with the membrane on both sides is also important and can be the rate determining step in the process of permeation. The permeation behaviour of MIEC's was analysed by Bouwmeester et al using Wagner theory for oxide formation on metal surfaces.[60]

Wagner theory describes the oxygen flux through a mixed conductor and may be described by the following equation.

$$J_{O_2} = -\frac{RT}{16F^2L}\int_{\ln pO_2'}^{\ln pO_2''}\frac{\sigma_e\sigma_i}{\sigma_e+\sigma_i}\delta\ln(pO_2) \qquad 2.13$$

Where J_{o2} is the oxygen flux (mol m^{-2} s^{-1})

R is the gas constant (8.314J $mol^{-1}K^{-1}$)

T is temperature (K)

F is the Faraday constant (9.649x 10^4 $Cmol^{-1}$)

L is the membrane thickness (m)

σ is the conductivity (Sm^{-1})

p_{O2} is the oxygen partial pressure

In practice the electronic conductivity is much higher than the ionic conductivity $\sigma_i \ll \sigma_e$.[5] The chemical potential difference $\Delta\mu_{O_2}$ can be calculated and simplifies equation 2.13

$$\Delta\mu_{O_2} = RT\frac{\partial\ln(pO_2)}{\partial x} \qquad 2.14$$

Substituting into 2.13 gives

$$J_{O_2} = -\frac{\sigma_i}{16F^2L}\Delta\mu_{O_2} \qquad 2.15$$

Thus it can be seen oxygen flux is proportional to the ionic conductivity and oxygen potential difference and inversely proportional to membrane thickness.

However there is also a chemical process at both surfaces, the reversible exchange of oxygen from the gas to solid phase. This occurs through a number of stages, which are described in the forward direction ie at the high pO_2 side. The reverse occurs on the other side.

Firstly gas adsorption

$$O_{2(g)} \leftrightarrow O_{2(ad)} \qquad 2.16$$

Charge transfer

$$O_{2(ad)} + e' \leftrightarrow O'_{2(ad)} \qquad 2.17$$

Charge transfer and dissociation

$$O'_{2(ad)} + e' \leftrightarrow 2O'_{(ad)} \qquad 2.18$$

Charge transfer

$$O'_{(ad)} + e' \leftrightarrow O''_{(ad)} \qquad 2.19$$

And finally the ions become part of the crystal structure.

$$O''_{(ad)} + V_O^{\bullet\bullet} \leftrightarrow O_o \qquad 2.20$$

There is an equilibrium constant for each of the above equations, each of which could be the rate limiting step for the adsorption process. The kinetics of the reactions above are a function of the concentrations of all the reactive species together with the activation energies of all the processes. The reaction rate constant for oxygen exchange has been shown to increase with vacancy concentration in a series of materials with different compositions[61]. The kinetics have been improved through the use of catalytic metal coatings which enhance the adsorption and dissociation steps[58, 59, 62].

For any membrane being used there are thus 3 principle regions of interest which control the flux through it, the adsorption of oxygen from the high pO_2 gas phase into the ionic structure, the transfer of oxygen through the membrane and finally desorption from the ionic structure and release into the low pO_2 gas phase. Therefore for optimum performance many parameters have to improved, for the ceramic reduced thickness and higher ionic conductivity give better oxygen flux (Equation 2.15). As the thickness is reduced then the flux limiting steps are surface exchange related.[60] There is thus a critical thickness (L_c) at which the surface exchange predominates as the rate limiting exchange. The values of L_c have been found to be in the range of microns to millimetres.[5] Also as the temperature varies the value of L_c also varies[59], this means that in the Arrhenius plot of ln(oxygen flux) against 1/T there is a break in slope corresponding to the transition from bulk diffusion to surface exchange control with high and low temperature activation energies of 0.2 and 0.4eV(19 and 38kJ mol^{-1}).

A number of studies have also shown in an Arrhenius plot an inflection indicative of a change in the conduction mechanism[63]. These changes have been related to changes in phase, spin state of the cobalt and order-disorder transitions[10, 64-66]. The dominant effect is however the surface exchange to bulk diffusion as this corresponds more closely to the thickness data.

Thus the overall factors, which have been shown to influence the oxygen flux, are temperature, composition, phase, microstructure, specimen thickness and oxygen partial pressure difference.

Compositional changes have been the chief means used to improve the properties of MIEC's. The addition of barium or strontium to $LaCoO_3$ and the eventual removal of lanthanum coupled with the introduction of iron have given better oxygen fluxes. Typical values are $5x10^{-6}$ mol $s^{-1}cm^{-2}$. The oxygen partial pressure gradient used in the measurement is often given but not used in calculating the oxygen flux and therefore comparisons of data are difficult.

Changes in the phase of ceramic also alter the oxygen flux. Loss of oxygen from the ceramic is a contributory factor in phase stability. Variation in δ has been studied and correlated with phase stability and oxygen partial pressure. In some cases reduction of the ceramic occurs through reaction with the sweep gas. Carbon dioxide has been shown to poison the system by adsorption on the reductive side of the membrane, though the effect is reversible[67].

Cobalt(3+)(d^6) has a low spin state in octahedral environments as is present in the perovskite structure. Loss of oxygen and defects distort the electrostatic field and can allow a high spin state to occur. Electron transfer is easier in the high spin state because less energy is needed for activation of the electron transfer process. Such changes have been given for variation in oxygen flux although electron transfer has not been identified as the rate-determining step in the oxygen transfer process.[54]

A number of studies have shown improved flux with thin samples[59, 60]. This has been attributed to a change in the rate determining step for the oxygen transfer process from oxygen hopping to the surface reaction of oxygen gas adsorbing, splitting and forming oxide ions[59, 60]. The surface vacancy concentration on each surface is also important as this affects the kinetics of oxygen exchange prior to ion diffusion through the bulk[68]. The two rate determining states and the oxygen vacancy concentration which is itself dependent on the local oxygen partial pressure and temperature combine to complicate the interpretation of permeability data.

The influence of microstructure has not been extensively studied partially due to the difficulty in making materials of high density and uniform phase. Increase in grain size has shown increased oxygen flux and no separate phase was found at the grain boundaries[69]. The densification rate has been shown to be slow and long sintering times and slow heating rates are used[70, 71]. One problem, which some workers but not all have reported, is the melting of the material[56]. The role of grain size has also been shown to be insignificant[56]. Consequently the roles of grain boundary and bulk grain processes have not been studied.

Changes in the microstructure have been observed on both sides of the membrane after oxygen permeation experiments. The perovskite phase disappears on the reductive side whereas no phase change occurs on the oxidative side. Changes in composition have been seen using EDS[72].

2.4.2 Electrical Properties

The electrical properties of MIEC's have been studied although in most cases they are part of a complete fuel cell[64, 73, 74]. Changes in conductivity both positive and negative have been observed in fuel cell structures as the measurement atmosphere has been changed between oxygen, air and argon. Measurement of pure nano-crystalline BSCF showed an improvement over conventional BSCF, the conductivity reaching a plateau at ~700K [75, 76].

One study measured the conductivity of $Ba_{0.5}Sr_{0.5}Co_xFe_{1-x}O_{3-\delta}$ over a range of temperatures and for x=0.8 oxygen partial pressure[77]. The behaviour seen with temperature varied with a maximum in conductivity at ~500°C being seen in all samples except x=1 which showed a continuous increase.(Figure 10) The maximum conductivity was associated with the onset of mobile oxygen vacancies. Further temperature increase gave loss of oxygen which resulted in a higher oxygen vacancy concentration and a reduction in the iron and cobalt oxidation state. Thus the number of electronic carriers is reduced.

In addition to direct current measurements of conductivity alternating current methods have been used to measure the electrical properties of mixed conductors. The details of the technique will be discussed later (Section 3.7). These techniques can allow more information about the material to be obtained.

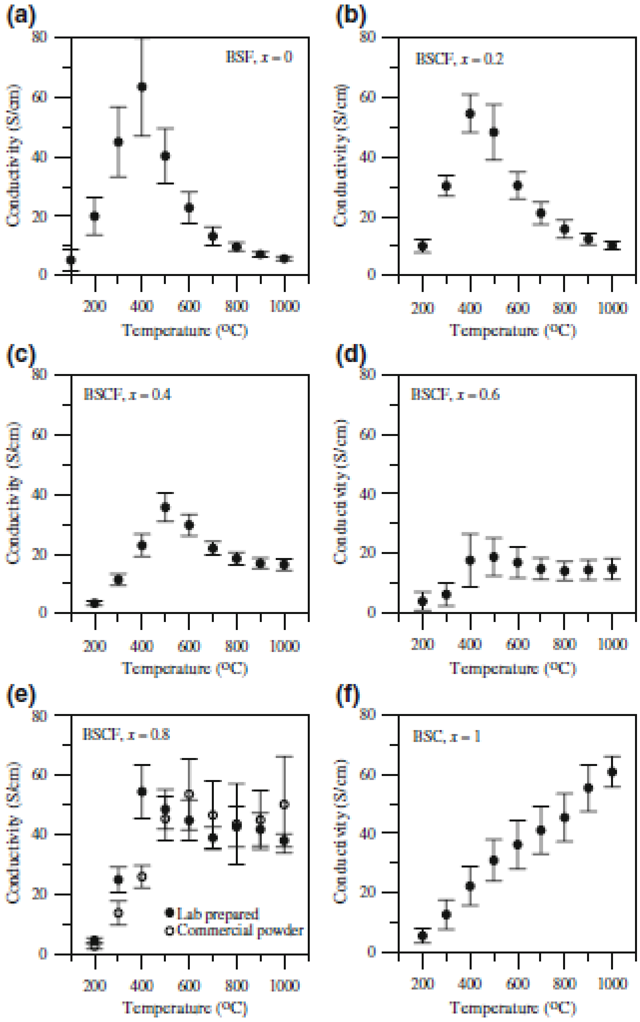

Figure 10 Variation of conductivity with temperature for different composition of BSCF (from Jung[77])

In contrast to purely ionic conductors e.g. tetragonal yttria-zirconia, which only have oxygen ions as mobile charge carriers, mixed ionic-electronic conductors have both electrons and oxygen ions as charge carriers. The combination of the two carriers gives rise to two parallel sets of conduction pathways. The electrons have one set of parameters for their conduction properties and the oxygen ions another. This means that the electrical models used for the results from ionic conductors may not be suitable for mixed conductors. A number of different models have been developed for the behaviour of mixed conductors.[43, 78-83](Figure 11).The measurement of electrical properties and the subsequent analysis frequently rely on the use of blocking electrodes which only allow the passage of one of the charge carriers usually the oxygen ions[43, 61, 81]. These charge blocking electrodes are therefore frequently ionic conductors such as tetragonal yttria-zirconia. When these electrodes are placed either side of the mixed conductor only oxygen ions can pass across the interface from the mixed conductor into the blocking electrode. Therefore only the oxygen ion conduction is measured.

The model shown in Figure 11 consists in part a of two parallel series of electrical components one series represents the ionic pathway and the other is the electronic pathway. The two are connected via a number of capacitors. At the end, which is marked interface, is a blocking electrode which does not allow the passage of electrons and therefore has a capacitor present.

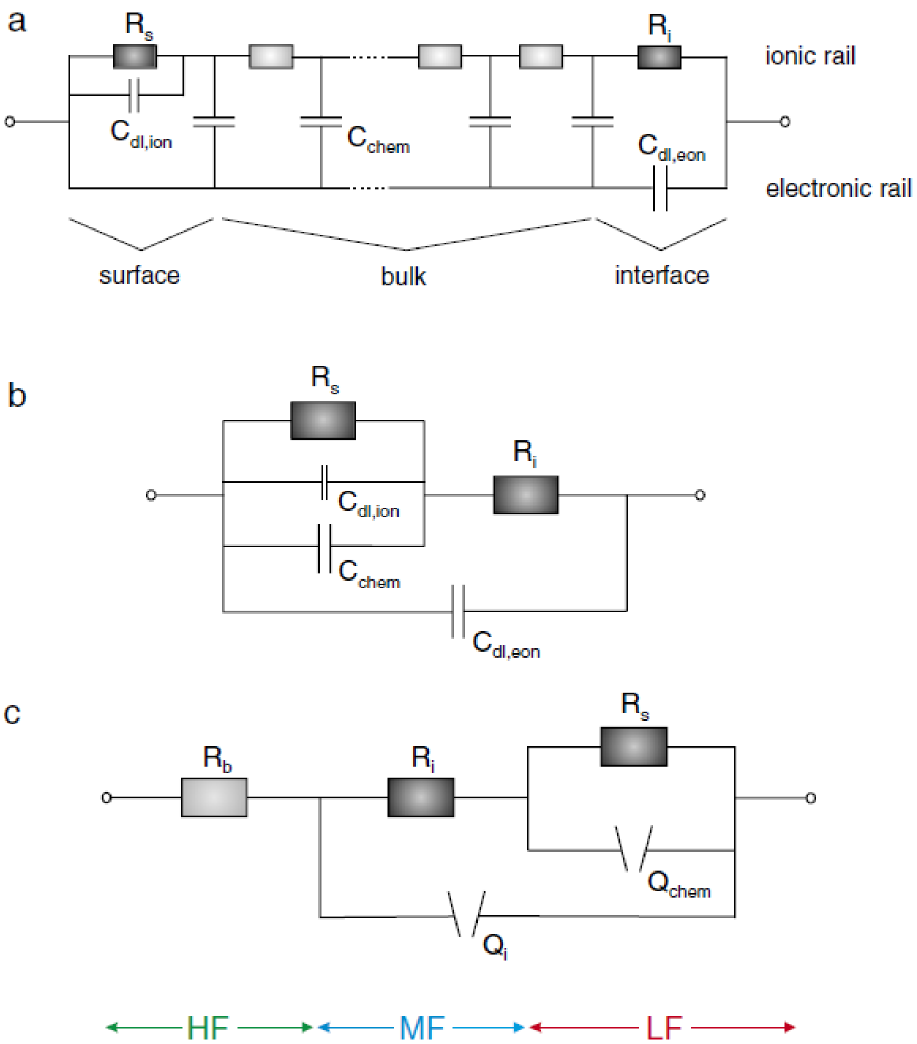

Figure 11 Circuit diagram for mixed conductor with blocking electrodes (from Baumann[81])

The two lines are simplified and the components further grouped to yield the model in b. This is further simplified to give the model c which comprises of three resistors and two constant phase elements (Q).(see section 3.7 for details of constant phase elements) The high frequency (HF) medium frequency (MF) and low frequency (LF) portions of the model are shown also. The component Q_{chem} is a chemical based constant phase element and is related to the surface exchange of the oxygen.[81]

In some studies[84-86] of the complex impedance properties of mixed conductors as electrodes in fuel cells the Nyquist plot (see section 3.7) shows positive values of Z” (the imaginary part of the impedance)(NB the direction of the ordinate is reversed).(Figure 12) These parts of the plots are generally not commented although they can be attributed to inductances in the measuring system at high frequency.[86, 87]

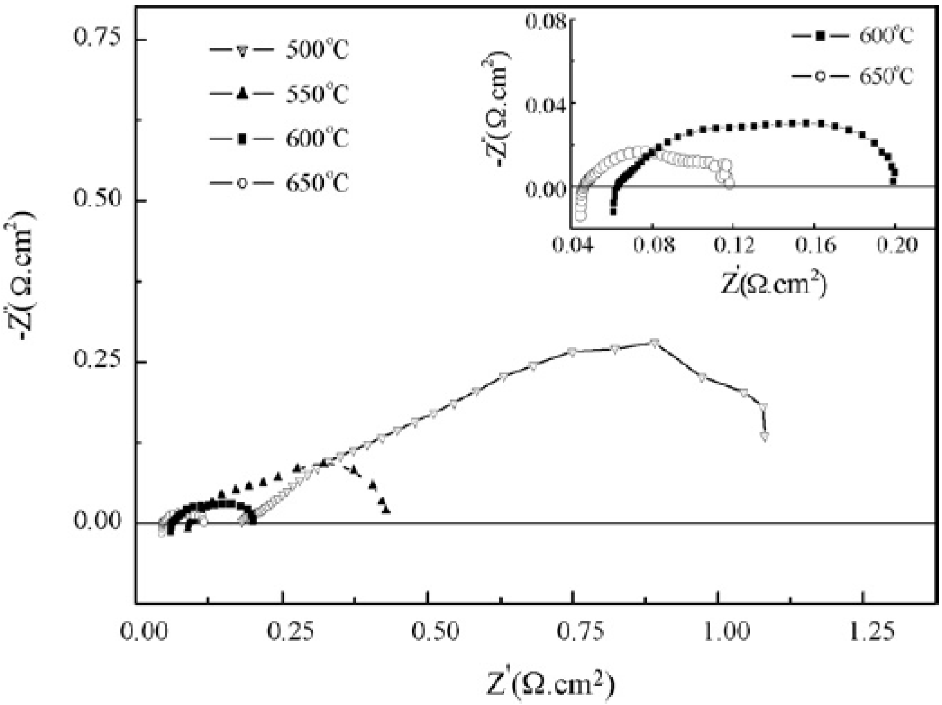

Figure 12 Impedance plot of MIEC cathode containing fuel cell (from Li[84])

In the case of BSCF, it has been shown using conductive mode microscopy at room temperature, that the electronic conduction in the grains and across the grain boundaries was similar.[88] (Figure 13) The image intensity from the current showed no change in slope between the two applied electrodes. This uniformity of behaviour across and within grains would simplify any modelling of the electronic part of the conductivity.

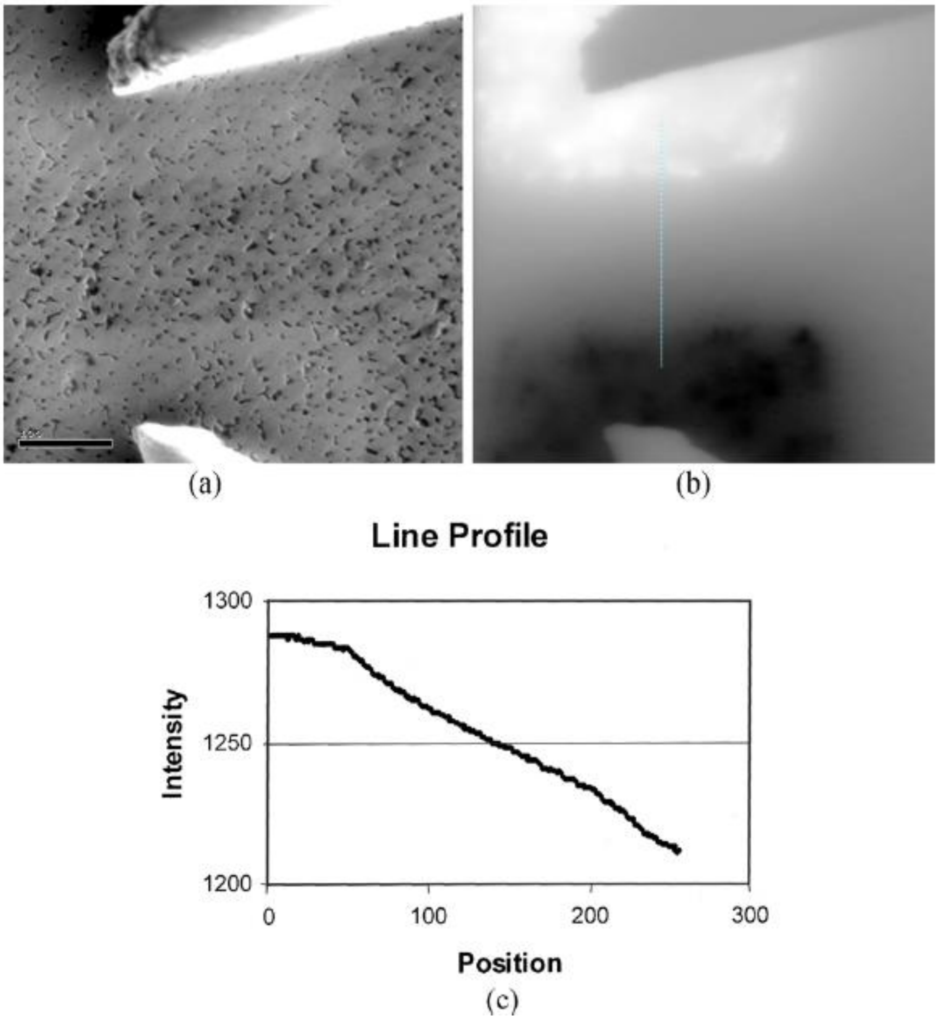
(a) (b)

(c)

Figure 13 Conductive mode microscopy of BSCF (a) Secondary electron image (b) conductive mode image (c) line profile between two electrodes(from Salehi[88])

2.4.3 Stoichiometry

As has been discussed above the role of the oxygen vacancy concentration has a profound effect on the oxygen permeability and stability of the MIEC.

A number of different methods have been adopted for measuring the value of δ in $Ba_{0.5}Sr_{0.5}Co_{0.8}Fe_{0.2}O_{3-\delta}$ especially at elevated temperature. The most common method is thermal gravimetric analysis and the weight loss as the material is heated is measured[89]. This needs a value of δ for the starting point or finishing point. If heated in a hydrogen atmosphere the following reaction occurs: -

$$Ba_{0.5}Sr_{0.5}Co_{0.8}Fe_{0.2}O_{3-\delta} + H_2 \rightarrow 0.5BaO + 0.5SrO + 0.2Fe + 0.8Co + H_2O \qquad 2.21$$

If the relative proportion of metal ions at the start (or the finish) are known and the weight at the end of the reduction a starting value of δ can be calculated assuming the products are as shown in equation 2.21. It is important also to ensure any adsorbed surface species, for example, water and carbon dioxide, are either removed prior to measurement or otherwise allowed for in the calculations[90].

Iodometric titration has also been used to determine the vacancy concentration. The sample is dissolved in acid and reacted with excess iodide prior to titration with thiosulphate[90]. Similar titrations have been carried out using Cu^+ and Fe^{2+} as the oxidant[91]. Care has to be taken in all the titrations to ensure complete dissolution and to prevent oxidation by air.

The stoichiometry has been shown to vary with temperature and time, and shows hysteresis on cooling. This change in vacancy concentration affects the long-term stability of the oxygen flux. Coupled with the change in δ is an associated compensatory change in the oxidation states of the iron and cobalt. For a value of $\delta = 0$, the oxidation state of the B site ions, if the A sites are occupied by strontium and barium, is 4+. However as δ moves to 0.5 then the oxidation state will reduce to 3+. These formal oxidation states are however the overall state and individual ions can be higher or lower. With values in the range of $0 < \delta < 0.5$, then there must be a mixture of oxidation states as otherwise fractional charges would be present.

For BSCF compositions, the determination of δ and thus the oxidation state of the B site cations has also looked at how the fractional charge has been distributed between the iron and cobalt. One study looked at the stoichiometry as a function of the cobalt-iron ratio.[92] They used two techniques iodometric titrations and thermogravimetry including hydrogen reduction. They assumed that the iron oxidation state behaviour on heating was constant over all compositions and that the cobalt changed independently. The sample with no cobalt was taken as the baseline for calculating the cobalt oxidation state. Their results showed that over the temperature range from room temperature to 900°C cobalt had a net oxidation state 0.3 to 0.1 lower than iron. Their ranges were, for $3-\delta$, 2.65 at room temperature to 2.35 at 900°C and the corresponding oxidation states were 3.3 to 2.6. This indicates the presence of 4+, 3+ and 2+ oxidation states.

Another study showed lower values for the non-stoichiometry[93]. They were using different techniques, in addition to thermogravimetry including hydrogen reduction, they used high temperature neutron diffraction. Their results gave lower values of 3-δ but they only gave data from 600-900°C. At the highest temperature a value of 2.25 was shown for 3-δ. In addition to conducting experiments in pure oxygen they also carried them at lower partial pressures (0.1, 0.01 and $0.001p_{O2}/p$).This resulted in lower values of the non-stoichiometry. The neutron diffraction data was analysed without any reference to the chemical analysis so could be regarded as an absolute value. However, their pretreatments of the powders were quite extensive and only after changes in the lattice parameter stopped during the isothermal hold at each temperature was the data taken for full pattern fitting. These results, therefore, give results lower than the ones based on dynamic methods where isothermal conditions do not exist. They did not report on any differences between the cobalt and iron oxidation states.

Mössbauer and x-ray absorption near edge spectroscopy (XANES) have also been employed to investigate the oxidation state changes during heating[63]. The Mössbauer data indicated that at room temperature the iron was present in three oxidation states 4+, “3+” and “2+” and the proportions varied with composition. The latter two oxidation states represent rapid hopping between the lower state indicated and a higher state (Table 2).

x	y	Fe^{4+}(%)	$Fe^{"3+"}$(%)	$Fe^{"2+"}$(%)
0.8	0.2	44	26	30
0.5	0.8	42	29	29
0.5	1.0	51	26	23

Table 2 Iron oxidation state in $Ba_{1-x}Sr_xCo_{1-y}Fe_yO_{3-\delta}$ (after Harvey[63])

The XANES data showed that the iron was mainly 3+ up to 960°C whereas the cobalt reduces to 2+ above 800°C. The conclusion was that the iron was in a higher oxidation state than the cobalt which was in agreement with the work of Jung described above.[92]

The oxidation states have also been measured using X-ray photoelectron spectroscopy (XPS).[94, 95] In the former paper[94], a ratio of Co^{3+} to Co^{4+} of 40:60 is reported. However no account is taken of the overlap of the barium and cobalt peaks which occurs with binding energies in the range 770 to 810eV. The same part of the spectrum was analysed separately for barium and cobalt and therefore no cognisance will be made of this paper. The second paper[95] shows that the iron is a mixture of Fe^{4+} and Fe^{3+} while the cobalt is present as Co^{3+}. These assignments were made on the basis that the two iron states have similar binding energies whereas the cobalt 4+ has a binding energy at a significant difference to the 3+ state. This latter paper confirms the previous discussion in that the cobalt is at a lower oxidation state than iron.

Electron energy loss spectroscopy (EELS) has shown that in BSCF the loss of oxygen is accompanied by a reduction in oxidation state of Co from 2.6-2.2 and of Fe from 3.0-2.8 over the temperature range 25-950°C[96]. Again the cobalt is in a lower oxidation state than the iron.

The oxygen non-stoichiometry can be measured by a variety of methods which when compared under the same conditions correlate well with each other. For a good comparison composition, pre-treatment conditions, atmosphere and time for equilibration need to be the same. However the contribution of the two B site cations to the overall resulting oxidation state is not as clear, the assignment of charge between the two cations and the 3+ and 4+ oxidation states is not unequivocal and involves a variety of assumptions which may not be verifiable. There is general agreement that cobalt has a lower oxidation state than iron. This may be due to the cobalt 3+ ion being a d^6 species which has a low energy low spin state as all the d electrons are paired.

2.4.4 Mechanical Properties

Good mechanical properties (strength, creep, thermal shock) of the ceramic membranes are important for long lifetimes in the applications[97-100]. The measurement against temperature of stiffness, toughness and fracture stress has shown discontinuities around 200°C[101-103]. (Figure 14),

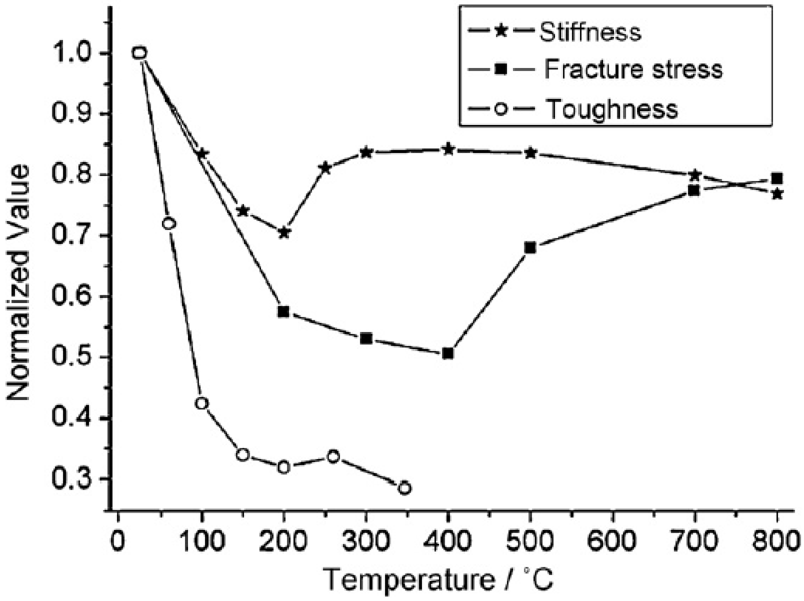

Figure 14 Mechanical properties of BSCF against temperature (from Huang[103])

The anomaly was related to changes in spin state as evidenced by variations in magnetic susceptibility (Figure 15). The changes in spin state for the cobalt 3+ ions result in an increase in ionic radius. The cobalt 3+ ion is d^6 and at low temperatures the electrons are all paired giving rise to no net electron spin. At higher temperatures some electrons move into high energy orbitals and the spins are no longer paired. There was also a reduction in thermal expansion coefficient at this temperature.[103]

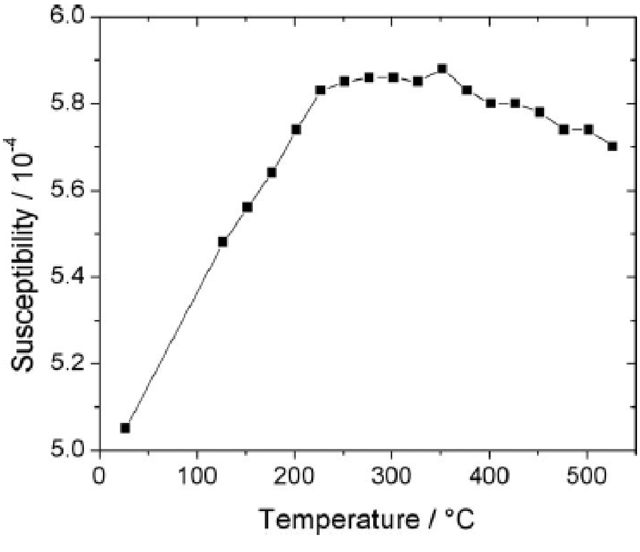

Figure 15 Magnetic susceptibility against temperature (from Huang[101])

The compressive creep rate has also been shown to have a change in behaviour at ~900°C[98, 100]. (Figure 16). The change in strain rate was attributed to the formation of second phases as the cubic system transformed to hexagonal during the duration of the experiment.

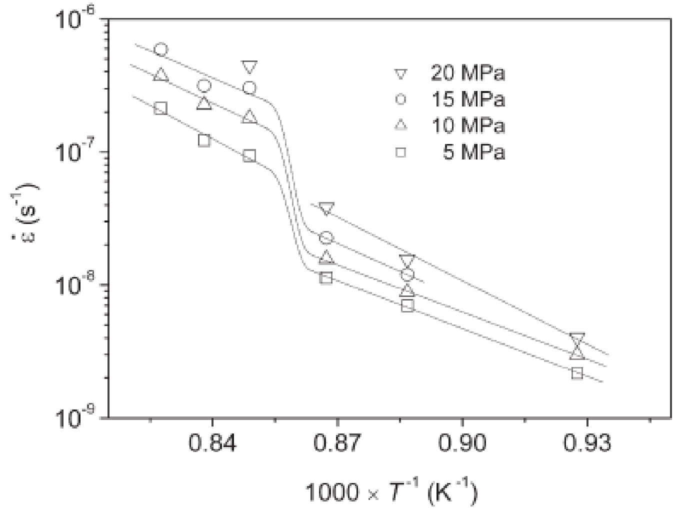

Figure 16 Variation of BSCF strain rate with temperature and oxygen partial pressure (from Yi[98])

The thermal expansion behaviour of BSCF ceramics with varying barium to strontium ratio was shown to have a change in slope at temperatures which were composition dependent[104].(Figure 17 and Figure 18) High temperature x-ray diffraction was used to determine a cause but the conclusion reached was that there was not an associated phase change[30, 105, 106]. TGA showed that the change was attributed to loss of oxygen, and the iron and cobalt were reduced from 4+ to 3+.The weight loss measured was insufficient to have complete reduction to 3+, however the starting point that all the ions were 4+ was not established. The change of oxidation state of the metals from 4+ to 3+ is accompanied by an increase in ionic radii.[107] The expansion associated with the B site oxidation change may be referred to as chemical expansion

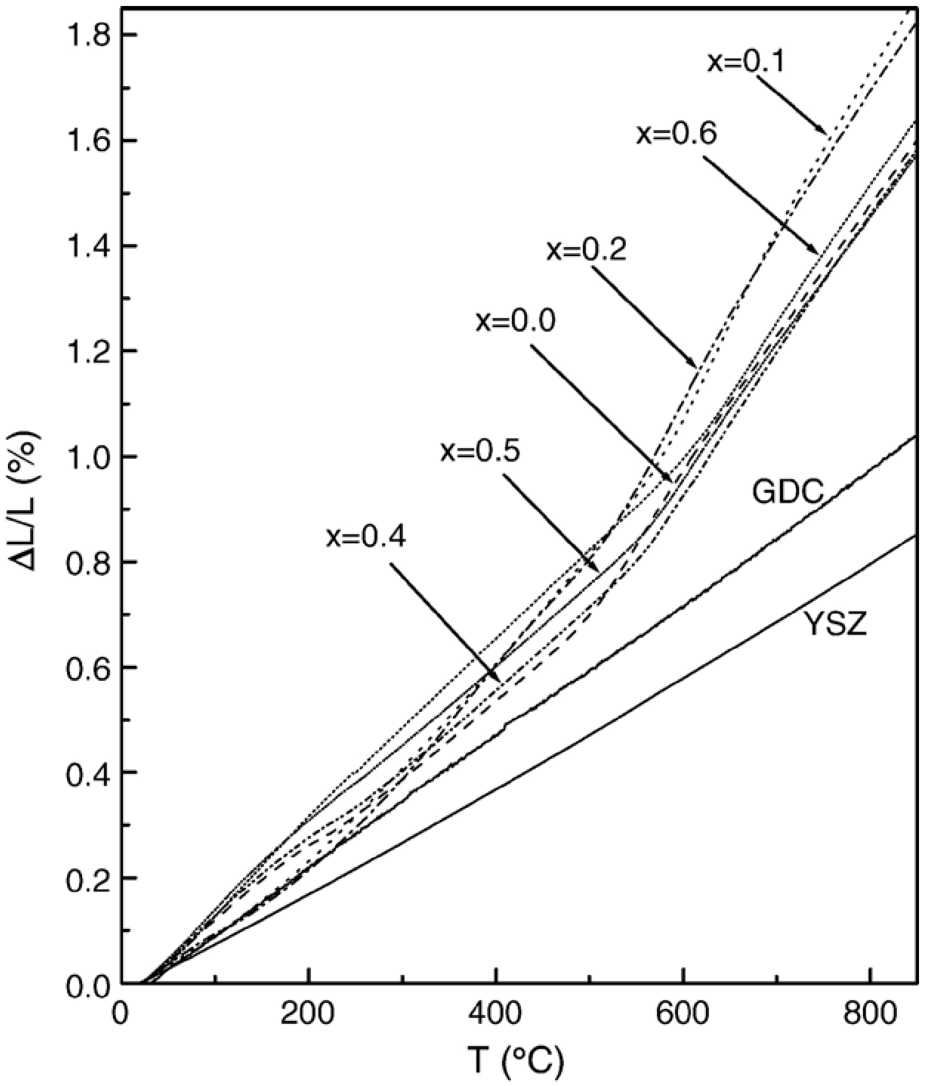

Figure 17 BSCF thermal expansion behaviour (from Zhu[104])

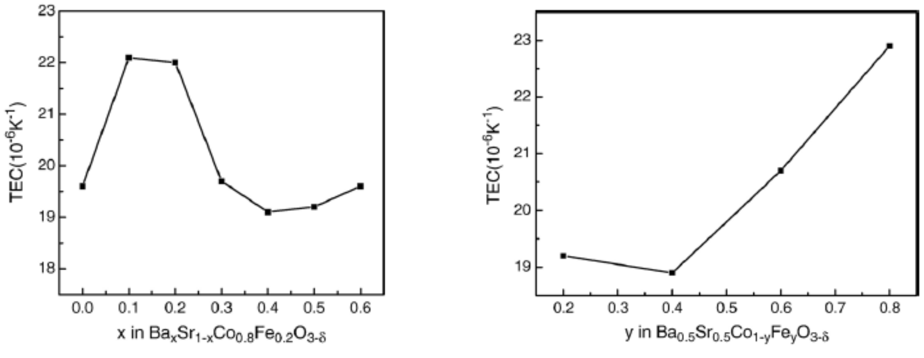

Figure 18 Variation of thermal expansion coefficient with composition of BSCF (from Zhu[104])

3 Experimental Methods

3.1 Density

The density of the sintered samples was measured using an Archimedes technique[108]. This technique measures the mass of the sample in air and whilst suspended in a liquid, in this case water. The difference in mass is equal to the mass of water displaced. By knowing the density of the liquid the volume displaced can be calculated and this is equal to the volume of the solid sample. The volume and mass of the solid are thus now known and the density can be calculated.

However the ceramic pellets measured contained pores. These pores could be either open in that they connected to the outside of the ceramic body or closed whereby they were totally enclosed in the ceramic with no access to the exterior of the body. When immersed in the liquid the air in the open pores may be displaced by the liquid whereas the liquid cannot enter the closed pores. There are thus 3 volumes that may exist for each object.

1) Bulk volume which corresponds to the sum of the solid volume, the open pore volume and the closed pore volume. This approximates to the volume as determined by measuring the volume of a regularly shaped solid.
2) True volume which corresponds to the volume of the solid with no pores. This cannot be measured using an Archimedes technique unless another independent method has verified the absence of closed pores.
3) Apparent solid volume which corresponds to the solid volume and the volume of closed pores.

The bulk volume and apparent solid volume can both be used in density calculations and give rise to the bulk and apparent solid density respectively.

Two methods were used to measure the density which differed in the way that the samples were degassed before the mass was measured in the liquid,

3.1.1 Methods

1) The sample was weighed in air (m_1)
2) The immersion process had two variants
   a) The sample was placed in a beaker of deionised water and boiled gently for 30minutes. After boiling the sample was left to cool back to ambient temperature. The boiling in some cases caused some chipping of the sample and therefore method b) was introduced.
   b) The sample was placed in a shallow petri dish containing deionised water, (which had been degassed by boiling) and ensuring the pellet was totally immersed. The petri dish was placed in a vacuum desiccator and evacuated until no more bubbles appeared from the sample. It was left under vacuum for 30 minutes before opening the valve and restoring the sample to atmospheric pressure.
3) The samples were then weighed under water using the suspension attachment on the balance.(m_2)
4) The sample was removed then dried quickly using a paper towel and then reweighed.(m_3)

Using the three weights and the density (ρ_L) of water (Table 2 in Reference [108]), the bulk (ρ_b) and apparent solid (ρ_s) densities were calculated according to the two equations below.

$$\rho_b = \frac{m_1}{m_3 - m_2} \times \rho_L \qquad 3.1$$

$$\rho_s = \frac{m_1}{m_1 - m_2} \times \rho_L \qquad 3.2$$

3.2 Iodometric Titration

The determination of δ, the amount of the oxygen deficiency in the $ABO_{3-\delta}$ formula can be achieved through iodometric titration.[91, 92, 109] In this method iodide ions are oxidised by the multi-valent metal cations, formed by dissolution of the solid in acid, to form iodine which is then titrated with standardised sodium thiosulphate solution. The oxidation of iodide by cobalt 4+ is shown in Equation 3.3 below

$$2I^- + Co^{4+} \rightarrow I_2 + Co^{2+} \qquad 3.3$$

The titration of the liberated iodine with sodium thiosulphate is shown in equation 3.4 below

$$\mathrm{I_2 + 2S_2O_3^{2-} \rightarrow 2I^- + S_4O_6^{2-}} \qquad 3.4$$

The above equations have been simplified because, in the presence of excess iodide ions, iodine readily reacts reversibly with them to form the tri-iodide ion $\mathrm{I_3^-}$.

$$\mathrm{I_2 + I^- \leftrightarrow I_3^-} \qquad 3.5$$

The sodium thiosulphate was standardised by titrating the iodine formed by reacting potassium iodide with a known amount of potassium iodate in a dilute acid solution. The reaction is shown below.

$$\mathrm{IO_3^- + 5I^- + 6H^+ \rightarrow 3I_2 + 3H_2O} \qquad 3.6$$

All the titrations were conducted whilst nitrogen was bubbled through the solution to prevent oxidation of the iodide ions by oxygen

$$\mathrm{4I^- + O_2 + 4H^+ \rightarrow 2I_2 + 2H_2O} \qquad 3.7$$

The presence of the excess iodide ions which forms the tri-iodide also helps prevent the loss of liberated iodine through volatilisation.

The method used assumes that the dissolution of the BSCF powder in acid occurs without any change in the oxidation state of the contained cations. If the excess iodide is not present before the powder is added to the hydrochloric acid chlorine is formed which indicates oxidation of the chloride by the cations prior to the addition of iodide.

3.2.1 Titration of BSCF powder method

1) The powders were calcined in air at 1000°C for 2 hours to remove all adsorbed water carbon dioxide and other volatiles. On cooling they were stored in a desiccator containing both silica gel and soda lime. The latter was to remove any carbon dioxide from the atmosphere.

2) Immediately prior to use the powders were ground in an agate mortar and pestle so that dissolution would be easier. This prevented long dissolution times which could lead to iodine loss by volatilisation.
3) 100cm^3 of 1M HCl were added to a stirred conical flask and 2g of potassium iodide added. Nitrogen was bubbled through the solution.
4) When the potassium iodide had completely dissolved, approximately 50mg accurately weighed of the BSCF powder were added to the flask.
5) When all the powder had dissolved (normally less than 5 minutes), the solution was titrated with approximately 0.02M sodium thiosulphate solution until it was a pale yellow colour.
6) 1cm^3 of 0.1% by weight starch solution was added and the titration was continued until the solution changed from intense blue to colourless.

3.2.2 Standardisation of the sodium thiosulphate solution

1) Approximately 2.14g of dried potassium iodate were accurately weighed into a 500cm^3 volumetric flask and the solution made up to the mark[109].
2) To a conical flask containing 25cm^3 of deionised water were added 10cm^3 of 1M HCl. Nitrogen was bubbled through the solution.
3) 5cm^3 of the potassium iodate solution were pipetted into the flask. 1g of potassium iodide was added and allowed to dissolve.
4) The solution was titrated with approximately 0.02M sodium thiosulphate solution until it was a pale yellow colour.
5) 1cm^3 of 0.1% by weight starch solution was added and the titration was continued until the solution changed from intense blue to colourless.

3.2.3 Calculation of δ in $Ba_{0.5}Sr_{0.5}Co_{0.8}Fe_{0.2}O_{3-\partial}$

The titration was set up so that iodide reacted with M^{2+p+} to form I_2 and M^{2+}.

$$M^{2+p+} + p\ I^- = M^{2+} + p/2\ I_2 \qquad 3.8$$

The iodine is then reacted with thiosulphate.

$$p/2\ I_2 + p\ S_2O_3^{2-} = pI^- + p/2\ S_4O_6^{2-} \qquad 3.9$$

Therefore p mole of $S_2O_3^{2-}$ is equivalent to p electrons/mole of reduction which in turn is equivalent to p/2 moles Oxygen in excess of that required for M^{2+}.

In 1g of sample there are CV/2w moles of oxygen in excess of that required for $Ba_{0.5}Sr_{0.5}Co_{0.8}Fe_{0.2}O_2$.

In one mole of sample there are 1-∂ moles of excess oxygen which equals (CV/2w) x $M_{BSCFO3-\delta}$.

Where C = concentration of thiosulphate solution (M)

V = volume of titre of thiosulphate solution (l)

w = weight of sample used (g)

$M_{BSCFO3-\delta}$. = molecular weight of $Ba_{0.5}Sr_{0.5}Co_{0.8}Fe_{0.2}O_{3-\partial}$.

$$1-\partial = \frac{\mathrm{CVM_{BSCFO3-\partial}}}{2\mathrm{w}} \qquad 3.10$$

The molecular weight in equation 3.10 is split into 2 parts.

$$1-\partial = \frac{\mathrm{CV}}{2\mathrm{w}}(\mathrm{M_{BSCFO3}} - \partial \mathrm{M_O}) \qquad 3.11$$

The bracket is expanded.

$$1-\partial = \frac{\mathrm{CV}}{2\mathrm{w}}\mathrm{M_{BSCFO3}} - \frac{\mathrm{CV}}{2\mathrm{w}}\,\partial \mathrm{M_O} \qquad 3.12$$

The equation is rearranged.

$$\frac{\mathrm{CV}}{2\mathrm{w}}\,\partial \mathrm{M_O} - \partial = \frac{\mathrm{CV}}{2\mathrm{w}}\mathrm{M_{BSCFO3}} - 1 \qquad 3.13$$

The equation is factorised.

$$\left(\frac{\mathrm{CV}}{2\mathrm{w}}\,\mathrm{M_O} - 1\right)\partial = \frac{\mathrm{CV}}{2\mathrm{w}}\mathrm{M_{BSCFO3}} - 1 \qquad 3.14$$

The equation is rearranged to give ∂.

$$\partial = \frac{\frac{CV}{2w}M_{BSCFO3} - 1}{\left(\frac{CV}{2w}\ M_O - 1\right)} \qquad 3.15$$

3.3 Surface Area and Pore Volume

Specific surface area and pore volume were measured by nitrogen adsorption on powders at the boiling point of nitrogen (77K)[110]. The technique involves the measurement of the amount of gas adsorbed as the nitrogen partial pressure above the powder is increased. This is accomplished by the introduction of a known amount of gas (nitrogen) into the sample holder which is initially under vacuum and waiting for the pressure to come to equilibrium. The amount of gas adsorbed is calculated by examining the difference between the expected and actual pressure difference on gas addition using the ideal gas law.

$$PV = nRT \qquad 3.16$$

Where P is the pressure in the system (Pa)
V is the volume of the system (m^3)
n is the number of moles of gas in the system
R is the gas constant (8.314J $mol^{-1}K^{-1}$)
T is temperature (K)

The adsorption of gas on a non-porous solid is generally explained by the BET (Brunauer, Emmett and Teller)[111] equation below.

$$\frac{\frac{p}{p_o}}{n\left(1 - \frac{p}{p_o}\right)} = \frac{1}{n_m c} + \left(\frac{c-1}{n_m c}\right)\frac{p}{p_o} \qquad 3.17$$

Where p is the partial pressure above the sample (Pa)
p_o is the saturation vapour pressure (Pa)
n is the amount of gas adsorbed ($molg^{-1}$)
n_m is the monolayer capacity of the powder ($molg^{-1}$)
c is a constant which is related to the net heat of adsorption of the gas.

The theory assumes a constant heat of adsorption of the gas onto the solid in the formation of a monolayer and that subsequent adsorption onto this layer has another constant heat of adsorption. During adsorption each layer need not be complete before a further layer is formed.

A plot of $\frac{\frac{p}{p_o}}{n\left(1-\frac{p}{p_o}\right)}$ against $\frac{p}{p_o}$ will give a straight line with

$$\mathrm{slope} = \left(\frac{c-1}{n_m c}\right) \qquad 3.18$$

$$\mathrm{intercept} = \frac{1}{\mathrm{n_m c}} \qquad 3.19$$

from which n_m and c can be calculated. From the value of n_m the specific surface area (A) can be calculated.

$$A = N_A \, n_m a_m \qquad 3.20$$

Where N_A is Avogadro's constant (6.022×10^{23} mol^{-1})
n_m is the monolayer capacity of the powder ($molg^{-1}$)
a_m is the area of the adsorbed gas molecule (m^2)

In the case of a porous solid, the adsorbed gas layer builds up and in a pore will form a meniscus corresponding to the pore diameter. The vapour pressure above a curved surface is given by the Kelvin equation

$$\ln\frac{\mathrm{p}}{\mathrm{p_o}} = \frac{-2\gamma V_L}{RT}\frac{1}{r_m} \qquad 3.21$$

where γ is the surface tension of the liquid adsorbate (Nm^{-1})
V_L is molar volume of the liquid adsorbate (m^3mol^{-1})
R is the gas constant ($8.314 J\ mol^{-1}K^{-1}$)
T is temperature (K)
r_m is radius of the meniscus (m).

Thus at any given relative pressure there is a maximum value of the filled pore diameter. At a relative pressure of 0.9810 the pore radius is 50nm which corresponds to the upper limit of mesopores as defined by IUPAC[112]. This assumes V_L= 34.68cm^{3}mol^{-1}, γ= 8.88Nm^{-1} and T=77.35K.

3.4 X-Ray Diffraction

3.4.1 Phase identification

X-ray diffraction is used to determine the crystal structures present within a material[113]. The technique consists of illuminating a sample with x-rays and collecting the diffracted x-rays as a function of angle relative to the incoming beam. A typical experimental set up is shown in Figure 19. The x-rays are collimated and passed through slits to achieve a narrow parallel beam illuminating the sample. The diffracted beam passes through more slits and a collimator before entering a monochromator which allows only a narrow range of x-ray wavelengths to pass through before entering the detector.

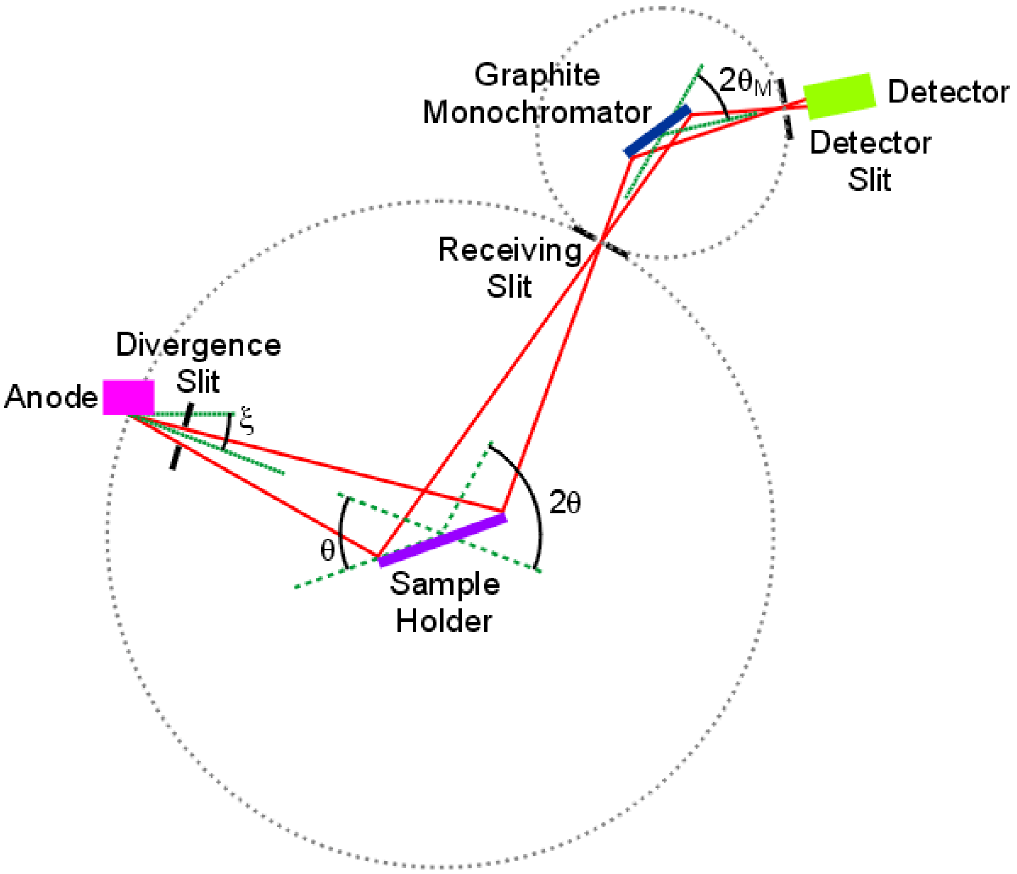

Figure 19 Schematic diagram of x-ray diffractometer[114]

A crystalline material consists of ions/atoms arranged in regular three dimensional arrays. The incident x-rays interact with the electrons around each atomic nucleus and are scattered. These scattered x-rays also interact with each other and if they are in phase will constructively interfere and can therefore be detected unlike the destructively interfering x-rays. The constructive interference occurs at definitive angles from the planes of atoms in the 3D structure. If the planes are at a distance (d) apart, and the wavelength (λ) of the x-rays is known, then their relationship is given by Braggs law (equation 2.13)

$$n\lambda = 2d\sin\theta \qquad 3.22$$

Where n = order of diffraction = 1 for x-ray diffraction
θ = diffraction angle

The intensity of x-rays against angle shows a series of peaks each representing a distinct interplanar distance (d). From the interplanar distances and the associated peak intensity crystal structures can be identified and the atomic positions within the structure determined. Structure identification was carried out using HighScore plus (Phillips). Further fitting and quantification was carried out using Topas software (Bruker)

The phase identification utilised the ICSD database and the High Score plus search and match routine. The ICSD database includes for the substance its name, formula, crystallographic parameters, peak list, atomic positions and an ideal diagram of its x-ray diffractogram. The initial stage was to identify the peaks present and then, after the selection of those elements present in the material, run the routine. The matching phases were recorded and their corresponding data file accessed to obtain the structural details for each phase. In many cases, typically those with a single phase, this was sufficient to obtain a good phase identification.

However in the multiphase materials this approach could not give an unequivocal match. The reasons for this include broad peaks, overlapping peaks and the very large number of Ba-Sr-Co-Fe-O systems that are present within the database. In these cases which included the dried and calcined powders, a good fit was taken and then used as a basis for refinement using Topas.

Topas is a whole pattern fitting program. In order to fit the experimental it requires an input of possible crystal structures. These inputs may be just the space group and lattice parameters for a Pawley fit or the space group, lattice parameters and atomic coordinates of all atoms within the unit cell for Rietveld fitting. The latter is the ideal route as it can reveal differences in site occupancy in a given structure. Differences in occupancy can be a result of initial inhomogeneity subsequent disproportionation or reactions occurring with the atmosphere. As good fits using Rietveld fitting could not be obtained as site occupancies greater than 1 were obtained, the simpler Pawley method was also used.

In addition to the crystal structures, the refinement requires information on the peak shape. X-ray diffraction peaks have a shape which is a convolution of Gaussian and Lorentzian peaks known as a pseudo-Voigt function. This can be chosen at the start of refinement. In addition to these preselected items the refinement also uses line breadth and background shape in optimising the fitting.

3.4.2 Line Broadening

In an ideal case the x-ray diffraction peaks are broadened by both instrumental and sample effects[115, 116]. The former include

- the x-rays not being monochromatic
- the x-rays not being parallel
- the finite size of the x-ray beam.

The sample can cause broadening through two principal properties sample crystallite size and inhomogeneous strain but could also include stacking faults and concentration gradients within a crystal. The presence of small crystallites means that there is not an infinite size to the diffracting planes and that the interference between the scattered x-rays does not give a sharp cut off between constructive and destructive interference. Non-uniform strain within the crystals means that there will be a variation in peak position around a central point. (Uniform strain produces a peak shift.)

If the instrumental broadening (b) can be measured using a large crystallite size strain free sample then the crystallite size (L) can be determined if the experimental broadening (B) is measured (equation 3.23), this assumes that there is a Gaussian relationship between the two broadenings[113]. First broadening from the sample (B_s) is calculated and the crystallite size is measured using the Scherrer equation (3.24).

$$B_s^2 = B^2 - b^2 \qquad 3.23$$

$$L = \frac{K\lambda}{B_s \sin\theta} \qquad 3.24$$

Where λ is the wavelength of the x-rays (nm)
Θ is the diffraction angle.

3.4.3 Glancing angle diffraction

Glancing angle x-ray diffraction is used to examine the crystallography of surface layers. As well as being diffracted the x-rays incident on a sample can be adsorbed, as can the diffracted beam, through a number of processes in which electrons adsorb the x-rays and change their state often being ejected from the substance as a photo electron (see section 3.9) or being excited to an outer orbital. These excited electrons can subsequently decay to the lower state and emitting x-rays of a specific wavelength. (This is the basis of x-ray fluorescence). The absorption of x-rays is dependent on the path length (t) and the absorption coefficient (μ) of the substance and is given by equation 2.16.

$$I = I_o e^{-\mu t} \qquad 3.25$$

Where I = reduced intensity after a distance t
I_o= Incident intensity

The absorption coefficient is derived for a material from the absorption coefficients from the constituent elements. In conventional diffraction the incident angle and diffracted angle are symmetrical with respect to the sample surface and the path length is the constant for all values of θ. In glancing angle mode the incident angle is kept constant and small this gives a longer path length for material at a greater depth and enhances the contribution of surface layers to the diffraction pattern.

3.5 Scanning Electron Microscopy

Scanning electron microscopy can be used to examine the microstructure and composition of specimens over a wide range of magnifications from 50x up to >30k. The basic operation of the microscope is to focus a beam of electrons onto the specimen and detect the result of the interaction of the electrons with the specimen. The principle results of the reaction of the electron beam with the atoms in the specimen are the emission of electrons (secondary, backscattered and Auger), light and x-rays[117]. A typical configuration is shown in Figure 20.

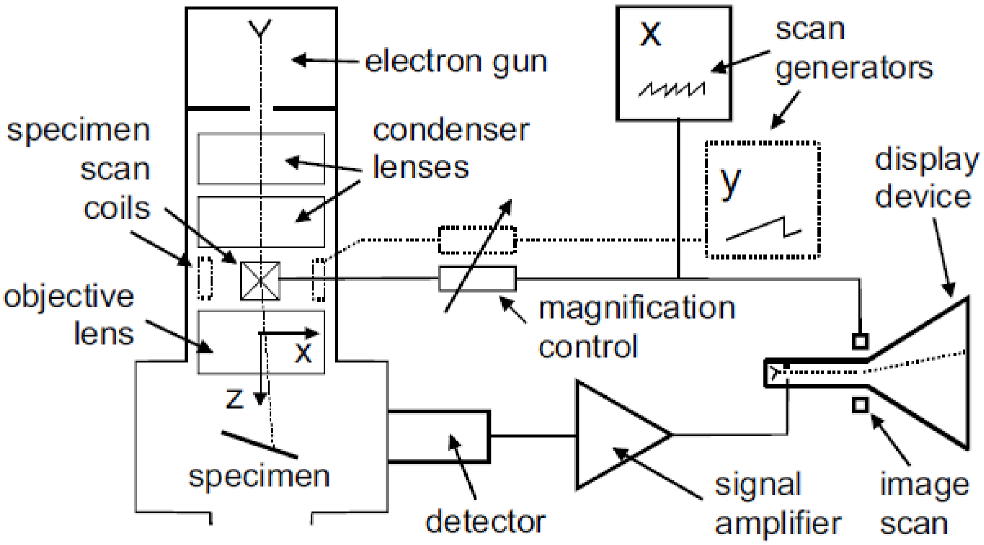

Figure 20 Schematic of a scanning electron microscope[117]

3.5.1 Imaging

In order to image the specimen, the electron beam is made to raster over the specimen. The image is then generated by correlating the detected signal with the position of beam in the raster.

When the electrons in the beam are accelerated towards the specimen, with typical energies of 2keV to 30keV, they interact with the specimen either elastically or inelastically. In the first case, which gives rise to back scattered electrons, the electrons have little change in energy and are reflected back out of the specimen. As the interaction is with the electrons in the atom there is a higher probability of such a reflection with high atomic number elements which have greater numbers of electrons. Thus this mode of operation is sensitive to variation in the average atomic number of specimen. The high energy of these electrons means that they can escape from within the specimen without being absorbed.

If the electrons in the beam interact inelastically they can cause inner core electrons to be lost from the atoms in the specimen these have low energy and may further interact with the specimen. These secondary electrons may leave the surface and then can then be detected. The electrons leaving the surface typically have energies of ~50eV[117], much less than the back scattered electrons. Their low energy means that only if they are very near the surface (~1nm for 3keV beam energy) will they be detected. This gives a better topological image of the specimen.

3.5.2 Elemental Analysis

When an inner core electron is removed from an atom, an outer core electron may drop into the unfilled inner core, as this core has a lower energy then energy will be released in the form of an x-ray with energy equal to the difference of the two core shells which are element specific[118]. The x-rays can be detected either by energy dispersive or wavelength dispersive detectors. In the former the signal from the detector is discriminated on the basis of its energy whereas in the latter the x-rays of different energies (wavelengths) are diffracted by a crystal to separate them before their detection.

The conversion of the x-ray energies and intensities into composition is by techniques similar to those used in x-ray fluorescence, (see section 3.6) in which the x-rays are produced by exciting the inner core electrons with x-rays and not electrons.

3.6 X-Ray Fluorescence Analysis

The elemental compositions of sintered pellets were measured by x-ray fluorescence using a MiniPal 4 energy dispersive x-ray fluorescence spectrometer. The standardless Ominian software was used for quantification.

X-ray fluorescence is a technique similar to energy dispersive x-ray analysis in electron microscopy.[119] In this case x-rays and not electrons are the excitation source. A beam of x-rays irradiate the sample and either excite inner core electrons to higher energy levels or excite them to leave the surface as photoelectrons.(see section 3.9 below) Electrons in the excited atom can drop into the vacant low energy level and simultaneously emit an x-ray whose energy is dependent on the two energy levels involved. The emitted x-rays are detected by an energy sensitive detector. The energy intensities are converted to elemental concentrations through the use of databases containing details of x-ray fluorescence yields and x-ray adsorption from all elements in the sample.[120]

3.6.1 Determination of method accuracy

Three pellets from 2 different samples were analysed to determine the errors in the measurement. The nominal compositions for the two samples were $Ba_{0.7}Sr_{0.3}Co_{0.8}Fe_{0.2}O_{3-\delta}$ and $Ba_{0.5}Sr_{0.5}Co_{0.8}Fe_{0.2}O_{3-\delta}$. The results are given in Table 3 and Table 4. Oxygen could not be measured in the instrument used. The raw data for the cations was normalised to 100% on a weight basis (wt%) and then converted to atomic ratios which were further normalised to a cation atomic composition of 100 (Mole %). In order to allow comparison with the empirical formula for each composition, the mole% was normalised to a total of 2 moles ie an assumption that the final composition was ABO_3. The only impurity found was calcium at approximately 0.3wt% which corresponded to 0.01 on the A site.

	Ba0.7Sr0.3Co0.8Fe0.2O3-δ									
		A			B			C		
	Theoretical Mole %	Wt %	Mole %	Mole ratio	Wt %	Mole %	Mole ratio	Wt %	Mole %	Mole ratio
Ca	0	0.079	0.16	0.003	0.103	0.20	0.004	0.097	0.19	0.004
Fe	10	7.019	9.95	0.199	6.889	9.79	0.196	7.389	10.28	0.206
Co	40	31.68	42.56	0.851	31.351	42.23	0.845	32.933	43.42	0.868
Sr	35	36.761	33.22	0.664	36.983	33.51	0.670	38.59	34.22	0.684
Ba	15	24.456	14.10	0.282	24.672	14.26	0.285	20.983	11.87	0.237

Table 3 XRF reproducibility data for $Ba_{0.7}Sr_{0.3}Co_{0.8}Fe_{0.2}O_{3-\delta}$

	Ba0.5Sr0.5Co0.8Fe0.2O3-δ									
		A			B			C		
	Theoretical Mole %	Wt %	Mole %	Mole ratio	Wt %	Mole %	Mole ratio	Wt %	Mole %	Mole ratio
Ca	0	0.1	0.21	0.004	0.206	0.43	0.009	0.194	0.41	0.008
Fe	10	6.39	9.73	0.195	6.61	9.95	0.199	6.605	9.95	0.199
Co	40	28.134	40.59	0.812	29.173	41.63	0.833	29.082	41.53	0.831
Sr	25	25.575	24.82	0.496	25.312	24.29	0.486	25.375	24.37	0.487
Ba	25	39.801	24.64	0.493	38.698	23.7	0.474	38.743	23.74	0.475

Table 4 XRF reproducibility data for $Ba_{0.5}Sr_{0.5}Co_{0.8}Fe_{0.2}O_{3-\delta}$

The mean and standard deviation for each composition are given in Table 5. The first set for $Ba_{0.7}Sr_{0.3}Co_{0.8}Fe_{0.2}O_{3-\delta}$ showed a less than 5% coefficient of variation in the standard deviation with the exception of the barium analysis which was 9%. For the samples for $Ba_{0.5}Sr_{0.5}Co_{0.8}Fe_{0.2}O_{3-\delta}$ the coefficient in variation was less than 2% for all analytes. The C sample for $Ba_{0.7}Sr_{0.3}Co_{0.8}Fe_{0.2}O_{3-\delta}$ seems to be an outlier though no reason for this variation could be found.

	$Ba_{0.7}Sr_{0.3}Co_{0.8}Fe_{0.2}O_{3-\delta}$		**$Ba_{0.5}Sr_{0.5}Co_{0.8}Fe_{0.2}O_{3-\delta}$**	
	Mean Wt%	St deviation	Mean Wt%	St deviation
Ca	0.09	0.012	0.17	0.058
Fe	7.10	0.259	6.54	0.126
Co	31.99	0.835	28.80	0.575
Sr	37.44	0.998	25.42	0.137
Ba	23.37	2.070	39.08	0.624

Table 5 Summary of XRF data

3.7 Electrical measurements

The measurement of the electrical properties of ceramic pellets was carried out using complex impedance spectroscopy also known as electrochemical impedance spectroscopy[87]. Using this technique an alternating voltage (V) is applied to the specimen and the corresponding magnitude and phase of current (i) are measured. For a pure resistance (R) Ohm's law is followed and the current is proportional to the applied voltage (equation 3.26). Resistance is independent of the frequency of the applied voltage and the current and voltage are in phase with each other

$$\mathrm{i} = \frac{\mathrm{V}}{\mathrm{R}} \qquad 3.26$$

However, for other electrical components, for example capacitors and inductances subject to an alternating voltage, the voltage and current are not in phase and the resistance becomes frequency dependent. This behaviour is described in terms of the impedance.

For a sinusoidally varying voltage of magnitude E_0, the potential (E_t) applied at time t is given by

$$E_t = E_0 \sin(\omega t) \qquad 3.27$$

where ω is the radial frequency (radian s^{-1}) and equals 2πf where f is the frequency (Hz)

E_0 is the amplitude of the applied signal (V)

Let the corresponding current (I_t) be given by

$$I_t = I_0 \sin(\omega t + \varphi) \qquad 3.28$$

where φ is the phase shift.

The impedance (Z(ω)) is given by

$$Z(\omega) = \frac{E_t}{I_t} = \frac{E_0 \sin(\omega t)}{I_0 \sin(\omega t + \varphi)} = Z_0 \frac{\sin(\omega t)}{\sin(\omega t + \varphi)} \qquad 3.29$$

Using Euler's relation[121] (equation 3.30) the expression for Z(ω) may be simplified as shown by

$$\exp(j\varphi) = \cos\varphi + j \sin\varphi \qquad 3.30$$

where j is √-1

$$Z(\omega) = Z_0 (\cos\varphi + j \sin\varphi) \qquad 3.31$$

This equation has a real and imaginary part and can therefore be plotted in the complex plane as a Nyquist plot. Impedance data is therefore collected from the sample under test over a range of frequencies whilst held at constant temperature. The temperature used for measurement is varied which allows impedance-temperature relationships to be studied

In addition the data from the measurements can be plotted as:- admittance (Y), relative electric modulus (M) and relative permittivity (ε).[122] Their relationship with each other and the impedance is given below,

$$Y = \frac{1}{Z} \qquad 3.32$$

$$M = j\omega C_0 Z \qquad 3.33$$

$$\varepsilon = \frac{1}{M} \qquad 3.34$$

where C_0 is the vacuum capacitance of the empty measuring cell.

The following figures show the data from a tetragonal yttria-zirconia (TZP) plotted for the four representations. In addition some are plotted against log(frequency).

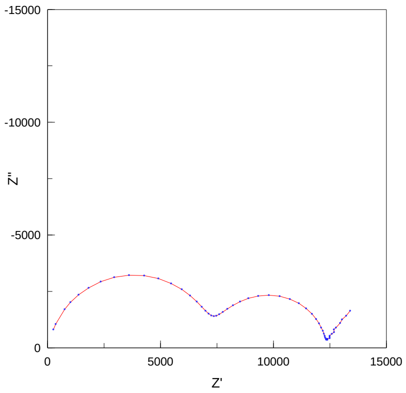

Figure 21 Nyquist plot (complex impedance) of TZP data

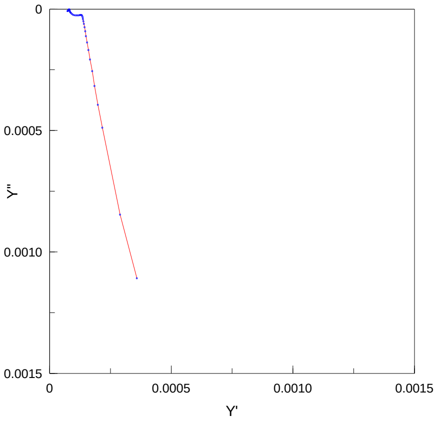

Figure 22 Complex admittance plot of TZP data

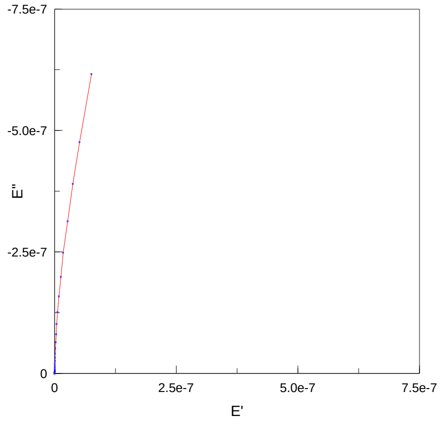

Figure 23 Complex permittivity plot of TZP data

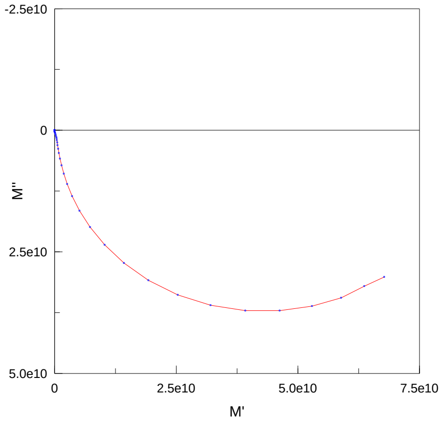

Figure 24 Complex electrical modulus plot of TZP data

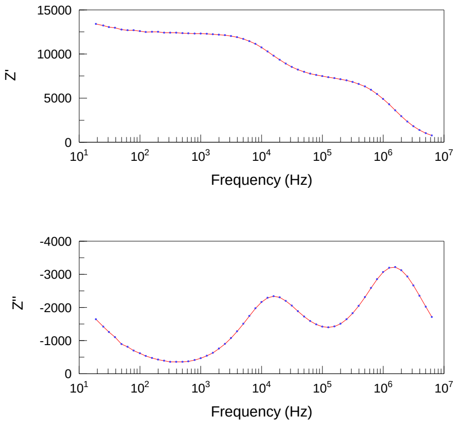

Figure 25 Plots of Z' and Z'' against log(frequency) for TZP data

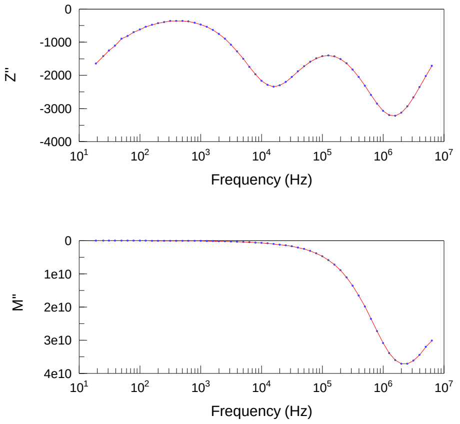

Figure 26 Plots of imaginary impedance and imaginary electrical modulus against log(frequency) for TZP data

One of the objectives of impedance spectroscopy is to separate electrical responses from different microstructural regions within the sample so that the electrical behaviour of these regions can be modelled as well as to determine the characteristics of the whole test piece. The processes involved in electrical conduction have different time constants and can thus be represented by different components and is accomplished through fitting the experimental data to equivalent circuits whose components can be related to the material under test.[122-124] It is important during this stage to ensure that a good fit is obtained in all the representations of the data.

The most common elements used to make up the model circuits are resistors and capacitors. It is often found that the capacitor does not give a good fit and that a constant phase element gives a better one. .The constant phase element is similar to a capacitor but with its phase angle not equal to 90°. The impedance of a resistor is given by equation 3.35 impedance of a capacitor is given by equation 3.36 and a constant phase element by equation 3.37.

$$\mathrm{Z} = \mathrm{R} \tag{3.35}$$

$$Z = \frac{1}{j\omega C} \tag{3.36}$$

$$Z = \frac{1}{(j\omega)^{\alpha} C} \tag{3.37}$$

Where Z is the impedance

R is the resistance

j is √-1

ω is the angular frequency

α is the exponent and equals 1 for a pure capacitor

C is the capacitance

In addition inductors can also be present often as a result of wires in the measuring jig not being shielded. An inductor has an impedance given by equation 3.42

$$Z = j\omega L \qquad 3.38$$

Where Z is the impedance

L is the inductance

j is √-1

ω is the angular frequency

A simple circuit which could represent a ceramic sample under test is given in Figure 27. This assumes the material under test has some conductivity, is homogenous at all scales and is held between two electrodes. This will be referred to as an R-RC circuit which represents a resistor in series with a parallel combination of a resistor and capacitor.

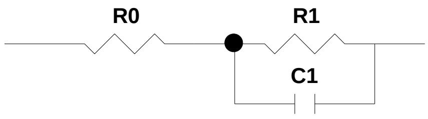

Figure 27 Model circuit known as R-RC

where R0 represents the resistance of the test leads and electrodes

R1 represents the resistance of the sample

C1 represents the capacitance of the sample

The Nyquist plot generated using the values (R0 = 100Ω, R1 = 1000Ω and C1 = $1\text{x}10^{-9}$F) is given below over the frequency range 5Hz to 12MHZ is shown in Figure 28. This frequency range is typical of that available from the instruments used for measurements.

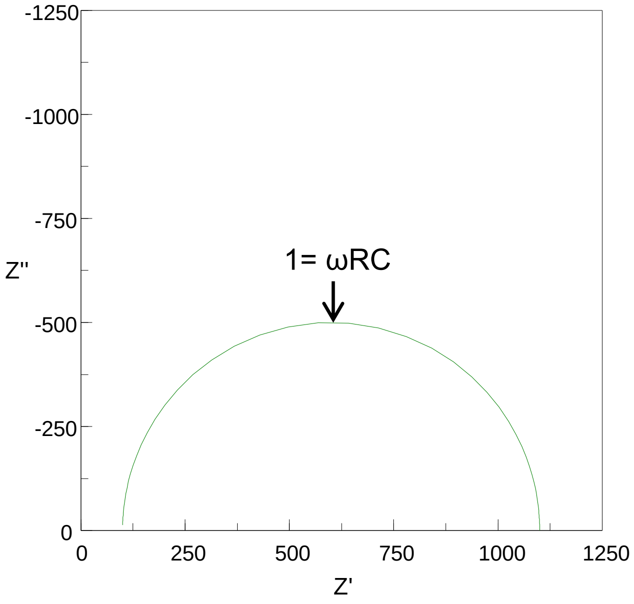

Figure 28 Nyquist curve for simple R-RC circuit

The low frequency data is at the right hand side moving anticlockwise to the highest frequency at the left hand side. From Figure 28 it can be seen that the curve is a semicircle with a diameter equal to the resistance of the RC part of the circuit. Also at the top of the semicircle the following relationship shown in equation 3.39 holds.

$$1 = \omega RC \qquad 3.39$$

The reciprocal of ω (the characteristic frequency) at the top of the semicircle is known as the relaxation time (τ) for the RC circuit. It can be seen at the high frequency part of the spectra the curve does not reach the axis at Z’= 100Ω. This occurs at higher frequencies.

In addition to the Nyquist plot, other plots can be made using the same data. Figure 29 shows a plot of the imaginary part of the impedance against the log of the applied frequency. This plot shows a peak at a frequency corresponding to the circuit’s relaxation time. In addition Figure 29 shows the imaginary part of the complex modulus plotted against log frequency.

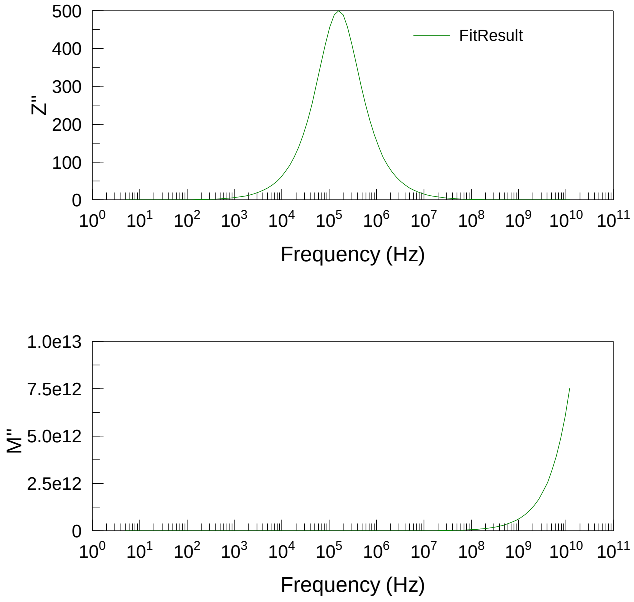

Figure 29 Alternative Impedance data plots a) Z'' v log f b) M'' v log f

The presence of one or more semicircles in impedance spectra of ceramics is widely observed[87, 122-124]. However a unique circuit cannot usually be found for any set of data. West et al [123] show a number of circuits that can be used to fit data showing two semicircles. (Figure 30)

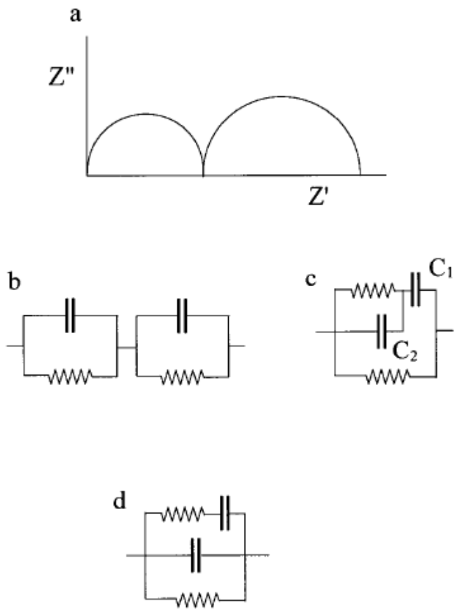

Figure 30 Idealized impedance complex plane plot showing a two semi-circular arcs and b,c,d plausible equivalent circuits (from West[123])

The choice of the appropriate circuit is based on the values of the components and their behaviour as for example the temperature is raised. In addition it has been found that the capacitances calculated fall into a number of different ranges and that these correspond to different microstructural and measuring system features as shown in Table 6[124].

Capacitance (F)	Feature Responsible
10^{-12}	Bulk
10^{-11}	Minor, second phase
10^{-11}-10^{-8}	Grain boundary
10^{-10}-10^{-9}	Bulk ferroelectric
10^{-9}-10^{-7}	Surface layer
10^{-7}-10^{-5}	Sample-electrode interface
10^{-4}	Electrochemical reactions

Table 6 Capacitance values and their interpretation (after Irvine[124])

Care must therefore be taken in the fitting and interpretation of complex impedance measurements. The circuit in Figure 30b can represent a ceramic with series connected grains and grain boundaries, whereas the other two circuits c and d have been shown to represent leaky dielectrics[123]. It is important to use an equivalent circuit which is in accord with the material being studied. In generating fits to the data the following criteria were employed:

1. The fits were made to several of the representations of the data
2. The model used fitted over a wide temperature range.
3. The values of resistance and capacitance were within the expected ranges.
4. The temperature variation was consistent for the assigned feature

3.8 Oxygen Permeability

3.8.1 Experimental Design

An experimental rig was designed and built to measure the oxygen permeability of dense BSCF ceramic pellets.

The criteria that were used in the design were:-

1. The test rig would be able to reach 900°C
2. The samples would be 1cm diameter 1mm thick cylinders
3. The volume of tubing and other dead spaces after the pellet would be minimised. This reduces the amount of time needed for equilibrium if the operating conditions are altered and lessens the diffusion of the measured gas ahead or against the overall gas flow ie the flow regime becomes nearer to plug flow.
4. The temperature of the pellet needed to be measured
5. The oxygen concentration and flow rate of the sweep gas needed to be measured
6. Sealing and removing the pellet would be easy.

A schematic of the rig is shown in Figure 31.

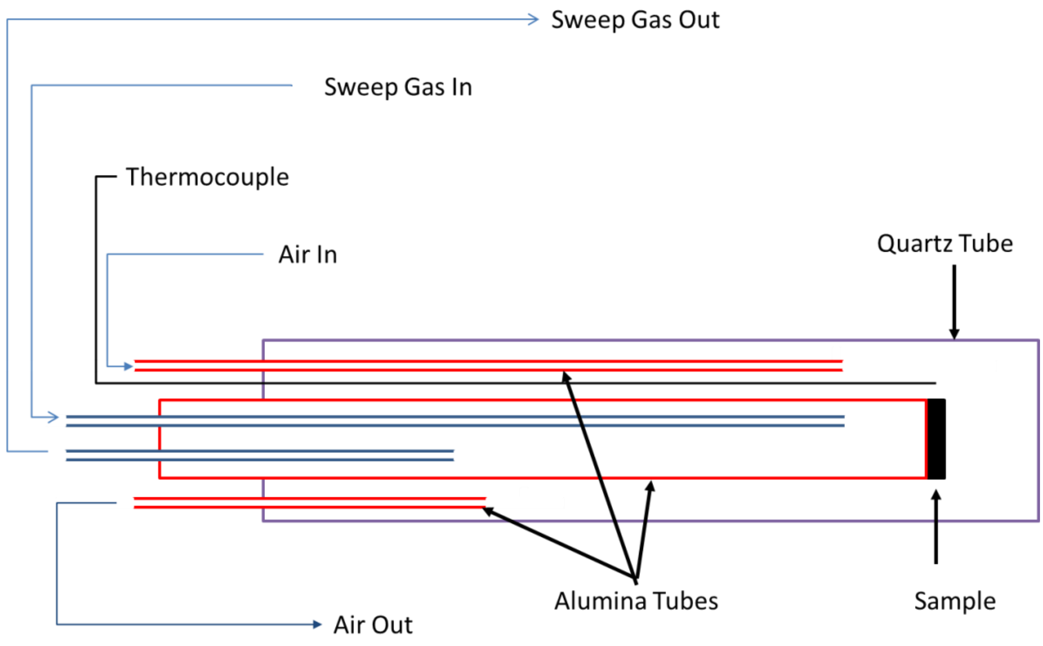

Figure 31 Schematic of oxygen permeation rig

The pellet was fixed to the alumina tube using an alumina cement (Aron Ceramic D, Toagosei Chemical Industry Co. Ltd., Tokyo, Japan.,) The end of the tube was first ground flat using 240 mesh SiC paper. The cement was painted on the end of the tube and the pellet which had been ground and polished with 1µm diamond placed onto the cement and left for 16 hours. The alumina tube was then placed in the outer quartz tube together with the thermocouple. The gas lines were then attached. The containing quartz tube was placed in a tube furnace taking care that the pellet was in the centre of the hot zone. The cement was further dried at 90°C for 1 hour and then cured at 150°C for another 1 hour.

During the drying and curing stages of the sample preparation the gases were passed through the system. This enabled all the oxygen to be removed from the sweep side of the system and thermal equilibrium to take place. There was a noticeable cooling effect when the gas flows were on; the air and sweep gas flow rates were both about 50 cm^3min^{-1}.

The gas flow rates were controlled via needle valves and measured on the inlet side via rotameters and on the sweep gas outlet after the oxygen meter (G1010 Mark 2 oxygen analyser, Hitech Instruments Ltd., Luton, England) using a mass flow meter (EFM17, Aalborg, Orangeburg, NY, USA) The flow meters were also checked against a bubble meter.

3.9 X-ray Photoelectron Spectroscopy

3.9.1 Introduction

X-ray photoelectron Spectroscopy (XPS) is a surface analysis technique that may give information on the chemical identity, concentration and chemical states of the elements present on the surface of a sample.[125] The technique consists of irradiating the sample with x-rays and measuring the kinetic energy of the emitted photoelectrons. The energy of the electrons is typically in the range of 0-1500eV and to prevent their interaction with gases the experiments are carried out at low pressures typically $<5x10^{-10}$ torr.

In the equipment used, the sample was irradiated with an Al Kα (hv= 1486.7 eV) x-ray source. The incident x-rays (hv_1) excite an inner core electron (e^-_p) which is emitted from the sample with a kinetic energy (KE) (see Figure 32). The relationship between the kinetic energy and the binding energy (BE) of the electron relative to the Fermi level of the sample, which is what is required for analysis, is given in the following equation.

$$KE = h\nu - BE - \Phi \qquad 3.40$$

where Φ is the work function from the sample to free space.

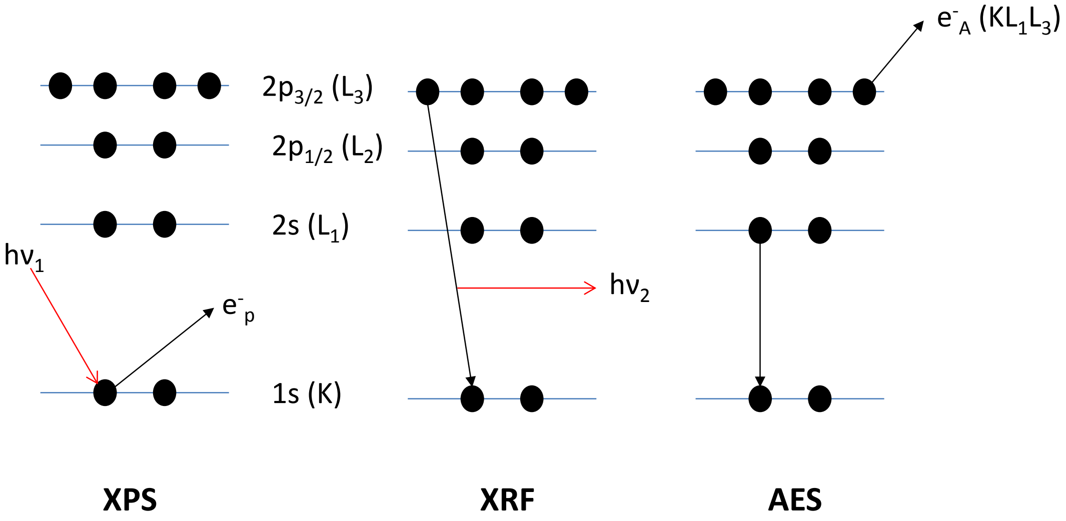

Figure 32 Schematic of processes in x-ray photoelectron spectroscopy (after Briggs[125])

For a conducting material which has a good electrical contact with the instrument the Fermi levels of the sample and instrument have the same energy and the work function is that of the instrument and is independent of the sample.[126] As the kinetic energy is the measured parameter, and binding energy is the analysed parameter graphs of XPS spectra are conventionally drawn with the binding energy decreasing from left to right on the abscissa.

In addition to the emission of the photoelectron from the excitation by the incident x-rays, other processes can occur. The emission of the photoelectron leaves a hole in a core electron shell. One of the outer electrons can fill this shell and in dropping down to the lower energy level will lose energy which can excite another outer shell electron (e^-_A) which will be emitted from the sample (see Figure 32). These are known as Auger electrons (AES). Their energy is only related to the energy differences between the three levels in the electronic structure of the atom involved.

The emission of the photoelectron causes an increase in the ionisation of the atom, this can lead to a change in the configuration of the outer valence electrons to an excited electronic state. During this process, the interaction of the emitted electron with this excited state causes a loss of energy in the emitted electron and thus it appears at lower kinetic energy and hence a higher binding energy. The resulting peak in the spectra is known as a shake–up or satellite peak.

X-ray emission (XRF) can also occur when inner core levels are filled by outer core electrons.

The positions of the peaks from different atoms are given in a number of databases both printed and online. [127] The positions of the peaks can change as a result of the local chemical environment of the atom and its oxidation state.

The nature of the peaks is dependent on the shell structure of the atom's electrons. The electronic shells can be described in terms of their quantum numbers. There are three of interest,

the principal quantum number (n), 1,2,3,4…

the orbital angular momentum quantum number (l), 0,1,2,3, corresponding to s,p,d,f orbitals

the spin angular momentum quantum number (s), ±½

However the spin and angular momentum numbers are combined to form a total angular momentum number (j),

$$\mathrm{j} = \mathrm{l} + s \qquad 3.41$$

This gives rise to singlet peaks for s orbitals and doublets for all other orbitals. The ratio of the two peaks is given by their respective degeneracies. The degeneracy (D) of the peaks is given by,

$$\mathrm{D} = 2\mathrm{j} + 1 \qquad 3.42$$

The following table shows the total angular momentum, values of degeneracy and peak area ratios.

Orbital Angular Momentum	j	Degeneracy	Peak area ratios
0…s	1/2	-	-
1…p	1/2, 3/2	2, 4	1:2
2…d	3/2, 5/2	4, 6	2:3
3…f	5/2, 7/2	6, 8	3:4

Table 7 Degeneracy and peak areas in XPS

Thus any peak fitting must take into account these peak area ratios.

The line width of the XPS peaks are a function of the electronic transition, the incident x-rays and the detector sensitivity. If these functions are assumed to be Gaussian the total line broadening ΔE can be expressed as below[125],

$$\Delta\mathrm{E} = (\Delta\mathrm{E}_\mathrm{n}^2 + \Delta\mathrm{E}_\mathrm{p}^2 + \Delta\mathrm{E}_\mathrm{a}^2)^{½} \qquad 3.43$$

Where ΔE_n is the electronic transition linewidth

ΔE_p is the energy width of the exciting x-rays

ΔE_a is the resolution of the analyser.

The last two are fixed for the instrument and can be minimised through the use of monochromators for the x-ray source and instrument design for the resolution.

The variation in the electronic transition line width is governed by the lifetime of the state resulting from the emission of the photoelectron. Using the uncertainty principle,

$$\Delta\mathrm{E}_\mathrm{n} = \frac{\mathrm{h}}{\tau} = \frac{4.1\mathrm{x}10^{-15}}{\tau}\ \mathrm{eV} \qquad 3.44$$

where h is Plank’s constant (eV s)

τ is the lifetime (s)

3.9.2 Analysis of spectra

A typical low resolution BSCF 5582 XPS spectrum from this study is shown in Figure 33 below. From the databases available the peaks can be assigned to the given transitions.

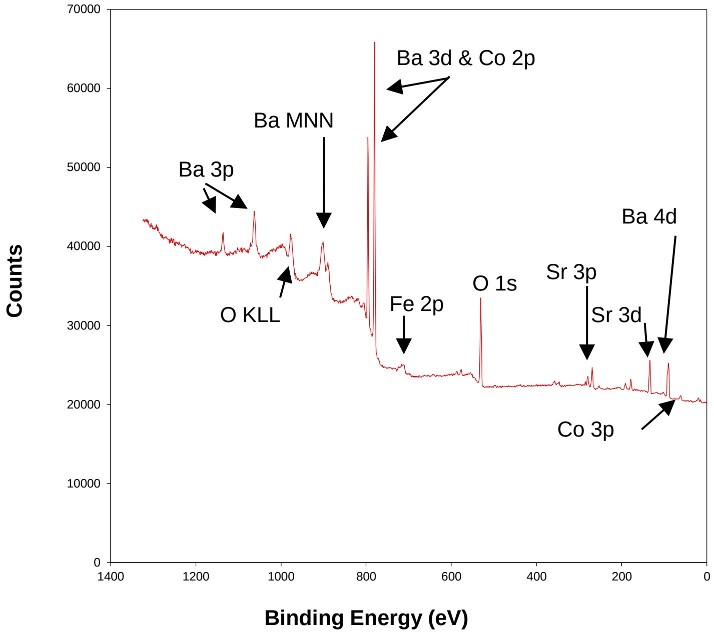

Figure 33 Low resolution XPS scan of BSCF

For quantitative analysis more detailed scans were carried out a higher resolution. The resulting spectra were analysed using CasaXPS software.[128]

The analysis consisted of a number of steps.

3.9.2.1 Subtraction of background

The background is subtracted so that the peak area can be measured. There are a number of ways of subtracting the background. The easiest, if the background level is horizontal both sides of the peak, is just a linear fit across the peak. However if there is a change in background level across the peak the choice of starting and ending points makes a difference in the peak area measured. A number of other different ways have been proposed for background subtraction across a peak.[129, 130] The Shirley background was used in this study when a sloping background was present.

3.9.2.2 Selection of peak shape

The peak shapes of XPS are found to have the form of a Voigt function which is a convolution of a Gaussian and a Lorentzian function. Within the CasaXPS software the mixing parameter (m) can be varied with m=100 representing a pure Lorentzian curve and m=0 a pure Gaussian curve. A value of m=30 was found to give the best fitting

3.9.2.3 Addition of constraints

A number of constraints can be put into the fitting procedure. The area ratio of doublets can be fixed to the values given in Table 7. The energy separation between the doublet peaks can be fixed, this was done for Sr 3d peaks which were separated by 1.79eV.[131]

Further details on fitting will be given in the experimental section.

3.10 Computerised X-Ray Tomography

Computerised x-ray tomography is a technique for producing 3-D representations of objects from a series of 2-D x-ray images[132]. The general technique is to take an x-ray image of the object and then rotate it a small amount and then image the object again. This is repeated approximately 2000 times over 180° of rotation. The resulting images show the adsorption of the x-ray beam as they pass through the object with absorption being proportional to the object's density and thickness. An example of the different images that are obtained from two images of a pair of cylinders is shown in Figure 34.

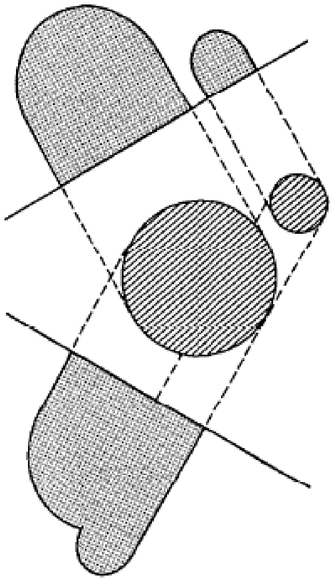

Figure 34 Images of two cylinders from different directions (from Kak[132])

Once the set of images have been obtained then they need to be transformed into a representation of the original object through a process known as reconstruction. Reconstruction is a Fourier transform of the intensity, detector position and rotation angle data from the x-ray images into a 3-D model of the original object. The use of x-rays allows internal structures to be modelled as well as the external form of the objects.

The experimental technique is to mount the object on a turntable in such a way that the whole of the object remains in view during the rotation. The x-ray source produces a cone of x-rays which allows different heights to be imaged at the same time otherwise as well as rotation the object being examined would have to be moved vertically. The distances between the source, sample and detector are adjusted to give the optimum magnification for the instrument.

An image of a BSCF ceramic pellet mounted on an alumina holder is shown in Figure 35. A filter is inserted after the source to attenuate the x-ray beam to ensure that approximately 20% of the beam passes through the sample at its most opaque part. This allows the grey scale range is optimum for the subsequent processing during reconstruction. After the reconstruction process the results are a series of images of horizontal slices through the pellet which show variations in intensity corresponding to the variation in density of the piece at those positions an example is shown in Figure 36.

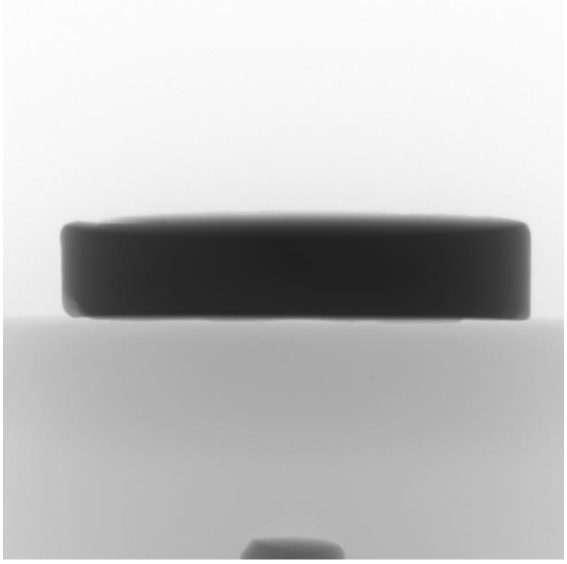

Figure 35 X-ray image of BSCF pellet on an alumina mount

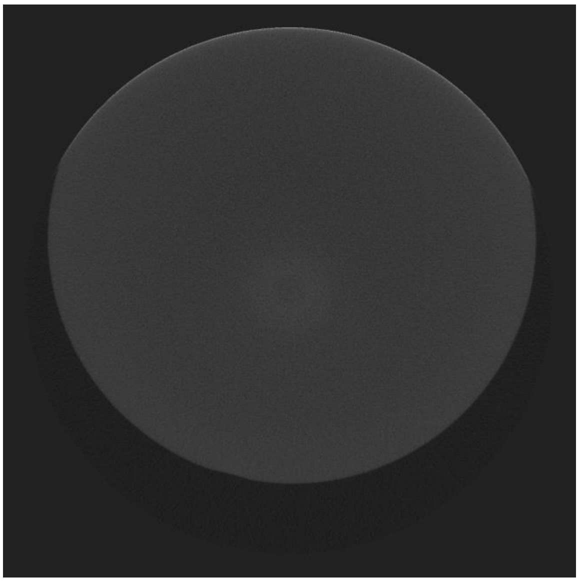

Figure 36 Reconstructed slice of BSCF pellet.

The images is then segmented, that is, it is divided up into areas of different intensity darks areas represent pores and light areas material of higher absorption

4 Development of Synthesis Route

4.1 Introduction

A wet precipitation route was chosen for the synthesis of the starting powders because this can allow for greater variation in the process if powder improvement is required, eg better homogeneity, easier milling or lower sintering temperatures. Three primary approaches were used for the synthesis of the mixed BSCF powders. After synthesis the powders were milled in propan-2-ol and then dried prior to pressing in a uniaxial press prior to sintering in air.

The process was to mix the metal salts in the required proportions, add precipitant and then filter and wash the precipitate prior to drying and calcination.

The precipitants chosen were ammonium hydroxide, sodium hydroxide and sodium carbonate. The three precipitants all had advantages and disadvantages.

Ammonium is a fugitive cation and will be removed on drying and calcination. However it is a weak base and a maximum pH of about 10 would be obtainable. This could be insufficient to fully precipitate out the barium and strontium as both their hydroxides have finite solubility in alkaline solutions[133]. The soluble portion barium and strontium hydroxides could be precipitated by the addition of hydrogen peroxide, which reacts to form an insoluble peroxide[134]. Furthermore the ammonia could form ammine complexes with the cobalt, which are soluble in alkaline solutions[135].

Sodium hydroxide does not form alkaline soluble complexes with cobalt, however even though higher pH's can be obtained when compared to ammonia the barium and strontium hydroxides still have significant solubility. Sodium must also be removed from the wet hydroxide precipitate otherwise it may form low melting point compounds which change the sintering characteristics, oxygen permeation and electrical properties.

Sodium carbonate precipitates carbonates, hydroxides and basic carbonates. However some or all of these are insoluble for the metals being used. Sodium removal is still necessary

4.2 Exploratory Series

In order to avoid problems with removal of chloride ions, which can inhibit densification even at low levels, the metal nitrates were chosen as starting materials. Stock solutions in deionised water were made for all the metals except barium. These solutions were made at 15% weight/weight (w/w) with the exception of iron, which was at 10% w/w. The concentrations are based on weight of element in solution. Barium nitrate has a low solubility 8.2%w/w (4.3%w/w as Ba)[133] and was added as a solid. One advantage of using stock solutions is that it avoids the problems of the hygroscopic nature of many metal nitrates.

The general method of preparation was as follows:-

1 The metal salt solutions were weighed into a beaker and the solid barium nitrate added. Further water was added to give a total metal concentration of 8% w/w. This value was chosen so that the volumes being processed did not become too large and the final suspension did not become too viscous and thus unable to be stirred. The mix was heated to 60°C to allow the barium nitrate to dissolve. It was then generally cooled to less than 30°C, although higher barium contents gave a precipitate if cooled much below 30°C.

2 The precipitant was diluted to give a 10% w/w solution and this was added drop wise over approximately an hour to the metal nitrate solution. At the end of the addition the suspension was left stirring for an hour.

3 The suspension was filtered using a Whatman 541 paper and washed with 3x the metal nitrate solution starting volume.

4 The precipitate was redispersed in water and filtered.

5 The precipitate was dried overnight at 100°C

6 The dried powder was calcined at 850°C for 4 hours with a 3°Cmin^{-1} heating and cooling rate.

7 10g of powder were vibro-milled for 24 hours with 10g zirconia balls in 10cm^3 of propan-2-ol.

8 The powder was dried at 85°C overnight.

9 Pellets were uniaxially pressed without any additives in a 1cm die at 100MPa.

10 Pellets were sintered in air.

The preparation with ammonia was carried out to pH 9 and then the hydrogen peroxide was added. This effervesced vigorously. On filtration the filtrate was highly coloured indicating that the cobalt and/or iron had not been fully precipitated. A separate experiment was carried with ammonia being added to cobalt nitrate. The final pH was varied. At pH 9, a precipitate was formed which slowly dissolved which indicated ammine formation. At pH 8, precipitation occurred though on settling there was evidence of colour in the supernatant. After 3 days some crystals appeared. These results showed that control of precipitation with ammonia would be hard to control and no further experiments were carried out with it.

Sodium hydroxide was used as precipitant and added until pH 11.4. A small sample was tested with hydrogen peroxide and as effervescence again occurred it was not added to the bulk. The mixture was filtered and washed. Some dilute sulphuric acid was added to the filtrate and a dense white precipitate occurred indicating the presence of strontium and barium. Strontium and barium sulphates are insoluble having very low solubility products. The use of sodium hydroxide was not continued.

Sodium carbonate was added to the mixed metal solution at 50°C until pH 8.1 or 9. In both cases the resulting filtrate had a just discernible pink colour Indicating incomplete cobalt precipitation. Also the colour of the precipitate formed close to the droplet changed during the addition process. At first it was an olive green and towards the end white. The precipitation of the transition metals was occurring first and then the alkaline earths.

The process was then changed so that the metal salt mixture was added drop wise into the 10% w/w sodium carbonate solution. The amount of sodium carbonate used was calculated to be 1.1 times that required for stoichiometric reaction. The precipitation carried out gave a constant colour of precipitate around the droplet although the overall colour changed from olive green to brown during the ageing step. However the pink colour was still present in the filtrate. The sodium carbonate excess was increased to be 1.5 times the stoichiometric and the pink colour in the filtrate was no longer present. This method was the basis for all the syntheses used. It is summarised in Figure 37 Schematic of synthesis route.

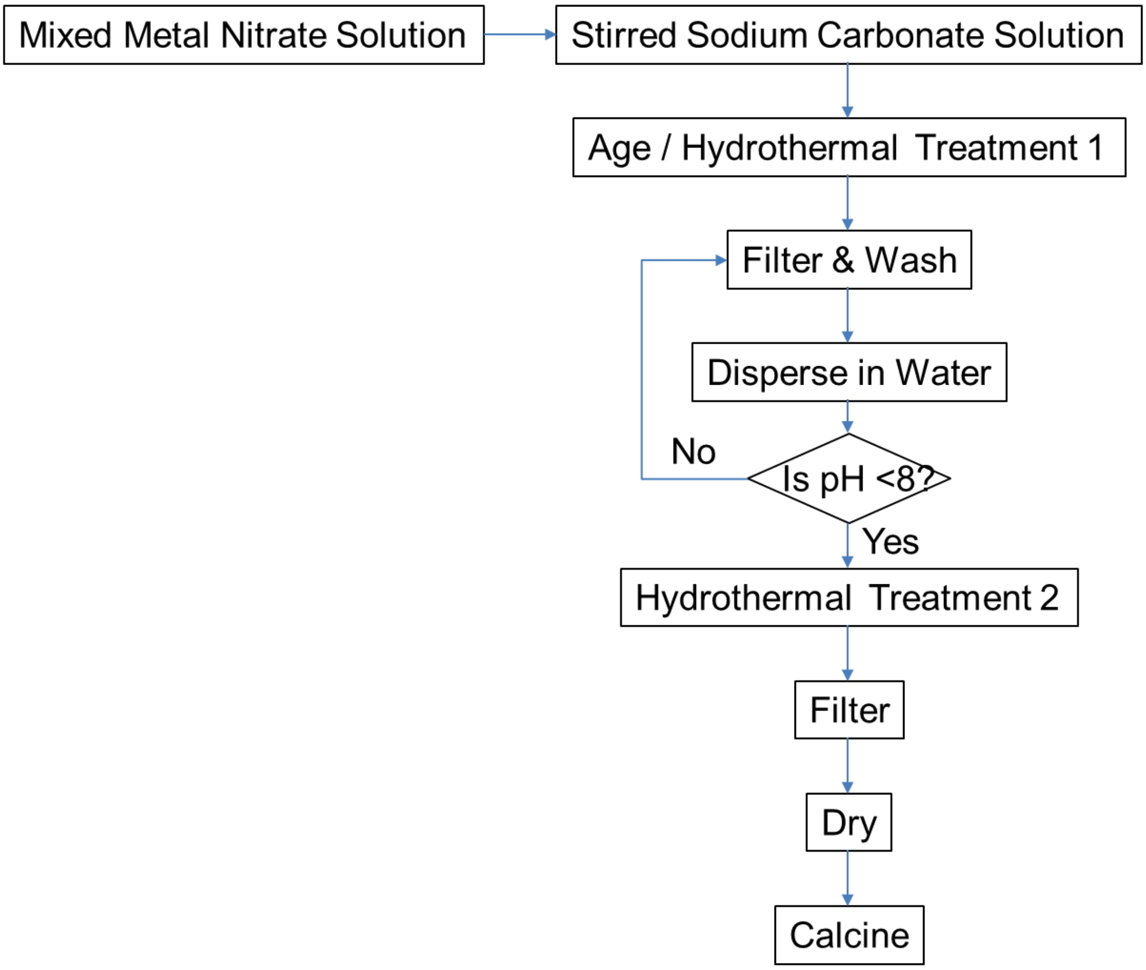

Figure 37 Schematic of synthesis route

4.3 Equilibrium Evaluation

MEDUSA chemical equilibrium software was used to verify the experimental observations of the completeness of precipitation.[52] The large number of potential species in the solution and in the solid phase meant that the diagrams for the complete Ba-Sr-Fe-Co-Na-H-CO_3-NO_3 system were extremely complicated and not suitable for analysis. Therefore one of each of the 4 components (Ba-Sr-Fe-Co) together with the total concentrations of Na CO_3 and NO_3, assuming the other components were present, were used in constructing the diagram. A diagram was also constructed for barium precipitation using sodium hydroxide. The concentrations used were those that would be present at the end of the addition stage but ignoring the other components. The diagrams were constructed over a pH range of 1-12. The diagrams follow, the first one is a complete diagram, the remaining ones have had many of the lines removed if they were similar to Na^+ that is, invariant or like H^+ and OH^- the same for all diagrams.

The diagrams show the log concentration of the species present against pH. The diagrams are calculated from the starting concentrations given for each component and the aqueous equilibrium constant data for all possible species within the system. The equilibrium constant data is contained within the software.

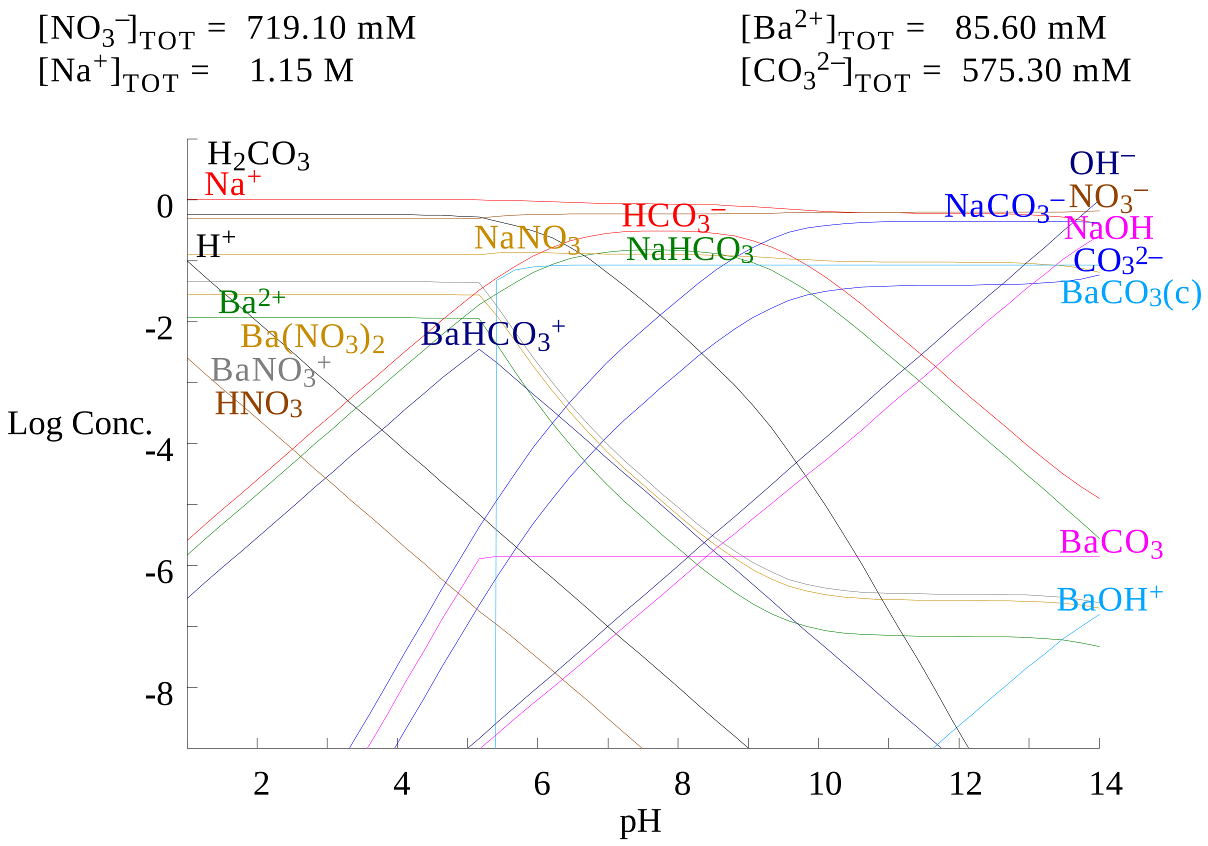

Figure 38 Barium nitrate plus sodium carbonate precipitation showing species present over pH range 1-14

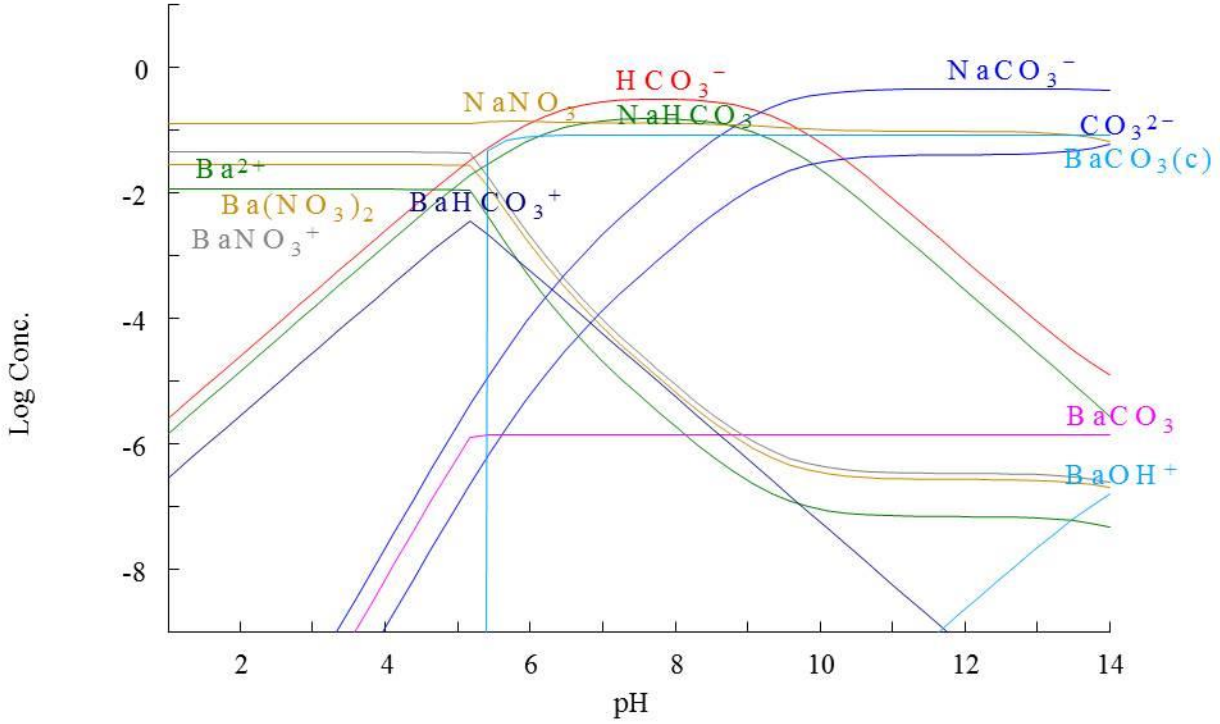

Figure 39 Barium nitrate plus sodium carbonate precipitation showing species present over pH range 1-14

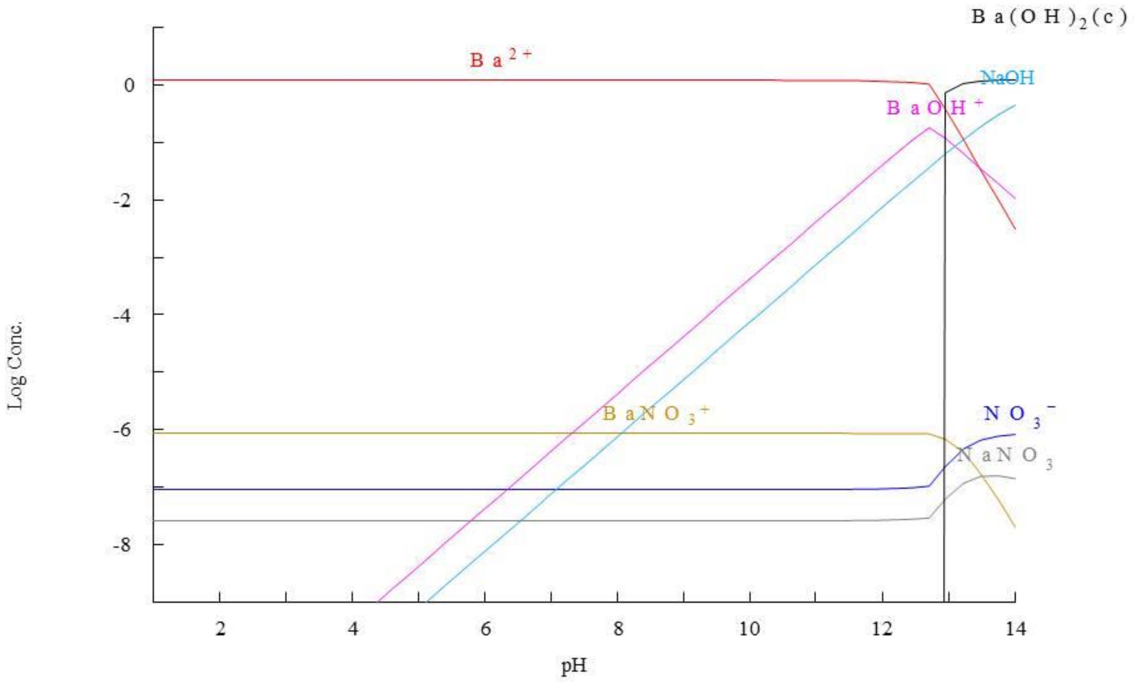

Figure 40 Barium nitrate plus sodium hydroxide precipitation showing species present over pH range 1-14

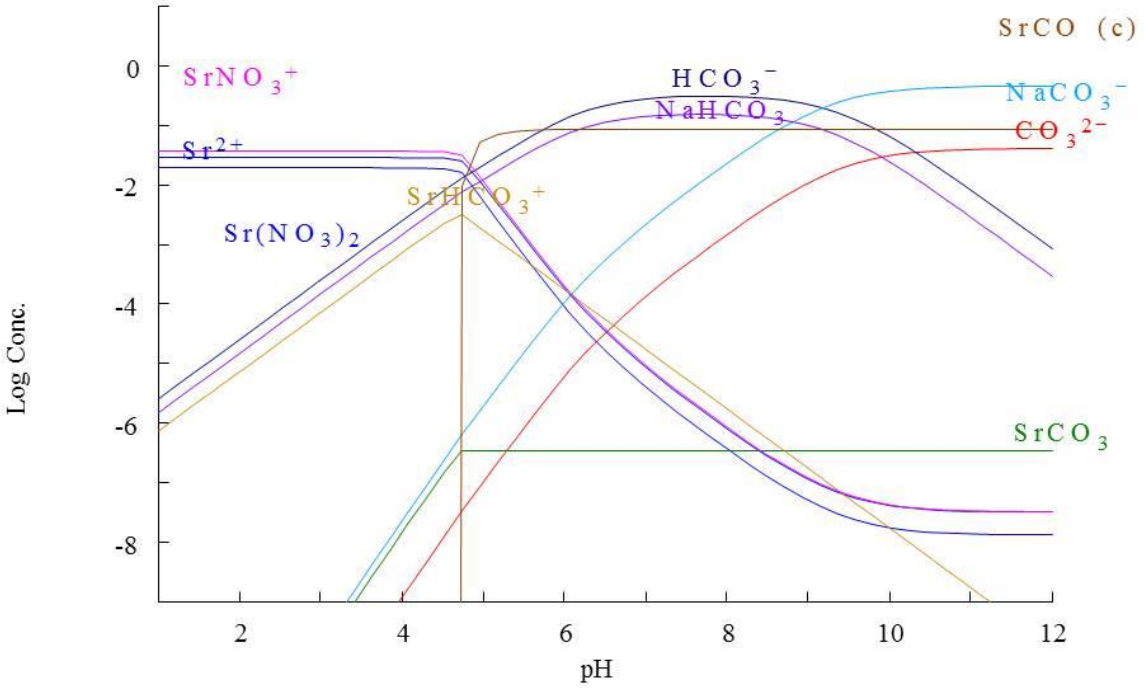

Figure 41 Strontium nitrate plus sodium carbonate precipitation showing species present over pH range 1-12

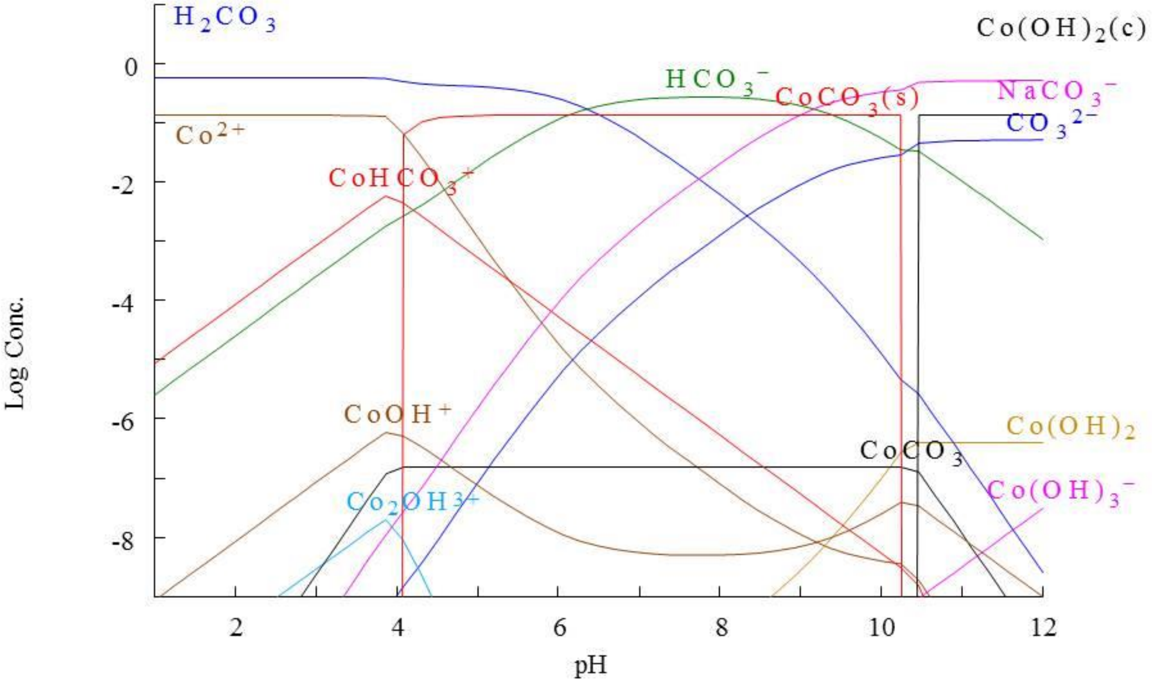

Figure 42 Cobalt(II) nitrate plus sodium carbonate precipitation showing species present over pH range 1-12

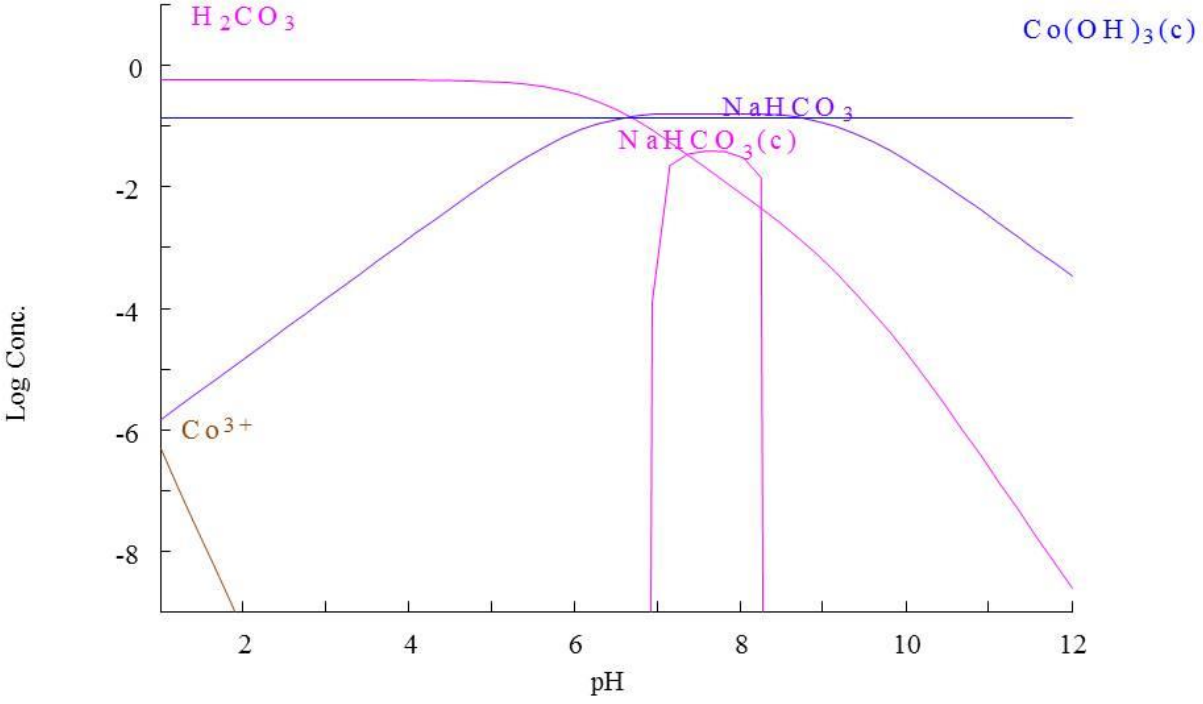

Figure 43 Cobalt(III) nitrate plus sodium carbonate precipitation showing species present over pH range 1-12

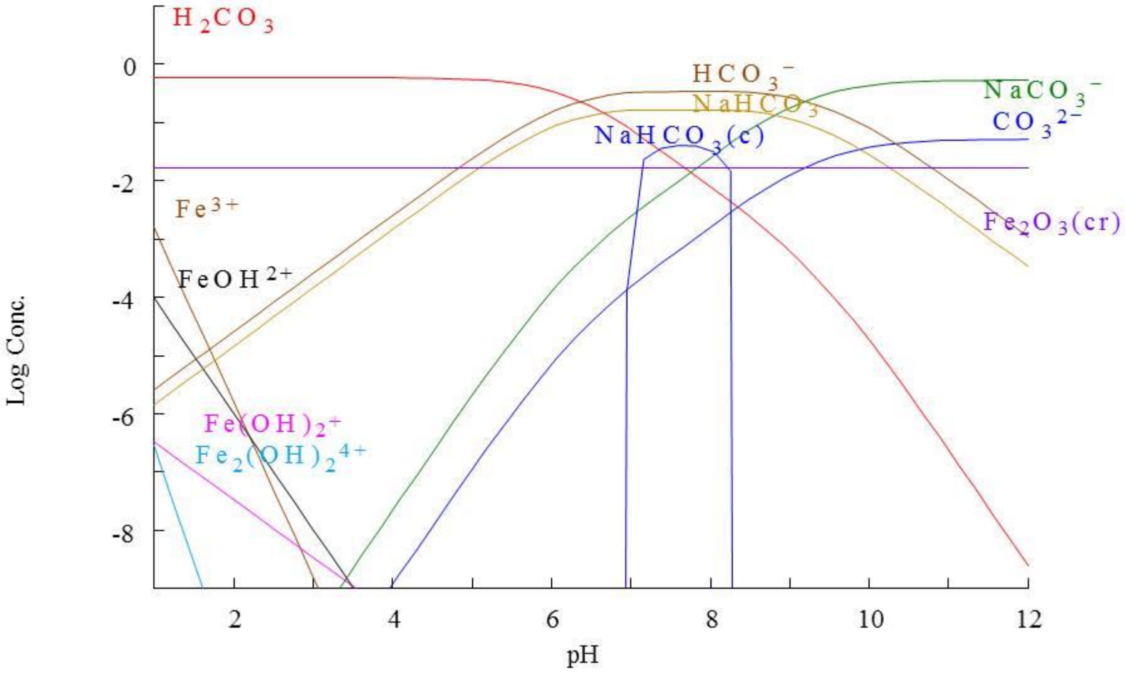

Figure 44 Iron nitrate plus sodium carbonate precipitation showing species present over pH range 1-12

Comparison of the use of sodium carbonate and hydroxide (Figure 38 and Figure 40) shows that with the former, there is a very low concentration 10^{-6} M of $BaCO_3$ in solution and that precipitation is complete above pH 5 and that at pH greater than 11.5 there is some reaction of the barium carbonate precipitate to give some $BaOH^+$ species in solution at very low concentrations. Whereas with sodium hydroxide as the precipitant there is no solid phase present until approximately pH 13 as was confirmed by the precipitation of barium sulphate (white solid) in the exploratory series of preparations. Strontium shows, as is expected, very similar behaviour to barium (Figure 41).

Cobalt(II) nitrate was used in all the experiments as the source of cobalt. However during the addition of the mixed salts solution the precipitate changed from an olive green to a chocolate brown colour, this is ascribed to oxidation of Co^{2+} to Co^{3+} [136.]. The equilibrium diagrams were constructed for both Co^{2+} and Co^{3+}. The Co^{2+} diagram (Figure 42) shows that the soluble Co species ($CoOH^+$ and $CoHCO_3^+$) drop to concentrations below 10^{-6}M at pH greater than 7 though they start to rise at pH 10.5 with the formation of $Co(OH)_3^-$. At about pH 10.3 the precipitated $CoCO_3$ is converted to $Co(OH)_2$. The Co^{3+} diagram (Figure 43) shows no soluble Co species above pH 2.

The iron diagram (Figure 44) shows no soluble species above pH 3.5. In both the Co^{3+} and Fe^{3+} diagrams sodium bicarbonate is indicated as being present as a solid phase in the pH range 6.9 to 8.3, to avoid sodium contamination in the final product careful washing of the precipitates would be needed.

As a result of the exploratory series and the analysis of the equilibrium diagrams the following series of experiments were performed to determine how robust the process was and whether it could be further optimised. The main parameters investigated were:-

1. Final pH
2. Boiling the precipitate
3. pH of boiling.

4.4 Experimental Plan

The object of the precipitation was to make a homogeneous precipitate so that on calcination it would be easier to prepare a single phase powder that could readily be sintered to a dense ceramic. The variation of final pH could allow hydroxide ions to react with any carbonate species to form metal hydroxides. The boiling process at either the precipitation stage or prior to the final filtration could allow further homogenisation of the precipitate by a combination of solution-dissolution or Oswald ripening. Table 8 below shows the plan.

	Precipitation @ pH 10	Precipitation @ pH 12
No Boil	✓	✓
Boil at Precipitation pH (High pH before wash) (Hydrothermal 1)	✓	✓
Boil at pH 7 (Low pH after wash) (Hydrothermal 2)	✓	✓

Table 8 Experimental plan

Some of the dried materials were taken for XRD (Philips PW 1050 Diffractometer) and thermal analysis (Netzsch TG 449 F3 Jupiter® Thermo-Microbalance).

The calcined powders were milled in propan-2-ol and dried at 85°C overnight. Their specific surface area and pore volume were measured (Coulter SA3100plus) after degassing in vacuum at 260°C. Particle size distributions were measured (Malvern Mastersizer) after external dispersion. The dispersion conditions were that to 50cm^3 of a 0.1% w/w suspension of powder in water 5 drops of 10% Dispex A40 solution (BASF SE, Ludwigshafen, Germany) were added prior to 5 minutes in an ultrasonic bath. These conditions were chosen to ensure the powder was properly wetted and that any loose agglomerates were broken down. The calcined powders were also examined by XRD, thermal analysis and SEM including EDS (Zeiss EVO60 or Philips XL30 FEGSEM).

The density of the sintered pellets was measured. The samples were ground using SiC papers and polished with 6 and 1μm diamond paste prior to further characterisation. The polished pellets were examined by XRD and SEM. The oxygen permeability was measured and the electrical properties determined using electrical impedance spectroscopy.

4.5 Results

4.5.1 Dried powders

The dried powders were dark brown in colour and friable.

4.5.1.1 X-ray Analysis

The x-ray analysis showed a mixture of phases. The predominant phase present was $Ba_{0.5}Sr_{0.5}CO_3$. Other mixed oxides and hydroxides were also present as shown in Figure 45 and Table 9 below.

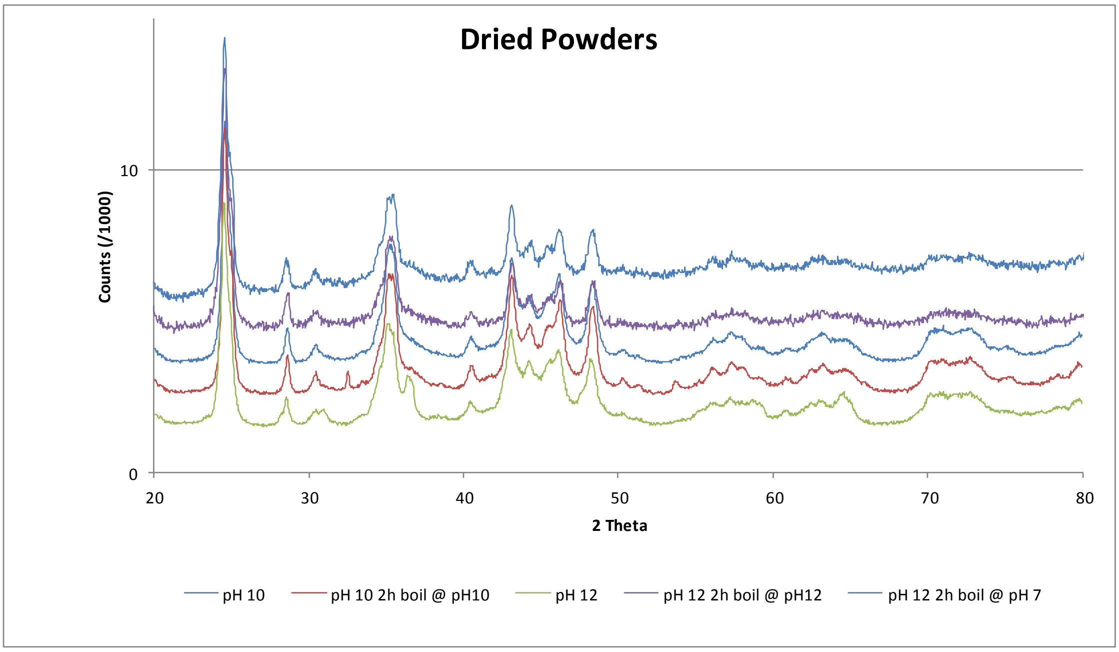

Figure 45 Diffraction patterns of dried powders

X-ray diffraction identifies the phases present in terms of their structure, however the High Score plus Software cannot always discriminate between phases of the same structural type but different composition. For example most of the phases present in this study are solid solutions where the ratio of the cations can have a wide range of values and the material will have the same structure although the lattice parameters will vary. Thus barium rich phases have larger lattice parameters than strontium phases do. Furthermore the very broad peaks present and their overlap with others also hinder phase identification. The broad peaks are due to line broadening caused by small crystallite size.

		pH 10		pH 12		
Phase	Structure	No Boil	High pH	No Boil	Low pH	High pH
$Ba_{0.5}Sr_{0.5}CO_3$	Orthorhombic	Y	Y	Y	Y	Y
$Fe_{2.67}O_4$	Cubic	Y				
$Co_{2.82}O_4$	Cubic			Y		
$Sr_2Co_2O_5$	Cubic				Y	Y
$Ba_{0.2}Sr_{0.8}Co_{0.8}Fe_{0.2}O_{2.9}$	Cubic		Y			
FeO(OH)	Cubic					Y

Table 9 Phases present in dried powders

The $Fe_{2.67}O_4$ and $Co_{2.82}O_4$ phases are iso-structural and although both are listed are probably solid solutions of each other, one being Fe rich and the other Co rich. The presence of Ba/Sr carbonate and the cubic spinel structured species is in agreement with earlier work.[54]

4.5.1.2 Thermogravimetric Analysis

Samples of the dried powder were examined using thermogravimetric analysis. The samples were heated to 1100°C and cooled back to room temperature in an air atmosphere using a heating and cooling rate of $5Kmin^{-1}$. A number of stages can be seen in the decomposition of the dried powders during heating. A typical heating curve is shown in Figure 46

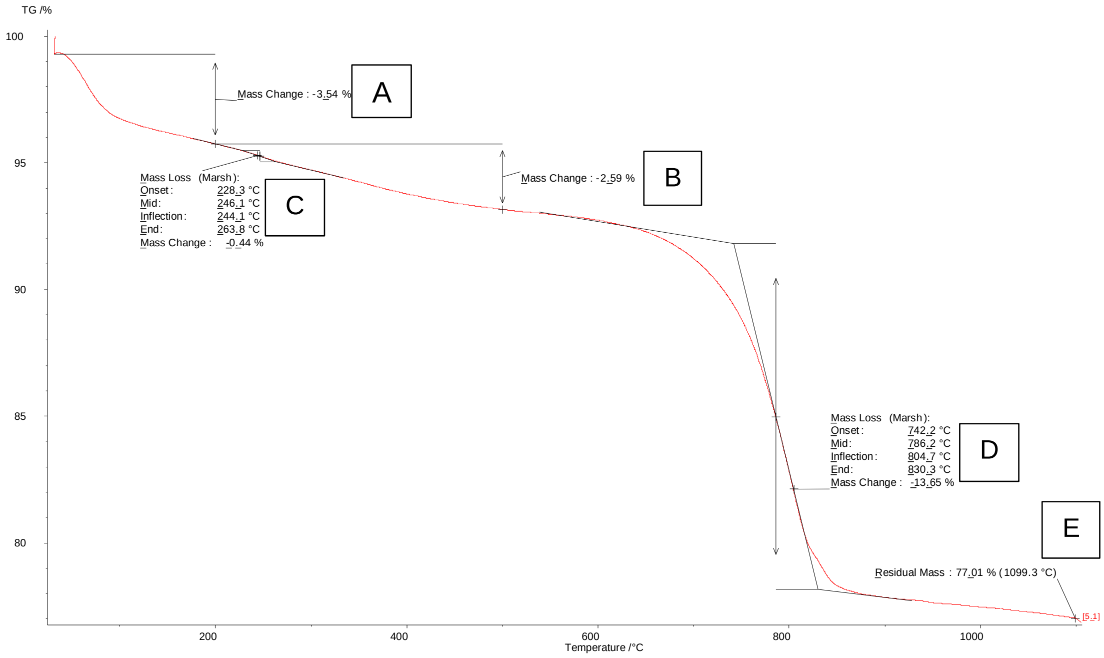

Figure 46 Thermogravimetric heating curve for dried pH12 precipitation in air with a heating rate of 5K min^{-1}

Five stages in the decomposition are noted, though one is included in another. The first stage up to 200°C is labelled on Figure 46 as A. There is a rapid loss of weight followed by a slower loss. This may correspond to loss of adsorbed moisture and the decomposition of hydroxide species which may be present either as discrete compounds or surface layers. The second stage (B) shows a relatively linear weight loss from 200°C to 500°C and continues the loss of hydroxides as water and the start of oxygen loss from mixed metal oxides. In some cases a distinct step (C) can be seen probably due to well-structured material decomposing. Between ~600°C and ~900°C there is a step change weight loss (D) superimposed on the steady weight loss which is evident from 500°C to 1100°C. This step change is assigned to the loss of carbon dioxide from the mixed barium strontium carbonate. The final residual mass at the end of the heating stage (E) is also recorded. The mass change details on Figure 46 are those calculated by the Netzsh evaluation software Proteus. It can be seen that the weight loss for stage D is calculated from the vertical distance between the extrapolated straight line parts of the weight curve before and after the step change. This eliminated the underlying slow weight change that was ascribed to oxygen loss.

On cooling the sample in air a much simpler pattern is observed as in Figure 47, the mass % is relative to the original starting weight prior to heating. As there is only ~1% difference in weight during cooling it is not as readily seen on a combined graph. This weight gain is designated F in the tables below.

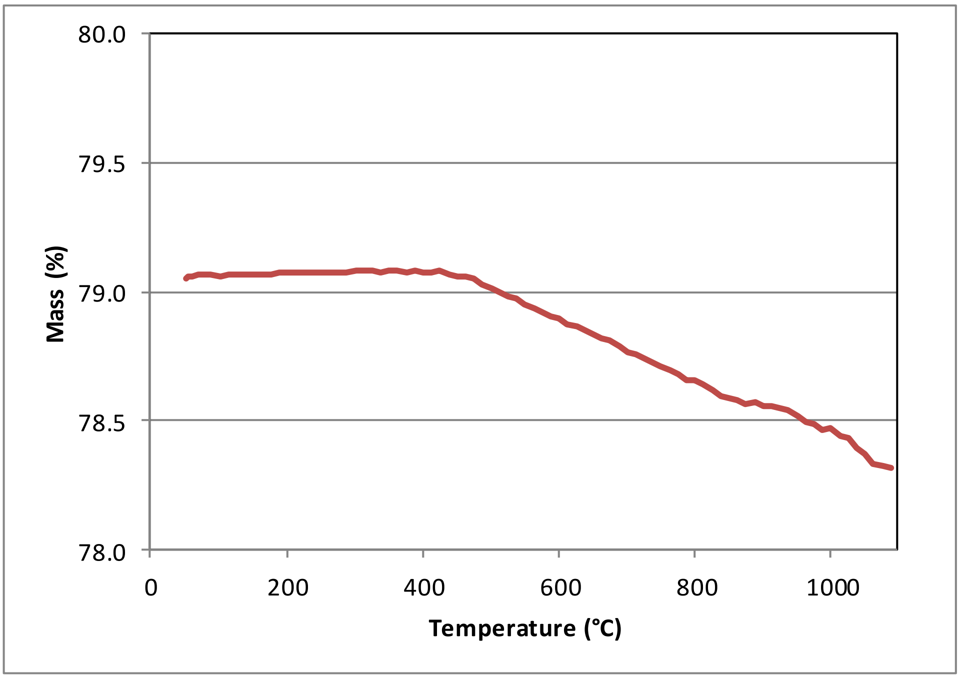

Figure 47 Thermogravimetric cooling curve for dried pH12 precipitation in air with a cooling rate of 5K min^{-1}

From the final residual mass at 1100°C there is a gradual increase of weight until ~450°C after which there is little if any weight change.

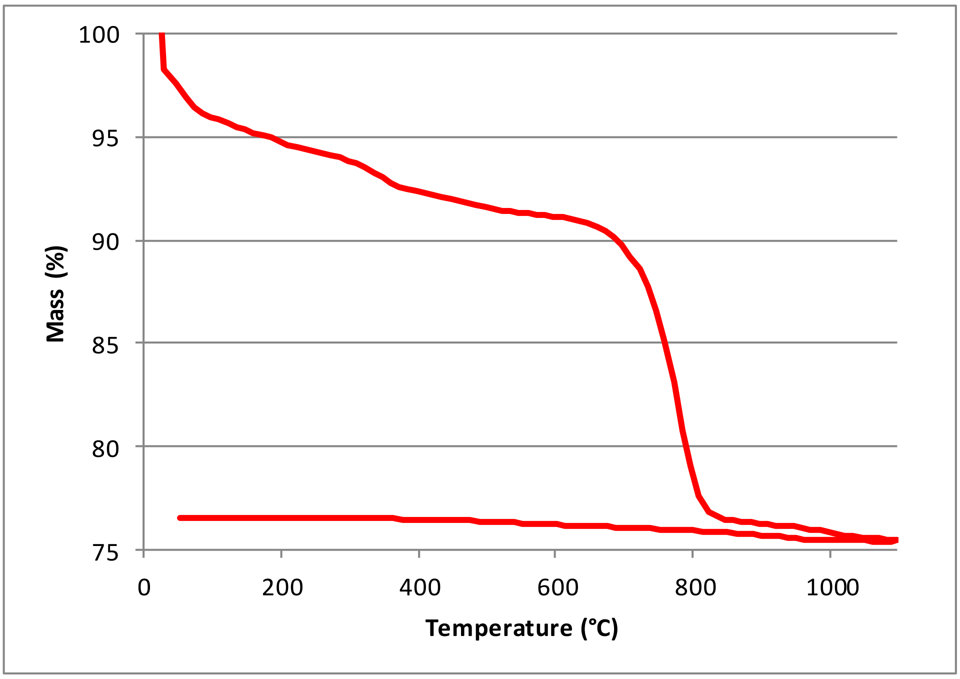

Figure 48 Thermogravimetric curve for dried pH10 precipitation in air with a heating and cooling rate of 5K min^{-1}

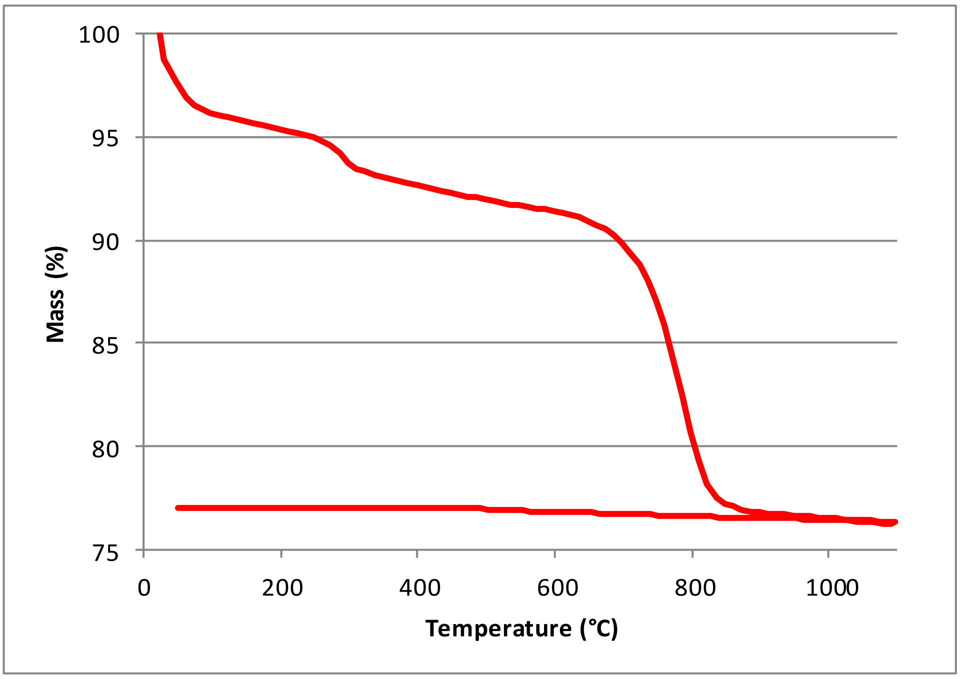

Figure 49 Thermogravimetric curve for dried pH10 precipitation boil @ pH10 in air with a heating and cooling rate of 5K min^{-1}

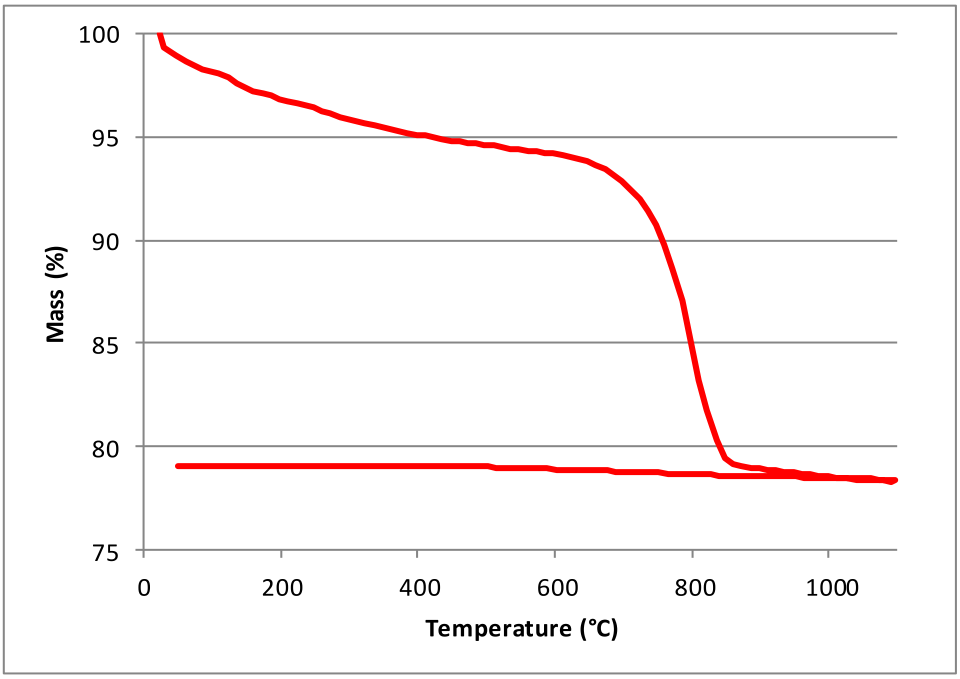

Figure 50 Thermogravimetric curve for dried pH12 precipitation in air with a heating and cooling rate of 5K min^{-1}

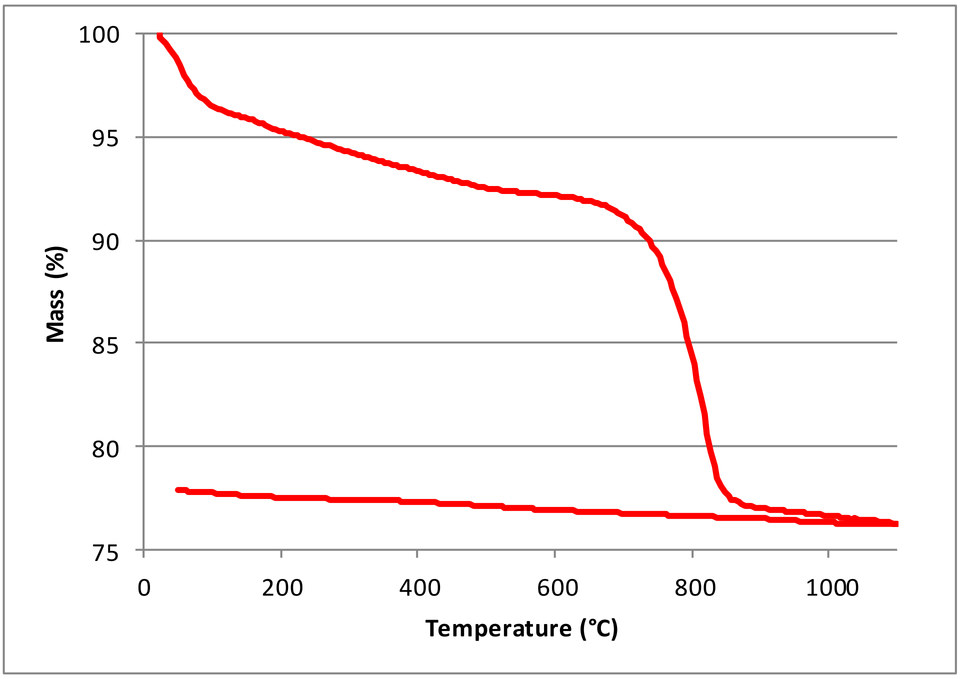

Figure 51 Thermogravimetric curve for dried pH12 precipitation boil @ pH7 in air with a heating and cooling rate of 5K min^{-1}

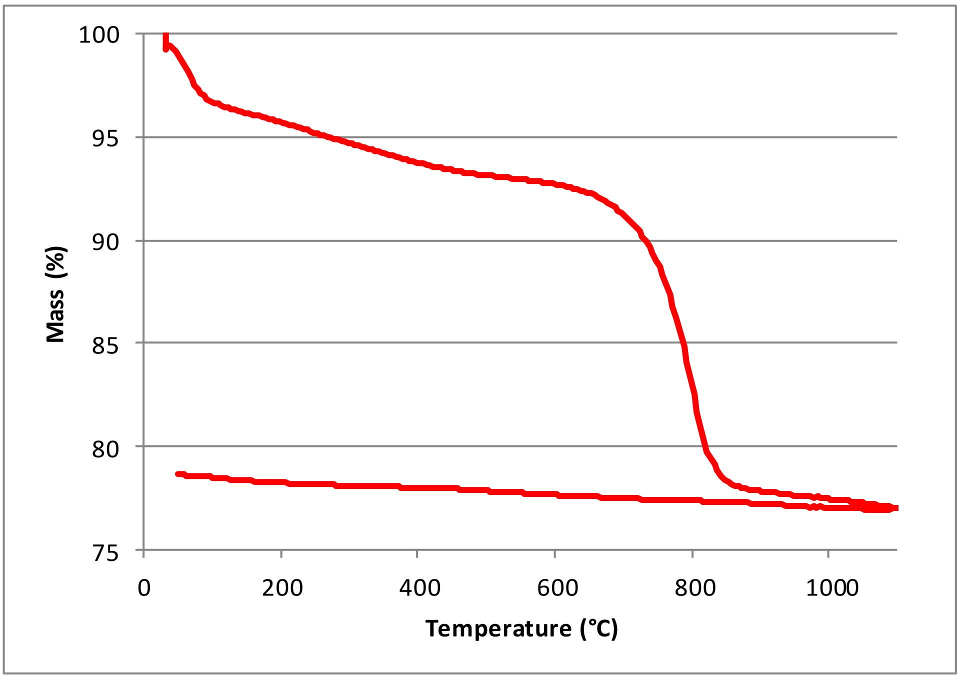

Figure 52 Thermogravimetric curve for dried pH12 precipitation boil @ pH12 in air with a heating and cooling rate of 5K min^{-1}

The thermogravimetric data were analysed in two ways firstly assuming that the final oxide material after heating the sample to 1100°C and cooling back to room temperature had a formula $Ba_{0.5}Sr_{0.5}Co_{0.8}Fe_{0.2}O_{3-\partial}$ where $\delta = 0.5$; this results in a molecular weight of 210.78.(X-ray analysis of the material after sintering at 1100°C showed it to be single phase (Figure 70 below)) The final weight after cooling of oxide was therefore equivalent to this molecular weight and all the other weight losses would proportionately correspond to the molecular masses shown in the columns labelled Δ MW in Table 10. Secondly, the iodometric titration results from section 4.5.2 were used to provide an experimental value for δ. The results are shown in Table 11. Although the two tables are different there are no significant changes in the conclusions drawn from the tables.

At the bottom of the two tables are lines labelled carbonate and delta. These are calculated by expressing weight loss D as a percentage of the molecular weight of carbon dioxide and weight gain F as a fraction of the atomic weight of oxygen, respectively. The value of carbonate is in the broad range of 80 to 90%. This indicates that on calcining the dried powders 0.8 to 0.9 moles of CO_2 are evolved per mole of final $Ba_{0.5}Sr_{0.5}Co_{0.8}Fe_{0.2}O_{3-\partial}$. This is almost equivalent to the total amount of Ba and Sr in the system which could be precipitated solely as the mixed carbonate. This conclusion is supported by the x-ray data above.

The dried precipitate therefore consists of a mixed barium strontium carbonate, and, mixed cobalt and iron compounds.

The initial weight loss A comprises an initial sharp loss in weight followed by a more gradual loss. This can be assigned to the loss of adsorbed and structural water. The latter potentially coming from both water of crystallisation and hydroxide decomposition to form oxides. The x-ray diffraction results indicated only one possible hydroxide structure goethite. The decomposition of goethite is as below

$$2\mathrm{FeO(OH)} \rightarrow \mathrm{Fe_2O_3} + \mathrm{H_2O} \qquad 4.1$$

Thus for each iron (and cobalt) ion in a goethite structure there would be half a water molecule lost. Examination of Table 11 shows that a ΔMW of ~9 occurs at stage B. This would support the hypothesis that a goethite structured oxy-hydroxide is precipitated. However the other weight losses and phases present prevent a definitive assignment being made.

		pH 10 No boil		pH10 boil @ pH10		pH 12 No boil		pH 12 boil @ pH 7		pH 12 boil @ pH12	
		Wt %	Δ MW	Wt %	Δ MW	Wt %	Δ MW	Wt %	Δ MW	Wt %	Δ MW
<200°C	A	-5.22	-14.38	-4.59	-12.56	-3.17	-8.45	-4.73	-12.80	-3.54	-9.49
200-500	B	-3.18	-8.76	-3.45	-9.44	-2.21	-5.89	-2.72	-7.36	-2.59	-6.94
	C	-1.05	-2.89	-1.25	-3.42	-0.79	-2.11	0.00	0.00	-0.44	-1.18
	D	-13.45	-37.04	-13.05	-35.71	-14.08	-37.54	-13.98	-37.85	-13.65	-36.59
Mass at 1100°C	E	75.40	207.67	76.28	208.75	78.32	208.83	76.24	206.39	77.01	206.41
Heating to 400	F	1.04	2.86	0.73	2.00	0.76	2.03	1.07	2.90	0.99	2.65
Final Mass		76.53	210.78	77.02	210.78	79.05	210.78	77.86	210.78	78.64	210.78
		Delta	0.18		0.12		0.13		0.18		0.17
		Carbonate	84.2		81.1		85.3		86.0		83.1
			If final product is delta =0.5								
			MW =	210.78							

Table 10 TGA data without correction

		pH 10 No boil		pH10 boil @ pH10		pH 12 No boil		pH 12 boil @ pH 7		pH 12 boil @ pH12	
		Wt %	Δ MW	Wt %	Δ MW	Wt %	Δ MW	Wt %	Δ MW	Wt %	Δ MW
<200°C	A	-5.22	-14.52	-4.59	-12.69	-3.17	-8.54	-4.73	-12.94	-3.54	-9.60
200-500	B	-3.18	-8.85	-3.45	-9.54	-2.21	-5.95	-2.72	-7.44	-2.59	-7.02
	C	-1.05	-2.92	-1.25	-3.46	-0.79	-2.13	0.00	0.00	-0.44	-1.19
	D	-13.45	-37.41	-13.05	-36.07	-14.08	-37.92	-13.98	-38.25	-13.65	-37.00
Mass at 1100°C	E	75.40	209.73	76.28	210.86	78.32	210.92	76.24	208.59	77.01	208.77
Heating to 400	F	1.04	2.89	0.73	2.02	0.76	2.05	1.07	2.93	0.99	2.68
Final Mass		76.53	212.87	77.02	212.91	79.05	212.89	77.86	213.02	78.64	213.19
		Delta	0.18		0.13		0.13		0.18		0.17
		Carbonate	85.0		82.0		86.2		86.9		84.1

Table 11 TGA data after iodometric correction

4.5.2 Calcined powders

The calcined powders were black in colour and were agglomerated. After milling the powders were floury in texture. The powder properties after milling are summarised in Table 12.

Precipitation pH	Hydrothermal Treatment	Surface area (m^2g^{-1})	Pore volume (cm^3g^{-1})	Delta	Particle Size d_{50} (µm)
pH 10	No boil	2.35	0.0151	0.366	5.4
	Low pH	0.91	0.0071	0.354	3.3
	High pH	1.64	0.0100	0.364	2.6
pH 12	No boil	0.85	0.0075	0.365	4.6
	Low pH	1.03	0.0063	0.357	3.6
	High pH	1.26	0.0079	0.346	3.7

Table 12 Summary of calcined powder properties

The surface area results are low and similar for all the preparations as are the pore volumes. From the surface area (SA) and the theoretical density (ρ) for $Ba_{0.5}Sr_{0.5}Co_{0.2}Fe_{0.8}O_{3-\delta}$ of $5.75gcm^{-3}$ the equivalent particle size (d in µm) may be calculated using equation 4.2. The results are given in Table 13. Also given are crystal sizes derived from the full width half height maximum (FWHM) of the largest peak in the x-ray diffraction traces using the Scherrer equation (see section 3.4.2).

$$d = \frac{6}{SA\ \rho} \qquad 4.2$$

Precipitation pH	Hydrothermal Treatment	Surface area (m^2g^{-1})	Particle Size ex Eq 4.2 (µm)	Particle Size d_{50} (µm)	Crystal Size ex XRD (nm)
pH 10	No boil	2.35	0.44	5.4	47
	Low pH	0.91	1.15	3.3	40
	High pH	1.64	0.64	2.6	21
pH 12	No boil	0.85	1.23	4.6	44
	Low pH	1.03	1.01	3.6	25
	High pH	1.26	0.83	3.7	22

Table 13 Comparison of measured and calculated particle size

The results from the calculated and measured particle sizes (Table 13) are in the ratio of approximately 1:4. This suggests that the particles are made of large dense crystallites as is confirmed by the low pore volume. Alternatively smaller particles could be sintered together to form very dense agglomerates with only some small external surface area. The latter explanation is supported by the x-ray line broadening data which shows a much smaller crystallite size. The crystallite size range of 20-50nm corresponds to a surface area, if not agglomerated, of 50-20m^2g^{-1}.

4.5.2.1 X-ray Diffraction Results

The x-ray traces of the milled calcined powders are shown in Figure 53.

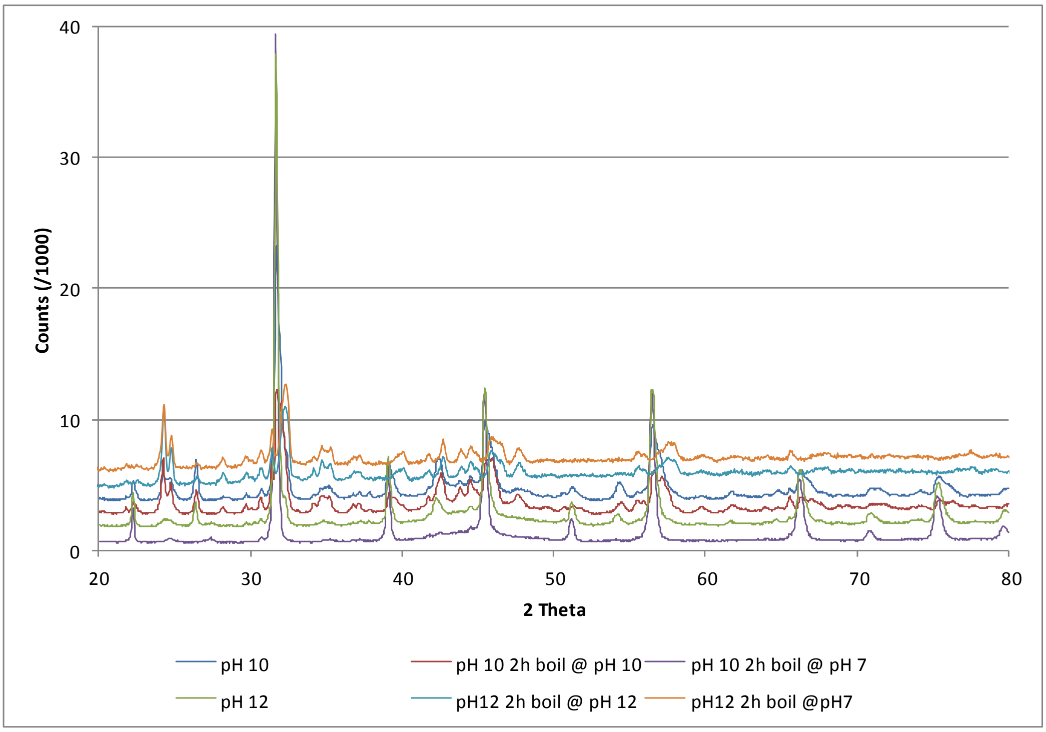

Figure 53 Diffractogram of calcined powders

It can be seen that there are a number of phases present in the calcined powders. The diffractograms were fitted using Topas. The phase compositions are summarised in Table 14. An example of the fitting is shown in Figure 54 to Figure 57. The red line is the fitting and the black line is the experimental data. Underneath is a grey line showing the residual differences. At the bottom just above the abscissa are tick marks indicating the peak positions for the different phases. For the last three figures in addition the individual contribution of the selected phase is shown together with an indication of which set of tick marks correspond to the selected phase. In all cases the goodness of fit (GOF) was less than 2.

		pH 10			pH 12		
Phase	Structure	No boil	Low pH	High pH	No boil	Low pH	High pH
$Ba_{0.5}Sr_{0.5}Co_{0.8}Fe_{0.2}O_{3-\delta}$	Cubic		✓			✓	
$Ba_{0.5}Sr_{0.5}CO_3$	Orthorhombic	✓		✓✓	✓	✓	✓✓
$BaFeO_{2.88}$	Hexagonal	✓	✓	✓		✓✓	✓✓
$Ba_8Co_7O_{21}$	Orthorhombic	✓		✓	✓	✓	✓

Table 14 Phases present in milled powders (✓✓ indicates 2 phases with this structure)

It can be seen that both the hexagonal and the orthorhombic oxide phases have sharper lines in the fitted pattern when compared to the barium/strontium carbonate phase. This implies that the latter has smaller crystallites.

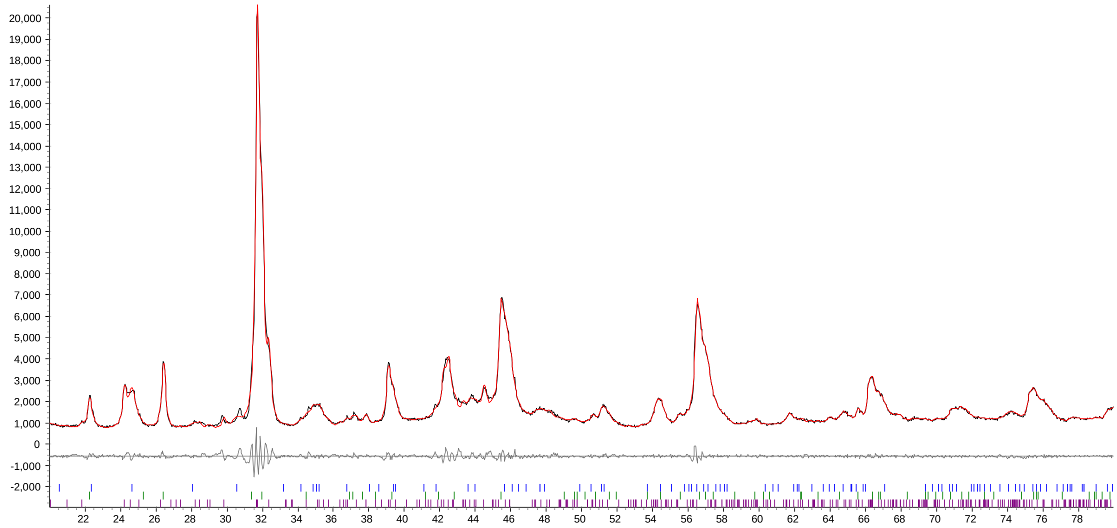

Figure 54 Fitting of calcined powder prepared at pH 10

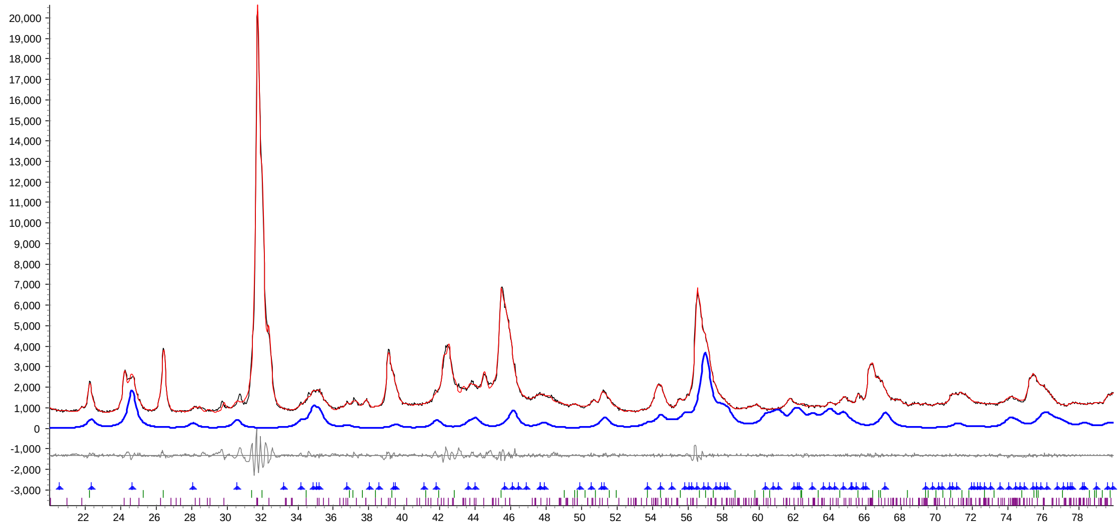

Figure 55 Fitting of calcined Powder prepared at pH 10 showing the contribution of the carbonate phase

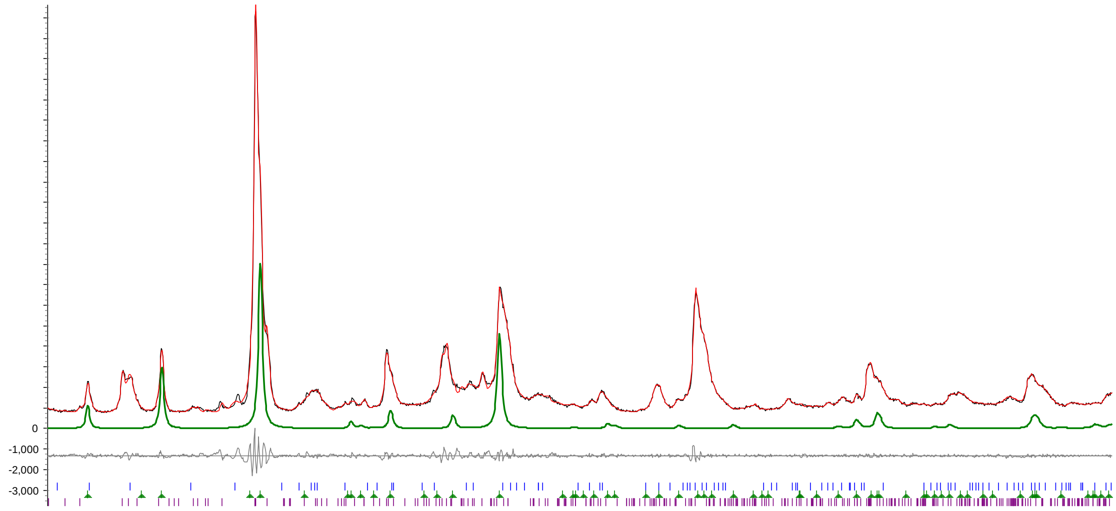

Figure 56 Fitting of calcined powder prepared at pH 10 showing the contribution of a hexagonal phase

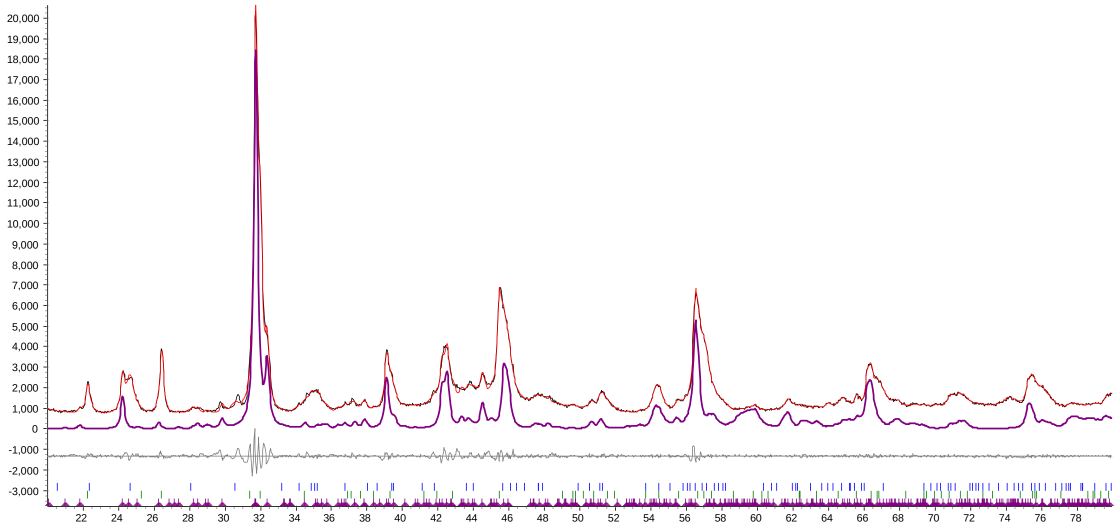

Figure 57 Fitting of calcined powder prepared at pH 10 showing the contribution of an orthorhombic phase

The phase assemblage of the dried powders (Table 9) is quite different as would be expected, however they contained the mixed barium strontium carbonate as does the milled powders and a number of simple oxide phases with cubic symmetry. Two samples contained the desired cubic BSCF 5582 phase. On calcination and milling most of the carbonate has been removed (see section 4.5.2.2 below) however the oxides have reacted with one another and formed a number of different structures with either hexagonal or orthorhombic structures. These structures are very similar to the desired cubic structure of BSCF 5582. The unit cell volumes for the phases from the fitting are shown in Table 15.

	pH10					
	Carbonate		**Hexagonal**		**Orthorhombic**	**Cubic**
No Boil	278.98		381.44		3,838.96	
Boil at pH 7			381.86			63.58
Boil at pH10/12	275.40	288.84	381.14		3,896.85	
	pH12					
No Boil	281.89				3,824.03	
Boil at pH 7	276.24		231.99	376.46	3,759.39	60.54
Boil at pH10/12	281.60	288.78	376.26	377.74	3,981.97	

Table 15 Unit cell volumes of phases in milled oxides (/Å^3)

The unit cell volumes of the mixed barium strontium carbonate (275-289Å^3) are within the published range (267-297Å^3) and correspond to the barium concentration in the $Ba_xSr_{1-x}CO_3$ of x=0.38 to 0.65.[137] The details are shown in Table 16.

	pH 10	pH 12
No Boil	0.45	0.51
Boil at pH 7		0.39
Boil at pH10/12	0.38 0.65	0.50 0.65

Table 16 Barium content in mixed barium strontium carbonate

The hexagonal phase in the three powders precipitated at pH 10 did not vary between the different post precipitation conditions. Without any boiling of the precipitate a single carbonate which was slightly rich in strontium was formed as well as an orthorhombic phase, The precipitate boiled at pH 7 produced the hexagonal phase and some cubic phase. After the high pH boil powders with two carbonate phases, one with a low and the other with a high barium content, were formed as well as the hexagonal and orthorhombic phases.

The powders produced from the higher pH 12 preparations showed variation in the hexagonal phase though it was only present in the samples that had been boiled. The carbonate phase in the unboiled and high pH preparation had 50% barium content although the latter also had a higher barium content mixed carbonate, The orthorhombic phase varied quite considerably in unit cell volume compared to the low pH materials. The cubic phase was only formed after boiling at pH 7, which was also found with the pH 10 material.

4.5.2.2 Thermogravimetric analysis

Samples of the milled calcined powder were examined using thermogravimetric analysis. The samples were heated to 1100°C and cooled back to room temperature in an air atmosphere using a heating and cooling rate of 5Kmin^{-1}. The graphs show as expected a much reduced overall mass loss of ~10%, when compared to the dried powders, as shown in Figure 58. There are a number of stages in the decomposition an initial weight loss up to 250°C, followed by a small gain in weight starting at ~300°C, a slight weight loss continues to ~650°C where a larger weight loss occurs prior to a further gradual weight loss to 1100°C. These stages are very similar to those seen for the dried powders (see section 4.5.1.2). The exception is the weight gain starting at ~300°C. This weight gain is assigned to uptake of oxygen as the system equilibrates as the temperature rises. As noted earlier there is a gradual increase in oxygen content of the $Ba_{0.5}Sr_{0.5}Co_{0.2}Fe_{0.8}O_{3-\delta}$ on cooling. However the oxygen transfer kinetics slow down as the temperature decreases. Although there is a thermodynamic driver for the continued oxygen addition, the slowness of the kinetics means that it comes to a halt on cooling ie thermodynamic equilibrium is not achieved. On heating, however, the kinetics for oxygen gain are increasing and oxygen can be added to the $Ba_{0.5}Sr_{0.5}Co_{0.2}Fe_{0.8}O_{3-\delta}$ until the point is reached at which loss of oxygen is thermodynamically preferred. The weight loss at lowest temperature is attributed to desorption of water and other volatiles adsorbed from the atmosphere. The large weight loss at 800°C is due to carbon dioxide being released from the samples.

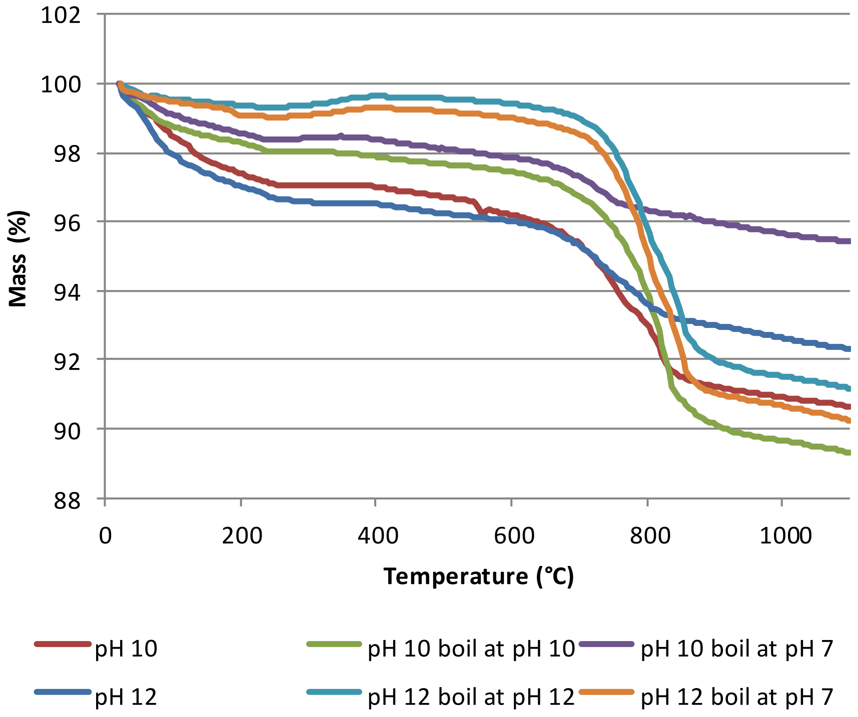

Figure 58 Thermogravimetric analysis of milled powders on heating in air with a heating rate of 5K min^{-1}

On cooling the powders a similar pattern to the dried powders occurs a gradual weight increase until ~400°C and then little further weight change as can be seen in Figure 59.

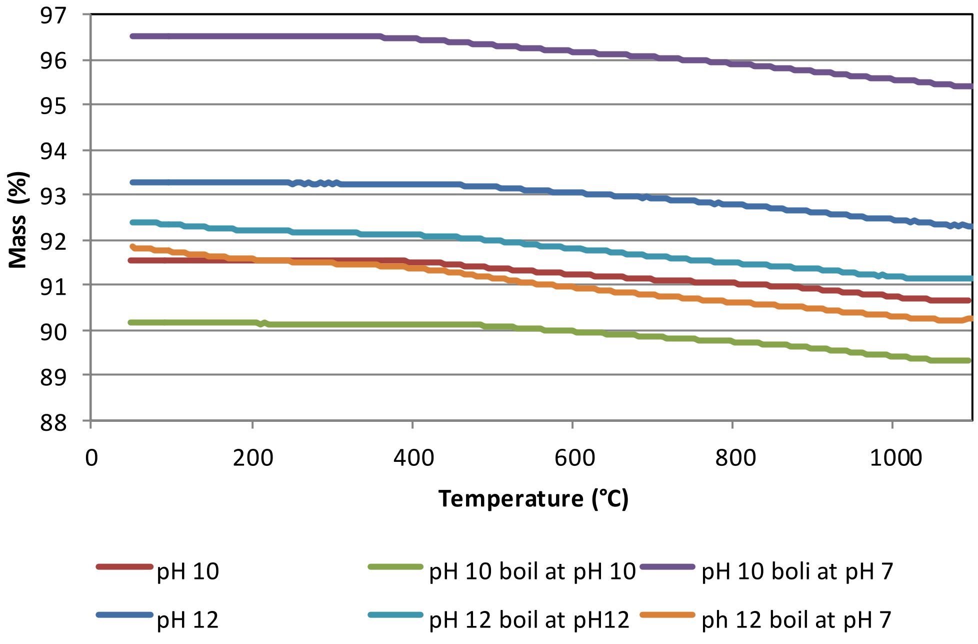

Figure 59 Thermogravimetric analysis of milled powders on cooling in air with a cooling rate of 5K min^{-1}

The details of the different stages of decomposition during the thermogravimetric analysis are shown in Table 17 and Table 18. As with the dried powders, the results are given assuming firstly δ=0.5 and then using the value measured from the iodometric titration. The carbon dioxide evolution around 700°C shows some variation between the different powders. Conversion of the weight loss from carbon dioxide to a mole percentage based on a change of molecular weight of 44 equalling 100% is shown in the last line of the tables. The value varies between 6 and 40%, this indicates that this proportion of the strontium and barium is present as carbonate. This is confirmation of the x-ray assignment. There was no systematic variation in the carbonate level in the calcined milled powders. Differences in the completeness of the decomposition during calcination are the most probable cause of the variation. Although the powders on a 40g scale were all calcined at 850°C with a dwell time of 4 hours the heat transfer rate or the kinetics of decomposition may not have been sufficient to remove totally the carbon dioxide.

There was a very similar uptake of oxygen during the cooling stage of the thermogravimetric analysis between all the samples.

		pH 10 No boil		pH 10 boil @ pH7		pH 10 boil @ pH10		pH12 No boil		pH 12 boil @ pH7		pH 12 boil @ pH1	
		Wt %	Δ MW	Wt %	Δ MW	Wt %	Δ MW	Wt %	Δ MW	Wt %	Δ MW	Wt %	Δ M
heat	<400	-3.00	-6.91	-1.62	-3.54	-2.11	-4.93	-3.49	-7.89	-0.70	-1.61	-0.37	-0.8
	650-850	-3.83	-8.82	-1.15	-2.51	-6.65	-15.55	-2.60	-5.88	-7.42	-17.03	-7.05	-16.0
	Max	90.64	208.73	95.42	208.36	89.31	208.82	92.32	208.61	90.24	207.13	91.16	207.9
cool	to 400	0.88	2.03	1.05	2.29	0.82	1.92	0.94	2.12	1.14	2.62	0.95	2.1
		91.53	210.78	96.53	210.78	90.15	210.78	93.28	210.78	91.83	210.78	92.40	210.7
	Delta		-0.13		-0.14		-0.12		-0.13		-0.16		-0.1
	Carbonate		20.05		5.71		35.34		13.35		38.71		36.5
			MW =	210.78									

Table 17 TGA data without correction

		pH 10 No boil		pH 10 boil @ pH7		pH 10 boil @ pH10		pH12 No boil		pH 12 boil @ pH7		pH 12 boil @ pH12	
		Wt %	Δ MW	Wt %	Δ MW	Wt %	Δ MW	Wt %	Δ MW	Wt %	Δ MW	Wt %	Δ MW
heat	<400	-3.00	-6.98	-1.62	-3.58	-2.11	-4.98	-3.49	-7.97	-0.70	-1.62	-0.37	-0.85
	650-850	-3.83	-8.91	-1.15	-2.54	-6.65	-15.71	-2.60	-5.93	-7.42	-17.21	-7.05	-16.27
	Max	90.64	210.80	95.42	210.66	89.31	210.93	92.32	210.70	90.24	209.33	91.16	210.33
cool	to 400	0.88	2.05	1.05	2.32	0.82	1.94	0.94	2.15	1.14	2.64	0.95	2.19
		91.53	212.87	96.53	213.11	90.15	212.91	93.28	212.89	91.83	213.02	92.40	213.19
	Delta		0.13		0.14		0.12		0.13		0.17		0.14
	Carbonate		20.24		5.77		35.69		13.49		39.12		36.97

Table 18 TGA data after iodometric correction

4.5.2.3 Scanning Electron Microscopy

Micrographs were taken of the milled calcined powders as shown in Figure 60.

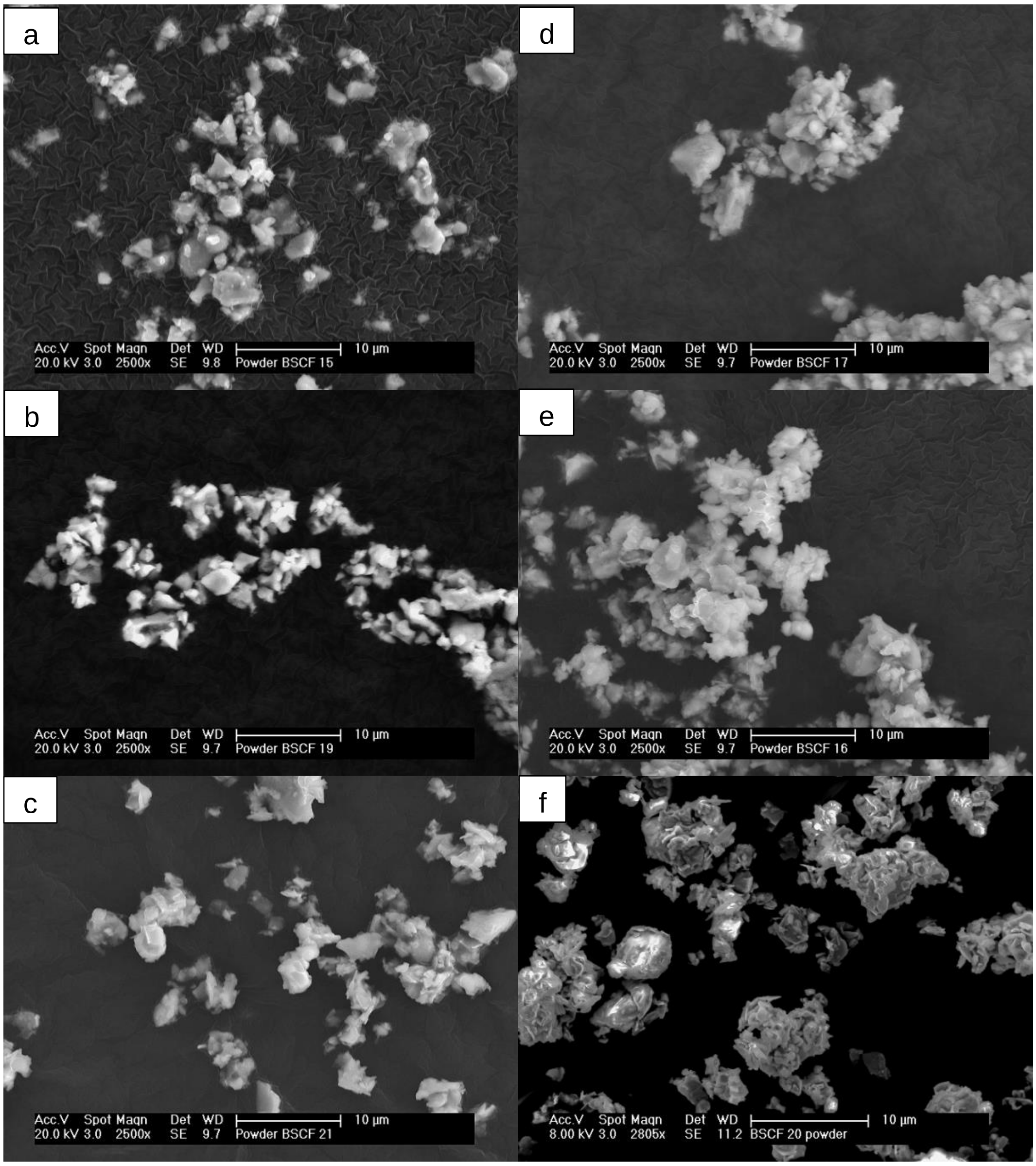

Figure 60 Micrographs of calcined milled powders a) pH10, b) pH10-pH 7 boil, c) pH10-pH10 boil, d) pH12, e) pH12-pH7 boil, f) pH12-pH12 boil

The milled powders consisted of agglomerates of 2-5µm made up of much smaller crystallites of ~200nm. In the materials which had been boiled at the higher pH the crystallites appeared a little smaller.

4.5.2.4 Discussion of Powder Formation

The formation of the calcined milled powders went through a number of stages from the initial starting point of an homogeneous mixed nitrate solution to the final mixed phase product. These final milled powders showed a number of differences principally the phase assemblage and to a lesser extent their particle/crystallite size. The addition of the metal salt solution to the sodium carbonate was designed to ensure simultaneous precipitation of all the metals to give a homogeneous precipitate. However as it can be seen in the x-ray diffraction and thermal gravimetric analysis of the dried products a mixture of phases resulted from the precipitation. From the thermal analysis it was concluded that 80% of the strontium and barium were precipitated as the mixed carbonate. The majority of the iron and cobalt were present as either oxides or oxyhydroxides. The hydrothermal treatment of the precipitates altered the phases present with mixed alkaline earth and cobalt phases being formed on boiling at high pH. A reaction sequence is outlined in Figure 61. The precipitation does not produce a single phase material, however after the calcination and sintering stages the single cubic phase is eventually formed. On precipitation, the barium and strontium form a mixed carbonate, and the iron and cobalt form mixed hydroxides and carbonate, which at high pH form mixed hydroxides. The higher pH's will tend to decrease the amount of carbonate in the iron/cobalt species because of the increased OH^- ion activity which will drive equation 4.3 to the right. In the equations here only one of the ions is used for simplicity but there will be a solid solution of the two ions.

$$\mathrm{CoCO_3} + 2\mathrm{OH^-} \leftrightarrow \mathrm{Co(OH)_2} + \mathrm{CO_3^{2-}} \qquad 4.3$$

In addition there will be oxidation of the cobalt (2+) to cobalt (3+) by air oxidation as evidenced by the change in colour from olive-green to brown of the precipitate due to the formation of cobalt oxyhydroxides (CoO(OH))[136]

$$4\mathrm{Co(OH)_2} + \mathrm{O_2} \rightarrow 4\mathrm{CoO(OH)} + 2\mathrm{H_2O} \qquad 4.4$$

On heating, during drying, any formed hydroxides can partially dehydrate to give the goethite structured oxyhydroxides as shown in equation 4.5, also there will be complete dehydration to oxides

$$\mathrm{Fe(OH)_3} \rightarrow \mathrm{FeO(OH)} + \mathrm{H_2O} \tag{4.5}$$

Cobalt hydroxide and cobalt oxyhydroxides have been shown to decompose on heating to CoO and Co_3O_4 respectively[136]

$$\mathrm{Co(OH)_2} \rightarrow \mathrm{CoO} + \mathrm{H_2O} \tag{4.6}$$

$$12\mathrm{CoO(OH)} \rightarrow 4\mathrm{Co_3O_4} + 6\mathrm{H_2O} + \mathrm{O_2} \tag{4.7}$$

During calcination there are also reactions between the mixed carbonate and the oxyhydroxides and oxides. The decomposition of the carbonate was not complete at 850°C as shown in the x-ray diffraction and thermal analysis. This may be due to the large samples (50g) used in the calcination compared to those in the thermal analysis (30mg). In the larger sample the mixed carbonate may decompose and because of the time taken for the released carbon dioxide to diffuse out of the powder bed it may react with barium oxide to form barium carbonate which has a higher decomposition temperature. In the thermal analysis experiments the carbon dioxide can easily be removed from the powder. This reabsorption behaviour was seen by Criado et al.[137] This proposal is further supported by the barium content of the mixed carbonates (Table 16) where high levels (>50%) of barium predominate.

$Ba(NO_3)_2 + Sr(NO_3)_2 + Fe(NO_3)_3 + Co(NO_3)_2$

↓ **Precipitation**

$(Ba,Sr)CO_3 + Fe(OH)_3 + CoCO_3$

↓ **pH increase**

$(Ba,Sr)CO_3 + Fe(OH)_3 + Co(OH)_3$

↓ **Ageing**

$(Ba,Sr)CO_3 + (Fe,Co)(OH)_3$

↓**Further Ageing**

$(Ba,Sr)CO_3 + (Fe,Co)O(OH) + (Fe,Co)_3O_4 + (Ba,Sr)(Fe,Co)O_3$ (Dried)

↓ **Calcination**

$(Ba,Sr)CO_3 + (Ba,Sr)(Fe,Co)O_3$ (Calcined)

Figure 61 Reaction sequence from precipitation to calcination

The particle size of the precipitates may also be affected by the pH of the solutions in which the materials are processed. As the hydroxides may be ion exchange materials at high and low pH's[138] they can react with the hydroxide ions present and become charged and form charged species which are mutually repulsive (equation 4.8)

$$\mathrm{MOH} + \mathrm{OH^-} \leftrightarrow \mathrm{MO^-} + \mathrm{H_2O} \qquad 4.8$$

This repulsion can prevent agglomeration and give rise ultimately to smaller particles. The agglomeration can also be prevented by the consequent high zeta potentials present on the particles.

4.5.3 Sintered Ceramics

Pellets were uniaxially pressed from milled calcined powders without any additives in a 1cm die at 100MPa.

4.5.3.1 Determination of sintering conditions

In addition to sintering at 1100°C for 10 hours a series of experiments were carried out to determine the sintering temperature for densification and to try to determine the concurrent pore size changes using computerised x-ray tomography. Evidence for the presence of continuous porosity would also be sought.

The sintering experiments were carried out by pressing pellets from BSCF 5582 powder and heating them to a maximum of 1125°C. Pellets were removed from the hot furnace when they reached the temperatures indicated in Figure 62. The last two pellets 1125-0 and 1125-5 were removed after 0 and 5 hours at temperature respectively.

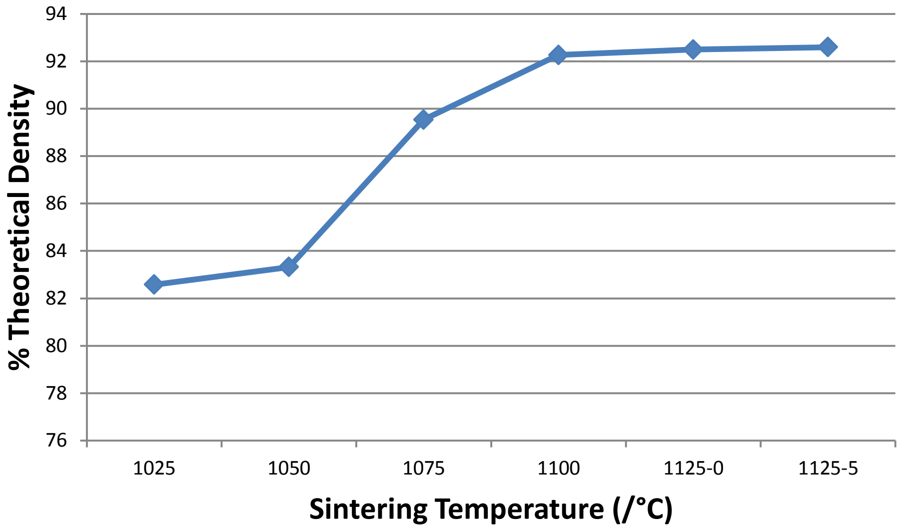

Figure 62 Densification of BSCF 5582

As there was little change in density at 1125°C compared to 1100°C, all further experiments used 1100°C sintering temperatures.

The closure of pores was important as the ceramic was to be used for oxygen permeation and if porosity went through the sample then there would be a simple diffusion pathway. This would mean that all the gases on the high pO_2 side of the membrane would pass and the selectivity would be much reduced.

Computerised x-ray tomography was carried out to see if the pore closure could be seen. Two instruments were used in the Manchester X-ray Imaging Facility (MXIF) which covered different size ranges. The first was the Nikon Metris Custom Bay which can measure objects from 10’s of centimetres in dimension down to 1 cm with a resolution with these small objects of ~2µm. The pores were not discernible at this resolution used because of a mixture of noise and their small size. The uniformity of the structure can be seen in Figure 36

A small piece was cut and ground to shape 1x1mm and mounted on a pin. This sample was imaged on the Xradia VersaXRM-510 which can resolve features down to 0.7µm. A sample sintered at 1050°C was examined as it was felt that pores would be visible as it had a relatively low density.

A slice through the sample is shown in Figure 63. It shows a pore towards the centre of the image and variations of intensity across the whole area.

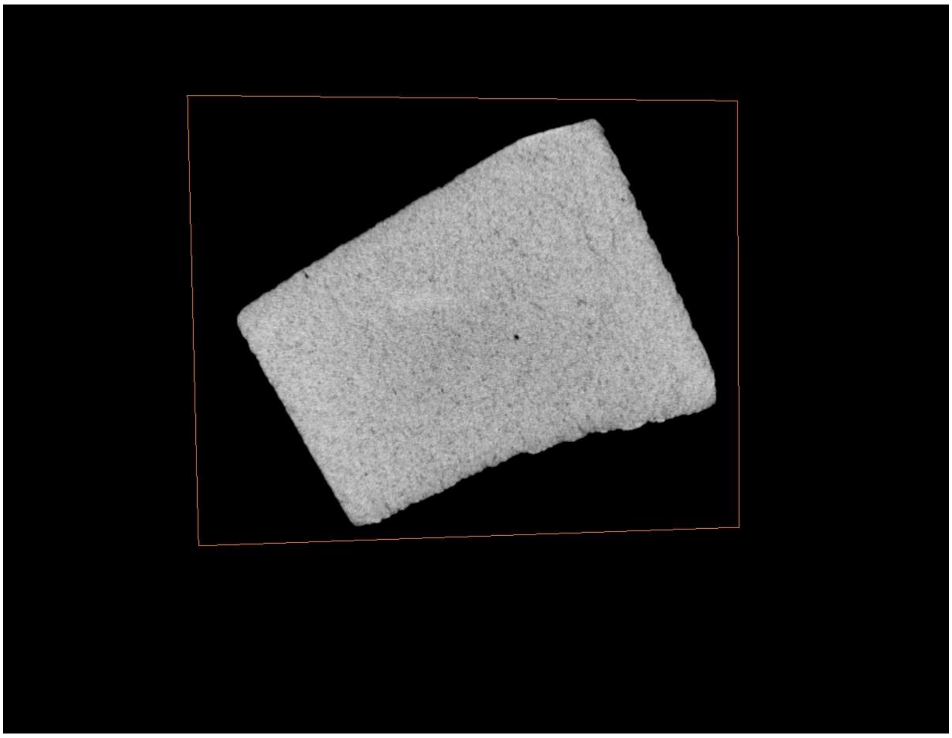

Figure 63 Reconstruction of ground piece of BSCF 5582

The slices can also be combined to show slices in the two orthogonal directions as shown in Figure 64. A crack from the edge of the sample can be clearly seen in Figure 64. The crack was probably caused by the cutting and grinding operations.

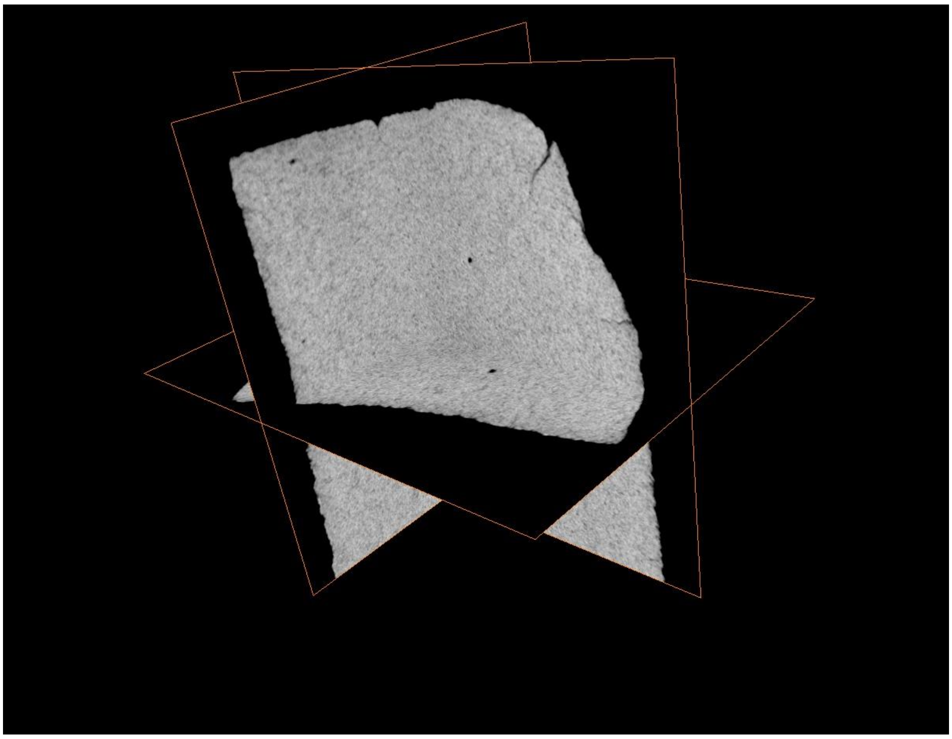

Figure 64 Orthogonal views of ground BSCF 5582

From these orthogonal images the ceramic and pores were selected through the selection of appropriate grey scale levels and the volume representation generated A 3-D image is shown in Figure 65 and a close up version in Figure 66. It shows the pores in pink with the outline of the piece in grey. The scale bar indicates microns. A large number of small pores (5µm) are visible with a few larger pores of about 30µm. There is no evidence on this scale of continuous porosity

.

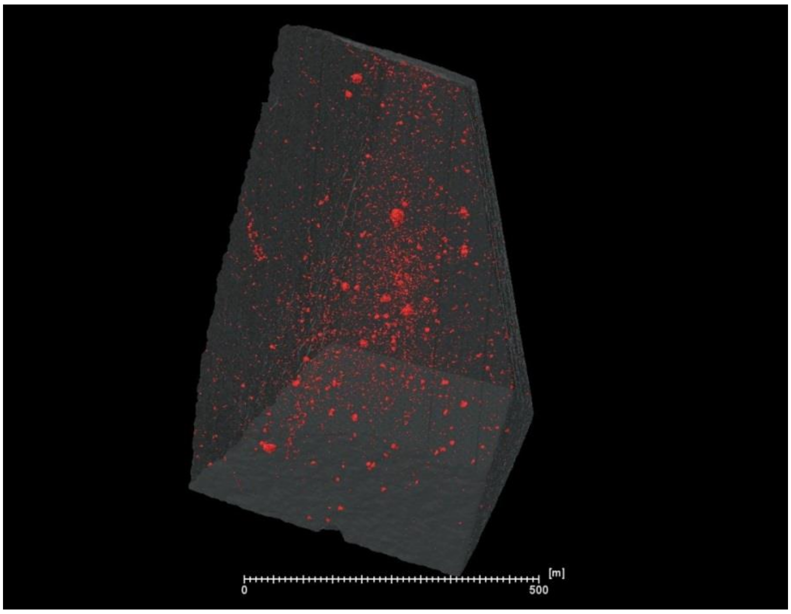

Figure 65 Volume reconstruction of BSCF5582 (scale bar = 500µm)

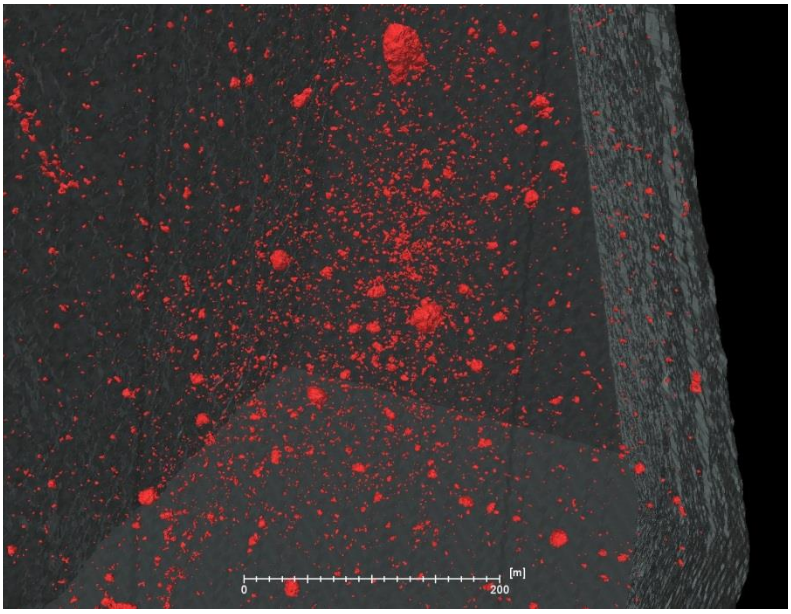

Figure 66 Enlargement of volume reconstruction of BSCF 5582 (scale bar = 200 µm)

A small piece of the same ceramic sintered at 1050°C was cut using a microtome and examined by SEM to reveal the pore structure as shown in Figure 67. The pores are of a similar size to the tomography results.

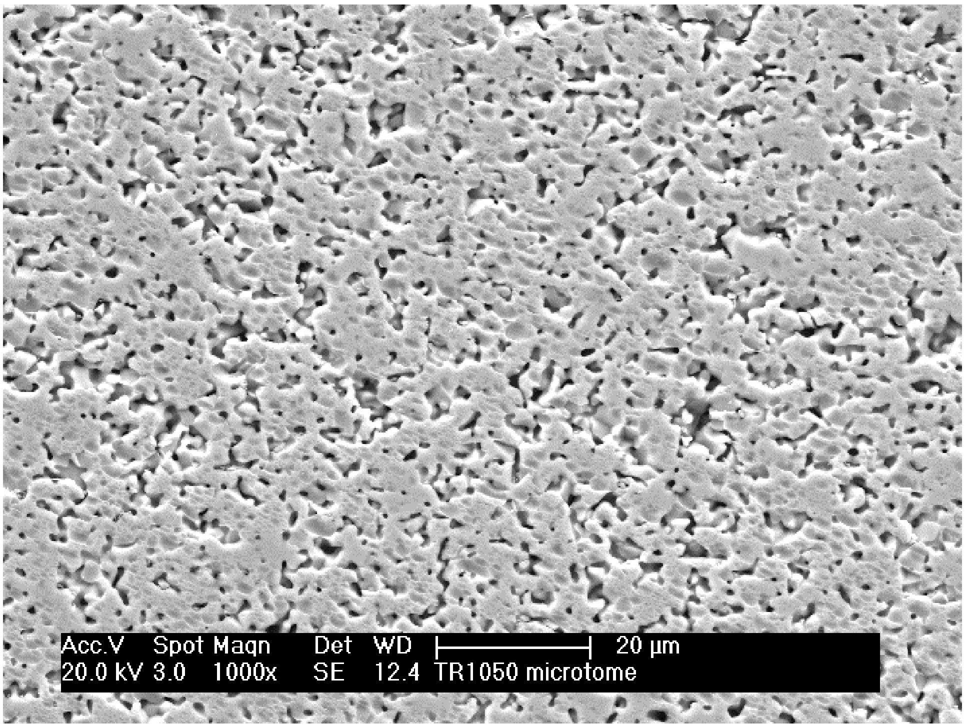

Figure 67 Cross section of BSCF 5582

Although there was extensive porosity in this sample it did not appear to have continuous porosity that would allow diffusion rather than permeation to occur through the specimens especially as they were of higher density.

4.5.3.2 General ceramic properties

Density measurements, microstructure analysis, x-ray diffraction, and x-ray fluorescence analysis were carried out on the samples sintered at 1100°C with a 10 hour dwell time at temperature. The density results are shown in Table 19.

	pH 10		pH 12	
	Apparent density	Bulk density	Apparent density	Bulk density
No Boil	5.23 (91)	5.18 (90)	5.21 (91)	5.19 (90)
Boil at pH 7	5.29 (92)	5.27 (92)	5.03 (87)	5.01 (87)
Boil at pH 12	5.05 (88)	5.07 (88)	4.90 (85)	4.79 (83)

Table 19 Densities of sintered pellets. (/gcm^{-3} and in brackets % theoretical)

4.5.3.3 Microstructure

The sintered ceramics were analysed by SEM after polishing and the micrographs are shown in Figure 68 and Figure 69. The grain size in all the ceramics was uniform with no evidence of bimodal distributions; this indicated that there was no secondary recrystallization or abnormal grain growth taking place[139]. The pores that were observed were found at grain boundaries and also within the grains. The grain and pore sizes are given in Table 20 .

	pH 10			pH 12		
	No boil	Boil @pH 7	Boil @ pH10	No boil	Boil @pH 7	Boil @ pH12
Grain (/µm)	20-50	20-40	10-50	20-50	10-35	30-50
Pore (/µm)	2-6	4-9	6-11	2-7	4-6	6-11

Table 20 Grain and pore size of sintered pellets

pH 10 pH 12

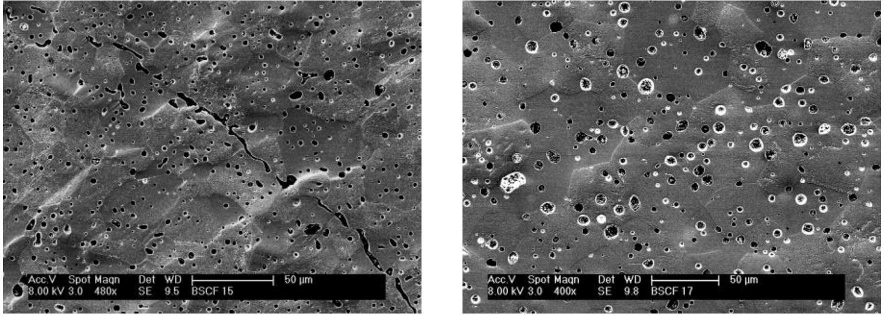

No Boil

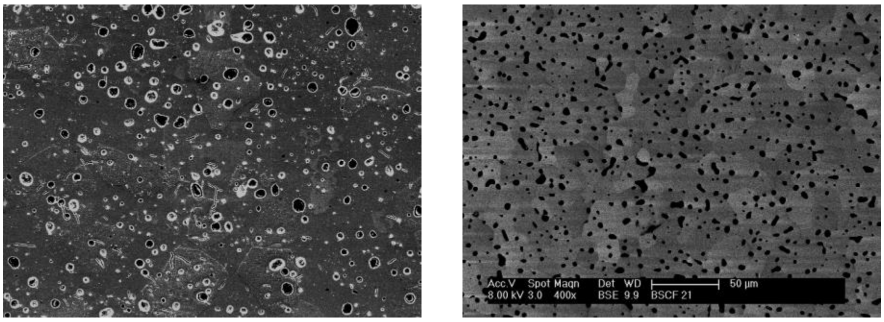

Boil at low pH

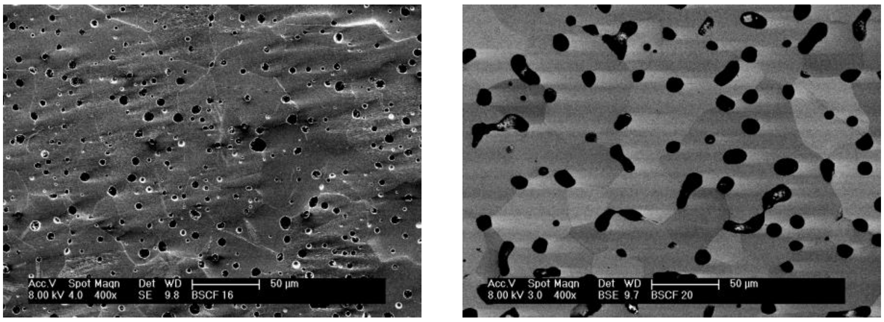

Boil at high pH

Figure 68 Microstructure of sintered pellets showing grains pH 10 pH 12

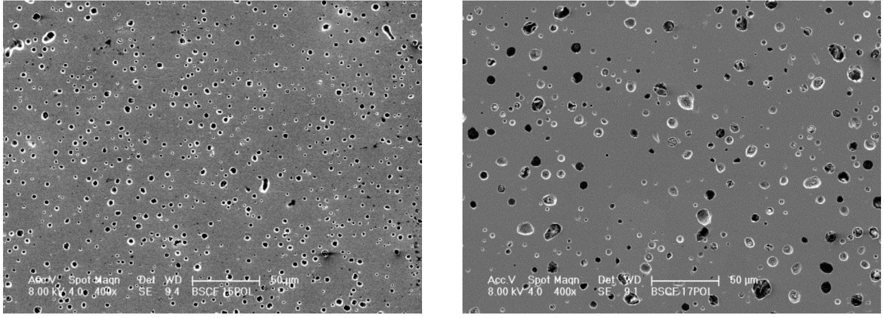

No Boil

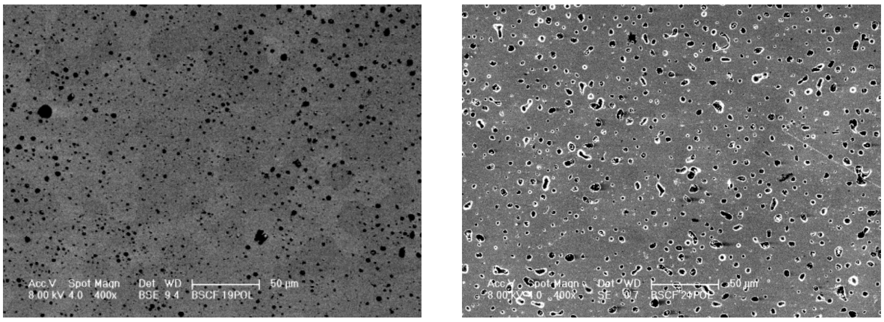

Boil at Low pH

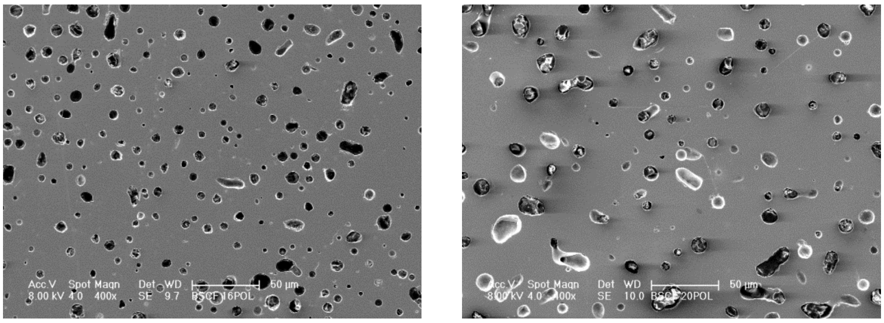

Boil at High pH

Figure 69 Microstructures of sintered pellets.

4.5.3.4 X-Ray Diffraction

The polished pellets were examined by x-ray diffraction as shown in Figure 70. All of the samples contained a single phase which was a cubic perovskite. The lattice parameters for the samples were calculated and are given in Table 21.

	No boil	Boil @pH 7	Boil @ pH10/12
pH 10	3.989	3.981	3.988
pH 12	3.985	3.985	3.983

Table 21 Lattice parameters of sintered pellets(/Å)

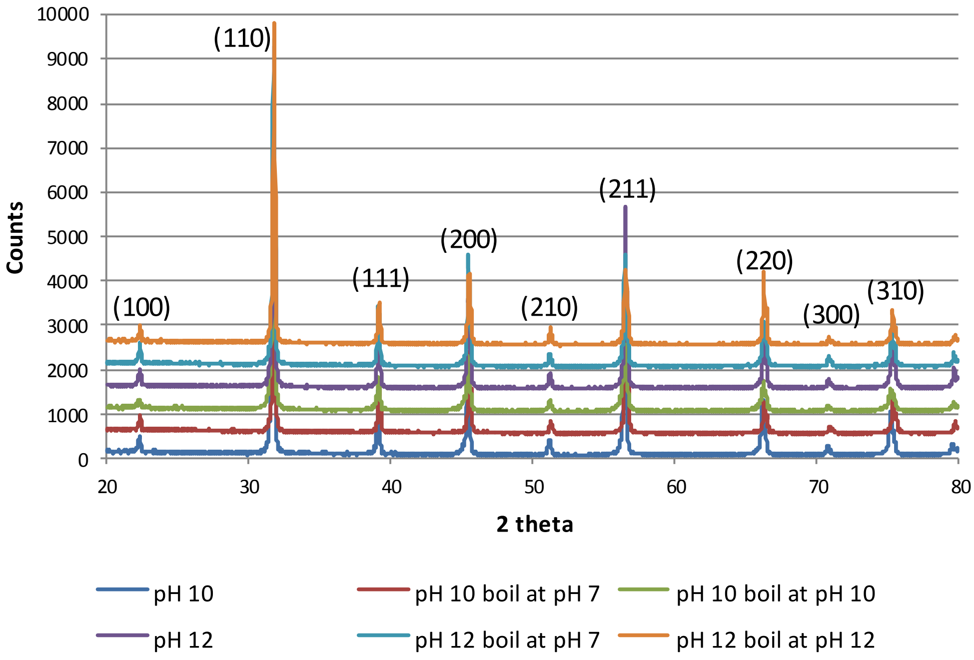

Figure 70 X-ray diffraction of sintered polished pellets

There were small differences in the lattice parameters which will be discussed in the next section.

4.5.3.5 X-Ray Fluorescence Analysis

The pellets were analysed by x-ray fluorescence and the results are as shown in Table 22. All the measurements were taken from polished pellets. The data has been converted to an empirical formula based on the total number of cations being equal to 2, (as explained earlier, Section 3.6). The only impurity found was calcium at approximately 0.3wt% which corresponded to a concentration of 0.01 Ca ions for each of the A sites.

	pH 10			pH 12		
	No boil	Boil @pH 7	Boil @ pH10	No boil	Boil @pH 7	Boil @ pH12
Ca	0.01	0.01	0.01	0.01	0.01	0.01
Fe	0.20	0.20	0.20	0.20	0.20	0.20
Co	0.83	0.82	0.82	0.83	0.83	0.83
Sr	0.48	0.50	0.49	0.48	0.48	0.50
Ba	0.48	0.47	0.48	0.48	0.48	0.46

Table 22 XRF analysis of sintered pellets

The composition data show that there was no significant difference between the six samples. In all cases there was a slight excess of the B site cations over the A site cations. A ratio of B site cations to A site cations of 1.02 B site cations to 0.96 A site cations was determined. This excess was due to higher cobalt content in the pellets compared to the desired composition. As there was complete precipitation of all the cations during the synthesis this excess may be caused by the initial composition of the cobalt nitrate being in error. There was a small variation in the Sr to Ba ratio between the samples. The Sr to Ba ratio was plotted against the lattice parameter and is shown in Figure 71.

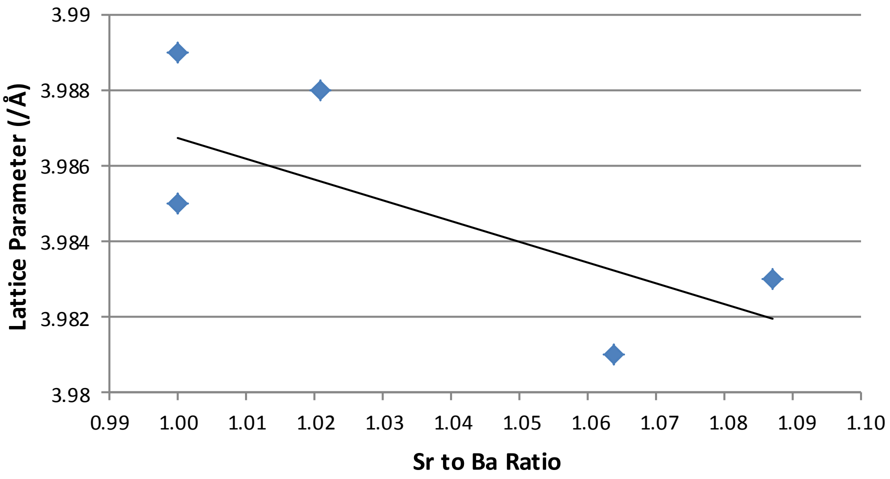

Figure 71 Plot of A-site cation ratio against lattice parameter

It can be seen that there is a trend towards lower lattice parameters for the high Sr to Ba ratio samples. This is to be expected as the Sr^{2+} ion is smaller than the Ba^{2+} ion 1.44Å to 1.61Å respectively for a coordination number of twelve[107] and will therefore give rise to a smaller unit cell. The more minor changes in the Fe to Co ratio were found not to affect the lattice parameter.

4.5.3.6 Oxygen Permeability

The oxygen permeability was measured on polished pellets after sintering at 1100°C for 10 hours. The pellets were polished to ensure that any surface impurities were removed prior to measurement. After the pellet had been fixed to the end of the alumina tube and the alumina cement had cured (section 3.8.1), the temperature in the furnace was then raised to the maximum temperature for the permeability experiment (typically 950°C) and the system left to come to equilibrium.

Equilibrium was measured in terms of both the internal temperature and the oxygen concentration in the gas stream. The temperature was then reduced in ~25°C steps waiting for equilibrium after each step until there was no longer any detectable oxygen in the sweep gas stream measured on the exit side. The oxygen flux was calculated according to equation 4.9. and is shown in Figure 72.

$$J_O = \frac{C_O f}{A V_m} \qquad 4.9$$

Where J_O is the oxygen flux (mol s^{-1} cm^{-2})

C_O is the oxygen concentration in the sweep gas (volume fraction)

f is the sweep gas flow rate (cm^3 s^{-1})

A is the area of the pellet (cm^2)

V_m is the molar volume of an ideal gas (22,400cm^3 mol^{-1})

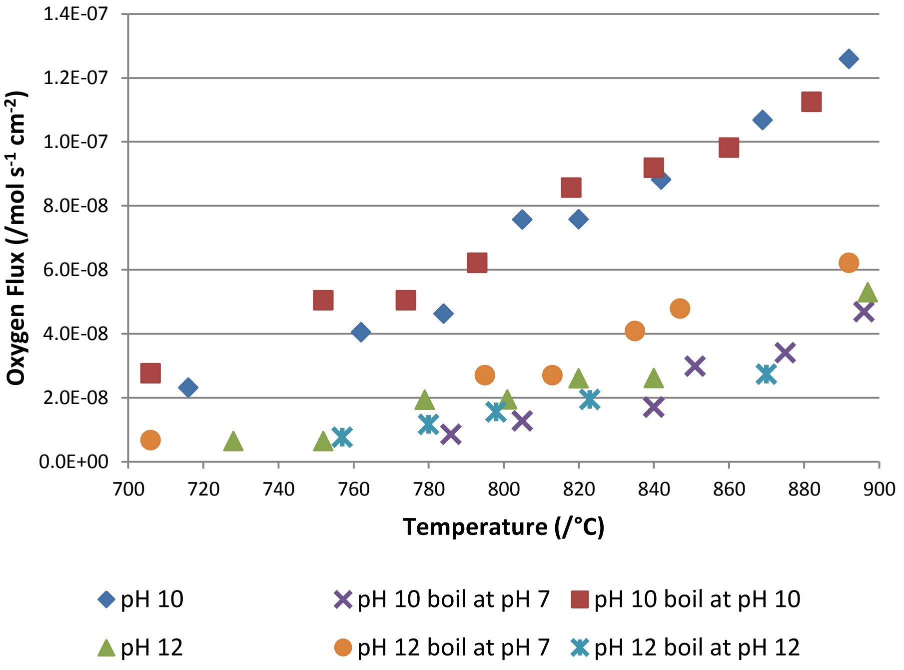

Figure 72 Oxygen flux through sintered pellets

An Arrhenius plot was made and is shown in Figure 73. From the slopes of the high temperature (low 1/T) linear part of the plots the activation energies for the oxygen flux were calculated and the results are given in Table 23. The low temperature portion ie 1/T >0.00096 was ignored as the low values of the oxygen flux had inherently larger errors so the straight line fit was poorer. The errors quoted were calculated from the fitting of the lines. In all cases the correlation coefficient for the fitting was greater than 0.9.

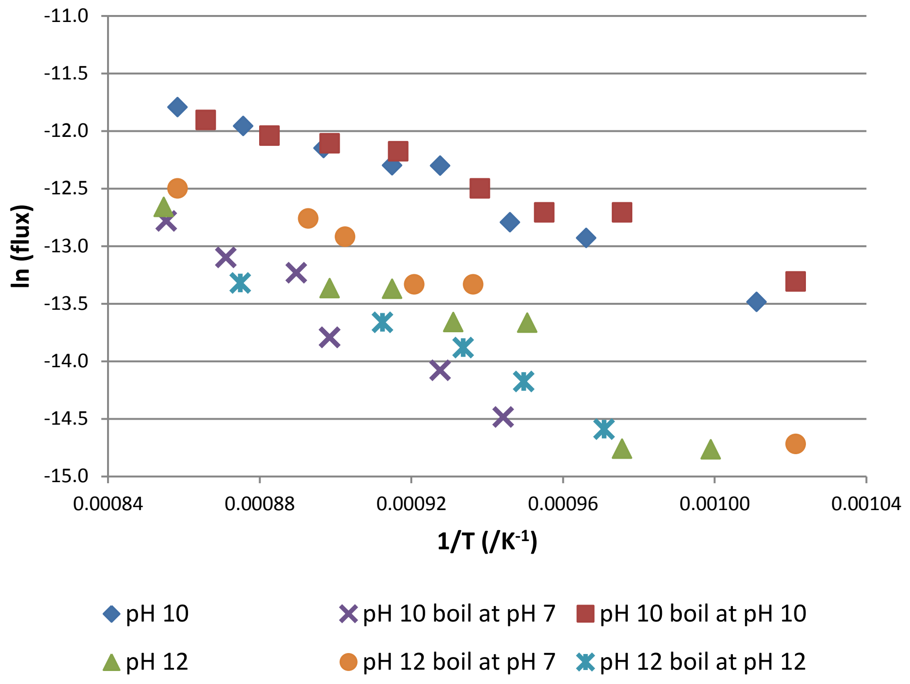

Figure 73 Arrhenius plot of oxygen flux

	No boil	Boil @pH 7	Boil @ pH10/12
pH 10	93±6	157±17	71±4
pH 12	126±17	116±10	108±10

Table 23 Activation energies for oxygen flux (/kJ mol^{-1})

The two materials with the highest oxygen fluxes of 6 x 10^{-8} mol s^{-1} at 800°C for the pH 10 material with no boil and boil at pH 12 showed the minimum activation energies for oxygen permeation.

4.5.3.7 Electrical Tests

4.5.3.7.1 Initial Experiments

Electrical measurements were made on pellets which had been polished to remove any surface impurities including carbonate phases. In order to ensure good collection of current from the surface, electrodes were put on the pellets. Before applying the electrodes the pellets were cleaned in acetone to remove any grease.

The use of sputtered gold as the electrode material gave impedance plots that were very unlike those seen for purely ionic conductors.(Figure 74) The main feature of difference was that the curve passed below the horizontal axis. This behaviour was initially ascribed to inductances in the measuring system as the leads run parallel with each other within the furnace where they were not shielded.. As this inductance like behaviour had not been seen before it was thought it may also be due to a Shottky barrier at the oxide-metal interface, possibly related to the oxygen exchange at the surface.[6] A build-up of charge related to the oxygen adsorption/desorption or slower kinetics than the frequency of measurement would lead to charge build up at the surface /electrode interface. In order to determine whether the effect was material or measuring system based, a sample of tetragonal yttria-zirconia was measured using the same experimental set-up.

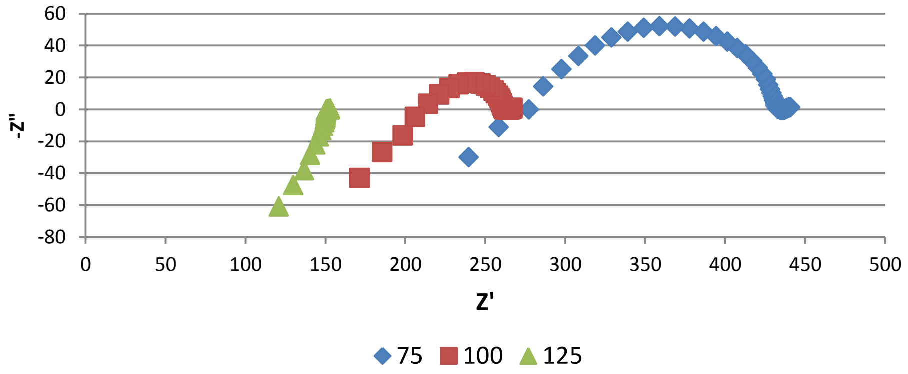

Figure 74 Impedance plots of BSCF 5582 pellet using gold electrodes

4.5.3.7.2 Tetragonal Yttria-Zirconia

The spectra obtained over a range of temperatures for the tetragonal yttria-zirconia are shown in Figure 75.

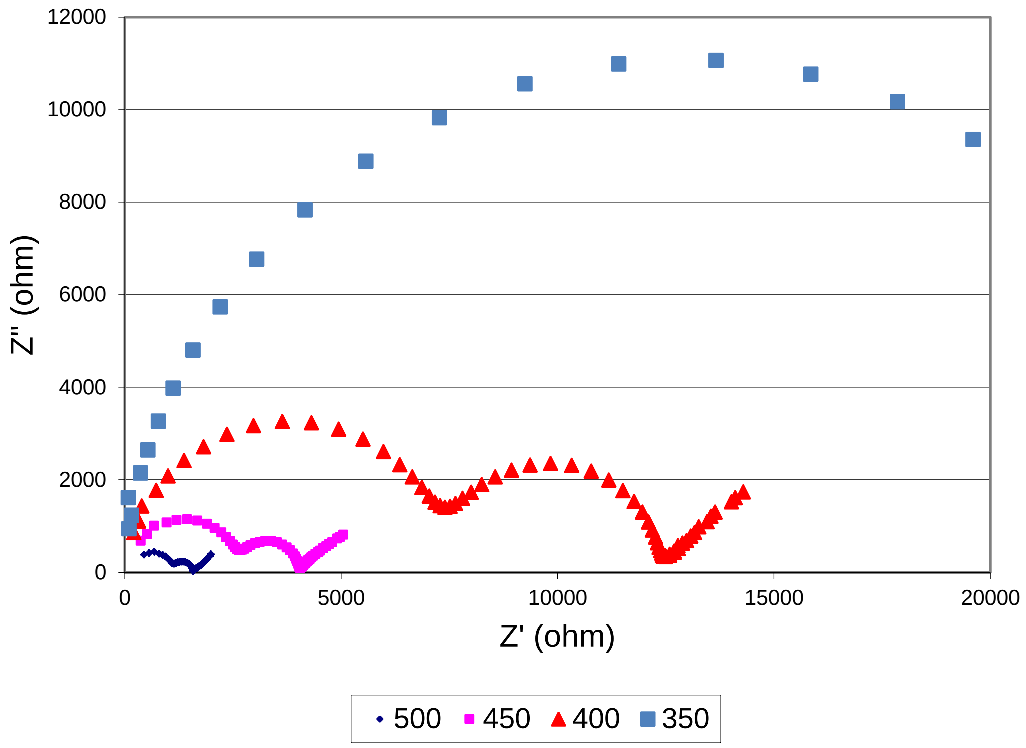

Figure 75 Impedance spectra of tetragonal yttria-zirconia

The three spectra at the highest temperatures (500°C, 450°C, 400°C) show a similar shape. It consists of two overlapping semicircles and a partial semicircle. (The 350°C data is similar in shape but the x-axis is shortened to allow the features of the other temperatures to be seen.) This suggests that there are two possibly three electrical elements making up the equivalent electrical circuit which have combined to generate the spectra that were measured. The plots of Z” and modulus M” against log(frequency) confirm the presence of three elements as they show peaks which correspond to the relaxation times of each element (see Figure 76).

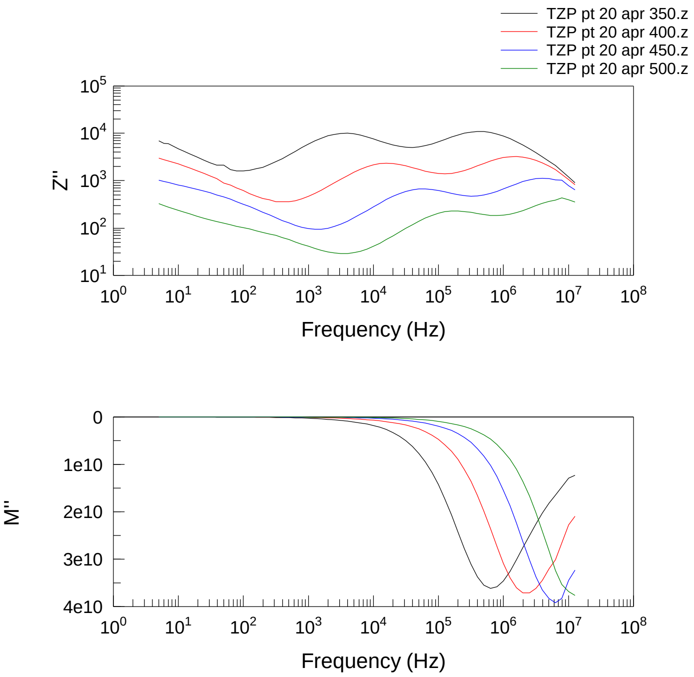

Figure 76 Impedance spectra of tetragonal yttria-zirconia showing Z” and M” against log(frequency)

The experimental data was collected using a frequency response analyser (HP 4192A LF Impedance Analyzer) and the data were fitted to equivalent circuits using ZView Software. The data were fitted with a model similar to that given in Figure 27 with 2 further parallel RC components present.(Figure 77) The values of capacitance and resistance are given in Table 24.

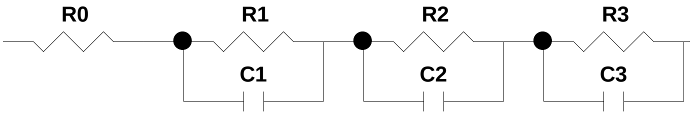

Figure 77 Equivalent circuit to represent three semi-circles

Temperature (°C)	R0	R1	C1	R2	C2	R3	C3
350	0	24573	5.07E-11	22453	5.04E-09	28055	6.32E-06
400	0	7413	7.10E-11	4857	4.06E-09	14109	1.85E-05
450	0	2725	1.11E-10	1274	2.95E-09	7924	8.08E-05
500	0	1196	4.00E-10	386.2	2.36E-09	4363	4.57E-04

Table 24 Values of components in equivalent circuit for tetragonal yttria-zirconia (R in ohms, C in Farads)

From the table it can be seen that the values change with the temperature of measurement. R1, R2 and R3 decrease. An increase in resistance with temperature is typical of metals whereas semiconductors and ionic conductors have a decrease in resistance with increasing temperature.[122] It was found that during fitting the magnitude of the errors was very large when the circuit included R0. The error as a percentage of the value was in some cases >10^6 The largest error was associated with R0, the value of R0 was ~0 ohms. When the value during fitting was fixed at 0 ohms all the other errors reduced and were typically <5% of the value. The four resistances can thus be tentatively assigned as follows R0 to leads (as the value was small (the empty cell had a resistance of ~2ohms)), R1 and R2 to the sample and R3 to the electrodes.

The capacitances shown in Table 24 may be assigned to behaviour based on Table 6 above. C1 is bulk/minor phase, C2 is grain boundary and C3 is sample electrode behaviour. The correspondence of the assignments of the resistance and capacitor in the RC elements further validates the model that was chosen.

The data from Table 24 are shown as Arrhenius plots below in Figure 78.

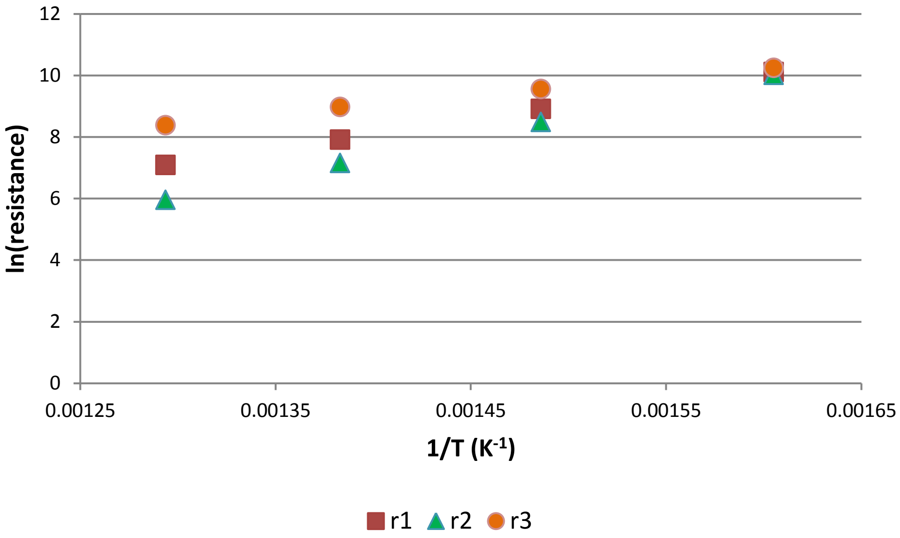

Figure 78 Arrhenius plots of TZP resistance data

The Arrhenius plots for R1, R2 and R3 give activation energies of 81±1kJ mol^{-1}, 108±1kJ mol^{-1} and 49±1kJmol^{-1}. The first two are similar to those quoted by Badwal[140] of 92kJ mol^{-1} for tetragonal yttria-zirconia. It can therefore be concluded that the process being measured is related to oxygen ion movement in the sample. R2 is associated with the grain boundaries and has a higher activation energy for the transfer of oxygen ions across the grain boundary compared to passage through the bulk due to segregation of impurities to the boundaries[140].

It can be seen that a single model fitted the data and that the shape of the curves obtained in the initial figure although similar are not identical as the limitations of the experimental set up do not allow the complete three semicircles to be seen.

However there was no inductance tail seen in any of the measurements. This study showed that there was no inherent problem with the experimental set-up and that the tail in the impedance spectra from BSCF pellets was sample related.

4.5.3.7.3 BSCF Results

Following the initial measurements with gold electrodes, two further materials were used as electrodes on a test sample (pellets from a pH 10 precipitation with a low pH boil); sputtered platinum using a Model 682 PECS™ (Gatan UK, Oxford) and painted indium-gallium alloy. The cleaning stage was especially important for the

InGa as it would not form a stable film on a “dirty” surface. Differences in performance have been seen in an electrochemical cell using BSCF 5582 as electrodes on samaria-ceria electrolyte between different current collectors (electrodes in this study).[141] The current collectors were various structures of silver and $LaCoO_3$.

For the lowest temperature data, the impedance curves were fitted with an R-RC circuit. At the higher temperatures the point at which the curve crossed the x axis was used to find R0. The values of R0 were used to plot the data in an Arrhenius plot (Figure 79)

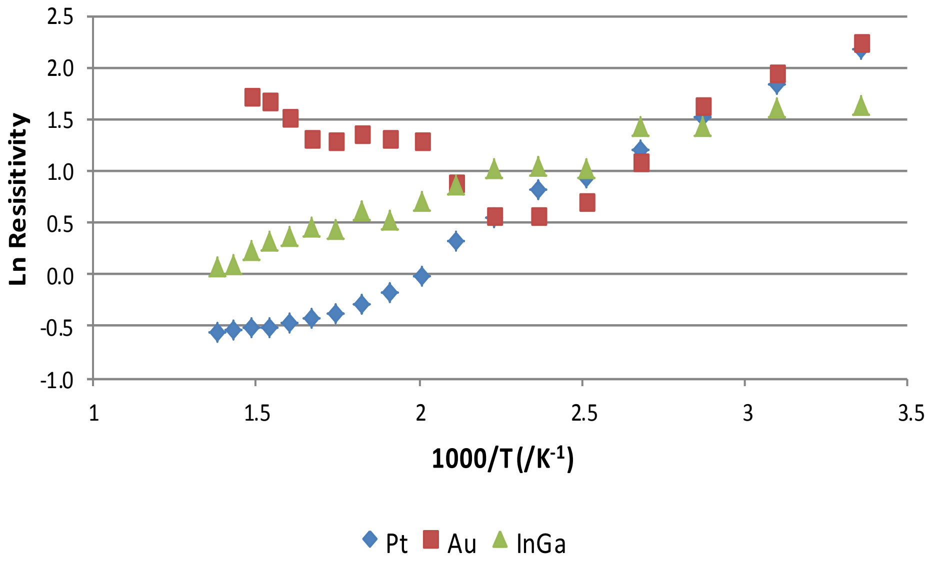

Figure 79 Arrhenius plot of resitivities using different electrodes.

At low temperatures the three electrodes behave quite similarly but at a temperature of about 150°C the resistivity of the gold electroded samples increased. This was ascribed to the gold sintering and breaking up thus not giving a complete conducting layer. The InGa showed much more linear behaviour. The platinum electrodes gave the best straight line behaviour at all temperatures below 300°C. The reasons for the flattening of the curve will be described later.

The activation energies for resistance change for each electrode was calculated from the straight line portion of the curves in Figure 79 and are given in Table 25.

Electrode	Activation Energy (kJ mol^{-1})
Platinum	-13.9
Gold	-15.0
Indium Gallium	-7.2

Table 25 Activation energies using different electrodes

The gold and platinum values are similar with the InGa having a lower value. This implies that any changes in resistance had the same mechanism for the noble metal coated samples and a different one for the InGa. This latter mechanism was thought to be the flow of InGa along grain boundaries which increased with temperature and thus effectively shortened the electrical pathway through the ceramic.

The Nyquist plots from the impedance measurements did not demonstrate the expected behaviour.[81, 82] That is they frequently did not show the three semicircles corresponding to bulk, grain boundary and electrode components. A set of curves are shown in Figure 80 and Figure 81. At low temperatures there are parts of one semicircle corresponding to one of the three components. At higher temperatures the semi-circle became smaller and showed a significant tail with negative values for Z”. This corresponds to an inductance in the circuit. It was thought that this inductance was coming from the leads and other parts of the jig. However measurements on other systems e.g. yttria stabilised zirconia pellets failed to give this inductance tail. It was therefore concluded that the instrumental set up per se was not the cause of the inductance tails.

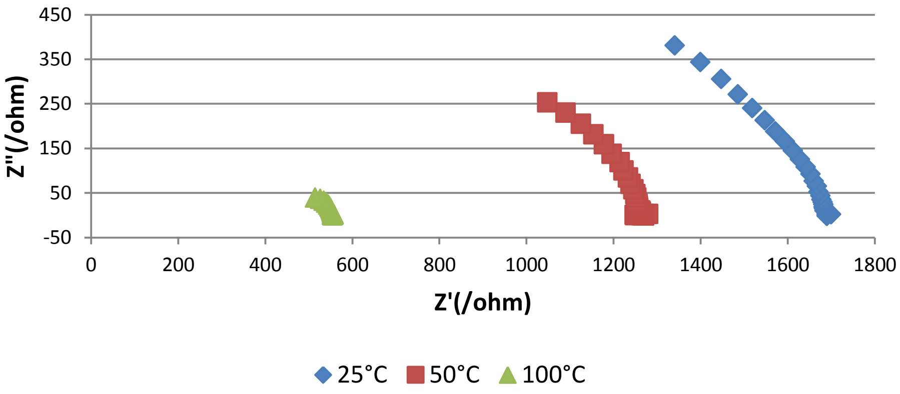

Figure 80 Low temperature impedance plots showing part of a semicircle

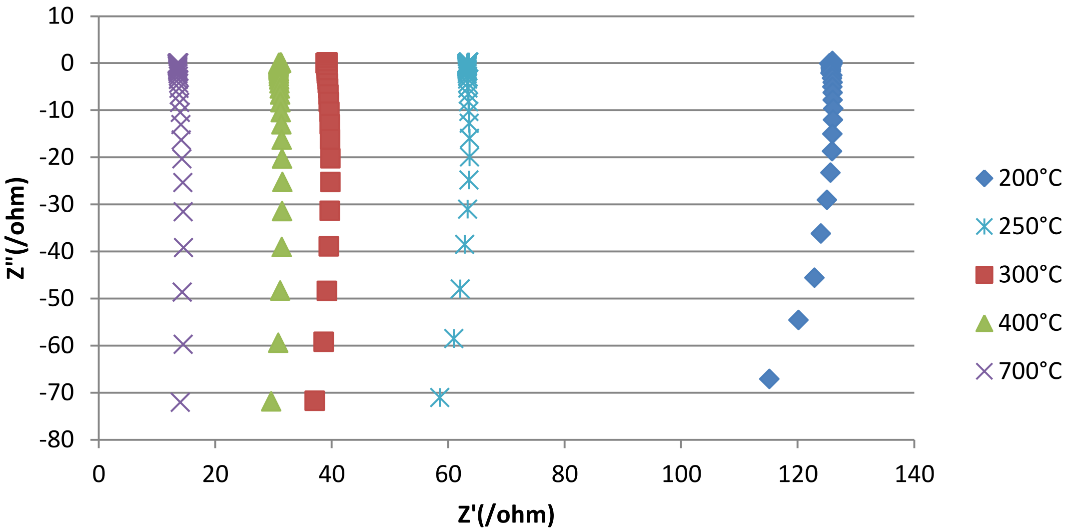

Figure 81 High temperature impedance plots showing inductance tail

The impedance data was fitted using Zview software and an equivalent circuit found which fit the experimental data over a wide range. The best fits were found with the circuit shown in Figure 82.It consisted of a resistor R0 in series with an inductor L0 which was followed by a combination of a resistor R1 and a constant phase element CPE1 in parallel. (This will be referred to as a R-L-RC circuit).

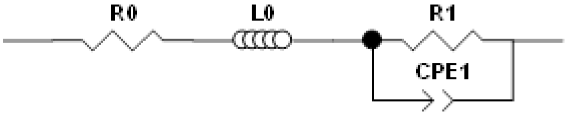

Figure 82 Equivalent circuit to fit impedance data

In order to test the circuit fitting further an external parallel resistor capacitor element was added in series to the test jig. This formed a R-L-RC-RC circuit. The overall change in resistance and capacitance were predicted from Zview simulations to remove or reduce the inductance tail in the Nyquist plots. This occurred because the change in the impedance of the whole system meant that there was no longer an inductance component as a result of the time constant for the system being changed.. The Nyquist plots with a 5nF capacitor and 100Ω resistor in parallel and together in series with the test jig are shown in Figure 83 and Figure 84.

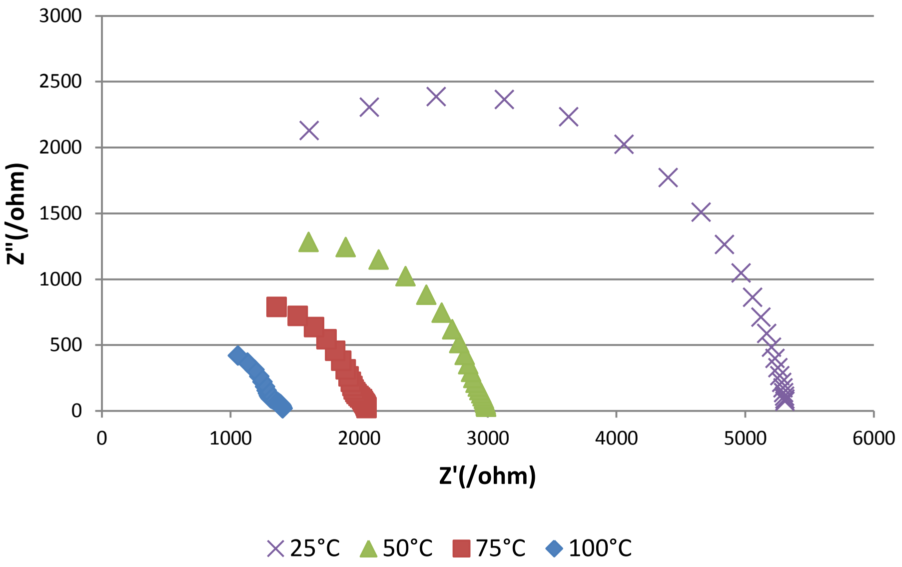

Figure 83 Low temperature impedance plots with an additional resistor-capacitor parallel element

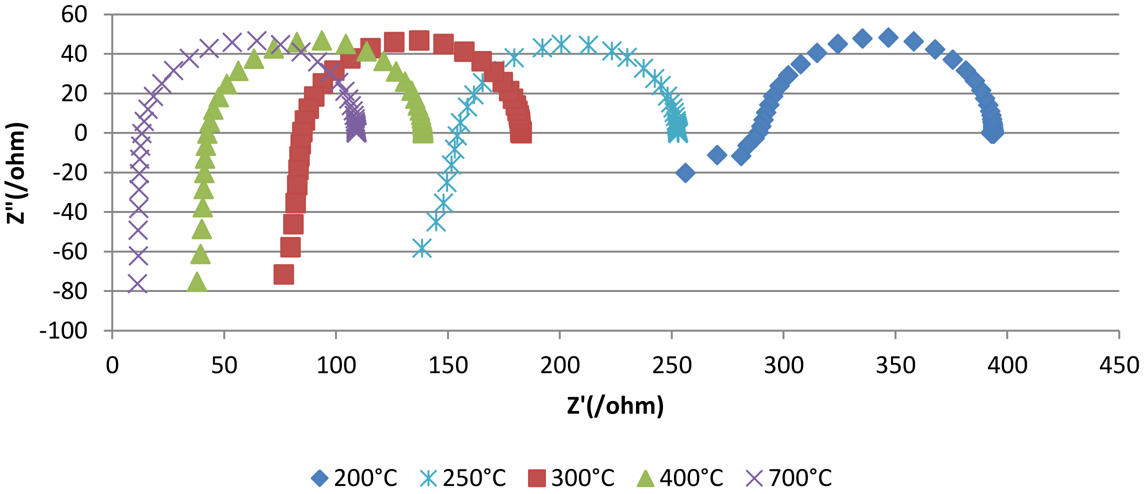

Figure 84 High temperature impedance plots with an additional resistor capacitor parallel element

It can be seen that the semicircles become better defined as a result of the additional resistor capacitor element. As predicted the inductance tail was much reduced at higher temperatures. The impedance was fitted and the resistances and capacitances calculated. Arrhenius plots of both were made and shown in Figure 85.

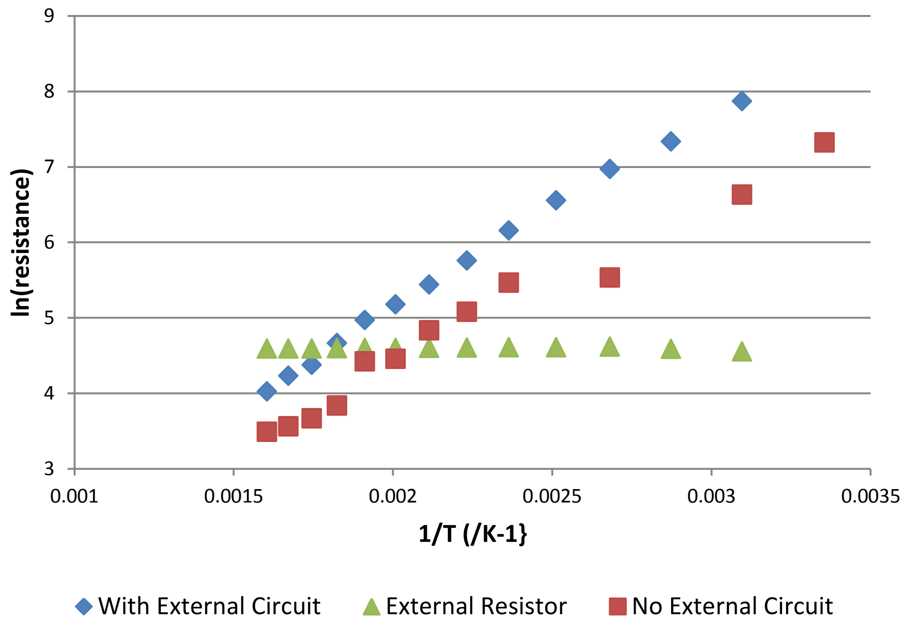

Figure 85 Arrhenius plot of sample resistance (red and blue) and external resistor (green)

There was no variation in the value of the external resistor which is as expected as it was outside the furnace and should not show any temperature variation. The two sets of data for the sample resistance show very similar behaviour and give very similar activation energies of 21.7kJ mol^{-1} and 22.8kJ mol^{-1} for the experiments with and without the external circuit element.

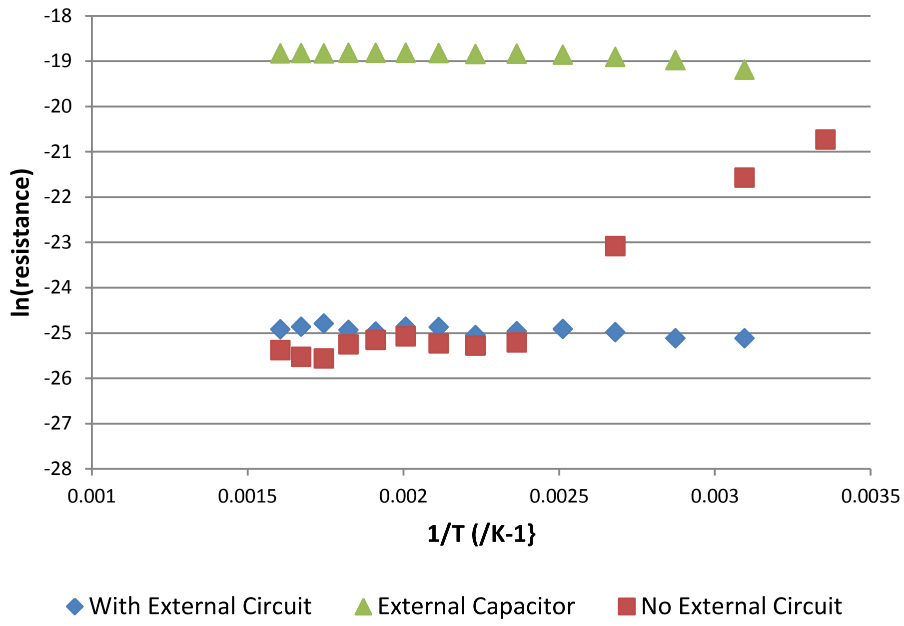

Figure 86 Arrhenius plot of sample capacitance (red and blue) and external capacitor (green)

There was no variation in the capacitance values except at the lowest temperatures. In the case without the external circuit the change in capacitance is related to the "semicircle" behaviour where the influence of the inductance was not significant.

The agreement of the results from the two methods indicated that the inductance was part of the system and a reasonable model for the system had been derived.

The R-L-RC circuit was used to fit samples from the six preparations and the values of the activation energies for the change in resistance are given in Table 26 . Compared to the variation in activation energies between the various methods described above much larger variations were seen. The data cannot be separated into groups as they form a continuous series from 13 to 34kJ mol^{-1}. The effect of density and microstructure on these activation energies will be discussed later.

	No Boil	Boil at low pH	Boil at high pH
pH 10	26.2	13.9	18.1
pH 12	17.8	33.8	22.8

Table 26 Variation in activation energy (kJ mol^{-1}) for resistance changes as a function of preparative route.

4.6 Discussion and Conclusions

The variations of the conditions at the precipitation stage of the powder synthesis gave rise to a number of differences in the powders after drying and calcining. Chief among these were the phase assemblages formed after drying and calcination. The predominant crystalline phase was a mixed barium strontium carbonate which on the large scale did not fully decompose on calcination at 850°C with a 4 hour hold at temperature . The size of the decomposition step at around 750-800°C indicated that ~80% of the alkaline earths were present as the double carbonate. The iron and cobalt formed a complex mixture of hydroxides, oxyhydroxides and oxides. There was some evidence for compound formation between the alkaline earths and the iron/cobalt at high precipitation pH's after the boiling.

The reaction sequence was found not to be identical to earlier work on coprecipitation techniques[42, 49-51, 54]. However on comparing Figure 8, Figure 9 and Figure 61 a similar pattern can be seen. The barium and strontium form carbonates which react with the formed cobalt and iron compounds to form perovskite type materials. The exact route shown differs partly as a result of the stages in the process at which x-ray diffraction and other analytical techniques are applied. In this study the x-ray diffraction was carried out on dried and calcined materials. The interpretation of the themogravimetry was used to identify the intermediate steps. However, the large loss of carbon dioxide above 750°C means that, until this temperature has been reached, there is little reaction with the iron and cobalt species which is common to the other works.

The hydrothermal process also gave smaller particle sizes (as measured by laser light scattering) and crystallite sizes (measured using x-ray line broadening) with the calcined powders. The high pH preparations showed a small increase in surface area as the hydrothermal treatment occurred at higher pH. This is probably due to the reactions of excess hydroxide/water with the precipitate to give a thermodynamically more stable precipitate ie the initial components within the precipitate reacted with each other and the hydroxide/water. The differences in the surface area were small and the agglomeration of the crystallites to form dense particles prevented the adsorbing nitrogen during surface area measurement accessing the crystallite surface. This is confirmed by the results of the pore volume measurements of the milled calcined powders, which were very small and indicated essentially non-porous powders. The particles after milling were agglomerates (4µm) of small crystallites (40nm). The crystallite sizes from x-ray line broadening were significantly smaller than that calculated from the surface area (Table 13 Comparison of measured and calculated particle size). A further indication of the dense nature of the agglomerates The crystallite sizes showed a reduction in size with hydrothermal treatment. This again indicates some reaction during the hydrothermal treatment of the type shown below..

$$(\mathrm{M}-\mathrm{OH}^{+}-\mathrm{M})+\mathrm{OH}\text{-} \leftrightarrow 2\ \mathrm{M}\ -\mathrm{OH} \tag{4.10}$$

After sintering at 1100°C the densities of the samples were similar at 90% of the theoretical density. The agreement between the apparent and bulk densities indicated that there was only a small proportion of open porosity and that the majority of the pores were closed.

The microstructure of the sintered ceramics showed some differences mainly an increase in pore size with increasing severity of the hydrothermal treatment (none < boil at pH 7 < boil at pH 10/12). There was also a greater preponderance of pores at grain boundaries compared to those within grains. The average grain sizes were similar for all the ceramics. The change in position of the pores suggests that the grain growth rate was lower in the ceramics with grain boundary pores as at high rates of growth, pores break away from the grain boundaries[139]. The powders with the lower crystallite size and particle size had fewer pores within the grains the sintering process probably started at a slightly lower temperature and thus enabled easier pore removal although overall there was no difference in the final densities.

The composition and the phase analysis of the ceramic pellets showed no significant differences other than the variation in lattice parameter correlated with the Ba/Sr ratio in the measured pellets. The effect of compositional changes on lattice parameter has been shown to be more dependent on the barium and strontium because they are more different in size than the cobalt and iron. [63, 92,142]

The activation energy for oxygen permeability for the pH 12 preparations decreased with the increase in the proportion of pores that were inter-granular. This suggests that the overall oxygen flux through the ceramic was limited by either the transfer of oxygen across the grains or by easier grain boundary transfer across the pores. In the first case the intra-granular pores would act as a barrier to the diffusion of ions through the lattice with desorption and adsorption steps needed. They also reduce the cross sectional area of the grains and therefore increase the flux. The correction of oxygen permeation data by compensating for the porosity did not lead to any change in the conclusions drawn.[143] Desorption and adsorption are also needed at the grain boundary pores if the oxygen is to pass across them. With neighbouring grains which are not crystallographically aligned then the anion cannot as easily move from its site in one crystal to a vacancy in the next grain. Increased grain size has shown both increased and decreased oxygen flux[69, 144, 145]. The reason for these differences is not clear but there was no evidence for grain boundary phases inhibiting oxygen transfer in a TEM study.[69] However this trend with pore size was not seen for the pH 10 preparations. The no boil and boil at high pH gave the two lowest activation energies together with the highest oxygen fluxes at 800°C of ~8 x 10^{-8} mol s^{-1} cm^{-2} compared with the other materials giving oxygen fluxes of ~2 x 10^{-8} mol s^{-1} cm^{-2}. These differences may be due to the flattening of the curve around the transition from bulk diffusion to surface control.[59] The transition temperatures were about 800-850°C dependent on thickness from 1.5 to 0.5mm respectively. However Shao showed variation as a function of composition from 730-820°C but did not indicate the pellet thickness.[11]

The differences seen in this study could also be due to variations in the polishing of the pellets despite all having the same polishing regime. These differences can then give rise to surface roughening on heating as a result of different depths of sub-surface damage, (similar to thermal etching) which consequently affects the surface area available for oxygen adsorption and desorption reactions.

The activation energy was found to be proportional to the lattice parameter as shown in Figure 87. Although the ceramics were nominally of the same composition, the minor variations, in their lattice parameters and chemical composition as shown in Table 21 and Table 22, show that these differences do affect the transport properties of the ceramics.

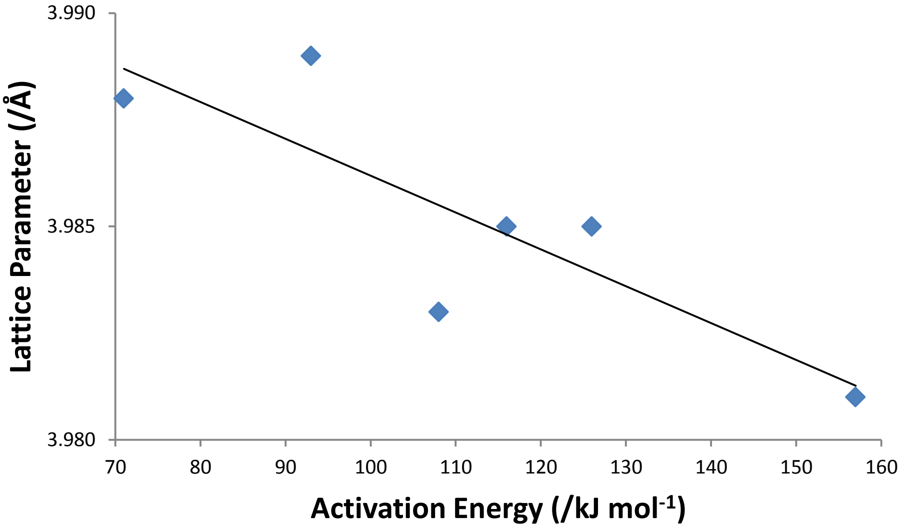

Figure 87 Variation of activation energy with lattice parameter

The samples with the largest lattice parameter show the lowest activation energy for oxygen permeation. Thus the larger unit cell could allow easier diffusion of oxygen ions from a lattice site to a neighbouring vacancy. However there is only 0.25% difference in the lattice parameter compared to a factor of 2 in the activation energy. The differences in the delta value were small both at room temperature and 1100°C.

There were differences in the activation energies from the electrical measurements however there was no systematic variation.

In conclusion, the synthesis method developed has been shown to be robust in that over a range of precipitation and hydrothermal treatment conditions consistent powders suitable for manufacturing BSCF pellets were obtained. However minor variations in the compositions were shown to have a significant effect on oxygen flux.

.

5 Variation of Cation Ratios in BSCF

5.1 Introduction

There have been a number of studies on changes in composition of $Ba_xSr_{1-x}Co_yFe_{1-y}O_{3-\delta}$ ceramic membranes.[11, 61, 63, 92, 146] The objective in this study was to see whether the mechanisms for formation described in the previous chapter were applicable over a broader range of compositions and whether the final electrical and permeation properties of the ceramic also had similar relationships.

It has been shown that by substituting Ba^{2+} ions for Sr^{2+} in $SrCo_{0.8}Fe_{0.2}O_{3-\delta}$ the thermal stability increased without altering the oxygen flux[10]. Although work on other systems chiefly involving doping $SrCoO_{3-\delta}$ showed an increase in oxygen flux with increasing size of A site dopants.[35]

Three additional compositions were synthesised and tested in order to determine what effect these changes had on the oxygen permeation and electrical properties as well as the powder formation pathways. The compositions studied are shown in the following table. The designation of the powders is that the numbers correspond in turn to **B**arium **S**trontium **C**obalt Iron(**F**e) within the oxide and represent ten times the value in the empirical formula ie $Ba_{0.3}Sr_{0.7}Co_{0.8}Fe_{0.2}O_{3-\delta}$ is BSCF 3782.

Designation	Ba	Sr	Co	Fe
BSCF 3782	0.3	0.7	0.8	0.2
BSCF 5582	0.5	0.5	0.8	0.2
BSCF 7382	0.7	0.3	0.8	0.2
BSCF 5564	0.5	0.5	0.6	0.4

Table 27 Compositions of cation variation materials

5.2 Synthesis

The synthetic route chosen for the preparation was as described in Figure 37 using a precipitation pH of 10 and no boil at either high or low pH. (see also Table 8 Experimental plan)

5.3 Results

5.3.1 Dried Powders

The dried materials were all similar brown friable powders.

5.3.1.1 X-Ray Analysis

The x-ray analysis showed that the main crystalline phase present was a mixed barium strontium carbonate. A variety of other minor phases, chiefly oxides and hydroxides, were also present as shown in Table 28 and Figure 88.

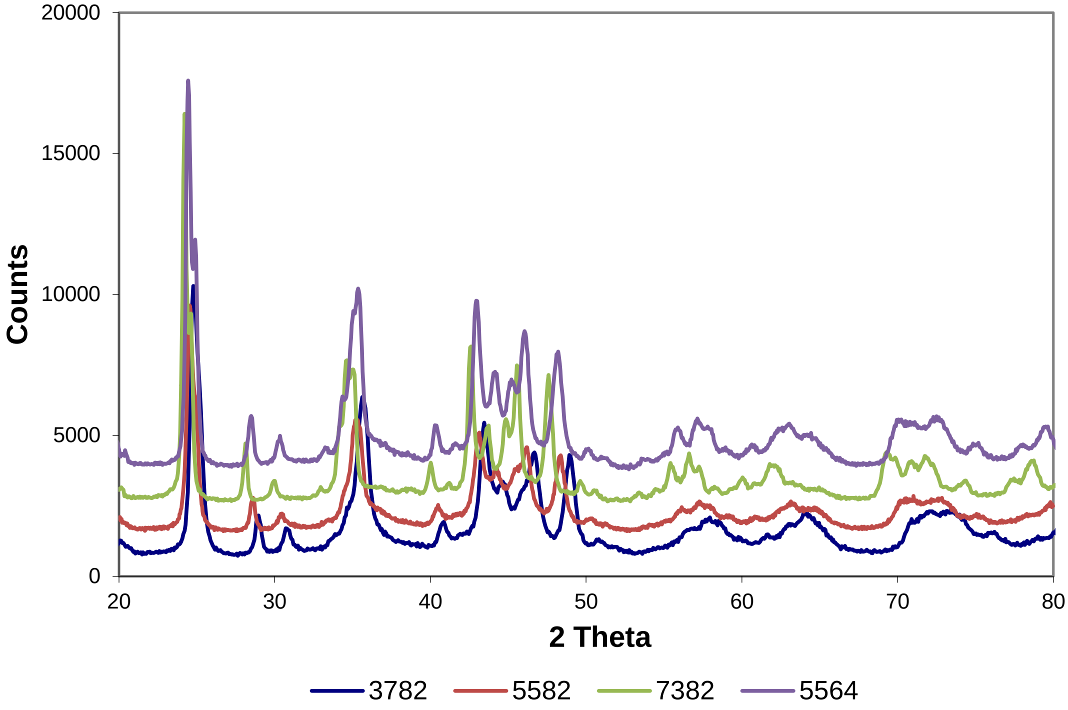

Figure 88 X-ray diffraction of dried powders

Composition	BSCF 3782	BSCF 5582	BSCF 7382	BSCF 5564
$Ba_{0.5}Sr_{0.5}CO_3$	Y	Y	Y	Y
$Fe_{2.67}O_4$		Y		Y
FeO(OH)			Y	Y
Fe_2CoO_4	Y			
Fe_2O_3	Y			
$BaFe_2O_4$			Y	

Table 28 Phase composition of dried powders

The phases present were similar to those found for the materials studied in the previous chapter for the BSCF 5582 composition. Again the exact composition could not be determined from the x-ray diffraction data. However the expected variation in lattice parameter for the mixed barium strontium carbonate was found, as shown in Table 29.[137] The BSCF 5564 composition contained two mixed carbonate phases; one had the approximately stoichiometric barium content and the other minor phase was strontium rich.

Composition	Unit cell volume	Equivalent Ba content
BSCF 3782	271.54	0.30
BSCF 5582	278.98	0.45
BSCF 7382	292.72	0.73
BSCF 5564	284.21, 272.18	0.56, 0.31

Table 29 Unit cell volumes of BaSr carbonate phase in dried powders (/Å^3)

5.3.1.2 Thermogravimetric Analysis

The thermogravimetric analysis was carried out and analysed in the same way as described earlier (section 4.5.1.2). The overall curves and data for the dried powders are shown in Figure 89 to Figure 91 and Table 30. The correction to the final molecular weight, from the iodometric data given in Table 31 below, was used in the calculations.

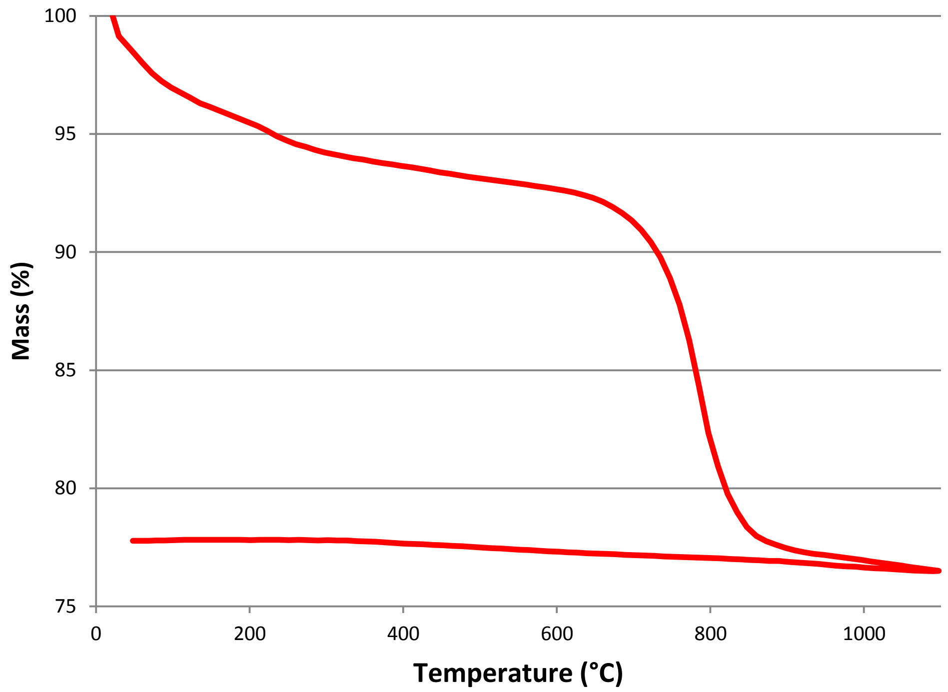

Figure 89 Thermogravimetric curve for dried BSCF 3782 in air with a heating and cooling rate of 5K min^{-1}

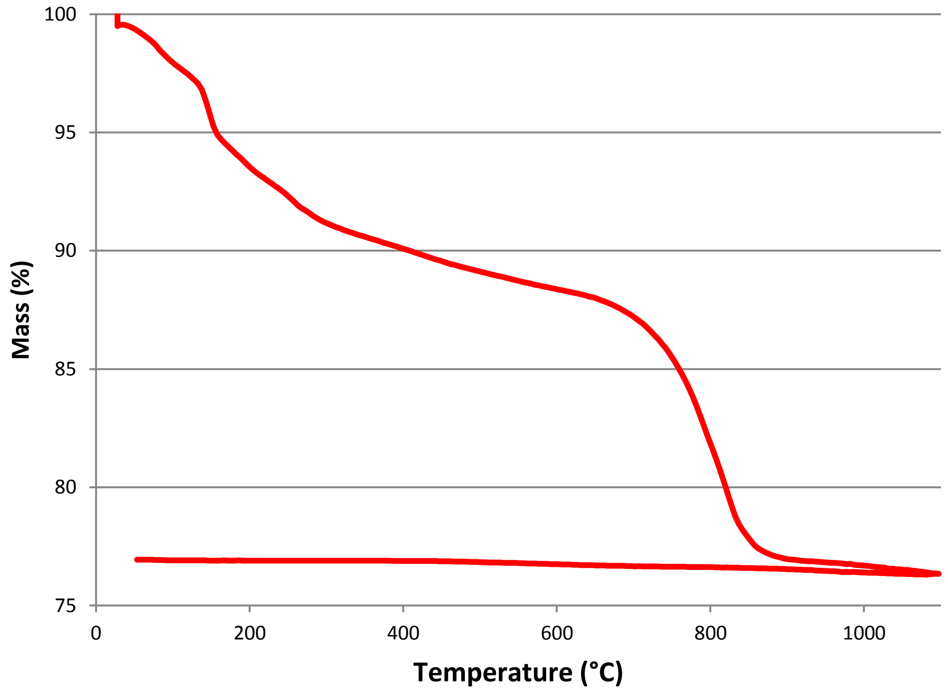

Figure 90 Thermogravimetric curve for dried BSCF 7382 in air with a heating and cooling rate of 5K min^{-1}

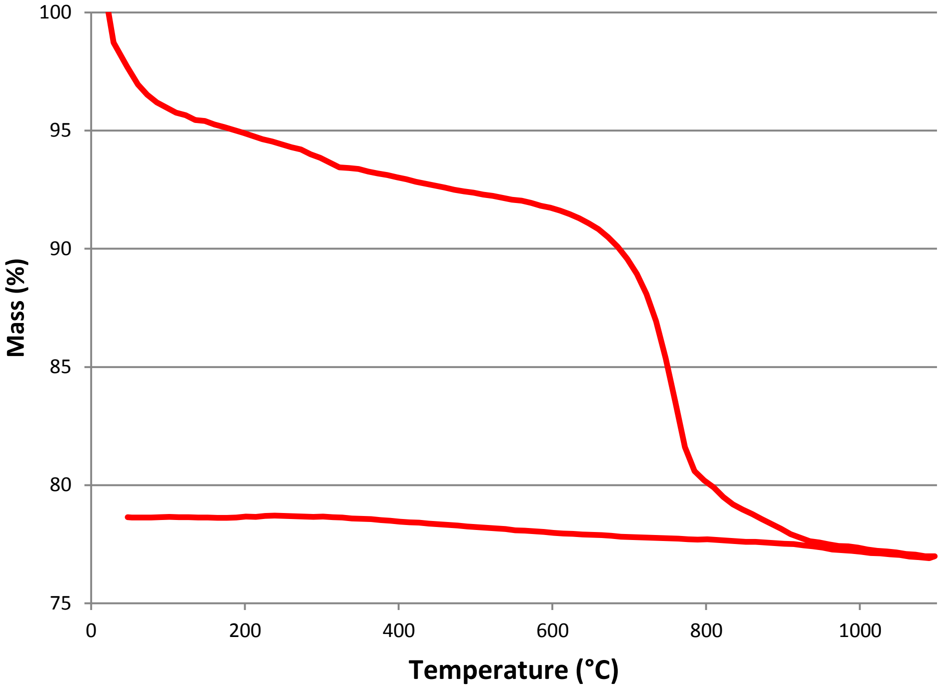

Figure 91 Thermogravimetric curve for dried BSCF 5564 in air with a heating and cooling rate of 5K min^{-1}

		BSCF 3782		BSCF 5582		BSCF 7382		BSCF 5564	
		Wt %	Δ MW	Wt %	Δ MW	Wt %	Δ MW	Wt %	Δ MW
<200°C	A	-3.9	-10.1	-5.2	-14.5	-6.4	-18.8	-4.6	-12.5
200-500	B	-3.2	-8.4	-3.2	-8.8	-4.4	-12.9	-3.3	-8.9
	C	-0.8	-2.2	-1.0	-2.9	-2.1	-6.2	-0.4	-1.1
	D	-13.8	-36.1	-13.4	-37.4	-10.0	.-29.2	-11.8	-32.0
Mass at 1100°C	E	76.5	200.2	75.4	209.7	76.3	223.0	76.9	208.3
Heating to 400	F	1.3	3.3	1.0	2.9	0.5	1.6	1.7	4.5
Final Mass		77.8	203.5	76.5	212.9	76.9	224.6	78.6	212.9
	Delta		0.21		0.18		0.10		0.29
	Carbonate		82.1		85.0		66.3		73.0

Table 30 Summary of TGA data for dried powders

The values of delta given in Table 30 reflect the change from 1100°C to room temperature on cooling.(Stage F) They show that the value decreases as the barium content increases (0.21 to 0.10) and that as the iron concentration increased so did the delta value. The carbonate content as calculated from the step change in weight between ~600°C and ~900°C (stage D) was variable with at least two thirds of the alkaline earths present as carbonate. The BSCF 7382 composition had the lowest concentration of carbonate present but it was also the only composition to have a barium or strontium oxide phase in the dried powder namely $BaFe_2O_4$. The BSCF 5564, which contained the two carbonate phases, shows a slight difference in the behaviour above 600°C. There is an initial sharp weight loss and then a more gradual one until at 940°C the weight loss corresponds to the oxygen loss. This difference is ascribed to the difference in decomposition temperature between the two carbonates[137]. Again the loss in mass between 200°C and 500°C (stage B) was equivalent to a ΔMW of 9 corresponding to the decomposition of a goethite type compound. (Equation 4.1)

5.3.2 Calcined Powders

The dried powders were calcined at 850°C with a 4 hour hold at temperature. Some was then further calcined at 1000°C for 4hours prior to measuring the delta value by iodometric titration, the results are given in Table 31.

Composition	Delta
BSCF 3782	0.33
BSCF 5582	0.37
BSCF 7382	0.26
BSCF 5564	0.32

Table 31 Delta value from iodometric titration

5.3.2.1 X-Ray Analysis

The x-ray traces of the milled calcined powders (850°C) are given in Figure 92 and Figure 93. A summary of the phases present is given in Table 32. The unit cell volumes of the mixed alkaline earth carbonate are given in Table 33.

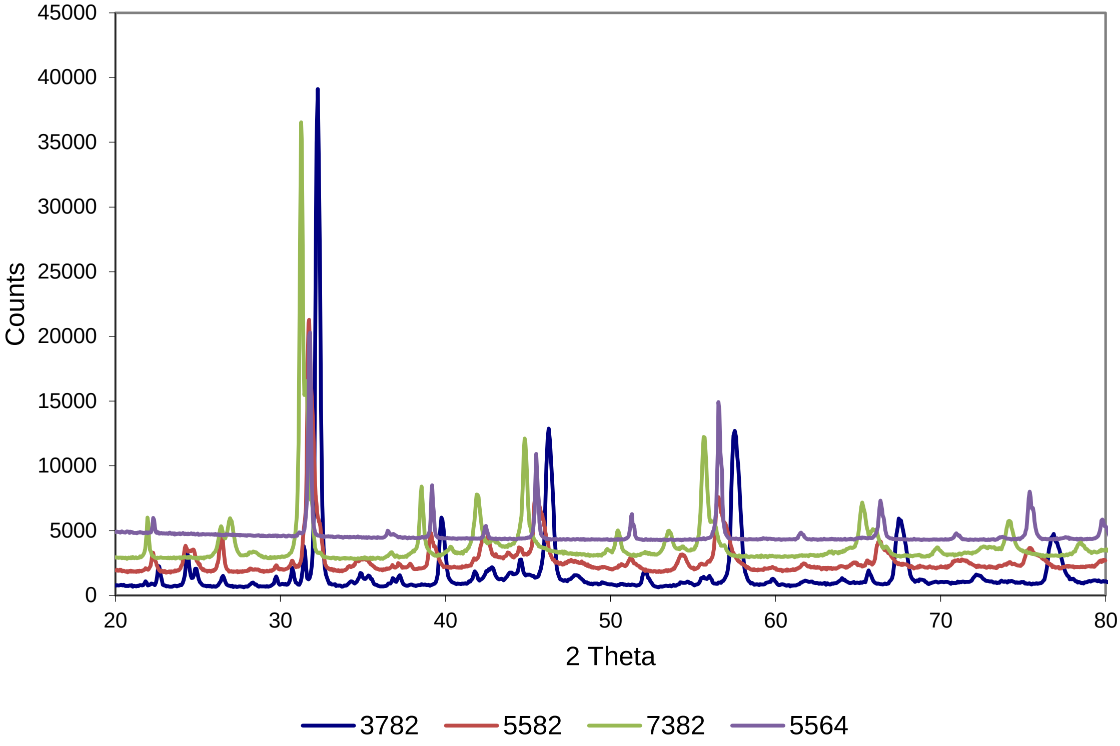

Figure 92 X-ray diffractograms of milled calcined powders

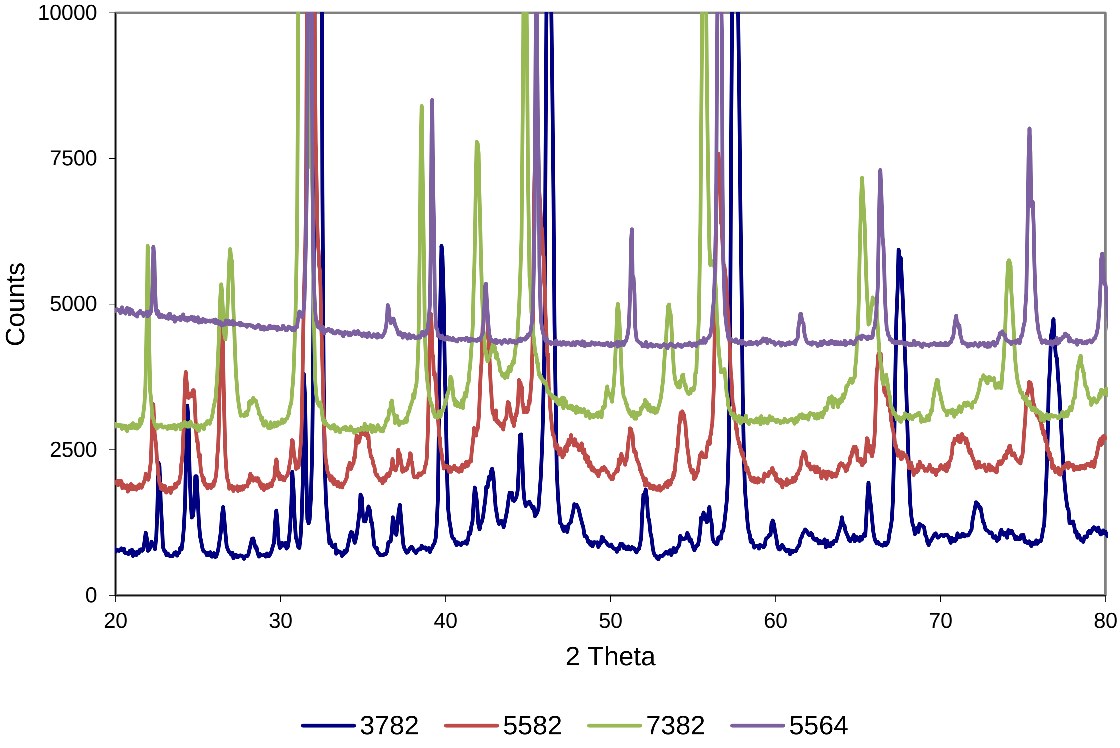

Figure 93 Enlargement of X-ray diffractograms of milled calcined powders

		Composition			
Phase		BSCF 3782	BSCF 5582	BSCF 7382	BSCF 5564
$Ba_{0.5}Sr_{0.5}CO_3$	Orthorhombic	Y	Y	Y	Y
$SrCoO_{2.29}$	Cubic	Y			
$BaFeO_{3-x}$	Hexagonal	Y	Y	Y	
$BaFe_2O_4$	Orthorhombic			Y	
$Ba_{12}Co_{11}O_{33}$				Y	
$Ba_{0.5}Sr_{0.5}Co_{0.8}Fe_{0.2}O_{3-x}$	Cubic				Y
$Ba_8Co_7O_{21}$	Orthorhombic		Y		
CoO	Cubic				Y
Co_3O_4	Cubic				Y

Table 32 Summary of phase analysis of milled calcined powders

There are a number of similar phases in the milled calcined powders although only the BSCF 5564 sample contains $Ba_{0.5}Sr_{0.5}Co_{0.8}Fe_{0.2}O_{3-x}$ phase. The carbonate phase is still present though the barium content derived from the unit cell volume[137] is more uniform across the samples indicating that the strontium may react at lower temperatures than the barium though the phases identified corresponding to the diffractogram peaks are predominately barium containing and not strontium containing.

Despite having the lowest cobalt content BSCF 5564 had free cobalt oxides present as both CoO and Co_3O_4; this indicates the presence in the dried powder of both $Co(OH)_2$ and CoO(OH)[136].

Composition	Unit cell volume	Equivalent Ba content
BSCF 3782	286.07	0.59
BSCF 5582	278.98	0.45
BSCF 7382	289.84	0.67
BSCF 5564	290.64	0.69

Table 33 Unit cell volumes of the carbonate phase in milled oxides (/$Å^3$)

5.3.2.2 Thermogravimetric Analysis

Figure 94 to Figure 96 and Table 35 show the results from the thermogravimetric analysis of the milled calcined oxides using a heating rate of 5K min^{-1}.

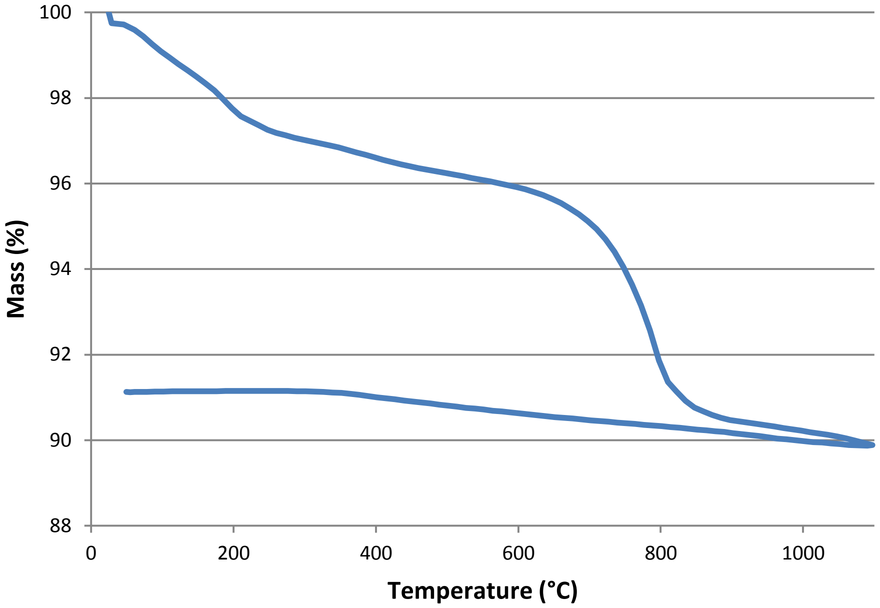

Figure 94 Thermogravimetric curve for milled calcined BSCF 3782 in air with a heating and cooling rate of 5K min^{-1}

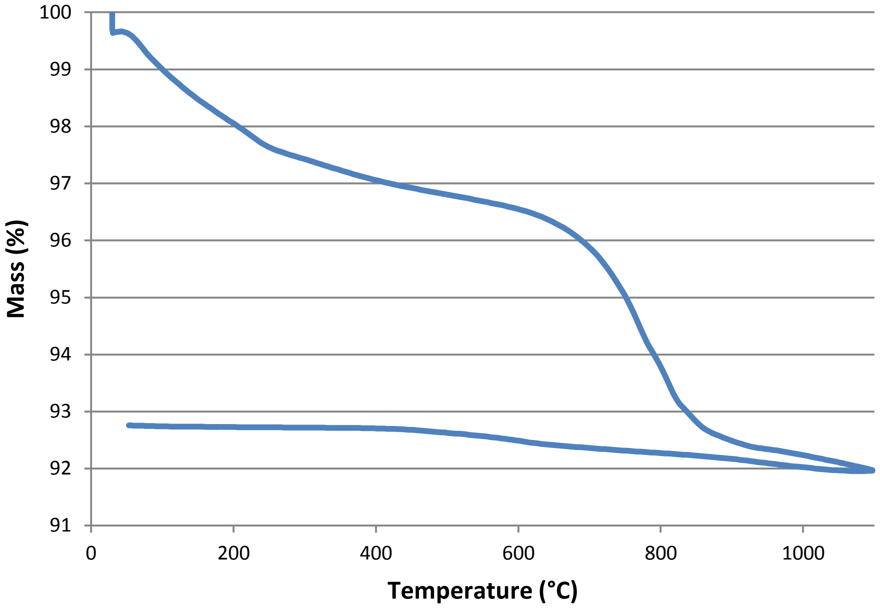

Figure 95 Thermogravimetric curve for milled calcined BSCF 7382 in air with a heating and cooling rate of 5K min^{-1}

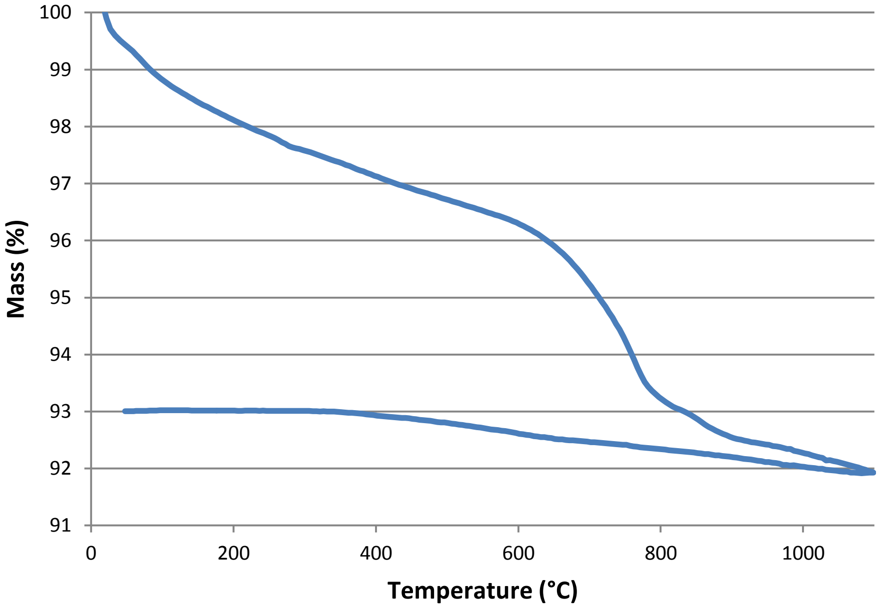

Figure 96 Thermogravimetric curve for milled calcined BSCF 5564 in air with a heating and cooling rate of 5K min^{-1}

The thermogravimetric data shows that after calcination at 850°C there is still carbonate present equivalent to about 20% of the alkaline earth present in the powders. There is a similar weight loss at low temperature indicative of loss of adsorbed water and other volatile species. The variation in delta values on cooling from 1100°C to room temperature is similar though when combined with the room temperature value they combine to give three values ~0.5 and one of 0.37 at 1100°C. (Table 34)

Composition	Delta (iodometric)	Delta 1100 → RT	Delta At 1100°C
BSCF 3782	0.33	0.17	0.50
BSCF 5582	0.37	0.13	0.50
BSCF 7382	0.26	0.11	0.37
BSCF 5564	0.32	0.15	0.47

Table 34 Variation of delta with temperature

		BSCF 3782		BSCF 5582		BSCF 7382		BSCF 5564	
		Wt %	Δ MW	Wt %	Δ MW	Wt %	Δ MW	Wt %	Δ MW
heat	<400	-3.4	-7.6	-3.0	-7.0	-2.9	-7.1	-2.9	-6.6
	650-850	-3.3	-7.5	-3.8	-8.9	-3.3	-8.1	-4.0	-9.3
	Max	89.9	200.7	90.6	210.8	92.0	222.8	91.9	-210.5
cool	to 400	1.3	2.8	0.9	2.0	0.9	1.8	1.1	2.4
Final Mass		91.1	203.5	91.5	212.9	92.7	224.6	93.0	213.0
	Delta		0.17		0.13		0.11		0.15
	Carbonate		17.0		20.24		18.4		21.13

Table 35 Summary of thermogravimetric data for milled calcined powders

5.3.2.3 Discussion of Powder Formation

As was shown in the previous chapter the formation of a large number of compounds occurs during the initial precipitation, drying and calcination of the powders. The most well defined compound is the mixed barium-strontium carbonate which after drying accounts for 66-85% of the barium and strontium in the powder if all the carbon is present as the mixed carbonate. The unit cell volume of the mixed carbonate is after drying proportional to the barium content in the system. However after calcination the unit cell volume is more uniform and higher. This indicates that the strontium reacts with the other components before the barium.

The assignments of the phases may seem to contradict this as the identified phases are mainly barium containing. This is because of the extreme broadness of the peaks together with their variable composition from the solid solutions formed. The phases present within HighScore plus may also not include those present especially the mixed hydroxides and oxyhydroxides. As such the phases are indicative of the types of compounds formed rather than those present.

On calcination the carbonate was reduced in the powder but was still present in significant amounts (~20%). Only one material BSCF 5564 was mainly the desired cubic oxide. The reason for its formation is due to the presence of two carbonates in the dried sample with barium contents of 0.56 and 0.31 which after calcination result in a single carbonate with a 0.69 barium content. This indicates the higher reactivity of the strontium towards the iron and cobalt. Furthermore the step like character of the CO_2 loss has changed with a rapid loss followed by a more gradual mass loss (compare Figure 91 and Figure 96) before the slow loss of oxygen. Also at lower temperature (<500°C) the weight loss is more continuous and less step like indicating more continuous reaction process.

5.3.3 Sintered Ceramics

The milled calcined powders were pressed in a 1cm diameter die at 100MPa and then sintered at 1100°C with a hold time at temperature of 10 hours. The heating and cooling rates were both 180K min^{-1}.

5.3.3.1 Microstructure

The sintered ceramics were examines by SEM after polishing and the microstructures are shown in Figure 97. The measured grain and pore sizes and the densities of the ceramics are shown in Table 36.

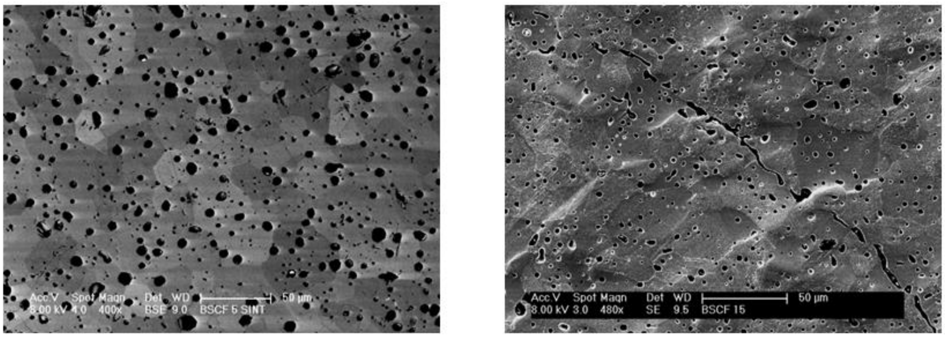

BSCF 3782 BSCF 5582

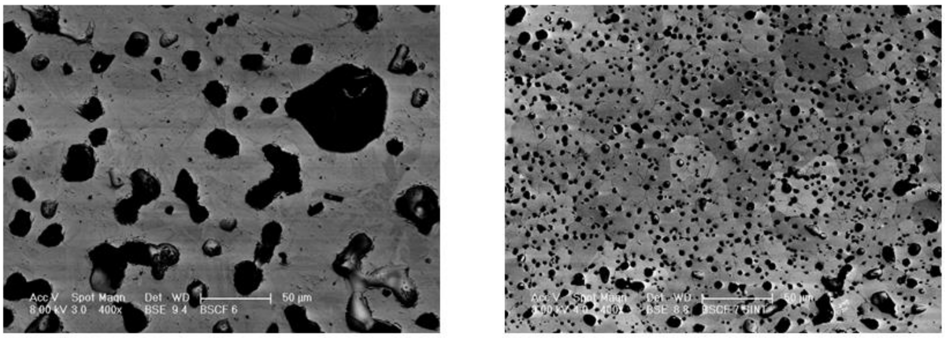

BSCF 7382 BSCF 5564

Figure 97 Microstructure of polished sintered pellets

Designation	Grain Size (/µm)	Pore Size (/µm)	Apparent Density (/gcm^{-3})	Bulk Density (/gcm^{-3})
BSCF 3782	10-50	2-9	4.95(89)	5.06(91)
BSCF 5582	20-50	2-6	5.16(89)	5.25(91)
BSCF 7382	20-50	8-50	5.27(88)	5.43(91)
BSCF 5564	10-40	2-8	5.00(87)	4.99(87)

Table 36 Microstructural properties of sintered ceramics (% theoretical density in brackets)

The grain size distribution was in all cases uniform with no evidence of secondary phases, (as indicated for BSCF 5564 in the xrd), the porosity was located in the grains and also at the grain boundaries. The grains in all samples were equiaxed and did not show any anisotropy. Similar densities (on a theoretical density basis) were obtained for all the compositions which showed that there was no effect of composition on the densification behaviour.

5.3.3.2 X-Ray Fluorescence

The pellets were analysed by x-ray fluorescence and the results are as shown in Table 37. All the measurements were taken from polished pellets which were weighed and measured for size prior to analysis. The data has been converted to an empirical formula basis as explained earlier.(Section 3.6) The only impurity found was calcium at approximately 0.3wt% which corresponded to a concentration of 0.01 Ca ions for each of the A sites.

	BSCF 3782	BSCF 5582	BSCF 7382	BSCF 5564
Ca	0.01	0.01	0.01	0.01
Fe	0.20	0.20	0.21	0.45
Co	0.86	0.83	0.84	0.66
Sr	0.68	0.48	0.31	0.44
Ba	0.26	0.48	0.63	0.44

Table 37 Composition of pellets based on empirical formula (ABO_3 where A+B=2)

As discussed earlier the ratio of strontium to barium was as expected though with the exception of the BSCF 5564 the cobalt concentration was higher than expected. This consequently affects the other compositions on an absolute basis.

5.3.3.3 X-Ray Analysis

X-ray diffraction traces of the polished sintered pellets are shown in Figure 98. Apart from BSCF 5564 all were single phase. The BSCF 5564 contained free

CoO phase which was also present in the calcined powders. The lattice parameter of the materials varied with the barium content of the A site and showed a linear variation with composition (Figure 99 and Table 38) It should be noted that the lattice parameters for BSCF 5582 and BSCF 5564 were so similar that they appear as one point in Figure 99.

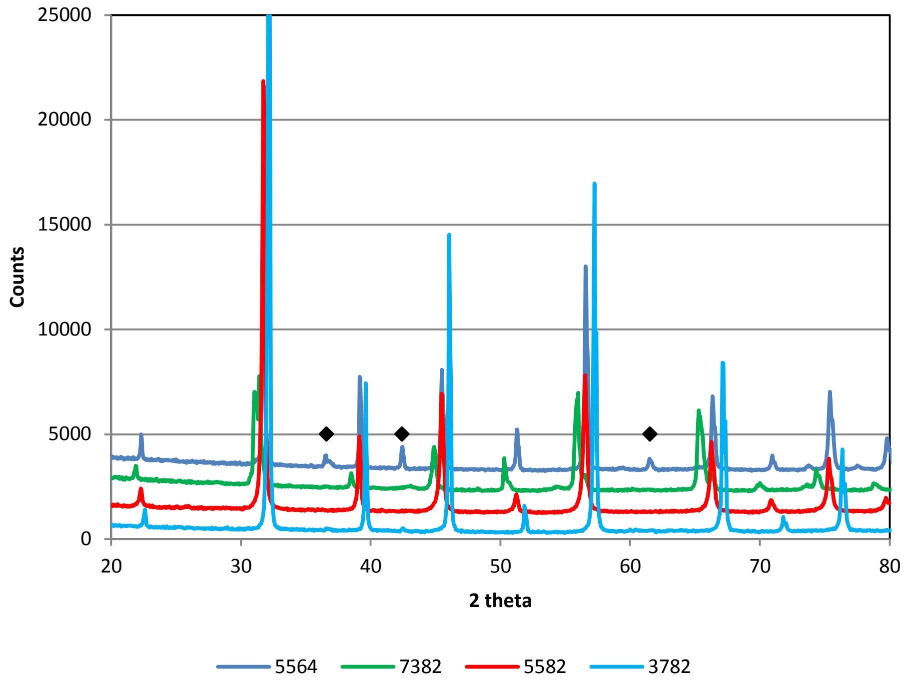

Figure 98 X-ray diffraction of sintered ceramics (♦ indicates CoO peaks)

Composition	Lattice Parameter (/Å)
BSCF 3782	3.939
BSCF 5582	3.988
BSCF 7382	4.031
BSCF 5564	3.987

Table 38 Variation of lattice parameter with composition

The x-ray results showed the expected behaviour the lattice parameter increased uniformly with the increase in concentration of larger barium ion on the A sites. The substitution of iron for cobalt on the B site made very little difference to the lattice parameter reflecting the similar size of the two ions. The presence of the free cobalt may be due to the lower reactivity of cobalt compounds during the heating stages.

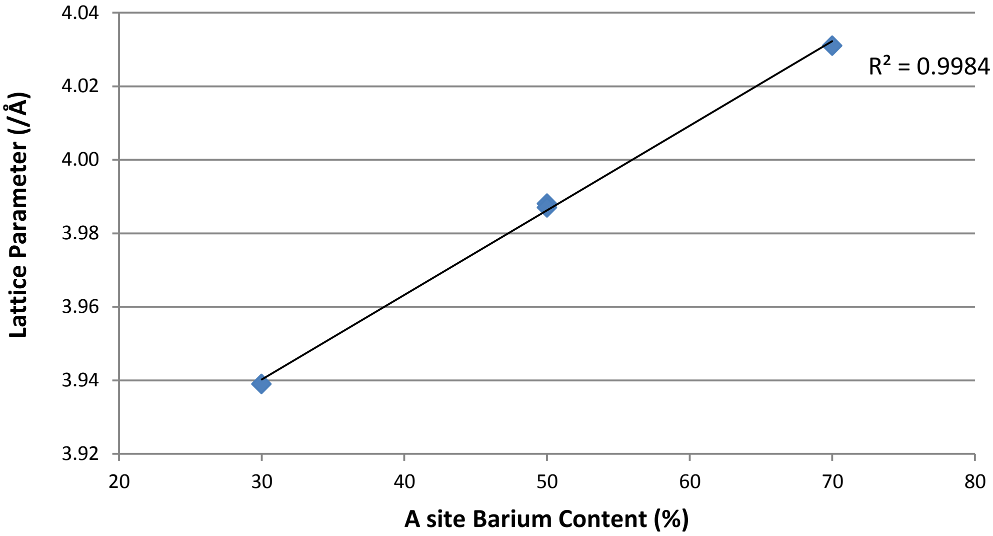

Figure 99 Variation of lattice parameter with composition

5.3.3.4 Oxygen Permeability

Polished pellets were used for the oxygen permeability measurements. The results are shown in Figure 100, Figure 101 and Table 39.

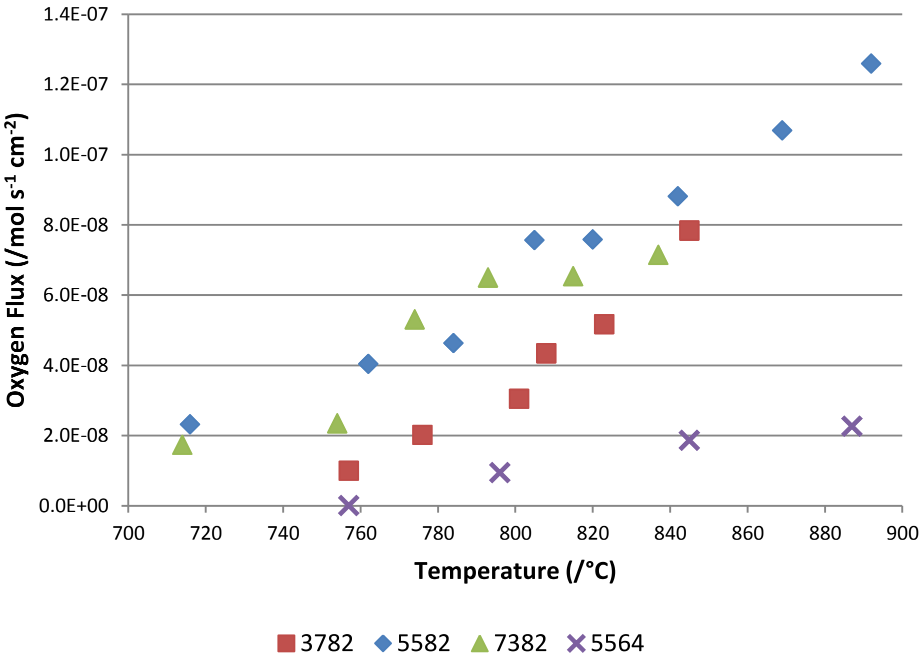

Figure 100 Oxygen flux through sintered pellets

The oxygen flux at 800°C varies between the samples over the range 1 to 8 x 10^{-8} mol s^{-1} cm^{2} and were in the order BSCF 5582>7382>3782>5564.

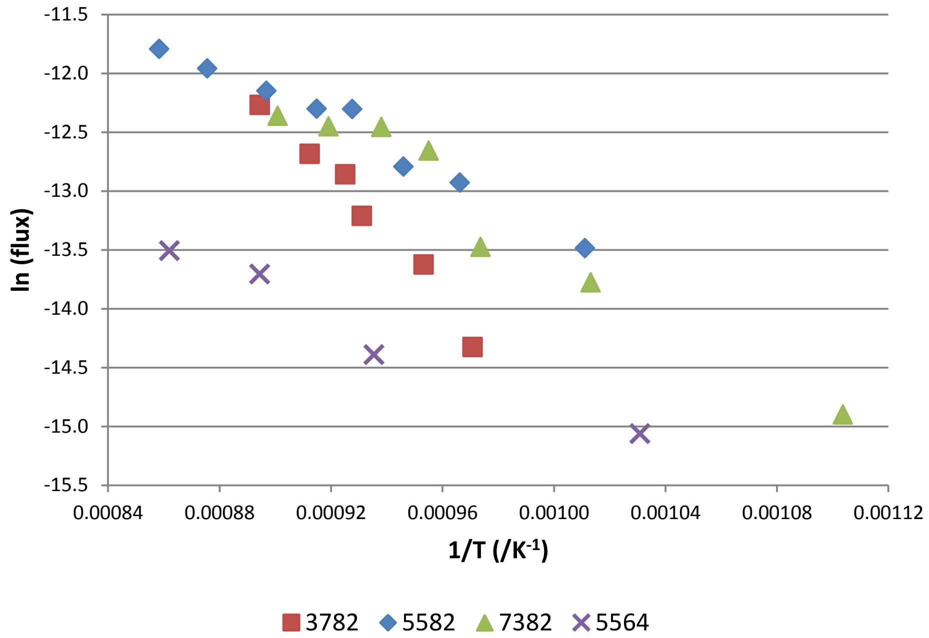

Figure 101 Arrhenius plot of oxygen flux

Composition	Activation Energy (/kJ mol^{-1})
BSCF 3782	218±15
BSCF 5582	93±6
BSCF 7382	117±23
BSCF 5564	78±10

Table 39 Activation energies for oxygen permeation

The activation energy variation suggests a change from surface exchange to bulk diffusion as the rate limiting steps. However the Arrhenius plot shows no indication of a slope change over the range studied.

5.3.3.5 Electrical Tests

Polished pellets were sputter coated with platinum using a Model 682 PECS™ (Gatan UK, Oxford) before being placed in the holder for impedance spectroscopy measurements. As described earlier (section 4.5.3.7.3), to enhance the data acquisition a 100Ω-5nF RC circuit was connected in series with the sample holder. The results are shown below (Figure 102) and in an

Arrhenius plot (Figure 103) and the corresponding activation energies at low temperature are shown in Table 40.

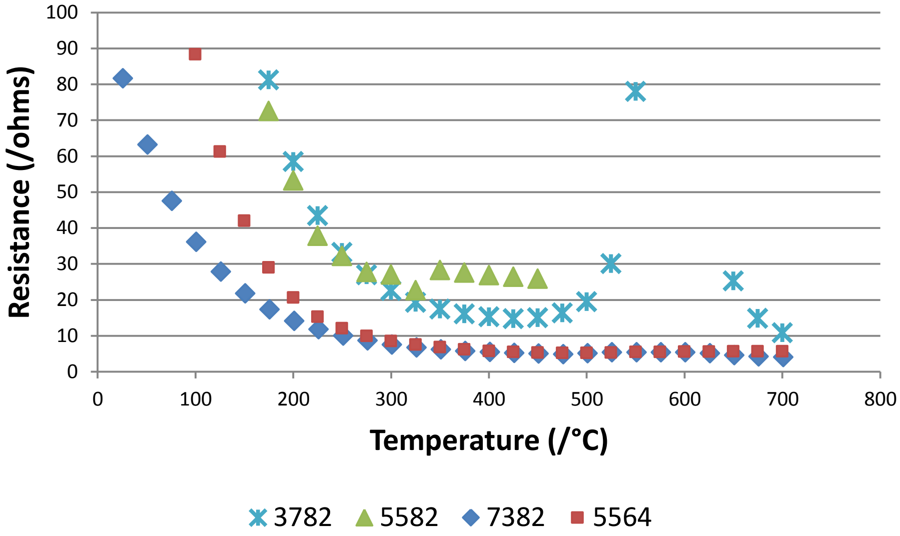

Figure 102 Resistance of compositional variants

The four materials all show similar behaviour as the temperature rises (1/T decreases) the ln(resistance) drops in a linear fashion and then levels out (BSCF 5582 and BSCF 5564) before dropping further (BSCF7382) and in one case going up before a further decline (BSCF 3782).

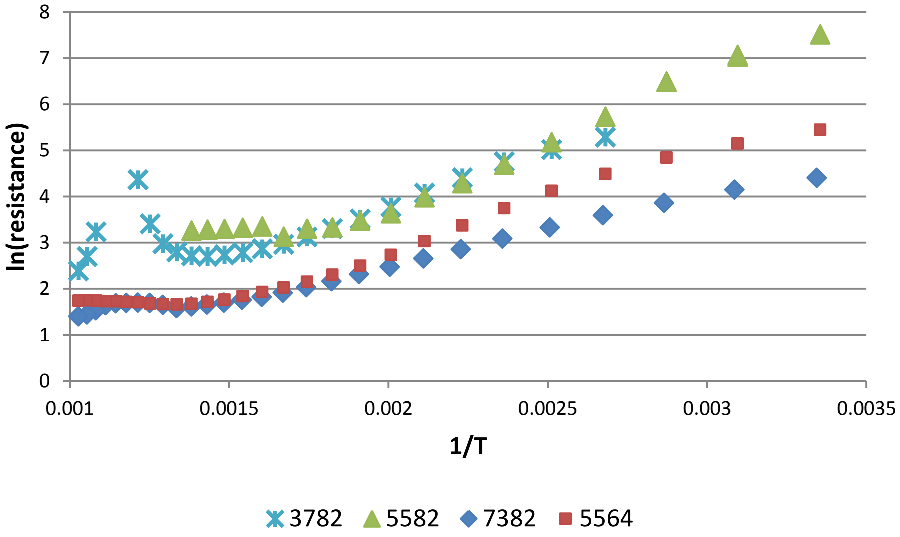

Figure 103 Arrhenius plot of resistance

Composition	Activation Energy (/kJ mol^{-1})
BSCF 3782	20±1
BSCF 5582	26±8
BSCF 7382	14±1
BSCF 5564	22±3

Table 40 Activation energies from low temperature portion of Arrhenius plot

The activation energies shown in Table 40 were calculated over a narrow range from 0.0015 to $0.0025K^{*1}$. There were no significant differences between the samples.

5.4 Discussion and Conclusions

The synthesis of the materials gave a similar pathway to the final single phase ceramic in all samples except the higher iron containing one BSCF 5564 which in addition contained cobalt oxide. There were some differences in the oxygen non-stoichiometry at room temperature with BSCF 7382 showing a lower value of $\delta=0.26$ compared to the others. This is attributed to the larger lattice parameter in BSCF 7382 as a result of its higher barium content. As the oxygen non-stoichiometry (δ) increases there is a corresponding decrease in the oxidation state of the B site cations with a consequent increase in their ionic size[107]. This too will cause an increase in lattice parameter of the mixed oxide phase. If the relative sizes of the A and B site cations change too much then the tolerance factor will become outside the stable range for the cubic phase. Thus there is a limit to the oxygen non-stoichiometry if the cubic phase is to be retained. It was not possible to measure the oxidation states of the B site cations in this system (see Chapter 7.3). Using the values of δ and assuming the oxidation state was the same for both B site cations then the following tolerance factors can be calculated (Table 31 and Table 41). No allowance was made for the change in size of the oxygen ions as a result of oxygen vacancies

Composition	Tolerance Factor
BSCF 3782	1.02
BSCF 5582	1.04
BSCF7382	1.05
BSCF 5564	1.04

Table 41 Tolerance factors calculated from delta and composition

These values of the tolerance factor fall between the curves for M^{4+} and M^{3+} as shown by Shao[11] (Figure 6). All the tolerance factors were similar though the BSCF 3782 was nearer to 1 and should therefore be more stable as the cubic phase.

Taking the tolerance factor in conjunction with the lattice parameter and the delta values it can be seen that the BSCF 5582 has an average lattice parameter of 3.985Å, a tolerance factor close to 1 and a high delta value of 0.37 which only rises to 0.5 at 1100°C. Shao[11] showed that the overall loss of oxygen during heating to 1000°C, ie the increase in delta, went through a minimum in the range 0.3 to 0.7 Ba in BSCF. The proportion lost at low temperature (<500°C) was greater for Ba=0.3 and for Ba=0.7 the majority of the oxygen was lost at high temperature (>700°C). This behaviour is similar to that reported here and by others.[92] However, Yang[147] showed a sudden reversible 1% weight loss on heating for BSCF 8282 composition at 855°C although there was some hysteresis on the uptake of oxygen at 820°C. This latter behaviour was not seen

This combination of lattice parameter, delta and tolerance factor results in the best oxygen flux. The other materials have relatively reduced flux because of the higher tolerance factor and lower delta value which gives fewer vacancies for ionic transport in BSCF7382 despite its larger lattice parameter. The smaller lattice parameter in BSCF 3782 gives poorer oxygen conduction despite its good delta value and tolerance factor. This is supported by its higher activation energy for oxygen flux. Finally BSCF 5564 has very similar properties to BSCF 5582 and yet despite its low activation energy does not act as a good oxygen transport membrane. The formation of cobalt oxide in the final ceramic could indicate it is close to decomposition into brownmillerite type structures and thus its oxygen permeation properties are reduced.[147]

The variation of activation energy for the three lower values (78-117kJ mol^{-1}) as a function of composition is similar to the range seen by Shao[11] (35-75kJ mol^{-1}) However their results were only for the high temperature (surface exchange controlled) part of the data. The inflexion point indicating the transition from bulk conduction to surface exchange as the rate determining step was not seen in this work which could be a result of thicker discs.

The electrical behaviour of the materials was similar to that reported earlier a decrease in resistance followed by an increase.[63, 92, 148]. There is however a small difference between these studies, in that the temperature of change from decreasing to increasing resistance is 300°C[92], >400°C[63], and 320°C (this work). This variation could be due to the experimental set up and temperature measurements as there are no significant differences in the materials used.

The electrical properties for the samples studied here were overall very similar with the exception of the high temperature behaviour of BSCF 3782. This material has the largest increase in delta in these samples. This means that at δ=0.5 both the B site cations will be in the 3+ oxidation state which will be stable over a temperature range similar to that shown for oxygen partial pressure[149]. At this point there can be no electron transfer between cations of the same oxidation state. On further heating M^{2+} ions will form on the B sites as more oxygen is lost and electron transfer can occur between M^{3+} and M^{2+} ions. The increase in resistance therefore occurs when the net oxidation state of the B sites comes to a plateau before decreasing further. When delta = 0.5, it is the composition at which the brownmillerite structures form[20, 105, 149]. The stability of the structure around delta = 0.5 is a point at which the behaviour of the electrical and permeation properties change. The maintenance of the composition at lower values of delta allows good permeation properties.

6 Addition of Copper to BSCF

6.1 Introduction

Starting from the work on the oxygen permeation of $SrCoO_{3-\delta}$, improvements have been sought through the substitution of other ions on the A and B sites[23]. The basis for these changes was that the substituents would either allow better phase stability during operation and/ or enhanced oxygen permeability. These studies have, in general, been carried out in two ways either examining the A site or the B site.

In his studies of the conductivity and oxygen permeability of $LnCoO_3$ (Ln = lanthanide)perovskites, Teraoka found the best oxygen permeability with copper doping $La_{0.6}Sr_{0.4}Co_{0.8}Cu_{0.2}O_{3-\delta}$.[32, 33] However since that time little work has been carried out with copper doped systems, although a cobalt free oxide, $Ba_{0.5}Sr_{0.5}Fe_{0.8}Cu_{0.2}O_{3-\delta}$ was described as having good properties for use as a cathode material in an intermediate temperature solid oxide fuel cell[148]

The use of .three cations on the B site has also been reported with bismuth[150], zirconium[37] and titanium[44] being used to modify phase stability and oxygen permeability. The addition of "*foreign oxides*" to enhance properties has also been described.[143] In this report first row transition metal oxides were added to $Ba_{0.5}Sr_{0.5}Co_{0.8}Fe_{0.2}O_{3-\delta}$ at 5% by weight. The objective was to find a good sintering aid that would give better densification of the ceramics. Copper oxide was the best additive in terms of densification but near the worst for electrical conductivity and oxygen permeability.

This study aims to examine the effect of the incorporation of copper directly into BSCF oxides rather than as a second phase additive added prior to sintering. The underlying aim was to determine whether the benefits of better sintering can be maintained but without losing the oxygen permeability properties.

The compositions listed in Table 42 were chosen for the study. The designation of the compositions is as described earlier (section 5.1) but rounded to one figure and with the addition of CuX, where X is again 10 times the value in the empirical formula.

Designation	Ba	Sr	Co	Fe	Cu
BSCF 5562Cu2	0.5	0.5	0.6	0.2	0.2
BSCF 5571Cu1	0.5	0.5	0.75	0.15	0.1
BSCF 5582Cu0.5	0.5	0.5	0.775	0.175	0.05

Table 42 Compositions of copper containing materials

6.2 Synthesis

The synthetic route chosen for the preparation was as described in section 4.4 using a precipitation pH of 10 and no boil at either high or low pH.(see also Table 8 Experimental plan). The copper was added as copper nitrate.

6.3 Results

6.3.1 Dried Powders

The dried powders were all brown friable materials.

6.3.1.1 X-Ray Analysis

The x-ray diffraction analysis showed that the dried powders were predominately composed of a mixed barium strontium carbonate.(Figure 104) The composition of this carbonate was the same for the three compositions. In addition to the carbonate, Iron oxyhydroxides peaks could be assigned together with some that corresponded to $(Ba,Sr)(Co,Fe)O_{3-\delta}$ phases. The broad peaks and extensive overlap did not make any definitive assignment possible.

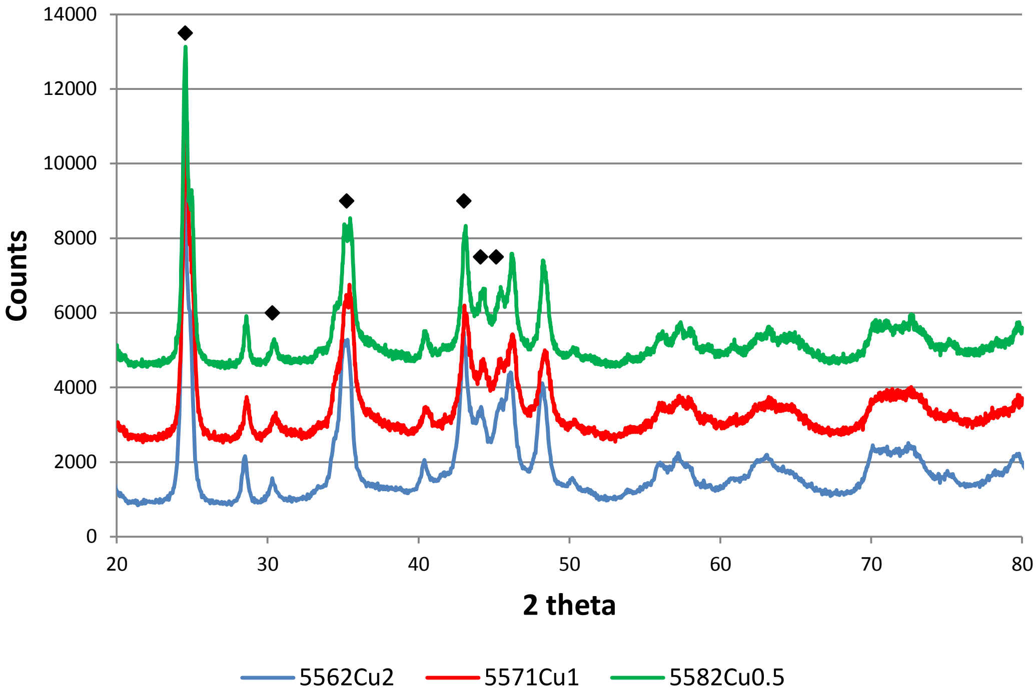

Figure 104 X-ray diffraction of dried powders (♦ indicates $Ba_{0.5}Sr_{0.5}CO_3$ peaks)

6.3.1.2 Thermogravimetric Analysis

The thermogravimetric analysis was carried out and analysed in the same way as described earlier (section 4.5.1.2). The overall curves and data for the dried powders are shown in Figure 105 to Figure 107 and Table 43. The correction to the final molecular weight, from the iodometric data given in Table 44 below, was used in the calculations.

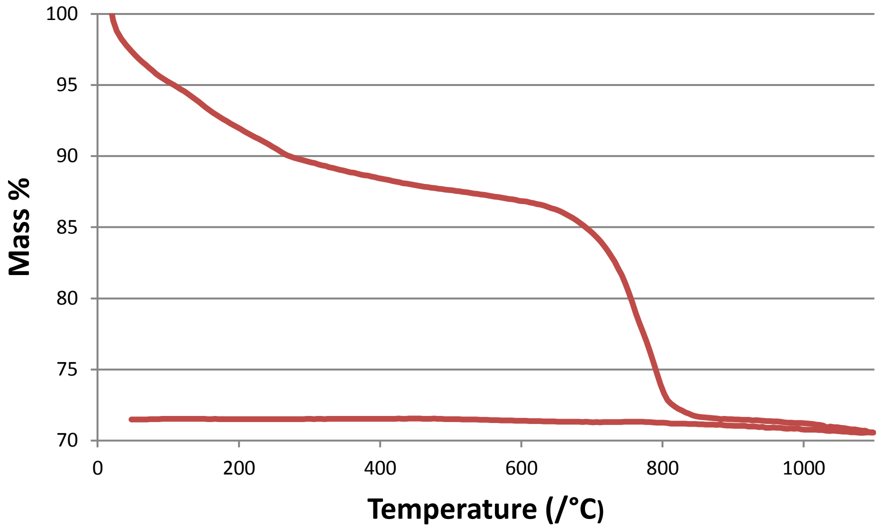

Figure 105 TGA of dried BSCF 5562Cu2 in air with a heating and cooling rate of 5K min^{-1}

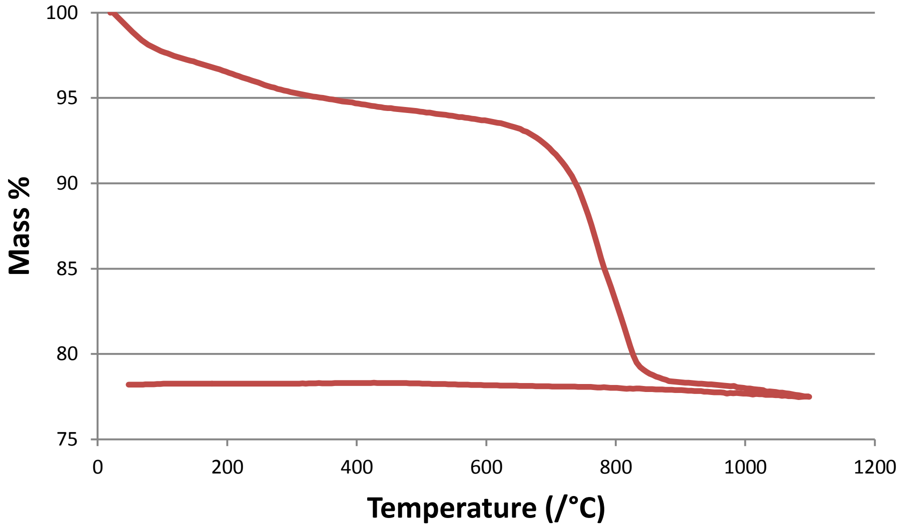

Figure 106 TGA of dried BSCF 5571Cu1 in air with a heating and cooling rate of 5K min^{-1}

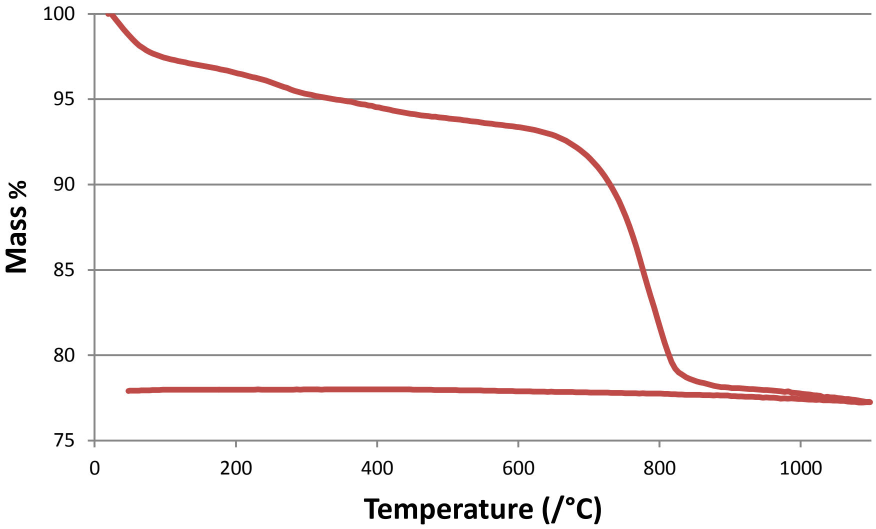

Figure 107 TGA of dried BSCF 5582Cu0.5 in air with a heating and cooling rate of 5K min^{-1}

The general form of the thermal decomposition of the three dried powders was similar. Up to 400°C there was a steady decrease in weight, which was followed by a steady decrease before a step decrease between 700°C and 850°C. After this step there was a continuation of the steady decrease up to the final temperature of 1100°C. Only the BSCF 5582Cu0.5 sample gave a measureable step decrease in the range 200°C to 450°C. On cooling there was an increase in weight up to ~400°C and then no further weight change.

		BSCF 5562Cu2		BSCF 5571Cu1		BSCF 5582Cu0.5	
		Wt %	Δ MW	Wt %	Δ MW	Wt %	Δ MW
<200°C	A	-8.0	-23.9	-3.5	-9.5	-1.2	-3.1
200-500	B	-4.4	-13.0	-2.3	-6.3	-2.7	-7.3
	C					-0.7	-2.0
	D	-14.0	-41.7	-14.4	-39.0	-14.3	-39.0
Mass at 1100°C	E	70.6	210.2	77.5	210.8	77.3	210.5
Heating to 400	F	1.0	2.9	0.8	2.1	0.8	2.0
Final Mass		71.5	213.1	78.3	212.9	78.0	212.5
	Delta		0.18		0.13		0.13
	Carbonate		95.8		88.7		88.6

Table 43 Summary of TGA data for dried powder

The analysis of the TGA data (Table 43) showed that the weight loss assigned to carbonate decomposition (D) was higher than previously seen (cf Table 11 and Table 30). The weight loss at temperatures over 200°C was less than previously seen and was only equivalent to a molecular weight change greater than 9 for BSCF 5562Cu2. This weight loss was ascribed to FeO(OH) decomposition. There seems therefore to be less of this compound type formed in these compositions. The BSCF 5562Cu2 composition also had a large change in delta value on cooling from 1100°C.

6.3.2 Calcined Powders

The dried powders were calcined at 850°C with a 4 hour hold at temperature. Some was then further calcined at 1000°C for 4 hours prior to measuring the delta value by iodometric titration, the results are given in Table 44

	delta
BSCF 5562Cu2	0.41
BSCF 5571Cu1	0.41
BSCF 5582Cu0.5	0.41

Table 44 Variation of delta with composition

6.3.2.1 X-Ray Analysis

The milled calcined samples (850°C) were analysed by x-ray diffraction and the results are shown in Figure 108. The phase analysis shows that the powders mainly had a cubic perovskite structure with a small amount of barium strontium carbonate.

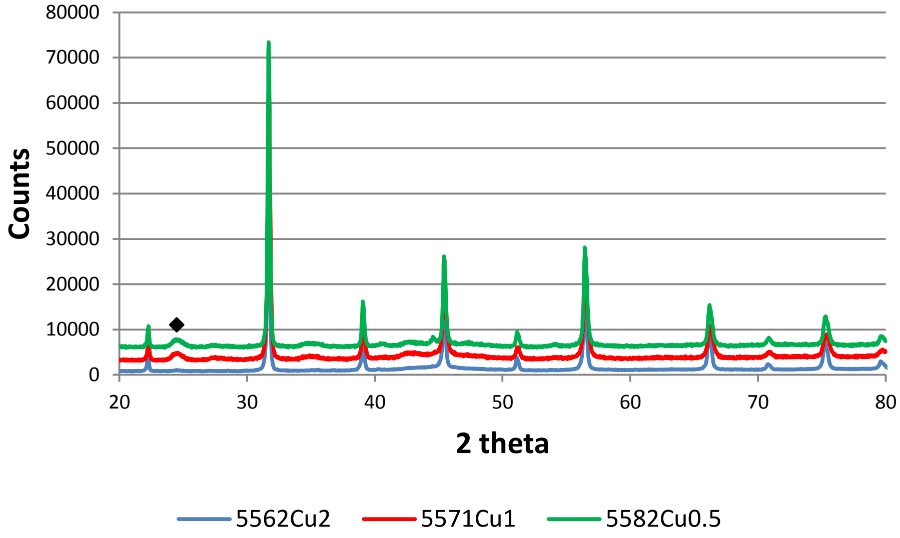

Figure 108 X-ray diffraction of milled powders (♦ indicates $Ba_{0.5}Sr_{0.5}CO_3$ peak)

6.3.2.2 Thermogravimetric Analysis

The milled calcined powders were examined by thermogravimetric analysis and the results are shown in Figure 109 to Figure 111 and Table 45.

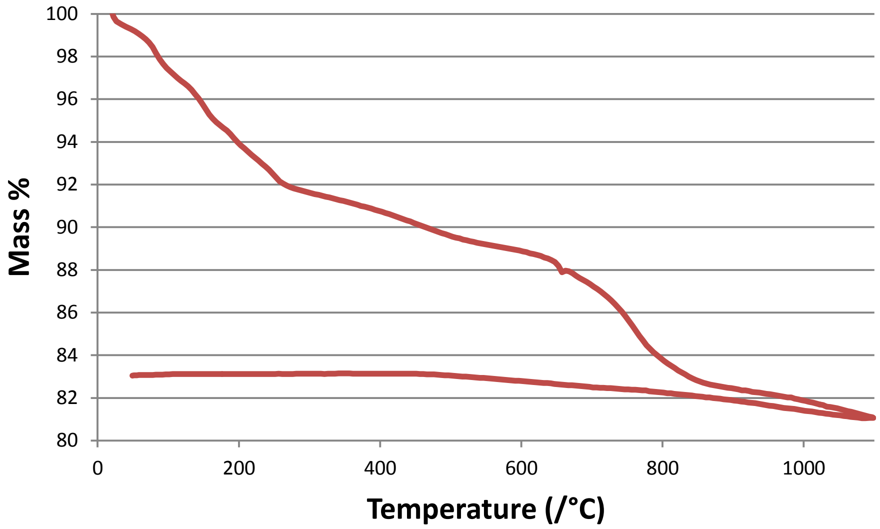

Figure 109 TGA of milled calcined BSCF 5562Cu2 in air with a heating and cooling rate of 5K min^{-1}

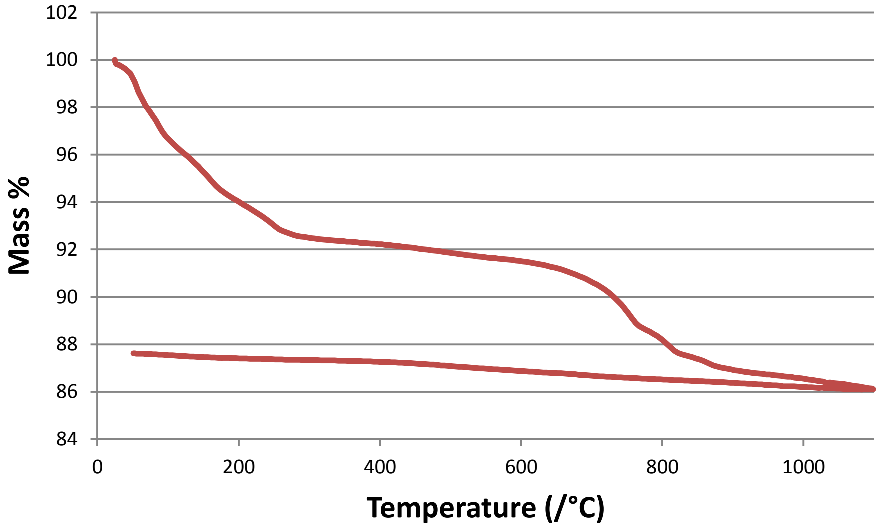

Figure 110 TGA of milled calcined BSCF 5571Cu1 in air with a heating and cooling rate of 5K min^{-1}

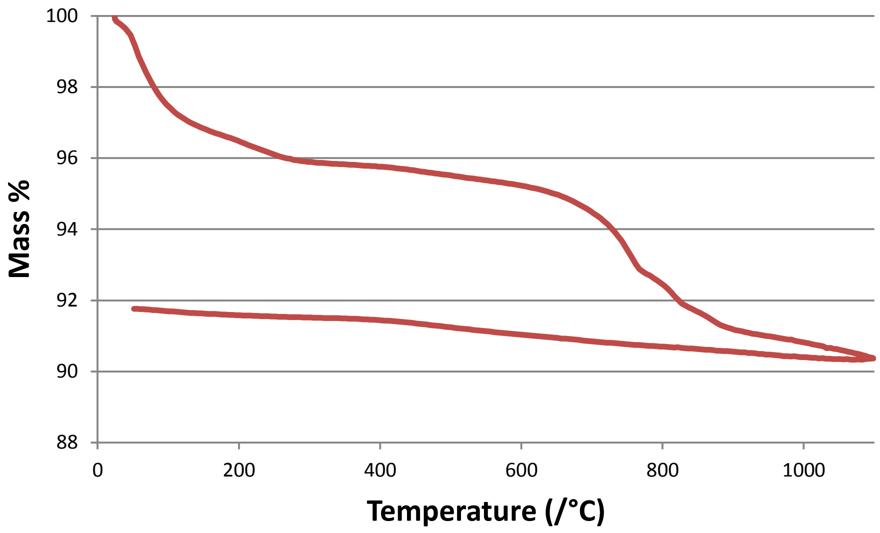

Figure 111 TGA of milled calcined BSCF 5582Cu0.5 in air with a heating and cooling rate of 5K min^{-1}

		BSCF 5562Cu2		BSCF 5571Cu1		BSCF 5582Cu0.5	
		Wt %	Δ MW	Wt %	Δ MW	Wt %	Δ MW
heat	<400	-9.3	-23.7	-7.8	-19.0	-4.2	-9.9
	650-850	-5.4	-13.9	-3.4	-8.3	-3.0	-6.9
	Max	81.1	207.9	86.1	210.1	90.4	210.1
cool	to 400	2.1	5.3	1.2	2.8	1.1	2.5
Final Mass		83.1	213.1	87.3	212.9	91.4	212.5
	Delta		0.33		0.18		0.16
	Carbonate		31.7		19.0		15.6

Table 45 Summary of thermogravimetric data for milled calcined powders

The three powders were all similar in their decomposition except that BSCF 5562Cu2 had a greater low temperature mass loss and also carbonate loss. The latter was equivalent to 32% of the barium and strontium content. This was not reflected in the x-ray traces which showed BSCF 5562Cu2 to have the smallest carbonate peak.(Figure 108). This coupled with the high low-temperature mass loss suggests that the carbonate is in an amorphous phase on the powder surface and has possibly formed after calcination and during storage The uptake of carbon dioxide on exposure to air is described in section 7.3.5.8. and Figure 147.

The oxygen deficiency (delta) of the copper containing materials was highest at both room temperature and at 1100°C when compared with the other materials (Table 34). This could be due to the greater reducibility and lower overall oxidation state of the copper ions. An increase in oxygen loss in $La_{0.7}Sr_{0.3}Cu_{02}Fe_{0.8}O_{3-\delta}$ at 1250K due to copper reduction has been reported[151].

Composition	Delta (iodometric)	Delta 1100 → RT	Delta At 1100°C
5562Cu2	0.41	0.33	0.74
5571Cu1	0.41	0.18	0.59
5582Cu0.5	0.41	0.16	0.57

Table 46 Variation of delta with temperature

There was no discernible difference in the shape of the TGA trace on cooling. The uptake of oxygen therefore occurred in a similar manner to the other materials studied herein.

6.3.2.3 Discussion of Powder Formation

There were no discernible visible differences in the behaviour of the copper doped systems during the precipitation and drying stages of the synthesis. On drying the phase assemblage was similar to that seen in the other systems, that is there was a major mixed barium strontium carbonate and a mixture of the transition metal hydroxides, oxy hydroxides and oxides. though none were clearly identifiable.

On calcination at 850°C there was a significant difference between all the copper containing powders and the BSCF powder with different ratios. In the former case the principal phase present was cubic perovskite with a minor amount of the mixed carbonate. The BSCF powders were a mixture of many phases. This comparison can be seen in Figure 115 where the scans have been normalised before shifting the BSCF 5571Cu1 trace up for clarity. The presence of copper has enhanced the formation of a single phase after calcination.

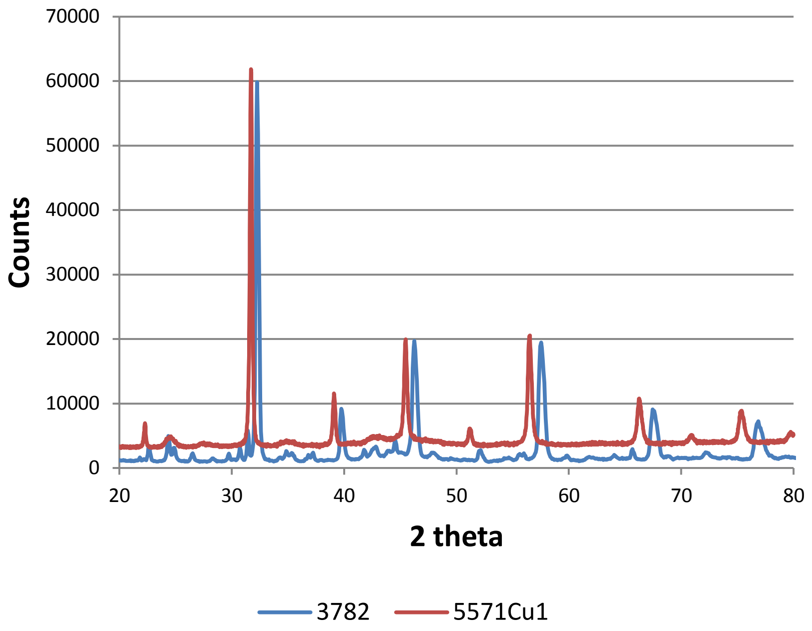

Figure 112 X-ray diffraction of BSCF 3782 and BSCF 5571Cu1

6.3.3 Sintered Ceramics

The milled calcined powders were pressed in a 1cm diameter die at 100MPa and then sintered at 1100°C with a hold time at temperature of 10 hours. The heating and cooling rates were both 180K min^{-1}.

6.3.3.1 Microstructure

The sintered ceramics were examined by SEM after polishing and the microstructures are shown in Figure 113. The measured grain and pore sizes and the densities of the ceramics are shown in Table 47.

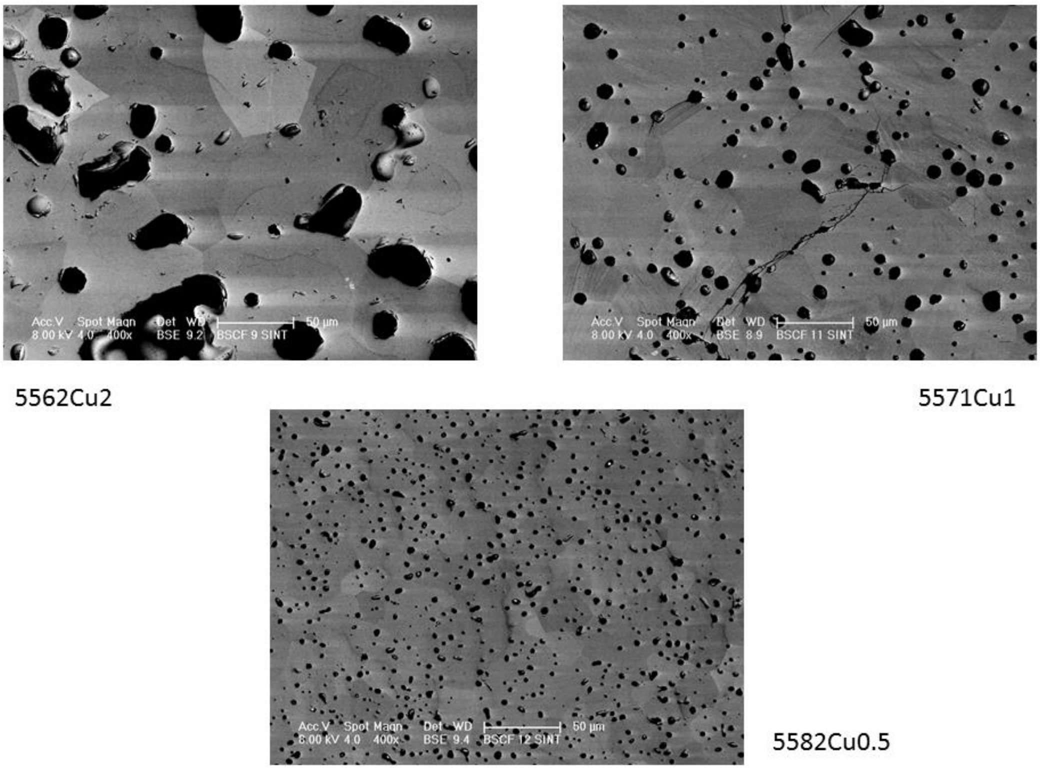

5562Cu2

5571Cu1

5582Cu0.5

Figure 113 Microstructure of sintered ceramics

Designation	Grain Size (/µm)	Pore Size (/µm)	Apparent Density (/gcm^{-3})	Bulk Density (/gcm^{-3})
5562Cu2	30-80	10-20	4.91(85)	4.91(85)
5571Cu1	15-60	2-10	4.99(87)	4.8(84)
5582Cu0.5	10-40	2-8	5.24(92)	4.81(84)

Table 47 Microstructural properties of sintered ceramics (% theoretical density in brackets)

The most noticeable difference between the ceramics is the increase in grain size with increasing copper content. The BSCF 5562Cu2 sample having grains ~50µm, much larger than the non-copper containing materials described earlier. The pores also increase in a similar way as the grain size increases.

The apparent density of the ceramics was slightly less than the other materials in this study which is reflected by the large pore sizes as they have not been eliminated during sintering. In addition the bulk densities are lower than the apparent densities and, again, indicate that the large pores have not been disconnected from the surface.

The chemical composition of the pellets was measured using energy dispersive spectroscopy. There was no evidence of any segregation of the cations within the ceramics. The considerable overlap of the x-ray peaks from iron, cobalt and copper did not allow for any quantification of the data using the available software.

6.3.3.2 X-Ray Fluorescence

The pellets were analysed by x-ray fluorescence and the results are as shown in Table 48. All the measurements were taken from polished pellets which were weighed and measured for size prior to analysis. The data has been converted to an empirical formula basis as explained earlier.(Section 3.6)

	5562Cu2	5571Cu1	5582Cu0.5
Ca	0.00	0.00	0.00
Fe	0.22	0.15	0.18
Co	0.71	0.80	0.82
Cu	0.09	0.07	0.03
Sr	0.51	0.51	0.49
Ba	0.47	0.46	0.48

Table 48 Composition of sintered ceramics

There was some variation in the strontium to barium ratio but at the limits of experimental error (±0.02 on the empirical formula). The copper analysis was low for the BSCF 5582Cu2 sample 0.09 cf. 0.2 expected; the other two compositions were also lower than expected, 0.07cf 0.1 and 0.03 cf 0.05 for BSCF 5571Cu1 and BSCF 5582Cu0.5 respectively. The reason for this discrepancy is that at low levels the accuracy of the XRF diminishes and is also coupled with the overlap of the x-ray peaks of the three transition elements. (see Table 49)

The transition metals were relatively in excess compared to the barium and strontium concentrations.

Element	$K_{\alpha1}$	$K_{\alpha2}$	$K_{\beta1}$
Fe	6,403.84 (100)	6,390.84 (50)	7,057.98 (17)
Co	6,930.32 (100)	6,915.30 (51)	7,649.43
Cu	8,047.78 (100)	8,027.83 (51)	8,905.29 (17)

Table 49 X-ray emission energies (eV) from elements (relative intensities in brackets)[118]

6.3.3.3 X-Ray Analysis

X-ray diffraction traces of the polished sintered pellets are shown in Figure 114. All were a single cubic phase. The lattice parameter of the materials varied linearly with the nominal copper content of the B site (Table 50). However, there was also a consequent variation in the iron to cobalt ratio, although a simple plot of copper content against lattice parameter does give a straight line (Figure 115), the other compositions cannot be ignored.

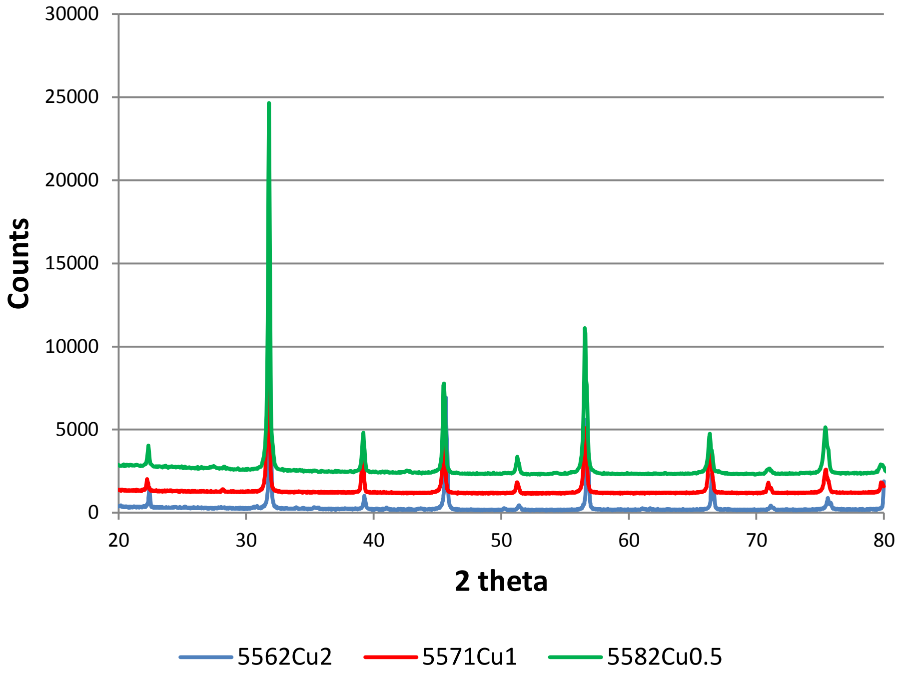

Figure 114 X-ray diffraction of polished ceramics

5562Cu2	5571Cu1	5582Cu0.5
3.9729	3.9825	3.9861

Table 50 Lattice parameters (Å) of polished ceramics

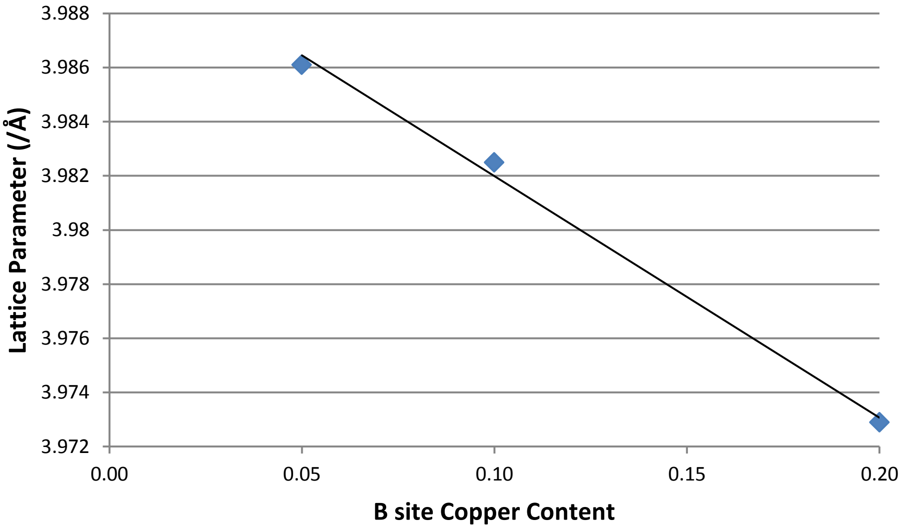

Figure 115 Variation of lattice parameter with copper content

6.3.3.4 Oxygen Permeability

The oxygen permeability of the copper doped pellets was measured using the method as described earlier (section 0), however only one sample (BSCF 5582Cu0.5) showed any oxygen permeation over the temperature range studied (900-700°C).

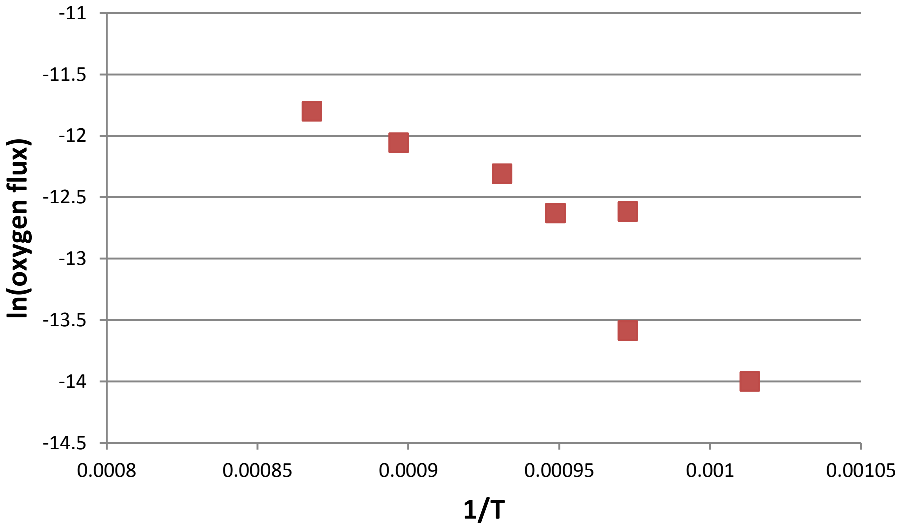

Figure 116 Arrhenius plot of oxygen permeation for BSCF 5582Cu0.5

The value of the activation energy over the whole temperature range was 123±25kJ mol^{-1}. At high temperatures the activation energy was 66±3kJ mol^{-1} and at low temperatures 178±80kJ mol^{-1}. The larger errors occurred because at low temperatures the oxygen concentration was also low thus increasing the inherent variability of the flux measurement.

6.3.3.5 Electrical Tests

Polished pellets were sputter coated with platinum using a Model 682 PECS™ (Gatan UK, Oxford) before being placed in the holder for impedance spectroscopy measurements. As described earlier (section 4.5.3.7.3), to enhance the data acquisition a 100ohm-5nF RC circuit was connected in series with the sample holder. The results are shown below (Figure 117) and in an Arrhenius plot (Figure 118).

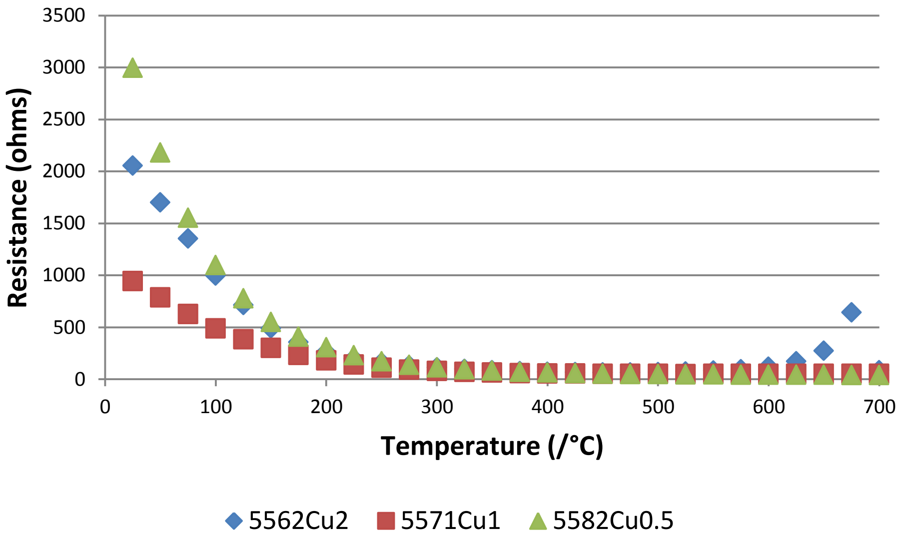

Figure 117 Resistance of copper doped materials

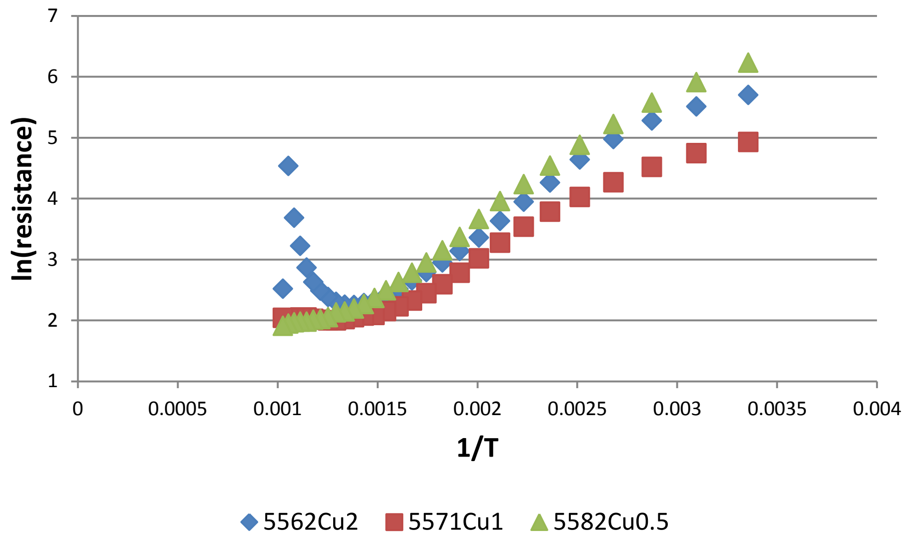

Figure 118 Arrhenius plot of resistance of copper doped samples

The Arrhenius plots do not have a straight line portion from which an activation energy can be calculated. The overall behaviour of the three copper doped materials is broadly similar. There is an initial decrease in resistance with increasing temperature before it levels off except in the case of the highest copper containing sample BSCF 5562Cu2 which at temperatures around 600°C starts to increase in resistance.

The variation of the capacitance of the materials is shown in Figure 119 and the Arrhenius plot for the data in Figure 120. It can be seen at low temperatures that BSCF 5562Cu2 and BSCF 5571Cu1 are very similar in behaviour. They both show a decrease in capacitance and then a levelling off. At higher temperatures only BSCF 5562Cu2 shows an increase in capacitance. In contrast the lowest doped material shows little change in capacitance until 200°C when the capacitance drops quite steeply before it too levels off. The values of the capacitance of generally less than 5×10^{-12} F are indicative of the changes being related to the bulk properties of the ceramic.

Again the Arrhenius plot shows no straight line portion, this indicates that the underlying physical bases for the resistance and capacitance changes are changing so that there is no constant activation energy for conduction or dielectric constant change. (The capacitance (C) of the sample is given by the following equation.

$$C = \epsilon_r \epsilon_0 \frac{A}{d} \qquad 6.1$$

Where ε_r is the dielectric constant

ε_0 is the electrical permittivity of vacuum (8.854 x 10^{-12} F m^{-1})

A is the area of the sample (m^2)

D is the thickness of the sample (m))

The electrical resistance and the capacitance were expected to vary with temperature as is known[6]. The temperature dependence of the conductivity (σ) of electronic and ionic conductors is given by the following equation

$$\sigma = \sigma_o \exp(-\frac{E}{\kappa T}) \qquad 6.2$$

Where E is the experimental activation energy and corresponds to half the band energy gap or the energy for vacancy movement

T is the temperature

κ is boltzmann's constant.

As the temperature increases the conductivity also rises as a consequence of more electrons being excited into the conduction band and easier movement of vacancies as a result of their higher vibrational energy. At ~400°C, when the TGA data indicated the loss of oxygen from the system a change in behaviour was expected as a result of increased vacancies on the oxygen sites and a change in the transition metal oxidation states. Although there was a non-linear change in the resistance it was not well defined as seen in the TGA.

Capacitance is also expected to change as a result of changes in the polarisability of the ions as oxygen is lost from the system, this was not seen for the BSCF 5582 series (Figure 86). The presence of the copper gave a marked change in capacitance with temperature possibly as a result of the many extra oxidation states possible with the transition metals (Fe^{2+}, Fe^{3+}, Fe^{4+}, Co^{2+}, Co^{3+}, Co^{4+}, Cu^{+} and Cu^{2+}). The copper could catalyse the reduction of the other metals allowing for easier charge transfer and electronic conductivity. However again there was no correlation between the capacitance changes and the mass changes.

It is clear therefore that the capacitance and resistance changes are not a simple combination of temperature dependence with, at temperatures over 400°C, an oxygen loss and associated reduction of the transition metals.

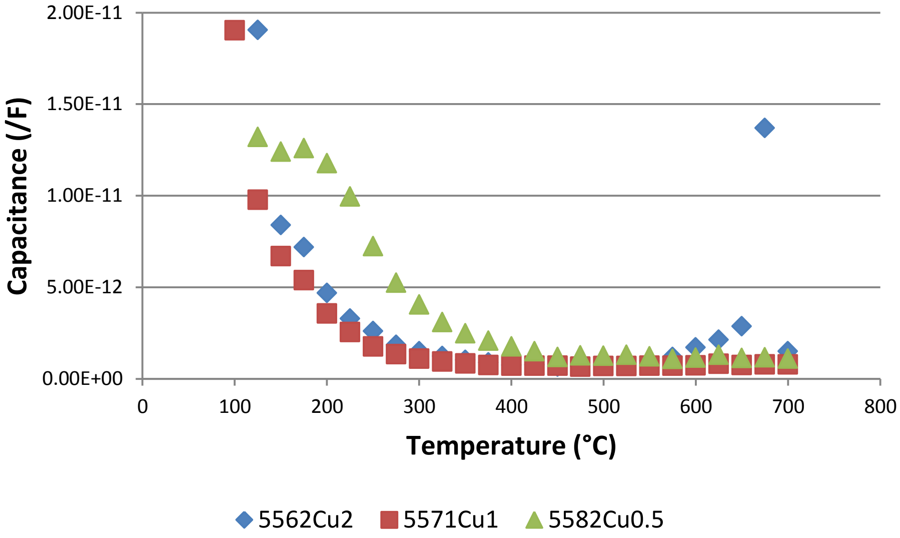

Figure 119 Variation of capacitance with temperature of copper doped materials

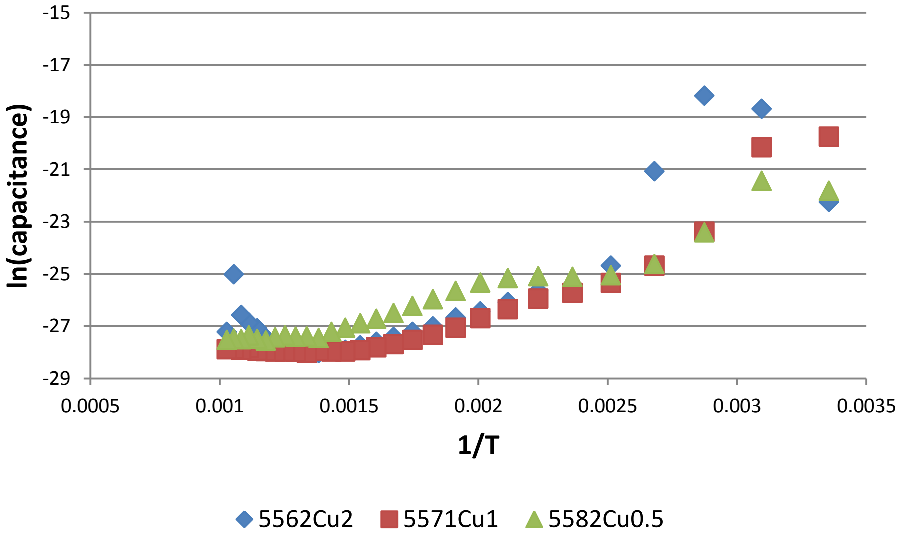

Figure 120 Arrhenius plot of capacitance of copper doped samples

6.4 Discussion and Conclusions

The incorporation of copper into a barium strontium cobalt iron oxide system was achieved and gave a final ceramic with a single cubic phase. The addition of the copper allowed much greater grain growth to occur though it was not accompanied by a comparable increase in densification. In addition the oxide phase development on calcining was more complete at 850°C than with the other materials synthesised. The melting at 950°C when CuO was used as a sintering aid[143] was not seen because the reactions of the copper compounds were complete at 850°C to give a system which did not subsequently melt incongruously.

The iodometric titrations, coupled with the thermogravimetric analysis on cooling, indicated that the final oxides were more oxygen deficient than the previously discussed samples, with delta values of 0.41 for the three samples on the 1000°C calcined powders. In addition there was an additional high loss of oxygen at high temperature for BSCF 5562Cu2 which gave a final delta value of 0.74. The assignment of formal oxidation states between the three cations on the B site could not be made with the available data. (The determination of the oxidation states in BSCF 5582 was one of the objectives of the high temperature XPS and is discussed in Chapter 7.3 below).

However if the following assumptions are made, some conclusions can be drawn.

1. Barium and strontium ions are always 2+
2. Oxygen ions are always 2-
3. The nominal compositions will be used for the analysis.

If the contribution of the copper is not fixed then the net B site cation oxidation state is as shown in Table 51. Although the same at room temperature there is a widening difference in the oxidation state as the temperature increases.

	Room Temperature	800°C	1100°C
BSCF 5562Cu2	3.18	2.80	2.52
BSCF 5571Cu1	3.18	2.97	2.82
BSCF 5582Cu0.5	3.18	2.99	2.86

Table 51 Net oxidation state of B site cations

The lattice parameter of the sintered ceramics decreases with increasing copper content. This suggests either the copper ions are smaller than the ions they are replacing or the average oxidation state of the B site cations is increasing. Higher oxidation state ions are smaller than the corresponding low oxidation ions.[107] As the delta value is the same there is no effect of vacancies on the structure. The vacancies necessarily increase with decrease in oxidation state of the B site cations in order to maintain electrical neutrality. As the materials are cubic it also suggests that the tolerance factor is close to unity.[24] The calculation of tolerance factor relies on knowing the number and oxidation state of the different ions present. Thus it may be concluded that the variation in lattice parameters is a result of small relative changes in the oxidation states of the three B site cations. However the presence of copper has overall given a higher value of δ and thus a greater vacancy concentration.

It should be noted also that he difference in room temperature lattice parameters is small 0.013Å compared with a difference in the lattice parameters of BSCF 3782 and BSCF 7382 of 0.1Å (see Table 38).

The higher concentration of vacancies should give rise to a higher oxygen ion flux through the samples. At 800°C it should therefore be expected that BSCF 5562Cu2 with the highest value of delta of the three copper doped samples would have the highest oxygen flux, however it is the worst and moreover BSCF 5571Cu1 is no better. These two materials, although at room temperature in the cubic phase, have at high temperature the vacancy concentration typical of brownmillerites[20] ie $\delta \geq 0.5$. The poor oxygen flux is probably therefore a consequence of clustering and ordering of the vacancies around the B sites. The change in behaviour as δ increases and reaches a critical value has been seen as the oxygen partial pressure is varied at constant temperature with changes at δ=0 and δ=0.5.[149]

The changes in electrical conductivity with temperature and composition can be rationalised in terms of the changes in oxygen vacancies and the B site cation oxidation state. The electronic conduction is due to electron transfer between B cation sites. In order to have the net oxidation states of 2.52 to 3.18 then there will be a range of oxidation states from M^{2+} to M^{4+}. The split of these among the three B site cations is unknown. However the ratios will be dependent on the temperature in two ways. Firstly the relative energies of the ionisation reactions shown below (equation 6.3) will vary and thus the most stable cation will vary with temperature.(An illustrative example is given in equation 6.4)

$$\mathrm{M}^{2+} \leftrightarrow \mathrm{M}^{3+} + \mathrm{e}^- \leftrightarrow \mathrm{M}^{4+} + 2\mathrm{e}^- \qquad 6.3$$

$$\mathrm{Co}^{4+} + \mathrm{Fe}^{3+} \leftrightarrow \mathrm{Co}^{3+} + \mathrm{Fe}^{4+} \qquad 6.4$$

Thus to begin with there is a gradual drop in resistance as is typical for mixed conductors and then it plateaus out before stating to rise at high temperatures for the BSCF5562Cu2 sample. This last behaviour is probably due to the more extensive reduction of the B site cations which reduces the number of available sites able to accept an electron during the conduction process.

The capacitance varies in a similar way and reflects the underlying relaxation times for the process. At first the hopping frequency becomes faster before slowing down as the potential sites is reduced.

Although the oxygen permeation and electrical properties of the copper doped materials are qualitatively different their dependence on the structural and chemical makeup of the materials is similar. The lowest addition level of copper was beneficial in terms of the desired oxygen flux but at higher levels no flow occurred. As was shown earlier the presence of copper was beneficial for sintering behaviour[143] but there were only positive effects on permeation at the lowest level of addition.

7 In situ High Temperature Studies

7.1 Introduction

In their applications, BSCF ceramics are used at high temperatures >500°C. As has been described earlier, a number of properties of the material changes on heating most notably the oxygen content and the electrical properties. In order to ascertain the nature and possibly the mechanisms of these changes in situ high temperature examinations of BSCF 5582 were undertaken. Two techniques were chosen, x-ray diffraction and x-ray photoelectron spectroscopy both using in situ heating so that the samples could be analysed at temperature as well as after a heating cycle.

The objectives of the x-ray diffraction were to determine whether there were any changes in lattice parameter, phase composition and oxygen site occupancy during heating and cooling of a sample in air. The TGA data presented earlier showed a weight loss at temperatures over ~400°C ascribed to oxygen loss during heating, it was hoped that this could be followed by the x-ray diffraction

The objectives of the x-ray photoelectron spectroscopy were to understand the oxidation states in BSCF 5582 in particular cobalt and iron, to see if in BSCF 5582 the oxygen environment changes with temperature and, if possible, to determine if a low - high spin transition occurs on heating BSCF 5582. The iodometric titrations described earlier gave a value for δ, the oxygen non-stoichiometry. However they could not show whether the reduction of the iron and cobalt from M^{4+} to M^{3+} or M^{2+} occurred equally with either ions or just one was preferentially reduced.

7.2 High temperature X-Ray Diffraction

7.2.1 Equipment

The high temperature x-ray diffraction equipment in the Department of Chemistry was used. This consisted of a Philips diffractometer fitted with an XRK Reactor chamber (Anton Parr GmbH). This was capable of reaching 900°C in air. The diffractometer had a position sensitive detector which meant good spectra could be obtained with a 20 minute scan.

7.2.2 Material

BSCF 5582 powder was prepared as described earlier (pH 10 precipitation no boil). After milling in propan-2-ol and drying, the powder was pressed at 100MPa and sintered in air at 1100°C with a 12 hour hold at temperature.

After sintering, the ceramic was ground and finally polished with 1µm diamond paste.

7.2.3 Experimental Settings

The pellet was placed on the holder and the holder was introduced into the reactor chamber. The height of the sample was then adjusted so that it was on the diffractometer axis. This was achieved by moving the detector to 0° 2θ and with minimum power and a thick Ni filter in place lowering the specimen until maximum x-ray intensity was observed. The specimen was then raised until the x-ray intensity was 50% of the maximum. At this point the specimen was obscuring half the x-ray beam and was assumed to be aligned with it at the centre of the rotation of the source and the detector.

The samples were heated at 10°C min^{-1} to the set temperature, held for 30 minutes to allow thermal equilibrium to occur before taking an x-ray scan. The program then continued in the same way to the next temperature. The same heating rate was used for cooling. Scans were also taken at room temperature at the start and finish of the programme.

7.2.4 X-Ray Results

The microstructure of the starting material is shown in Figure 121.

The x-ray diffractograms for the heating and cooling stages are shown in Figure 122 and Figure 123 respectively. It can be seen that in Figure 122 there is little change in the pattern until 800°C is reached. Though at 750°C the noise level increases which is indicative of the start of the phase changes which are clearly seen at 800°C. The starting material has the cubic perovskite BSCF phase

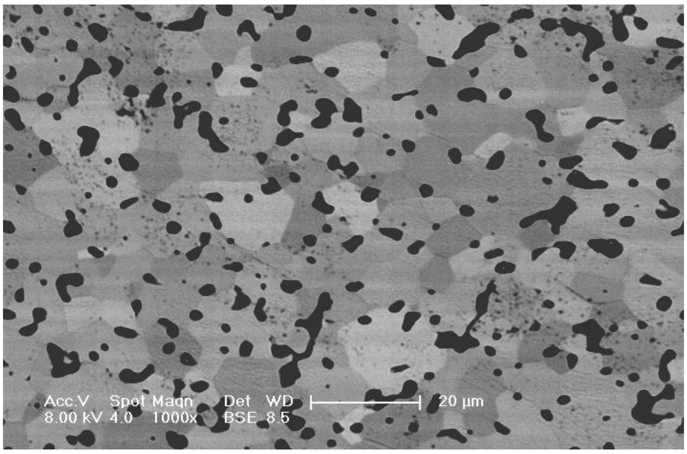

Figure 121 Backscattered electron image of microstructure of samples for high temperature studies

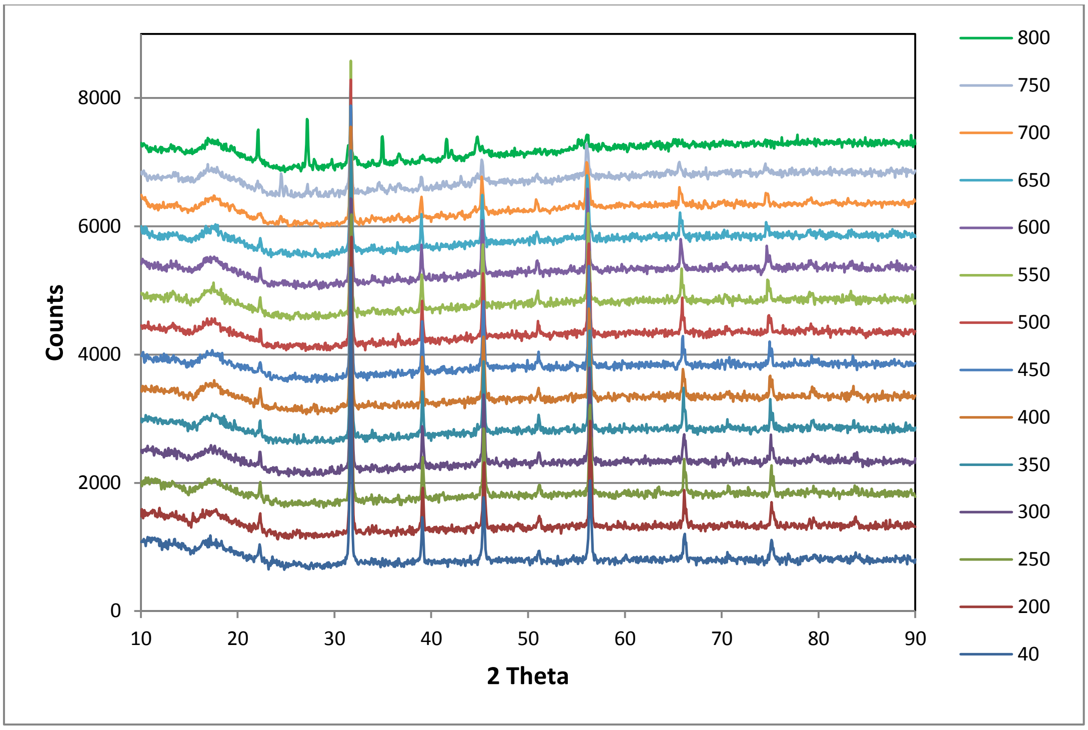

Figure 122 In situ high temperature x-ray diffraction during heating

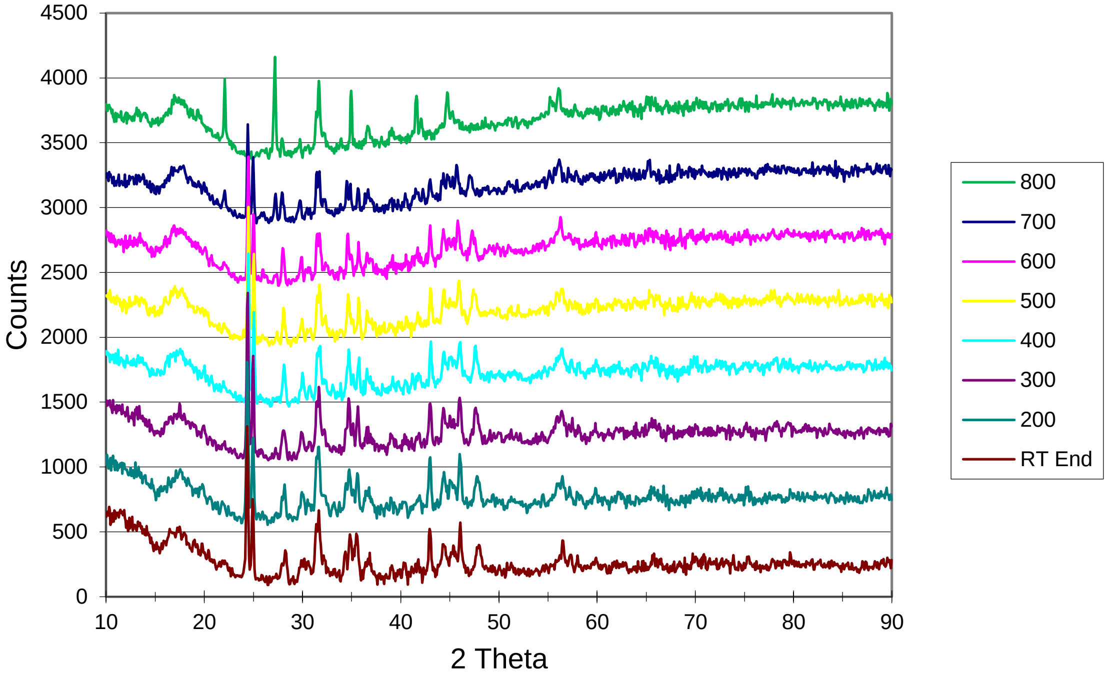

Figure 123 In situ high temperature x-ray diffraction during cooling

In order to determine the lattice parameter changes during heating, the x-ray data was fitted using Topas software.[152] A cubic structure was used for the structure fitting. A Goodness of Fit (GOF) below 2 was taken to indicate good fitting. A typical fitting is shown in Figure 124 (experimental data in blue, fitting line in red). The difference curve is shown below the diffractogram.

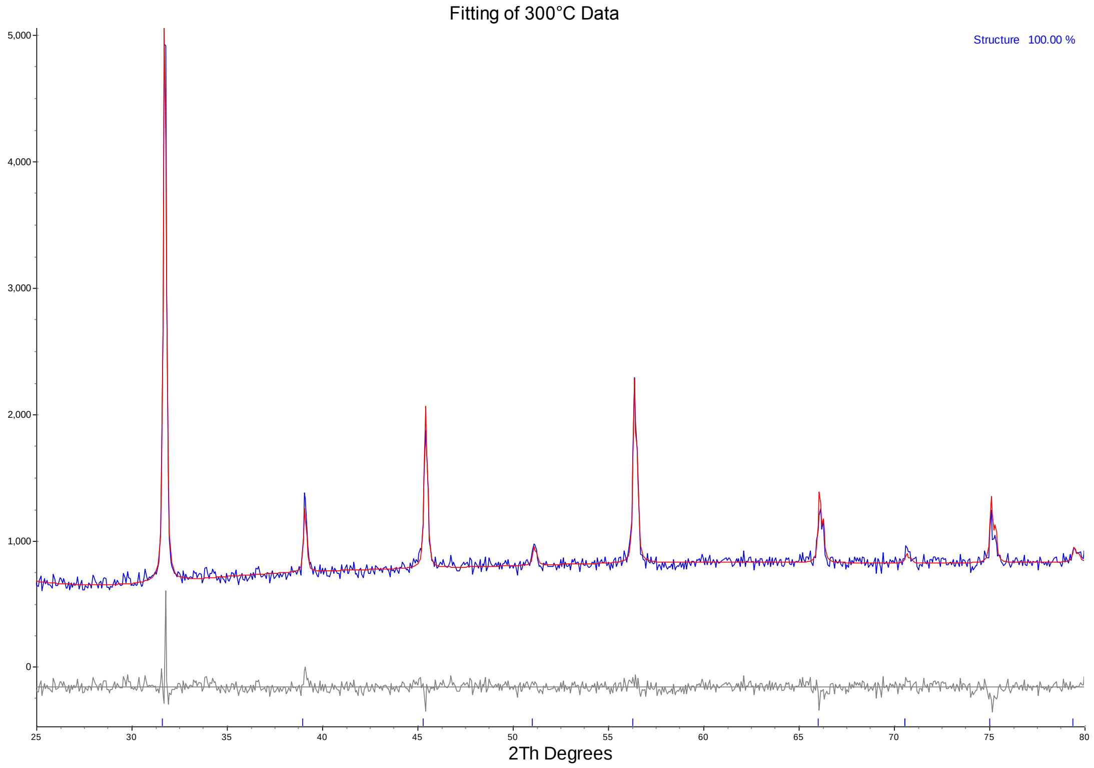

Figure 124 Example of fit using Topas

In order to obtain good fits it was necessary to allow the sample height to be a variable. This was because during the heating of the sample, it and its support would expand and move height relative to the central position set prior to the start of the experiment. This height difference changes the geometry of the diffraction slightly and causes a variation in the angles at which the spectra are recorded. It was found that the sample height correction was linear with respect to the temperature.

The variation in lattice parameter with temperature is shown in Figure 125 It can be seen the change is linear up to 450°C and then changes to a steeper linear curve with a levelling of the lattice parameter at 750°C to 800°C. The slope of these lines can be used to calculate the thermal expansion coefficient (α) in the two temperature regimes.

$$\alpha = \frac{\frac{\Delta L}{L_o}}{\Delta T} \qquad 7.1$$

Where
ΔL is the lattice parameter change (Å)
L_o is the lattice parameter at the lower temperature (Å)
ΔT is the temperature difference (K)

The values of the thermal expansion coefficients are for the low temperature regime 13.4±0.2x10^{-6} K^{-1} and for the high temperature regime 22.9±0.7x10^{-6} K^{-1}. A number of different values for thermal expansion coefficients are given in the literature see Table 52.

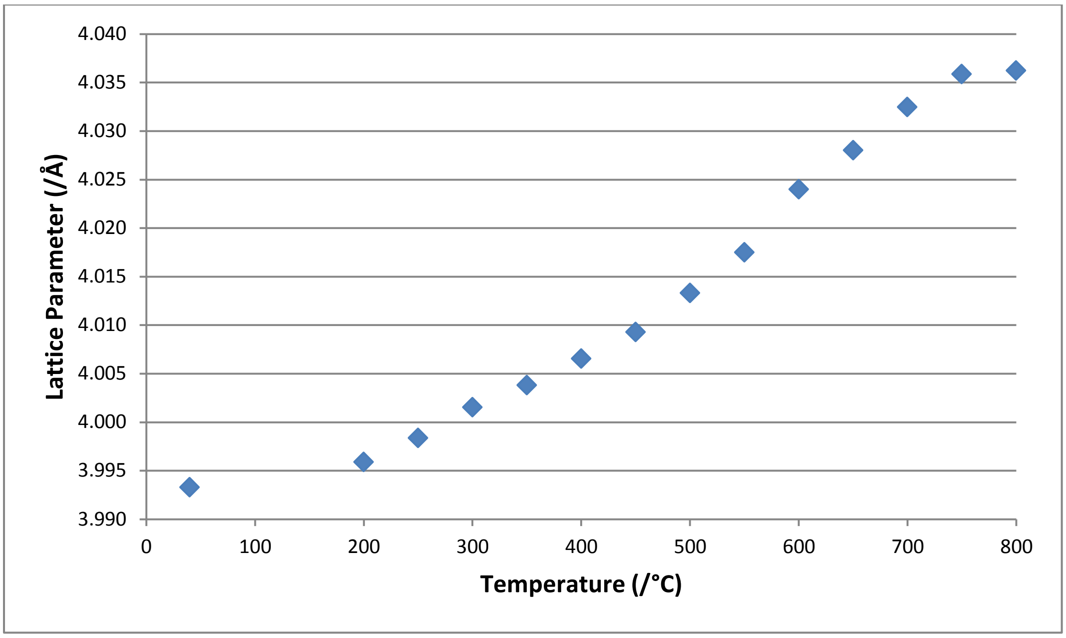

Figure 125 Lattice parameter as a function of temperature during heating

A (x10^6 K^{-1})	Temperature Range (/K)	Method	Author	Reference
11.5	300-1273	HT XRD	Wang	106
16.5	300-1233	HT XRD	Harvey	63
19.2	298-1123	Dilatometer	Zhu	104
21.0	298-1273	HT XRD	Zeng	153
23.2	873-173	Neutron diffraction	McIntosh	30

Table 52 Summary of literature values of thermal expansion coefficient

There is good agreement with the results of McIntosh[30] in the high temperature region. At the lower temperature there is some agreement with the value of the thermal expansion coefficient but not over the full range. The reasons for the discrepancies may be due to details of the measurement and/or the exact composition of the materials as although they all had the same nominal composition, ($Ba_{0.5}Sr_{0.5}Co_{0.8}Fe_{0.2}O_{3-\delta}$) the exact compositions may be different as there were no analytical data in the papers. Zhu[104] studied the effect of composition on $Ba_xSr_{1-x}Co_{1-y}Fe_yO_{3-\delta}$ and found thermal expansion coefficients varying from 19.2-22.9 x 10^{-6} K^{-1}.

The reason for the change in slope of the lattice parameter plot and consequent effect on the thermal expansion coefficient is that on heating above 400-450°C BSCF loses oxygen. (See section 4.5.2.2) This has two effects firstly in order to maintain electrical neutrality the B site cations which have variable oxidation states are reduced on the loss of the oxygen.(Equation 7.2) The reduced ions are bigger than those with higher oxidation states. Secondly as a result of the formation of vacancies on the oxygen sites, there is less coulombic repulsion between the cations and a further expansion can result.

$$M^{n+} + O^{2-} \leftrightarrow M^{n-2+} + ½O_2 \qquad 7.2$$

The difference in slope between the low temperature and high temperature parts of the lattice parameter variation can also be seen in an Arrhenius plot of ln(lattice parameter) against 1000/K (Figure 126). The differences in slope here represent a difference in the activation energy of the changes causing the thermal expansion.

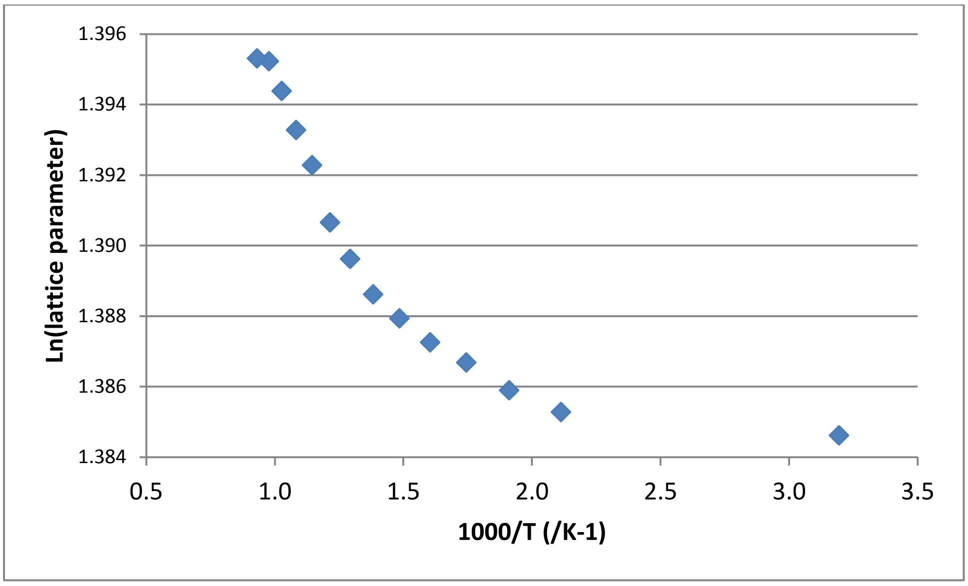

Figure 126 Arrhenius plot of temperature and lattice parameter during heating

The change in the slope in an Arrhenius plot is normally associated with a change in the kinetics of a reaction. In this case the low temperature region

(<450°C) has no chemical reaction taking place and the slope is consequently low. The increase in lattice parameter is due to increased vibrational energy in the crystal structure. However at higher temperatures (>450°C) there is a chemical reaction taking place (Equation 7.2) which has an associated activation energy. The reaction taking place has a number of steps similar to those outlined earlier for the oxygen permeation with desorption and oxygen atoms combining to form oxygen molecules (Equations 2.16 to 2.20).

The assignment of phases to the patterns from the cooling part of the experiment was difficult due to the many overlapping peaks and low signal to noise ratio. Studies of changes in phase during the cooling stage of in situ high temperature x-ray diffraction have shown mixed results. Wang et al[106, 145] showed no change in the phases present on cooling, they used a heating/cooling rate of $5K^{-1}$ with a 70 minute hold at each temperature. Similarly although their work was in an oxygen partial pressure range of $10^{-5}<pO_2<10^{-1}$atm, no change was found by Ovenstone et al[154]. Harvey et al[63] showed the formation of 3 small peaks in the diffractogram which they ascribed to carbonates or oxides. Muller et al[155] showed the decomposition of materials after annealing at temperatures between 700°C and 1000°C to form hexagonal and a lamellar phase.

Table 53 shows the phases present during the cooling stage. At first at 800°C there is some separation of an iron oxide and 2 phases with hexagonal and orthorhombic phases. On cooling there is the additional formation of Ba and BaSr carbonates. The decomposition of the starting cubic compound into the different phases could not be quantified by Rietveld analysis because of the low resolution of the starting data

800°C		700°C		Room Temperature	
Structure	“Composition”	Structure	“Composition”	Structure	“Composition”
Hexagonal	BaFeO	Hexagonal	BaFeO	Hexagonal	BaFeO
Orthorhombic	BaCoO	Orthorhombic	BaCoO	Orthorhombic	BaCoO
Cubic	Fe2.67O4	Cubic	Fe2.67O4	Cubic	Fe2.67O4
		Orthorhombic	$BaSrCO_3$	Orthorhombic	$BaSrCO_3$
		Orthorhombic	$BaCO_3$	Orthorhombic	$BaCO_3$

Table 53 Phases present during cooling of BSCF

Figure 127 shows a very different microstructure when compared with the starting material in Figure 121. Most notable are the small white circular dots which seem to be near the grain boundaries. These have been assigned to CoO[155], however this phase was not found in this study of the XRD diffractograms. It is likely to be the iron oxide phase with cobalt present in solid solution. The pattern of the grains with a central area devoid of the white phase, surrounded by the speckled area along the grain boundaries is consistent with the grains being cubic with the hexagonal phase[155] at the grain boundaries together with the transition metal oxide.. It was not possible with EDS to confirm the composition of the phases because of their small size which means that beam spreading effects give rise to signal from a much larger area.

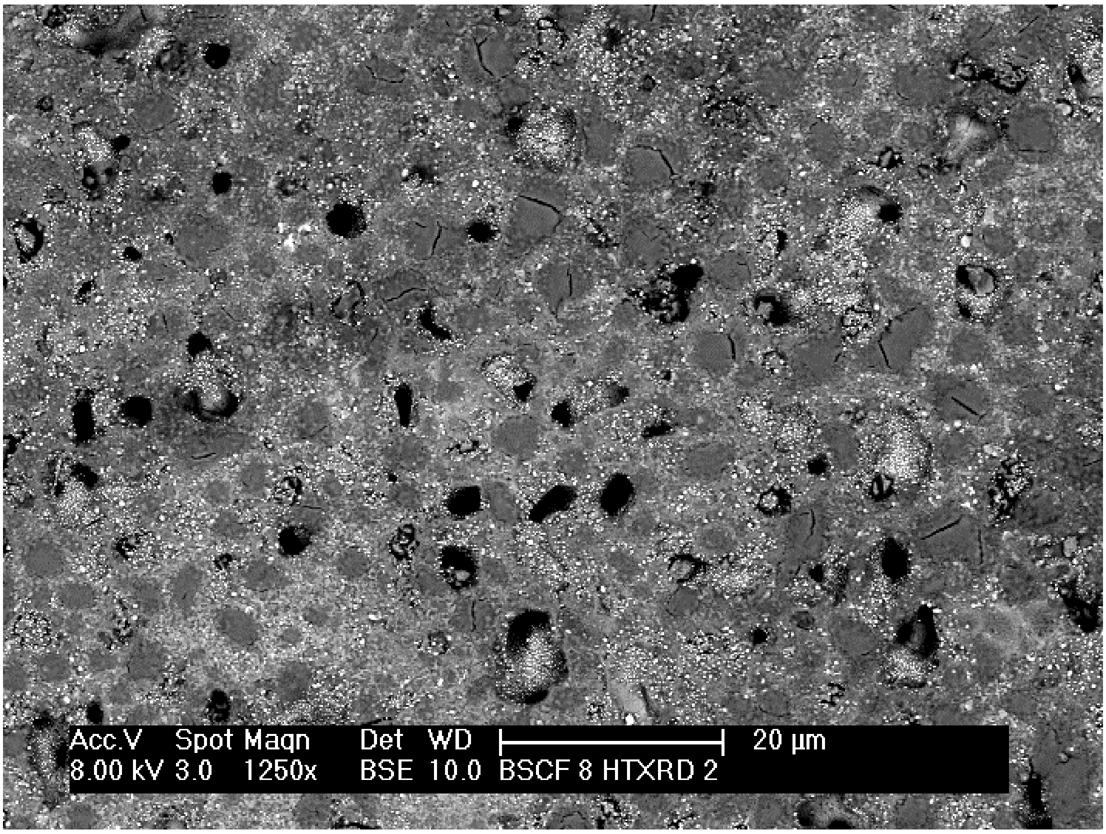

Figure 127 Micrograph of polished surface after HT XRD

7.3 In situ High temperature X-Ray Photoelectron Spectroscopy

7.3.1 Equipment

The x-ray photoelectron spectroscopy was carried out at the National Centre for Electron Spectroscopy and Surface Analysis (NCESS) at Daresbury Laboratory. The Scienta ESCA300 photoelectron spectrometer was capable of high intensity, high energy resolution and high spatial resolution. The instrument used a high power rotating anode, monochromatised Al Kα (hv= 1486.7 eV) x-ray source.[156]

The spectrometer had 3 chambers that were kept under vacuum through which the sample had to pass prior to measurement. The first was the sample chamber which connected via an air lock to the outside. This had to be evacuated to a pressure of $<5 \times 10^{-5}$ torr before the sample could be passed into the preparation chamber. The preparation chamber was where the ex situ heating was carried out. On achieving a pressure $<2 \times 10^{-7}$ torr the sample could be introduced into the analysis chamber where the pressure was $<5 \times 10^{-10}$ torr.

There were 2 methods of heat treatment that were employed ex situ and in situ. The ex situ stage was a metal plate with a hole over which the sample was placed and held firmly using stainless steel mesh. The stage was placed on the heating platform which heated the sample using a mixture of radiative and electron beam heating.

The in situ heating stage allowed studies over the range from ambient to 300°C. It used resistance heating for temperature control. This operated in the analysis chamber and allowed measurement at temperature. The sample was held in place using a collar that fitted over the mount.

Both the stages were thoroughly cleaned with acetone before use to prevent contamination of the vacuum chambers.

7.3.2 Material

BSCF 5582 powder was prepared as described earlier (section 4.4, pH 10 precipitation no boil). After milling in propan-2-ol and drying, the powder was pressed at 100MPa and sintered in air at 1100°C with a 12 hour hold at temperature.

After sintering, the ceramic was ground and finally polished with 1µm diamond paste and then thoroughly cleaned in acetone.

7.3.3 Experimental Settings

The photoelectrons generated during an experiment could have a range of energies from 0 to just less than 1486.7eV, the exciting energy. Therefore, two types of energy scan were performed a survey scan which covered the whole range and a series of narrow ranges which each covered the peaks arising from 1 or 2 elements. The details of the measuring ranges are given in Table 54.

Scan Name	Start eV	Finish eV	Step size meV	Scans	Frames
Survey	0	1325	1000	1	10
Ba 3d + Co 2p	772	808	50	20	2
Fe	698	735	50	50	2
O 1s	525	542	50	10	2
C 1s + Sr	262	295	50	20	2
Sr	126	143	50	10	2

Table 54 Energy ranges for XPS scans

The following procedure was used to examine the BSCF 5582 pellet on the ex situ heating stage. An initial survey scan and complete set of narrow range scans were carried out. The pellet was then moved from the analysis chamber back to the preparation chamber. It was heated to 500°C using the settings given in Table 55. It was held at temperature for 30 minutes before being allowed to cool and returned to the analysis chamber where the measurements were repeated. The same cycle was used for heating the sample to 800°C using the settings in Table 55.

Setting	500°C	800°C
LT Filament Current	5A	6.5A
HT Voltage	100V	300V

Table 55 Instrument settings for ex situ heating stage

The in situ sample was measured using the survey scan and detailed scans as for the ex situ heated sample. The heating current for the stage was turned on at 0.5A and after 30 minutes a survey scan carried out. As this showed no clear differences when compared to the original survey scan, the heating current was increased to 0.75A and the survey scan run again after 30 minutes hold at temperature. Further increases to 1.0A and 1.5A were made and at 1.5A differences were seen. There was broadening in the Ba 3d and Co 2p peaks. Detailed scans were then taken. The heater electrical supply failed and no further heating could be undertaken. On cooling in situ a survey scan and the detailed scans were taken. The sample was removed from the instrument and left in the ambient atmosphere. It was remeasured for both the survey and detailed scans 48 hours later. 1.5A corresponded to a sample temperature of 300°C.

7.3.4 Sample Characterisation

The samples were examined by x-ray diffraction before and after the XPS measurements.

7.3.5 Results

7.3.5.1 General

The samples for the XPS studies were 92% of theoretical density. The grain size showed 10-20µm grains which were equiaxed. Pores of up to 5µm were present in both inter-granular and intra-granular positions. This can be seen in the backscattered image of a polished surface in Figure 121. The measured density (92%) is a little low for permeation studies as there is a possibility of the pores having a fully interconnected network that allows diffusion of the gases through the membrane rather than just allow semi-permeation of oxygen. However, it was felt that as the firing cycle was typical of that used elsewhere in this study and that the microstructure was not dissimilar to the more dense samples, the analysis by XPS would allow comparisons with the other data collected. Furthermore, XPS is a low resolution technique that cannot differentiate between very fine scale structures and thus any differences between the low and high density samples would not be discernible.

X-ray diffraction was also carried out on the polished surface prior to the XPS measurements as is shown in Figure 128. Only the BSCF perovskite phase was present.

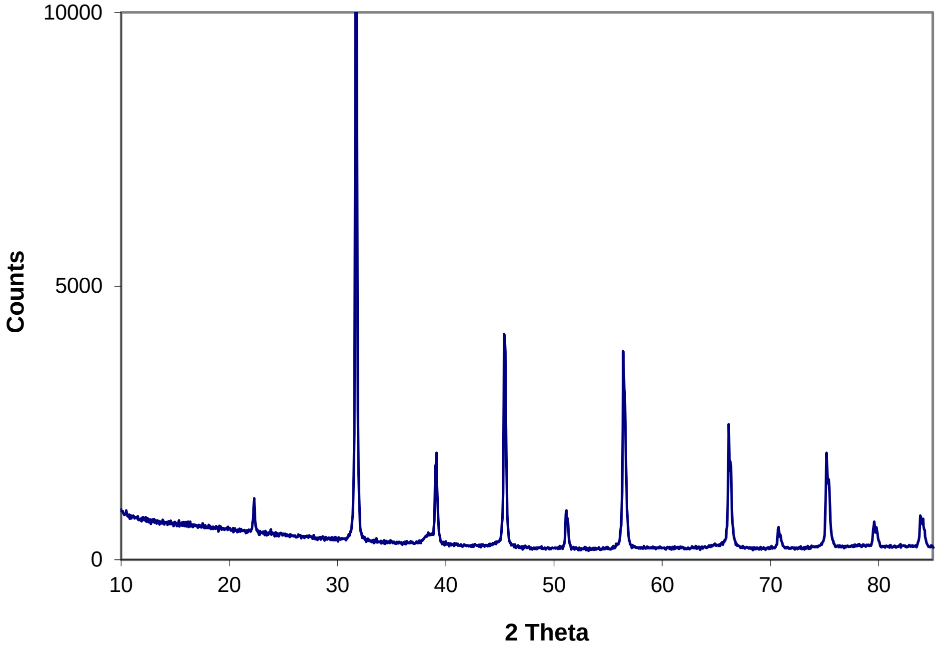

Figure 128 X-ray diffractogram of sample prior to XPS measurements

7.3.5.2 Low Resolution XPS Scans

The low resolution scans were carried out to allow an overall view of how the spectra varied as the temperature was changed. Using the ex situ heating stage scans were performed at three temperatures including ambient. These scans are shown in Figure 129. The major difference between the scans that is visible is the size of the C 1s peak at 285eV. As the treatment temperature increases the carbon, (some of which is adventitious - see section 7.3.5.8) burns off and this peak reduces in size. The burning off of the carbon was accompanied by a significant rise in pressure in the preparation chamber which meant the heating rate had to be adjusted to prevent too a high a pressure developing within the chamber. As a consequence of this loss in carbon the signal to noise ratio of the other peaks increases as there is no longer any attenuation of the peaks due to the surface layer of carbon. This is particularly true for the Fe 2p peak which is barely discernible at the start of the experiment.

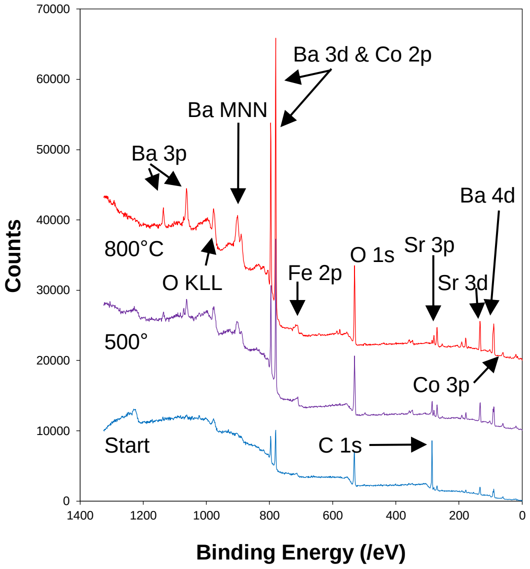

Figure 129 Low resolution XPS scans after ex situ heating

The low resolution scans of the in situ heating experiments are given in Figure 130. There is much less carbon burn off in this experiment as there is little change in the C 1s peak at 285eV. The major difference was the broadening of the overlapping Ba and Co lines at 795 and 780eV. These are shown in an expanded view of Figure 130 shown in Figure 131.

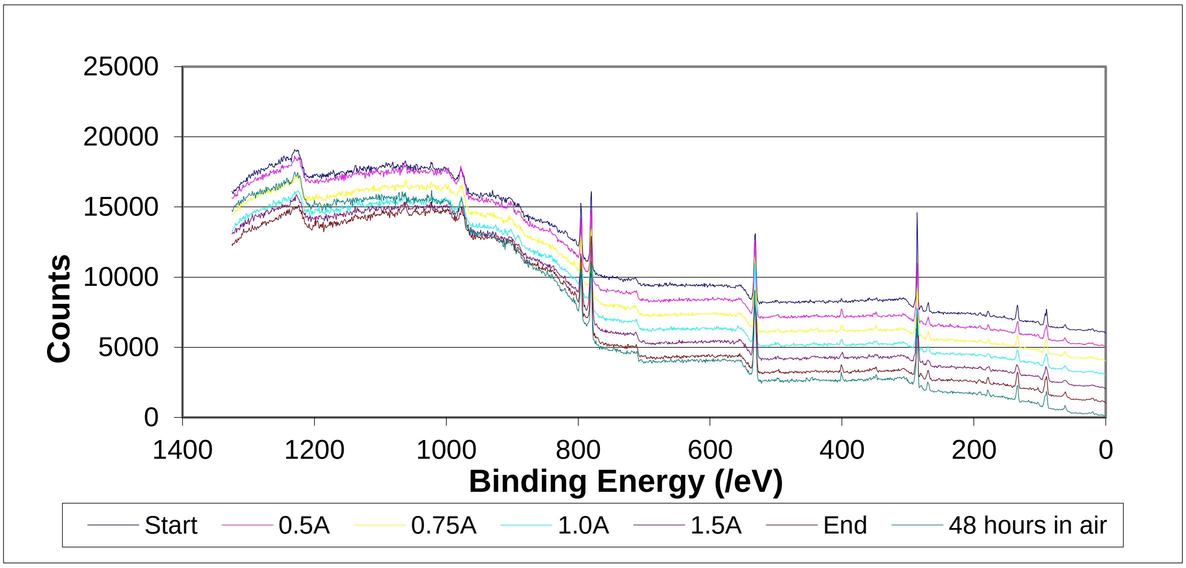

Figure 130 Low resolution XPS Scans during in situ heating experiment

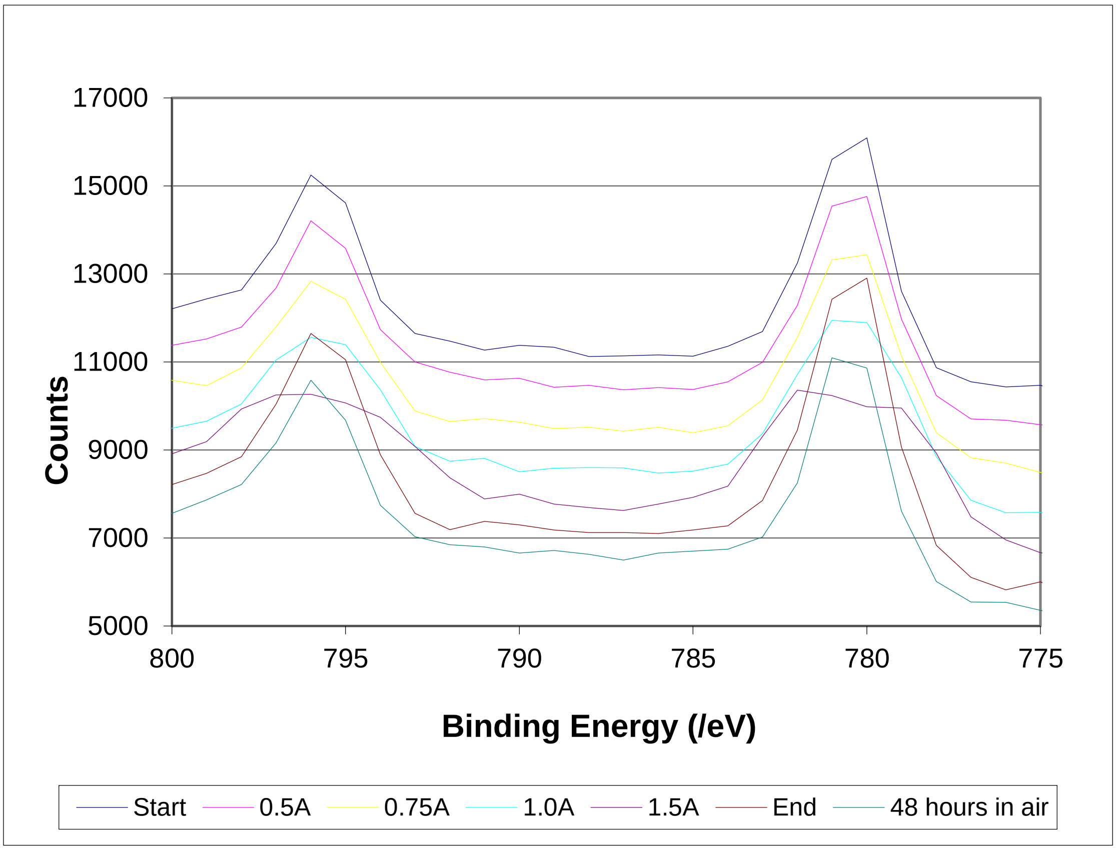

Figure 131 Expansion of low resolution XPS in situ scans

The curve with the heating current at 1.0A showed slight broadening but that at 1.5A which corresponded to 300°C showed definite line broadening. On cooling the line shape had reverted to the original width.

7.3.5.3 High Resolution XPS Scans

The high resolution scans using a 50meV step size were carried out over the ranges indicated in Table 54 for Ba 3d and Co 2p, Fe 2p, O 1s, C1s and Sr 3p, and Sr 3d. This enabled the transitions to be studied in detail. Each of the scan ranges will be discussed in turn as the exact nature of the chemical species undergoing the transitions are identified. Following this the data will be quantified with respect to those species previously identified.

7.3.5.4 Ba 3d and Co 2p High Resolution Scans

Figure 132 shows the high resolution scan of the initial sample over the range 772eV to 808eV. This scan was taken at room temperature and shows the Ba 3d and Co 2p peaks. In this scan the Ba 3d 5/2 and Co 2p 3/2 peaks overlap at around 780eV. The Ba 3d 3/2 and Co 2p 1/2 peaks overlap at around 796eV. The results of the fitting are also shown in Figure 132. For ease of interpretation all the figures in this section will have the following colour scheme

Blue	Experimental Data
Red	Component Peaks from Fitting
Black	Computed Envelope & Background

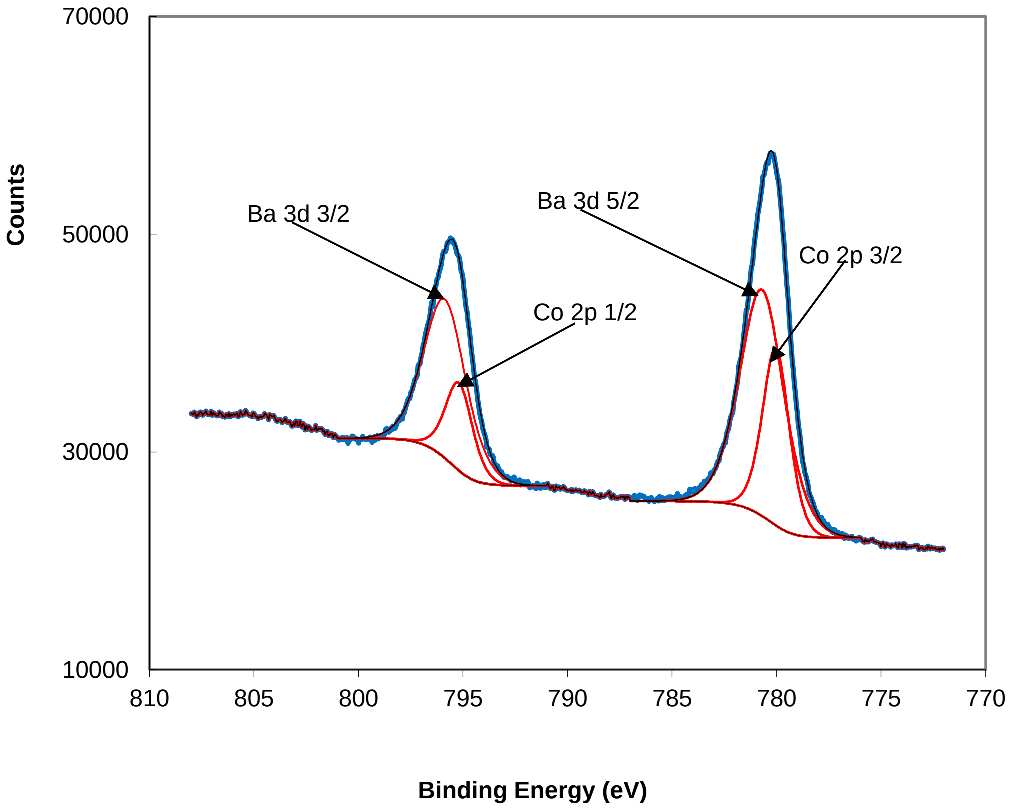

Figure 132 Room temperature XPS scan of Ba and Co region

The barium peaks are in both cases at slightly higher binding energy than the cobalt peaks. The background fitting used was a Shirley type[130]. The position of the Co 2p 3/2 peak at 780.0eV and the difference in energy between the Co 2p

3/2 and Co 2p 1/2 peaks of 15.2eV indicates that the cobalt is in the 3+ oxidation state.[157, 158]

After heat treatment at 500°C and 800°C the 4 peaks were retained at their original positions but additional peaks were also necessary for complete fitting of the data. This is shown in Figure 133 and Figure 134.

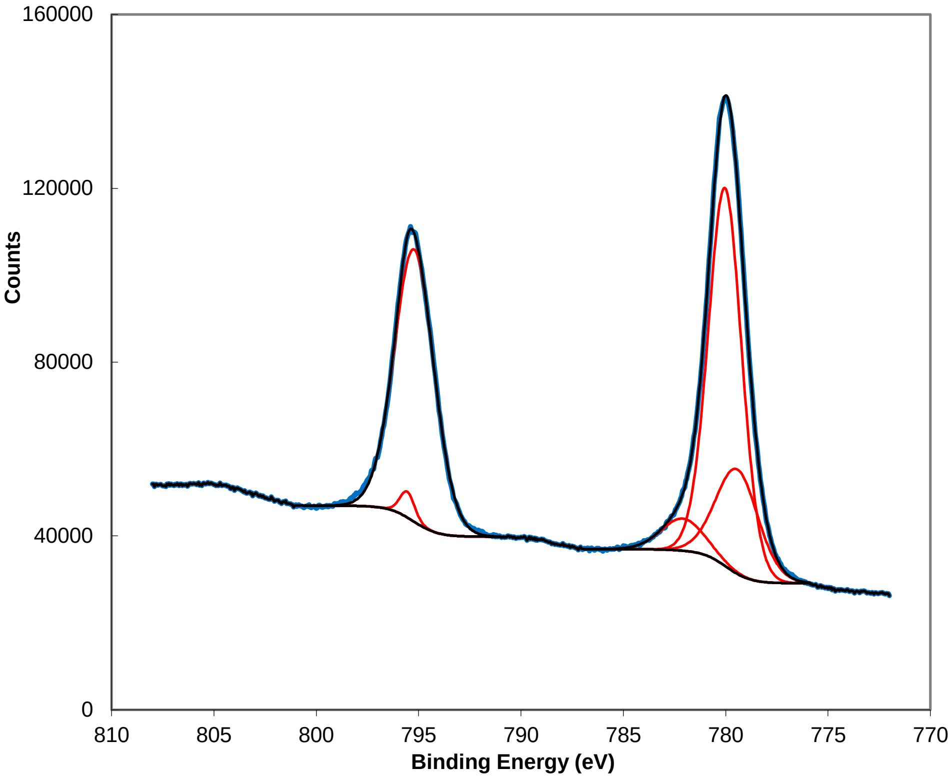

Figure 133 Room temperature XPS scan of Ba and Co region after heating to 500°C

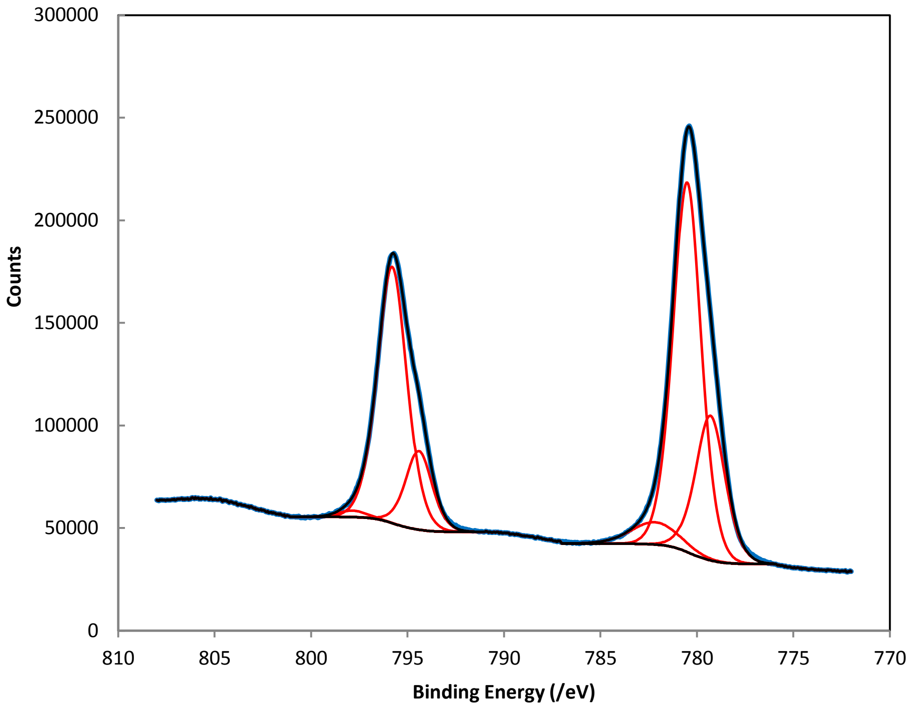

Figure 134 Room temperature XPS scan of Ba and Co region after heating to 800°C

These additional peaks at 779.4 and 795.2eV have been attributed to the presence of a cobalt oxide (Co_3O_4) at the surface.[159] For this compound which contains a mixture of $Co^{3=}$ and Co^{2+} ions, shake up peaks from electrons emitted excited Co^{2+} ions would be expected if indeed Co_3O_4 was present[157, 159]. Their presence was inferred from the difference data in the curve fitting but they were of small size and overlapped with the other peaks. This meant it was not possible to quantify them A comparison of the areas of the 2 Co peaks at 779.4eV (corresponding to Co^{2+} (in Co_3O_4)) and at 780.0eV (corresponding to Co^{3+}) showed that approximately 25% of the cobalt was reduced at high temperature in vacuum

The extra peaks were not found in the sample heated in situ to 300°C when measured after cooling to room temperature. Thus the reduction of the cobalt ions to Co^{2+} only occurred after the heating to the higher temperature of 500°C. This is in accordance with the TGA data which indicates a weight loss starting at around 400°C as described in section 4.5.2.2.

The situation during in situ heating is different to the post heating room temperature results as was shown earlier (Figure 131). The high resolution scans of the Ba and Co region are shown in Figure 135. The broadening of the two peaks can be seen clearly.

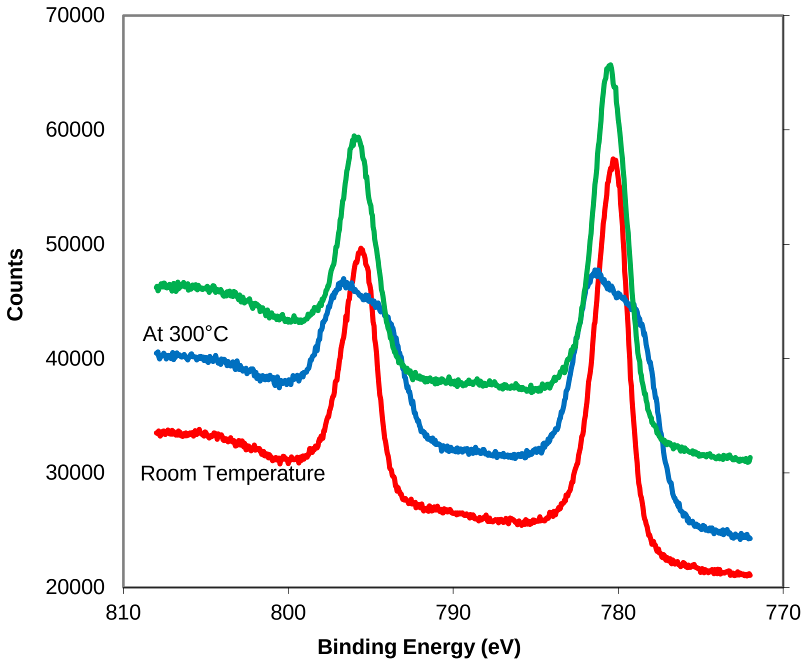

Figure 135 High resolution XPS scan before, during and after heating at 300°C

The scan at 300°C was fitted and the results shown in Figure 136.

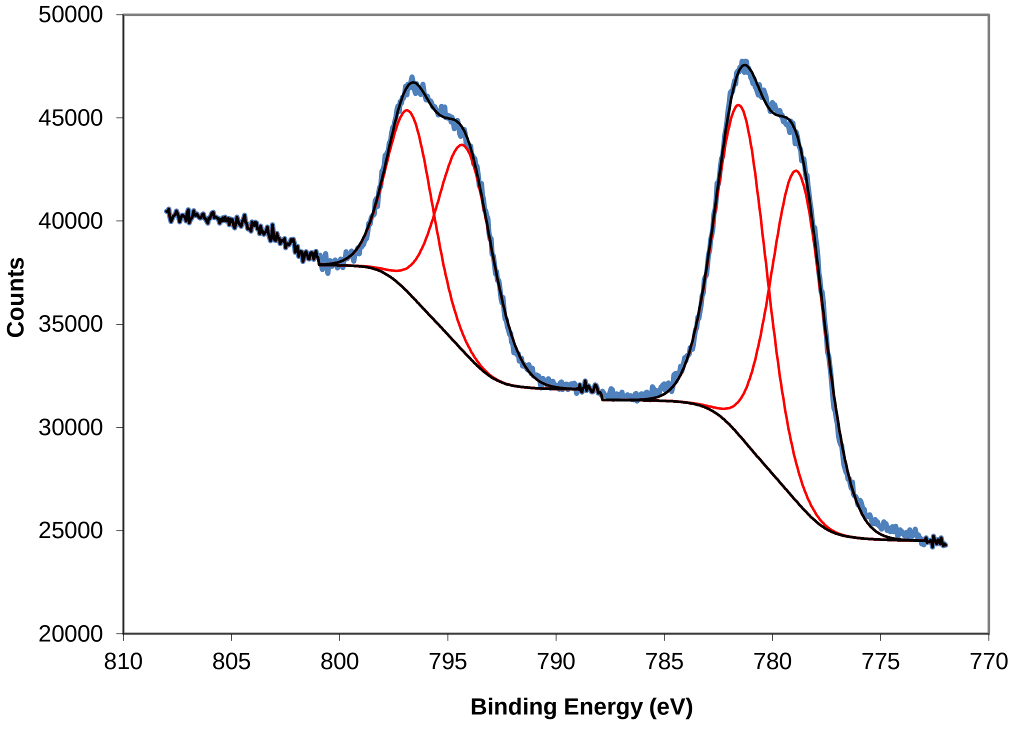

Figure 136 High resolution XPS scan at 300°C

The fitting shows that the broadening has occurred through an increased separation of the overlapping peaks at 781 and 796eV from Ba and Co rather than the appearance of new peaks. The cobalt 2p 1/2 and 2p 3/2 both show lowered binding energy compared with the initial values. A drop of approximately 1.2eV to 794.2 and 778.8eV though the separation at 15,6eV has not changed much from the original at 15.2eV. In contrast the Ba 3d 3/2 and 3d 5/2 peaks both shifted to higher binding energies by about 0.9eV with their separation changed from 15.2 to 15.3eV on heating.

On cooling the peaks returned to their original position. There were no extra peaks found during the fitting process; however the shake up peaks were more noticeable from the difference data. This suggests that there was some reduction of the cobalt to Co^{2+}. This may suggest that the change in cobalt peak position may be due to reduction at temperature.

7.3.5.5 Fe 2p High resolution Scans

It was not possible to fit the Fe 2p data at 710eV due to their small size as can be seen in Figure 137. The Fe 2p 1/2 and 2p 3/2 peaks occur at approximately 719 and 709eV respectively.[159]

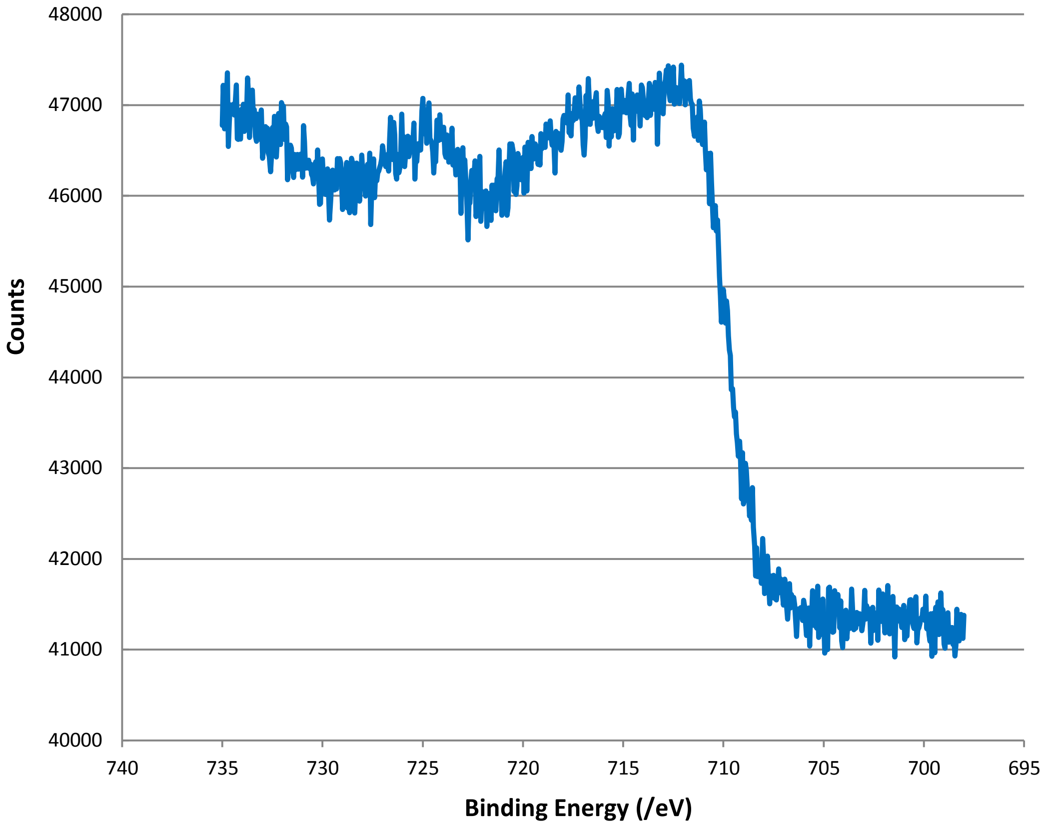

Figure 137 High resolution XPS of Fe 2p region

However as can be seen in Figure 129 and Figure 137 there are changes in the height of the adsorption edge for Fe at around 710eV.The height of this edge was used to estimate the amount of iron present. This was achieved by comparing its height with the height of the Co 3p adsorption edge at 60eV. It was found that the ratio of the heights of the two adsorption edges did not vary under any of the experimental conditions used. It was therefore concluded that there were no significant changes in the Co/Fe ratio as measured.

7.3.5.6 Sr 3p and Sr 3d high resolution XPS scans

The surface Sr was analysed using two sets of peaks, those that correspond to Sr 3p and Sr 3d. The Sr 3p 1/2 and 3p 3/2 peaks at 280 and 269eV respectively were fitted in all cases by a single peak. This suggests that there is no change in the electronic state of the higher binding energy electrons as a result of any of the heat treatments performed in this study. There was a slight shift in the peak position as can be seen in Figure 138.

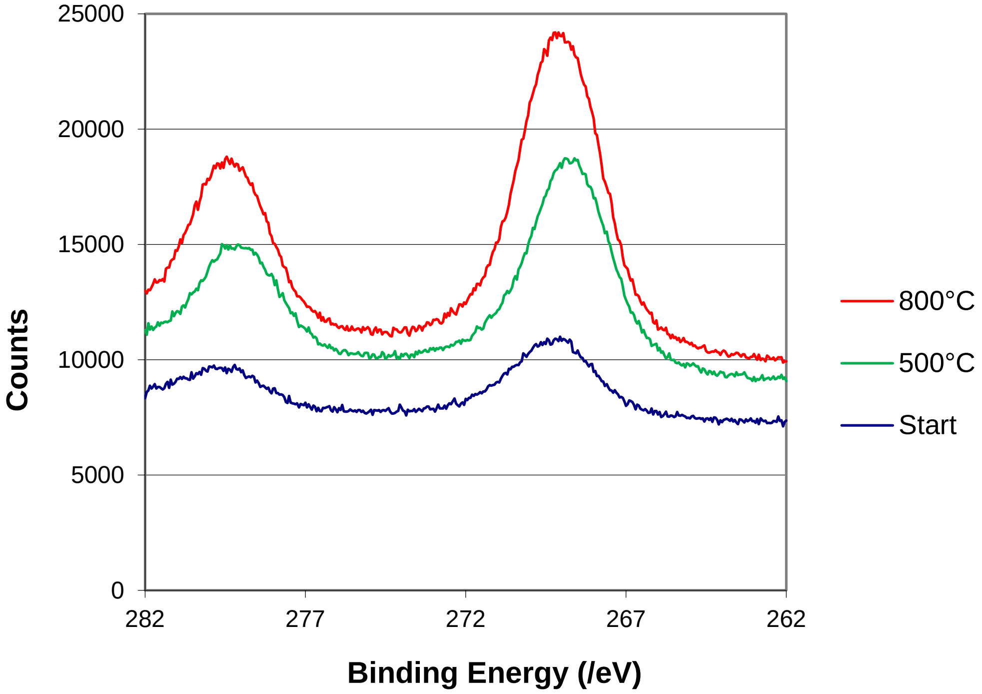

Figure 138 High Resolution XPS Scan of Sr 3p Peaks

The initial scan at room temperature showed a single doublet for the 3d peak at approximately 133eV as shown in Figure 139. This was attributed to a surface Sr-O environment.[160] After heat treatment at 500°C and 800°C a second doublet was fitted to the data as is shown in Figure 140. This has been previously assigned to Sr^{2+}.[160] However by comparing the counts recorded it can be seen that after the 800°C heat treatment the peak count has increased from 5500 to 15000. This three-fold increase is due, as has been noted earlier, to the loss of carbon from the surface. The removal of the surface carbon may allow previously undetected species to become evident as the sensitivity to sub-surface moieties increases.

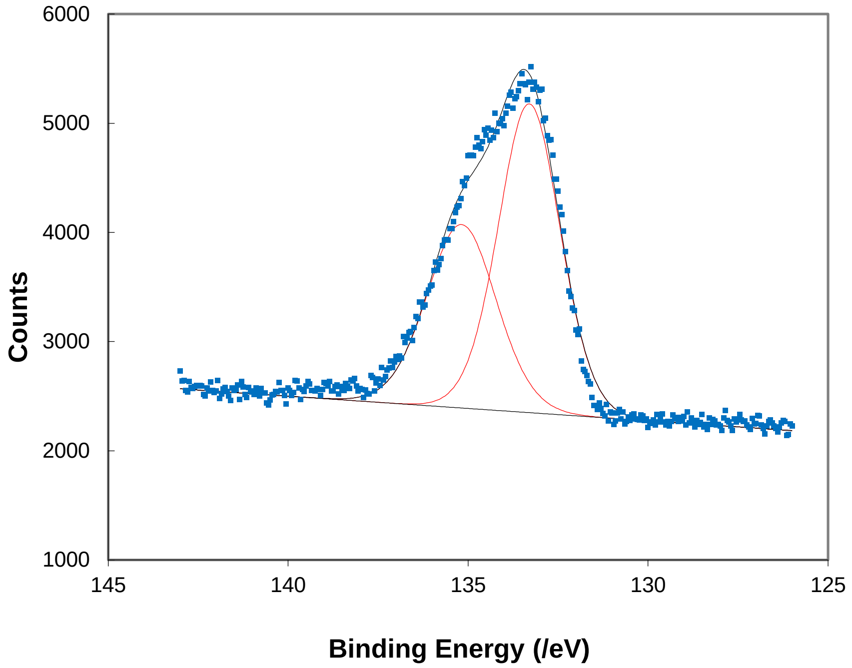

Figure 139 High resolution XPS scan of Sr 3d before heating.

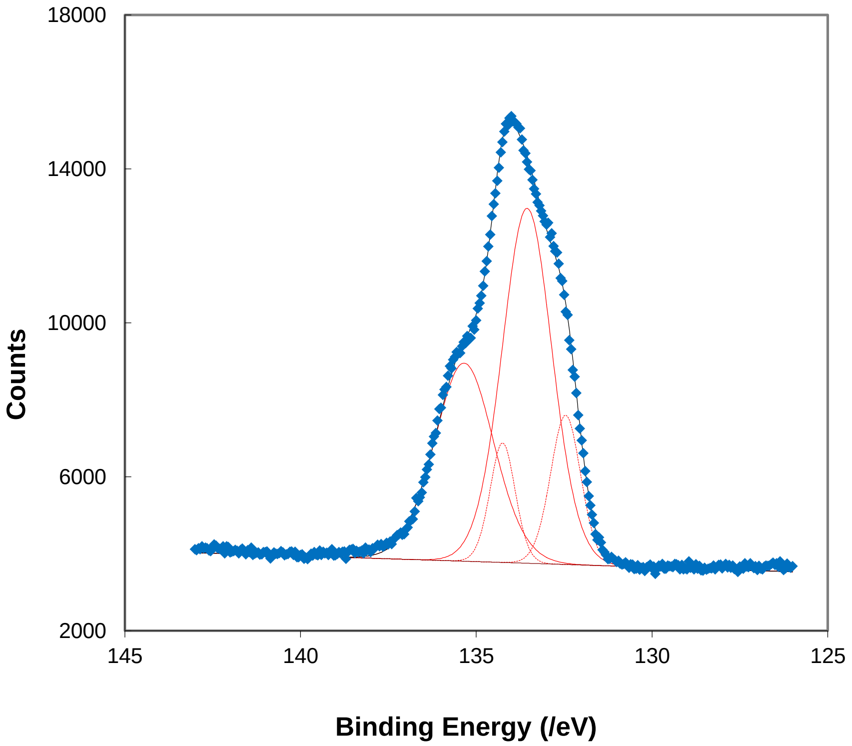

Figure 140 High resolution XPS scan of Sr 3d after heating to 800°C

7.3.5.7 O 1s High Resolution XPS Scans

The oxygen 1s peak appears at approximately 530eV. During the fitting of these peaks it was found to necessary to constrain the FWHM of the component peaks so that they were the same. The reason this was done was that the line width is inversely proportional to the life time of the excited state (see Equation 3.44). The line widths are thus similar for the same element in different environments. The FWHM were all fixed to be the same. Deconvolution of the peak from the initial scan indicated that there were 4 components at 529.4, 531.0, 532.2 and 534.3eV as is shown in Figure 141. These are assigned, according to van der Heide[160], to surface (A-site) – O (529eV), surface (B-site) – O (531eV), surface CO_3^{2-} (532eV) and adsorbed oxygen species (533.2eV).

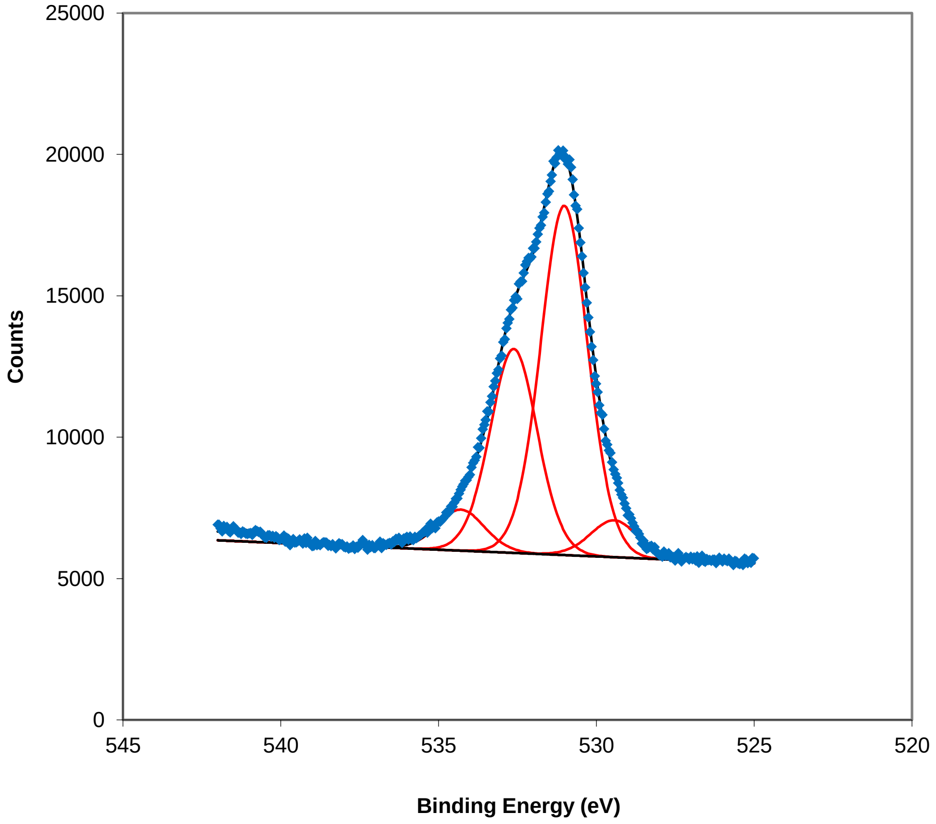

Figure 141 High resolution XPS scan of O 1s before heating

After heat treatment five components were seen as shown in Figure 142. The peak positions were similar to those for the initial room temperature scan (529.2, 530.8, 532.0, and 534.5eV) with the addition of a peak at 533.2eV.

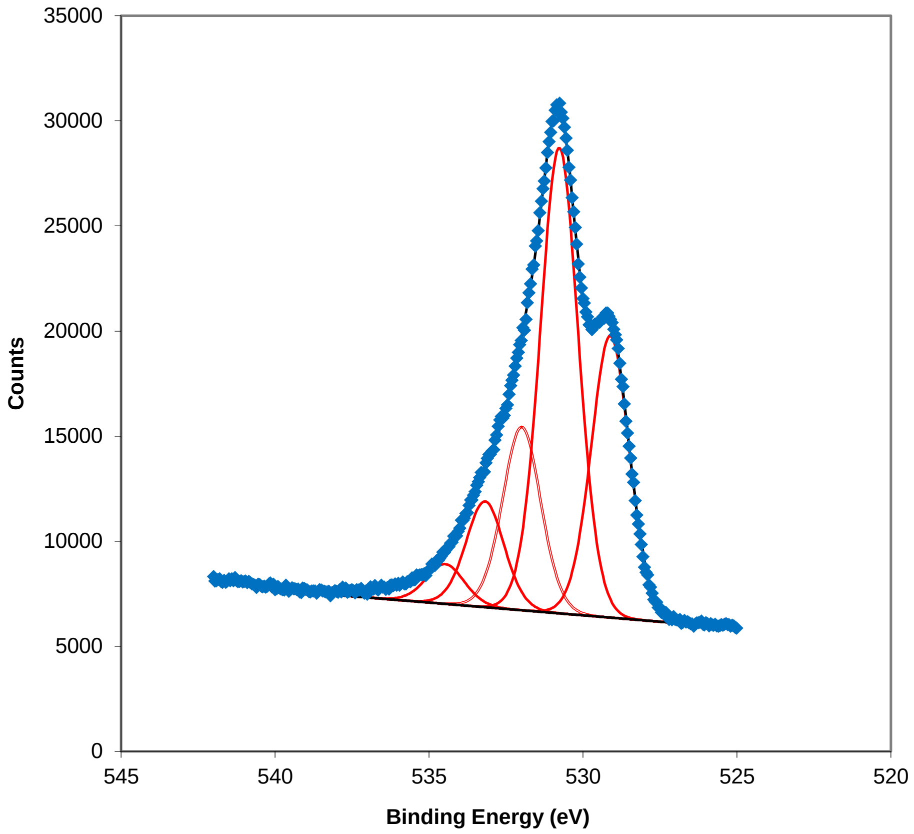

Figure 142 High resolution XPS Scan of O 1s after heating to 500°C

The peak at 534.5eV had not previously been attributed. Other studies[160, 161] have shown that the highest energy peaks are associated with adsorbed oxygen species. Prior to the heat treatment the major species present are surface carbonate and B site – O peaks with minor amounts of A site - O and adsorbed oxygen peaks. After the heat treatment the A site – O peak increased in size and there was a corresponding decrease in surface carbonate.

7.3.5.8 C 1s High Resolution XPS scans

The C 1s scan showed 3 peaks at 285.4, 286.1 and 288.8eV which correspond to two forms of adventitious carbon and carbonate species.[160] These are shown in Figure 143.The accumulation of carbon on surfaces in XPS is a well-known phenomenon.[162] The sources of this adventitious carbon has been ascribed to contamination from the air or vacuum oil which give rise to adsorbed hydrocarbons and graphite-like phases on the surface. These compounds may react at the surface of oxides to form CO and CO_2 which can then form carbon through further reaction.[162]

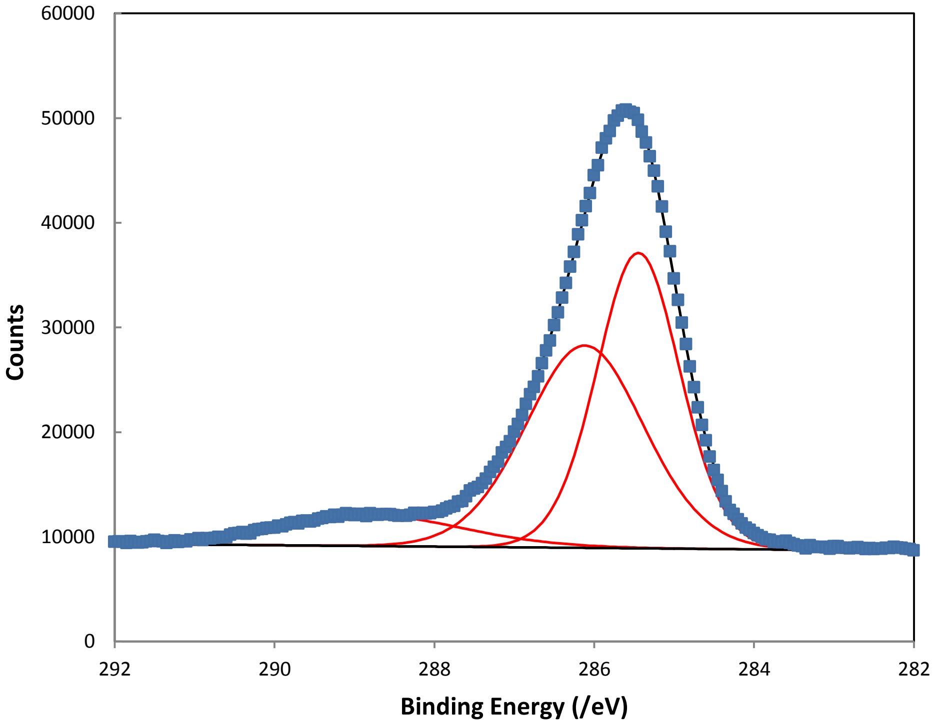

Figure 143 C 1s high resolution XPS scan before heating

Unlike the other species described above after the heat treatments at 500° and 800°C there was a marked decrease in intensity of the carbon peaks as is shown in Figure 144. This is due to the burn off of carbon during heating.

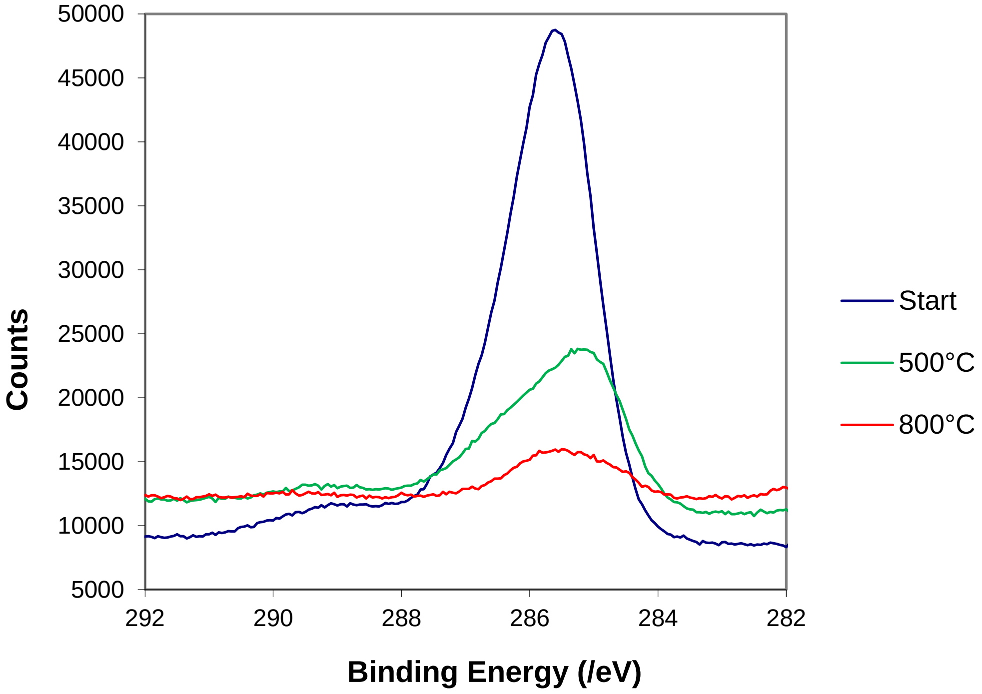

Figure 144 C 1s high resolution XPS scans before and after heating

7.3.5.9 Quantification of Composition

Following the assignment of the peaks in the spectra to the different species present, the elemental compositions of the surfaces were calculated. The CasaXPS software has built in relative sensitivity factors. These factors are tabulated in a number of databases are calculated and measured from the photoelectron yield for pure elements.[128]

The compositional data are shown in Table 56.

	Element %				
Temperature (°C)	Ba	Sr	Co	O	C
RT	1.80	1.76	1.75	25.33	69.36
300	0.23	1.36	5.56	26.46	66.38
500	0.25	5.27	19.57	45.77	29.14
800	12.12	10.01	9.12	58.75	10.00

Table 56 Room temperature elemental composition from XPS

The high concentration of carbon on the surface, and its reduction as a consequence of heating, made comparison of the relative concentrations of the elements difficult. The trends were hard to discern. Therefore the data was normalised with respect to the cobalt concentration. The cobalt concentration was set at 0.8 which corresponds to its concentration in the ceramic pellet. As the Co/Fe ratio from the adsorption edge measurements was constant then it was inferred that there was little relative mobility of the B-site cations. This does not imply that there was no movement of B-site cations but allows a convenient method for comparison of the data. Also implied is that there was no relative movement of the Fe and Co ions in the material. The normalised data is shown in Table 57

	Element %				
Temperature (°C)	Ba	Sr	Co	O	C
RT	0.82	0.81	0.80	11.60	31.75
300	0.03	0.20	0.80	3.81	9.55
500	0.01	0.22	0.80	1.87	1.19
800	1.06	0.88	0.80	5.15	0.88

Table 57 Room temperature elemental composition from XPS after normalisation

From the normalised data shown in Table 57, the initial Ba and Sr ion concentrations were similar to each other but a higher level (0.82 and 0.81 respectively) than was expected from their bulk concentration of 0.5. They are therefore slightly enriched on the surface relative to the Co ions.

On heating the samples to 300°C and 500°C there is a significant change in the two A-site ions' concentrations relative to the Co Concentration. They have both decreased in concentration with the Ba ions almost disappearing. However on further heating to 800°C the surface concentrations are restored to values comparable to the starting concentrations.

This behaviour is in agreement with other studies on similar systems who found during the reduction of the mixed oxide $La_{0.6}Sr_{0.4}CoO_3$, a relative decrease in the surface concentration of the A-site cations.[160] This decrease in surface A-site cations after intermediate temperature range heating may be caused by an increased mobility with the loss of carbonate from the surface and consequent migration into the bulk. This process is reversed at higher temperatures to return to the initial surface concentration. There is also the possibility that in addition to the cation diffusion processes surface relaxation and reconstruction occurs which may also contribute to the surface changes. It was noted earlier during the high temperature X-ray diffraction that the lattice parameter does not change much at 800°C relative to its value at 750°C. This was associated with the formation of secondary phases in addition to the cubic phase initially present. (Figure 128). After 300°C heating some CoO phase can be seen in the x-ray Diffractogram as shown in Figure 145.

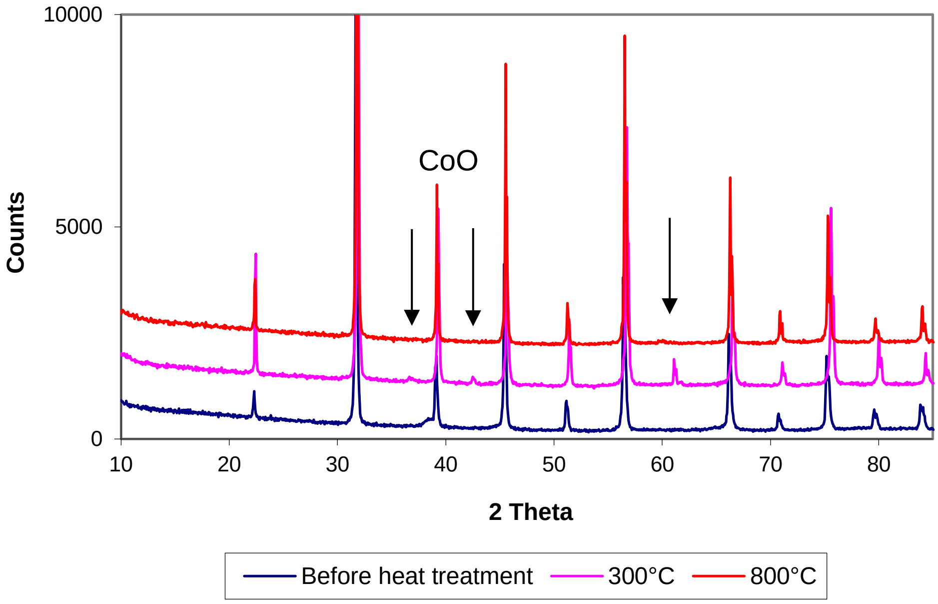

Figure 145 X-ray diffractogram of samples before and after heating

The sample which was heated to 800°C, however only showed a single phase. The differences, between the high temperature x-ray diffraction and the XPS studies, include a longer time at temperature and air atmosphere for the XRD and vacuum for the XPS.

The CoO formed after heating to 300°C in vacuum is not just a surface feature as glancing angle x-ray diffraction showed no significant difference in peak areas when compared with conventional x-ray diffraction as shown in Figure 146. The data has been normalised so that the main peak heights for both traces are the same.

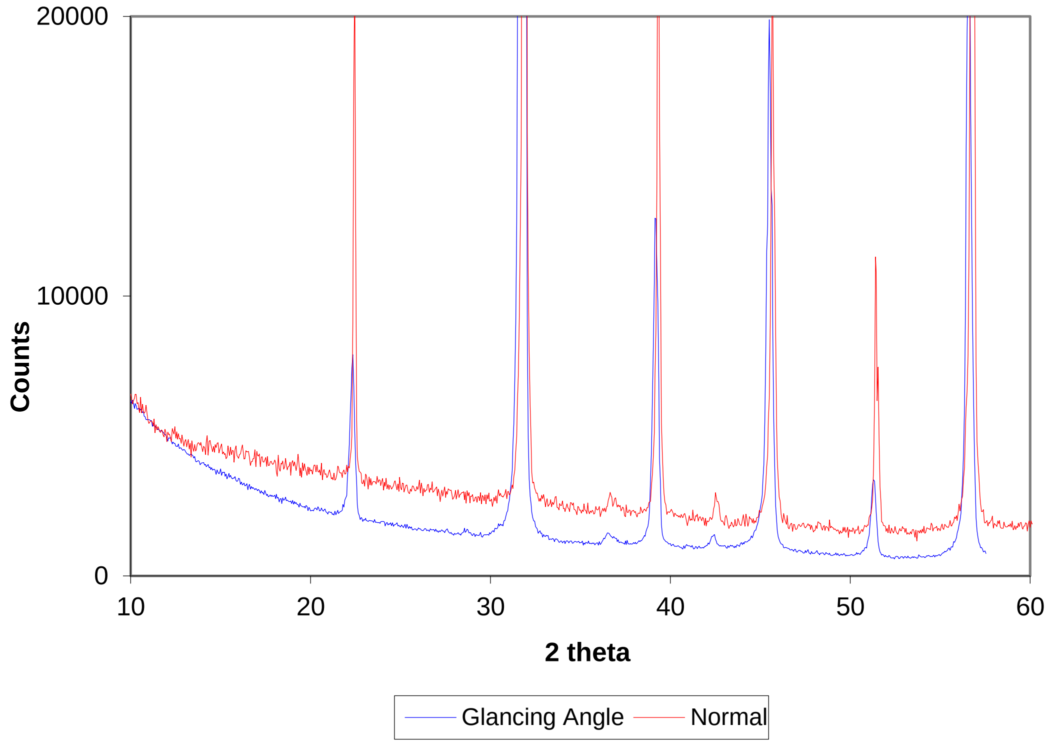

Figure 146 X-ray diffractogram of sample after 300°C heating

The oxygen ratio to cobalt also changed as a result of the heat treatments. Following the iodometric titrations described earlier (Table 12) a value for the oxygen concentration of 2.65 would be expected. This corresponds to a δ value of 0.35. Initially a much higher oxygen concentration is present which decreases to 1.87 on heating up to 500°C and then increases to a final value of 5.15 after the 800°C treatment. As has been described earlier (section 7.3.5.7), a number of different oxygen species were identified during the curve fitting. The proportions of these species as a function of heat treatment were calculated with the two adsorbed oxygen peaks at high energy being combined. The results are shown in Table 58 and Figure 147.

Oxygen Species	Heat Treatment				
	None	300	500	800	after 48 hours in air
B site-O	55.3	46.0	43.6	53.7	48.2
CO_3^{2-}	32.3	23.2	15.0	12.4	29.8
A site-O	5.8	17.9	26.4	31.5	12.9
Adsorbed O	6.5	12.9	15.0	2.4	9.2

Table 58 Variation of oxygen species with heat treatment

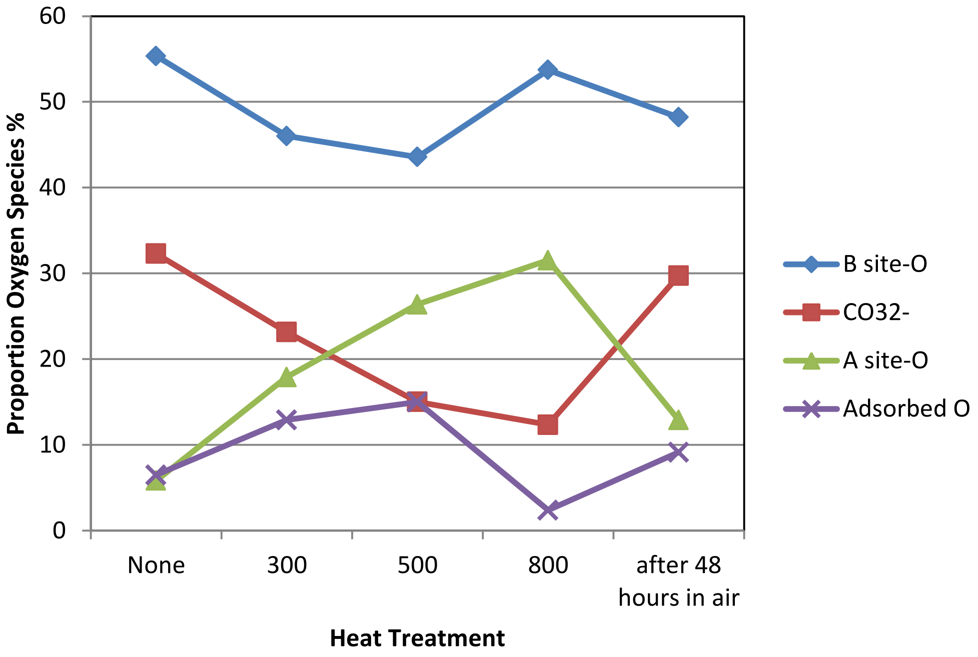

Figure 147 Variation of oxygen species with heat treatment

The initial proportions of the oxygen surface species is 55% as B-site – oxygen, 32% as carbonate oxygen and 6% as A-site – oxygen with the remaining oxygen as adsorbed species. On heating the sample the carbonate – oxygen species reduces to 12% of the total after 800°C heat treatment. There is a corresponding increase in the A-site oxygen species. The adsorbed oxygen also decreases after the highest temperature treatment. These results are in line with the changes in the cation concentrations as discussed earlier, in that the A-site cations are associated with surface carbonates. The A-site oxygen proportion increases from 6 to 32% on heat treatment. After exposing the sample to the air for 48 hours the adsorbed oxygen and carbonate species both increased in proportion whereas the A-site oxygen proportion decreased.

7.4 Discussion and Conclusions

The high temperature x-ray diffraction showed that on heating to 450°C there is a gradual expansion of the lattice parameter with a thermal expansion coefficient of $13.4\text{x}10^{-6}$ K^{-1}. Above this temperature the thermal expansion coefficient increases to $22.9\text{x}10^{-6}$ K^{-1}. These values are in line with the literature if the appropriate temperature ranges are taken into account[30, 104, 105]. The fitting in the literature does not always use two ranges. This increase in thermal expansion is due to the onset of oxygen loss (chemical expansion[30]) from the structure making the value of δ increase. On cooling the cubic phase disproportionates into a number of different phases and adsorbs carbon dioxide from the air to form alkaline earth carbonates.

The x-ray photoelectron spectroscopy showed that the surface composition of BSCF changed during the heating processes. At intermediate temperatures the cobalt (and iron) was concentrated at the surface relative to the barium and strontium. At higher temperatures the barium and strontium returned to levels slightly higher than at the start of the heat treatment. In addition the carbonate content of the surface decreased during heating with a consequent increase in the A site – O oxygen.

In contrast to the high temperature x-ray diffraction results there was little change in the x-ray pattern in the samples after XPS. There was only a small amount of CoO detected. This phase was identified by Muller et al[155] as being present in their ceramics after heat treatment and cooling although they used much longer annealing times at temperature 100hrs compared with this works 30mins. The main difference between the HTXRD and XPS heat treatments was the atmosphere. The former was carried out in ambient air whereas the latter was at either ~$2x10^{-5}$ or ~$5x10^{-9}$ torr. Changes in the value of δ during the experiments could not be measured, although the results from section 4.5.1.2 show that a change of value approximately equal to 0.1 could be expected on heating to 800°C. It would be higher in the vacuum present in the XPS. Increases in δ result in an increase in the oxygen vacancies which allows easier movement of the oxygen. This can promote the formation of the new phases. Also the carbon dioxide concentration would be lower which could not react to form carbonates on cooling.

The decomposition of BSCF at high temperature in air would be enhanced by the presence of carbon dioxide[163, 164]. As shown in the XPS at 800°C there is a surface enrichment of barium and strontium. This leads to the decomposition of the cubic phase into the hexagonal phase. It has been shown that during oxygen permeation experiments at 875°C with carbon dioxide in the sweep gas that the surface layer on the sweep gas side becomes depleted in iron and cobalt[67]. This behaviour is reversed when the carbon dioxide is removed from the sweep gas. Thus in the presence of carbon dioxide the barium and strontium become surface enriched. However in the XPS experiment the surface enrichment of barium and strontium only occurs when there was a significant carbonate concentration on the surface. This confirms the necessity of carbon dioxide to obtain surface enrichment. There was no reaction on the feed side of the system[67]. The alkaline earth enriched surface can therefore react with atmospheric carbon dioxide which is readily adsorbed by the BSCF at room temperature (see Figure 147). The presence of this surface carbonate can then further catalyse the decomposition of the single phase into the multi-phase assemblage. As shown in Figure 46 the loss of carbon dioxide from the dried powders is not complete until 830°C, thus at the highest temperatures used in these XRD and XPS studies carbonates are present on the surface, though not visible using XRD.

During the heat treatment of BSCF ceramic pellets the surface composition changes in terms of the relative amount of the A site and B site cations present. During heating there were no noticeable phase changes up to 700°C, thereafter some decomposition occurred in air though not vacuum. On cooling the air cooled sample showed decomposition into a number of different phases. Whereas the vacuum treated sample showed a small amount of CoO formation. The presence of carbon dioxide can affect the decomposition of the BSCF material.

8 Conclusions

An inorganic synthetic route was developed for the formation of single phase barium strontium cobalt iron oxide mixed ionic electronic conductors without the use of organic reagents. This was based on a reverse precipitation route and used sodium carbonate as the precipitant to ensure complete precipitation of all components. The use of reverse precipitation in which the acidic mixed salt solution was added into the excess alkaline precipitant ensured that all the metals were precipitated immediately and not sequentially.

The precipitation did not give a single phase in the dried and calcined powders but they were of such small crystallite size that they reacted readily on sintering to form a single phase on sintering. A common reaction pathway was found with minor changes as a result of hydrothermal treatment at high and low pH.

The process was thus robust in that the changes in the experimental parameters (pH and hydrothermal treatment) gave similar ceramic pellets. The incorporation of copper was also accomplished without any changes to the experimental process. The addition of copper caused a significant difference in the results in that after calcination the resulting powder was mainly the desired cubic phase with a smaller amount of a mixed barium strontium carbonate. The other difference with the copper doped samples in the formation of the ceramic pellets was higher grain growth during sintering. Only at the lowest addition level copper was found to be beneficial in promoting oxygen permeation.

The oxygen permeability of the ceramics was measured and was found to be dependent on three factors the lattice parameter of the ceramic, the tolerance factor for the crystal structure and the oxygen non-stoichiometry (δ). Together they gave a good indicator of the oxygen flux as long as the rate determining step in the oxygen permeation was the same. The larger lattice parameters were better as they allowed oxygen ions to pass from one site to another with less restriction as the interatomic distances were bigger. The tolerance factor was important as it indicated the stability of the crystal structure. The oxygen non-stoichiometry indicated an upper limit for good oxygen transfer as when $\delta \geq 0.5$, the vacancies could then start to order and additionally there were fewer variations in the B site oxidation state and thus less electronic transfer.

One of the objectives of this study was to relate the electrical properties of the ceramic to the oxygen permeation. The electrical properties did not match exactly the oxygen permeation behaviour but varied with a similar dependence on the three factors. They are both functions of lattice parameter, tolerance factor and oxygen non-stoichiometry. There was a distinct change in resistance when the value of δ was close to or greater than 0.5, which corresponded to the net oxidation state on the B site cations being 3+ and there therefore being no transfer between cations of different oxidation state.

The lack of correlation between the activation energies of the resistance and oxygen permeation dependence indicated that the electrical measurements were not measuring the critical stage of the multi-step oxygen permeation process. The two critical steps were different for the mainly electronic conduction and the oxygen permeation. The use of blocking electrodes together with a better estimation of the transition metal oxidation states would allow further understanding of the relationship between changes in electrical properties and oxygen permeation to be made.

The results from BSCF 5582 of the thermogravimetric analysis on cooling together with the high temperature x-ray diffraction showed that oxygen was reversibly lost from 400°C continuously up to 1100°C (maximum temperature used). The onset of oxygen loss was marked in the diffraction experiments by an increase in the thermal expansion coefficient on heating. On slow cooling there was decomposition into a mixture of other phases both simple oxides and mixed perovskite-like orthorhombic and hexagonal structures.

The surface composition was measured using high temperature x-ray photoelectron spectroscopy and showed that during heating and cooling there was migration of the alkaline earth ions from the surface at intermediate temperatures with a return at high temperature. The oxygen spectra showed behaviour which indicated the loss of surface carbonates from (Ba,Sr)CO_3 on heating which accompanied the initial loss of barium and strontium from the surface.

The changes seen in surface composition using x-ray photoelectron spectroscopy have shown that the removal of carbonate from the surface at high temperatures is necessary to have a “clean” surface. The absorption of carbon dioxide by the sample under ambient conditions showed the facile uptake of carbon dioxide. Therefore care needs to be taken to ensure that carbonate is removed from the surface prior to starting any experiment on permeation. However on heating to high temperature and then cooling (as done in this work) may allow the BSCF materials to transform from the cubic phase.

9 Further Work

1. Compare electrical measurements with and without the use of blocking electrodes.
2. In order to clarify the phase development during powder formation, synthesise the end members of the series containing only one A site and one B site cation.
3. Investigate the use of slower heating rates during sintering to improve densification by preventing pore breakaway
4. Investigate high temperature XRD with controlled atmospheres at well-defined oxygen partial pressures with and without carbon dioxide present.
5. Examine more compositions using XPS to determine the variation of surface chemistry with composition.

10 References

1. Kneer, R. et al. OXYCOAL-AC: Towards an integrated coal-fired power plant process with ion transport membrane-based oxygen supply. *Energy Environ Sci* **3**, 196-207 (2010).
2. Repasky, J.M., Anderson, L.L., Stein, V.E., Armstong, P.A. & Foster, E.P. in International Pittsburgh Coal Conference 2012 (Air Products and Chemicals Inc, Pittsburgh USA, 2012).
3. Smith, A.R. & Klosek, J. A review of air separation technologies and their integration with energy conversion processes. *Fuel Processing Technology* **70**, 115-134 (2001).
4. Hashim, S.S., Mohamed, A.R. & Bhatia, S. Oxygen separation from air using ceramic-based membrane technology for sustainable fuel production and power generation. *Renewable and Sustainable Energy Reviews* **15**, 1284 (2011).
5. Geffroy, P.M., Fouletier, J., Richet, N. & Chartier, T. Rational selection of MIEC materials in energy production processes. *Chemical Engineering Science* **87**, 408-433 (2013).
6. Moulson, A.J. & Herbert, J.M. Electroceramics (Wiley, 2003).
7. Sunarso, J. et al. Mixed ionic-electronic conducting (MIEC) ceramic-based membranes for oxygen separation. *J Membrane Science* **320**, 13-41 (2008).
8. Faraji, S., Nordheden, K.J. & Stagg-Williams, S.M. A comparative study of $Ba_{0.5}Sr_{0.5}Co_{0.8}Fe_{0.2}O_x$ (BSCF) and $SrFeCo_{0.5}O_x$ (SFC) ceramic membranes used for syngas production. *Applied Catalysis B: Environmental* **99**, 118 (2010).
9. Jiang, H. et al. Hydrogen Production by Water Dissociation in Surface-Modified $BaCo_xFe_yZr_{1-x-y}O_{3-\delta}$ Hollow-Fiber Membrane Reactor with Improved Oxygen Permeation. *Chemistry – A European Journal* **16**, 7898 (2010).
10. Shao, Z. et al. Investigation of the permeation behaviour and stability of a $Ba_{0.5}Sr_{0.5}Co_{0.8}Fe_{0.2}O_{3-\delta}$ oxygen membrane. *J Membrane Science* **172**, 177-188 (2000).
11. Shao, Z., Xiong, G., Tong, J., Dong, H. & Yang, W. Ba effect in doped $Sr(Co_{0.8}Fe_{0.2})O_{3-\delta}$ on the phase structure and oxygen permeation properties of the dense ceramic membranes. *Sep. Purif. Technol* **25**, 419-429 (2001).
12. Emsley, J. in Nature's Building Blocks: An A-Z Guide to the Elements (Oxford University Press, 2001).
13. Burdyny, T. & Struchtrup, H. Hybrid membrane/cryogenic separation of oxygen from air for use in the oxy-fuel process. *Energy* **35**, 1884 (2010).
14. Colombo, K.E., Kharton, V.V. & Bolland, O. Simulation of an Oxygen Membrane-Based Gas turbine power Plant: Dynamic Regimes with Operational and Material Constraints. *Energy Fuels* **24**, 590-608 (2010).
15. Dyer, P.N., Richards, R.E., Russek, S.L. & Taylor, D.M. Ion transport membrane technology for oxygen separation and syngas production. *Solid State Ionics* **134**, 21-33 (2000).

16. He, Y., Zhu, X., Li, Q. & Yang, W. Perovskite Oxide Absorbents for Oxygen Separation. *AIChE Journal* **55**, 3125-3133 (2009).
17. Zhu, X., Sun, S., He, Y., Cong, Y. & Yang, W. New concept on air separation. *J Membrane Science* **323**, 221.224 (2008).
18. http://www.vattenfall.com/en/ccs/oxyfuel-combustion.htm. (Accessed August 2013).
19. http://www.vattenfall.com/en/ccs/precombustion.htm. (Accessed August 2013).
20. Bouwmeester, H.J.M. Dense ceramic membranes for methane conversion *Catalysis Today* **82**, 141-150 (2003).
21. Park, C.Y., Lee, T.H., Dorris, S.E. & Balachandran, U. Hydrogen production from fossil and renewable sources using an oxygen transport membrane. *International Journal of Hydrogen Energy* **35**, 4103 (2010).
22. Balachandran, U., Lee, T.H., Wang, S. & Dorris, S.E. Use of mixed conducting membranes to produce hydrogen by water dissociation. *Int J Hydrogen Energy* **29**, 291-296 (2004).
23. Zhou, W., Ran, R. & Shao, Z. Progress in understanding and development of $Ba_{0.5}S_{r0.5}Co_{0.8}Fe_{0.2}O_{3-\delta}$ based cathodes for intermediate-temperature solid-oxide fuel cells: A review. *Journal of Power Sources* **192**, 231 (2009).
24. Goldscmidt, V.M. Die Gesetze der Krystallochemie. *Die Naturwissenschaften* **21**, 477-485 (1926).
25. Wells, A.F. in Structural Inorganic Chemistry 584 (Oxford, 1984).
26. Le Toquin, R., Paulus, W., Cousson, A., Prestipino, C. & Lamberti, C. Time-resolved in Situ Studies of Oxygen Intercalation into $SrCoO_{2.5}$, Performed by Neutron Diffraction and X-ray Absorption Spectroscopy. *J Am Chem Soc* **128**, 13161-13174 (2006).
27. de la Calle, C., Alonso, J.A., Aguadero, A. & Fernandez-Diaz, M.T. Phase transformations in $Sr_{0.8}Ba_{0.2}CoO_{2.5}$ brownmillerite: correlation between structure and transport properties. *Dalton Transactions*, 4104 (2009).
28. Itoh, T. et al. Study of charge density and crystal structure of $(La_{0.75}Sr_{0.25})MnO_{3.00}$ and $(Ba_{0.5}Sr_{0.5})(Co_{0.8}Fe_{0.2})O_{2.33-\delta}$ at 500-900 K by in situ synchrotron X-ray diffraction. *Journal Of Alloys And Compounds* **491**, 527-535 (2010).
29. Ganopadhyay, S. et al. Understanding oxygen vacancy migration and clustering in barium strontium cobalt iron oxide. *Solid State Ionics* **181**, 1067 (2010).
30. McIntosh, S., Vente, J.F., Haije, W.G., Blank, D.H.A. & Bouwmeester, H.J.M. Oxygen stoichiometry and chemical expansion of $Ba_{0.5}Sr_{0.5}Co_{0.8}Fe_{0.2}O_{3-\delta}$ measured by in situ neutron diffraction. *Chemistry of Materials* **18**, 2187 (2006).
31. Vashook, V.V. et al. Oxygen non-stoichiometry and electrical conductivity of the binary strontium cobalt oxide SrCoOx. *Solid State Ionics* **99**, 23-32 (1997).
32. Teraoka, Y., Nobunaga, T., Miura, N. & Yamazoe, N. Influence of constituent metal cations in substituted $LaCoO_3$ on mixed conductivity and oxygen permeability. *Solid State Ionics* **48**, 207-212 (1991).

33. Teraoka, Y., Nobunaga, T. & yamazoe, N. Effect of cation substitution on the oxygen semipermeability of perovskite-type oxides. *Chem Lett*, 503-506 (1988).
34. Svarcova, S., Wiik, K., Tolchard, J., Bouwmeester, H.J.M. & Grande, T. Structural instability of cubic perovskite $Ba_xSr_xSr_{1-x}Co_{1-y}Fe_yO_{3-\delta}$. *Solid State Ionics* **178**, 1787-1791 (2008).
35. Kharton, V.V. et al. Perovskite-type oxides for high-temperature oxygen separation membranes. *J Membrane Science* **163**, 307-317 (1999).
36. Ishihara, T. et al. La (Sr) Ga (Fe) O_3 Perovskite Oxide as a New Mixed Ionic-Electronic Conductor for Oxygen Permeating Membrane. *Journal Of The Electrochemical Society* **150**, E17-E23 (2003).
37. Chen, W., Zuo, Y.B., Chen, C.S. & Winnubst, A.J.A. Effect of Zr^{4+} doping on the oxygen stoichiometry and phase stability of $SrCo_{0.8}Fe_{0.2}O_{3-\delta}$ oxygen separation membrane. *Solid State Ionics* **181**, 971 (2010).
38. Liang, F. B-site La-doped $BaFe_{0.95-x}La_xZr_{0.05}O_{3-\delta}$ perovskite-type membranes for oxygen separation. *J Mater Chem A* **1**, 746-751 (2013).
39. Shao, Z., Zhou, W. & Zhu, Z. Advanced synthesis of materials for intermediate-temperature solid oxide fuel cells. *Progress in Materials Science* **57**, 804-874 (2012).
40. Pechini. (US 3,330,697, 1967).
41. Ring, T.A. Fundamentals of Ceramic Powder Processing and Synthesis (Academic Press, 1996).
42. Patra, H., Rout, S.K., Pratihar, S.K. & Bhattacharya, S. Effect of process parameters on combined EDTA-citrate synthesis of $Ba_{0.5}Sr_{0.5}Co_{0.8}Fe_{0.2}O_{3-\delta}$ perovskite. *Powder Technology* **209**, 98 (2011).
43. Baumann, F.S., Fleig, J., Habermeier, H.U. & Maier, J. $Ba_{0.5}Sr_{0.5}Co_{0.8}Fe_{0.2}O_{3-\delta}$ thin film microelectrodes investigated by impedance spectroscopy. *Solid State Ionics* **177**, 3187-3191 (2006).
44. Bi, L., Fabbri, E. & Traversa, E. Novel $Ba_{0.5}Sr_{0.5}(Co_{0.8}Fe_{0.2})_{1-x}Ti_xO_{3-\delta}$(x=0, 0.05, and 0.1) cathode materials for proton-conducting solid oxide fuel cells. *Solid State Ionics* **214**, 1 (2012).
45. Moharil, S.V., Nagrare, B.S. & Shaikh, S.P.S. Nanostructured MIEC $Ba_{0.5}Sr_{0.5}Co_{0.6}Fe_{0.4}O_{3-\delta}$ (BSCF5564) cathode for IT-SOFC by nitric acid aided EDTA-citric acid complexing process (NECC). *International Journal of Hydrogen Energy* **37**, 5208 (2012).
46. Zhao, Z. et al. Carbonates formed during BSCF preparation and their effects on performance of SOFCs with BSCF cathode. *International Journal Of Hydrogen Energy* **37**, 19036-19044 (2012).
47. Feldhoff, A., Martynczuk, J. & Wang, H. Advanced $Ba_{0.5}Sr_{0.5}Zn_{0.2}Fe_{0.8}O_{3-\delta}$ perovskite-type ceramics as oxygen selective membranes: Evaluation of the synthetic process. *Progress In Solid State Chemistry* **35**, 339-353 (2007).

48. Babakhani, E.G., Towfighi, J. & Nazari, K. Synthesis of BSCFO Ceramics Membrane Using a Simple Complexing Method and Experimental Study of Sintering Parameters. *Journal of Materials Science & Technology* **26**, 914-920 (2010).
49. Pelosato, R. et al. Co-precipitation in aqueous medium of $La_{0.8}Sr_{0.2}Ga_{0.8}Mg_{0.2}O_{3-\delta}$ via inorganic precursors. *Journal Of Power Sources* **195**, 8116-8123 (2010).
50. Pelosato, R. et al. Co-precipitation synthesis of SOFC electrode materials. *International Journal Of Hydrogen Energy* **38**, 480-491 (2013).
51. Toprak, M.S., Darab, M., Syvertsen, G.E. & Muhammed, M. Synthesis of nanostructured BSCF by oxalate co-precipitation – As potential cathode material for solid oxide fuels cells. *International Journal Of Hydrogen Energy* **35**, 9448-9454 (2010).
52. Puigdomenech, I. Chemical Equilibrium Software MEDUSA and Data Base HYDRA, http://www.kemi.kth.se/medusa/.
53. Lupo, F. et al. Hydrothermal crystallisation of doped zirconia: An in situ X-ray diffraction study *Phys Chem. Chem. Phys* **6**, 1837-1841 (2004).
54. Arnold, M., Gesing, T.M., Martynczuk, J. & Feldhoff, A. Correlation of the formation and the decomposition process of the BSCF perovskite at intermediate temperatures. *Chemistry Of Materials* **20**, 5851-5858 (2008).
55. Martynczuk, J., Arnold, M., Wang, H., Caro, J. & Feldhoff, A. How $(Ba_{0.5}Sr_{0.5})(Fe_{0.8}Zn_{0.2})O_{3-\delta}$ and $(Ba_{0.5}Sr_{0.5})(Co_{0.8}Fe_{0.2})O_{3-\delta}$ Perovskites Form via an EDTA/Citric Acid Complexing Method. *Adv Mater* **19**, 2134-2140 (2007).
56. Baumann, S. et al. Influence of sintering conditions on microstructure and oxygen permeation of $Ba_{0.5}Sr_{0.5}Co_{0.8}Fe_{0.2}O_{3-\delta}$ (BSCF) oxygen transport membranes. *Journal of Membrane Science* **359**, 102 (2010).
57. Girdauskaite, E. et al. Oxygen transport properties of $Ba_{0.5}Sr_{0.5}Co_{0.8}Fe_{0.2}O_{3-x}$ and $Ca_{0.5}Sr_{0.5}Mn_{0.8}Fe_{0.2}O_{3-x}$ obtained from permeation and conductivity relaxation experiments. *Solid State Ionics* **179**, 385-392 (2008).
58. Leo, A., Liu, S. & Diniz da Costa, J.C. The enhancement of oxygen flux on $Ba_{0.5}Sr_{0.5}Co_{0.8}Fe_{0.2}O_{3-\delta}$ (BSCF) hollow fibers using silver surface modification. *Journal of Membrane Science* **340**, 148 (2009).
59. Hong, W.K. & Choi, G.M. Oxygen permeation of BSCF membrane with varying thickness and surface coating. *Journal Of Membrane Science* **346**, 353-360 (2010).
60. Bouwmeester, H.J.M., Kruidhof, H. & Burggraaf, A.J. Importance of the surface exchange kinetics as rate limiting step in oxygen permeation through mixed-conducting oxides. *Solid State Ionics* **72**, 185 (1994).
61. Wang, L., Merkle, R. & Maier, J. Surface kinetics and mechanism of oxygen incorporation into $Ba_{1-x}Sr_xCo_yFe_{1-y}O_{3-\delta}$ SOFC microelectrodes. *Journal of the Electrochemical Society* **157** (2010).

62. Guo, Y. Electrochemical contribution of silver current collector to oxygen reduction reaction over $Ba_{0.5}Sr_{0.5}Co_{0.8}Fe_{0.2}O_{3-\delta}$ electrode on oxygen-ionic conducting electrolyte. *International Journal Of Hydrogen Energy* **37**, 14492-14500 (2012).
63. Harvey, A.S. et al. Oxidation states of Co and Fe in $Ba_{1-x}Sr_xCo_{1-y}Fe_yO_{3-\delta}$ (x, y = 0.2-0.8) and oxygen desorption in the temperature range 300-1273 K. *Physical Chemistry Chemical Physics* **11**, 3090 (2009).
64. Chen, Z., Ran, R., Zhou, W., Shao, Z. & Liu, S. Assessment of $Ba_{0.5}Sr_{0.5}Co_{1-y}Fe_yO_{3-\delta}$ (y = 0.0-1.0) for prospective application as cathode for IT-SOFCs or oxygen permeating membrane. *Electrochimica Acta* **52**, 7343 (2007).
65. Taskin, A.A., Lavrov, A.N. & Ando, Y. Achieving fast oxygen diffusion in perovskites by cation ordering. *Appl Phys Lett* **86**, 091910 (2005).
66. Z H Yang, Y.S.L. Synergetic thermal effects for oxygen sorption and order-disorder transition on perovskite-type oxides. *Solid State Ionics* **176**, 89-96 (2005).
67. Arnold, M., Wang, H. & Feldhoff, A. Influence of CO_2 on the oxygen permeation performance and the microstructure of perovskite-type $(Ba_{0.5}Sr_{0.5})(Co_{0.8}Fe_{0.2})O_{3-\delta}$ membranes. *Journal of Membrane Science* **293**, 44-52 (2007).
68. Shao, Z. & Haile, S.M. A high-performance cathode for the next generation of solid-oxide fuel cells. *Nature* **431**, 170 (2004).
69. Arnold, M., Martynczuk, J., Efimov, K., Wang, H. & Feldhoff, A. Grain boundaries as barrier for oxygen transport in perovskite-type membranes. *Journal of Membrane Science* **316**, 137 (2008).
70. Alaee, M.A. & Mohammadi, T. Preparation and characterisation of $Ba_xSr_{1-x}Co_{0.8}Fe_{0.2}O_{3-\delta}$ perovskite-type membranes: Part II. *Membrane Technology* **2009**, 7-11 (2009).
71. Ali Alaee, M. & Mohammadi, T. Preparation and characterisation of $Ba_xSr_{1-x}Co_{0.8}Fe_{0.2}O_{3-\delta}$ perovskite-type membranes: Part I. *Membrane Technology* **2009**, 6-12 (2009).
72. Alaee, M.A., Movahednia, M.M. & Mohammadi, T. Effect of Ba Content on Oxygen Permeation Performance of $Ba_xSr_{1-x}Co_{0.8}Fe_{0.2}O_{3-\delta}$ (x=0.2, 0.5, and 0.8) Perovskite-Type Membrane. *Journal of Chemical and Engineering Data* **54**, 3082-3091 (2009).
73. Bo, Y., Wenqiang, Z., Jingming, X. & Jing, C. Microstructural characterization and electrochemical properties of $Ba_{0.5}Sr_{0.5}Co_{0.8}Fe_{0.2}O_{3-\delta}$ and its application for anode of SOEC. *International Journal of Hydrogen Energy* **33**, 6873-6877 (2008).
74. Grunbaum, N. et al. Rate limiting steps of the porous $La_{0.6}Sr_{0.4}Co_{0.8}Fe_{0.2}O_{3-\delta}$ electrode material. *Solid State Ionics* **180**, 1448-1452 (2009).
75. Darab, M., Toprak, M.S., Syvertsen, G.E. & Muhammed, M. Nanoengineered BSCF Cathode Materials for Intermediate-Temperature Solid-Oxide Fuel Cells. *Journal Of The Electrochemical Society* **156**, K139-K143 (2009).
76. Ge, L., Ran, R., Zhang, K., Liu, S. & Shao, Z. Oxygen selective membranes based on B-site cation-deficient

$(Ba_{0.5}Sr_{0.5})(Co_{0.8}Fe_{0.2})_yO_{3-\delta}$ perovskite with improved operational stability. *Journal of Membrane Science* **318**, 182 (2008).

77. Jung, J.I., Misture, S.T. & Edwards, D.D. The electronic conductivity of $Ba_{0.5}$Sr0.5$Co_xFe_{1-x}O_{3-\delta}$ (BSCF: x = 0~1.0) under different oxygen partial pressures. *Journal of Electroceramics*, 1 (2009).
78. Jamnik, J. & Maier, J. Treatment of the Impedance of Mixed Conductors. Equivalent Circuit Model and Explicit Approximate Solutions. *J Electrochem Soc* **146**, 4183-4188 (1999).
79. Jamnik, J. Impedance spectroscopy of mixed conductors with semi-blocking boundaries. *Solid State Ionics* **157**, 19-28 (2003).
80. Riess, I. Mixed ionic-electronic conductors - material properties and applications. *Solid State Ionics* **157**, 1-17 (2003).
81. Baumann, F.S., Fleig, J., Habermeier, H.U. & Maier, J. Impedance spectroscopic study on well-defined (La,Sr)(Co,Fe)$O_{3-\delta}$ model electrodes. *Solid State Ionics* **177**, 1071-1081 (2006).
82. Lee, J.S., Jamnik, J. & Maier, J. Generalized equivalent circuits for mixed conductors: silver sulfide as a model system. *Monatsh Chem* **140**, 1113-1119 (2009).
83. Jamnik, J. & Maier, J. Generalised equivalent circuits for mass and charge transport : chemical capacitance and its implications. *Phys Chem. Chem. Phys* **3**, 1668-1678 (2001).
84. Li, S., Lü, Z., Ai, N., Chen, K. & Su, W. Electrochemical performance of $(Ba_{0.5}Sr_{0.5})_{0.9}Sm_{0.1}Co_{0.8}Fe_{0.2}O_{3-\delta}$ as an intermediate temperature solid oxide fuel cell cathode. *Journal of Power Sources* **165**, 97 (2007).
85. Yan, A.Y., Maragou, V., Arico, A., Cheng, M. & Tsiakaras, P. Investigation of a $Ba_{0.5}Sr_{0.5}Co_{0.8}Fe_{0.2}O_{3-\delta}$ based cathode SOFC II. The effect of CO_2 on the chemical stability. *Applied Catalysis B-Environmental* **76**, 320-327 (2007).
86. Liu, B., Zhang, Y. & Zhang, L. Oxygen reduction mechanism at $Ba_{0.5}Sr_{0.5}Co_{0.8}Fe_{0.2}O_{3-\delta}$ cathode for solid oxide fuel cell. *International Journal of Hydrogen Energy* **34**, 1008 (2009).
87. Barsoukov, E. & Macdonald, J.R. Impedance Spectroscopy Theory, Experiment, and Applications (Wiley Interscience, New Jersey, 2005).
88. Salehi, M. et al. A case study of the effect of grain size on the oxygen permeation flux of BSCF disk-shaped membrane fabricated by thermoplastic processing. *Journal of Membrane Science* **382**, 186 (2011).
89. Bucher, E., Egger, A., Ried, P., Sitte, W. & Holtappels, P. Oxygen nonstoichiometry and exchange kinetics of $Ba_{0.5}Sr_{0.5}Co_{0.8}Fe_{0.2}O_{3-\delta}$. *Solid State Ionics* **179**, 1032 (2008).
90. Haas, O., Ludwig, C. & Wokaun, A. Determination of the bulk cobalt valence state of co-perovskites containing surface-adsorbed impurities. *Analytical Chemistry* **78**, 7273-7277 (2006).
91. Karppinen, M., Matvejeff, M., Saloma, K. & Yamauchib, H. Oxygen content analysis of functional perovskite-derived cobalt oxides. *J Mater Chem* **12**, 1761-1764 (2002).

92. Jung, J.-I., Misture, S.T. & Edwards, D.D. Oxygen stoichiometry, electrical conductivity, and thermopower measurements of BSCF ($Ba_{0.5}Sr_{0.5}Co_xFe_{1-x}O_{3-\delta}$, $0 \leq x \leq 0.8$) in air. *Solid State Ionics* **181**, 1287 (2010).
93. McIntosh, S., Vente, J.F., Haije, W.G., Blank, D.H.A. & Bouwmeester, H.J.M. Structure and oxygen stoichiometry of $SrCo_{0.8}Fe_{0.2}O_{3-\delta}$ and $Ba_{0.5}Sr_{0.5}Co_{0.8}Fe_{0.2}O_{3-\delta}$. *Solid State Ionics* **177**, 1737 (2006).
94. Liu, B., Zhang, Y. & Tang, L. X-ray photoelectron spectroscopic studies of $Ba_{0.5}Sr_{0.5}Co_{0.8}Fe_{0.2}O_{3-\delta}$ cathode for solid oxide fuel cells. *International Journal of Hydrogen Energy* **34**, 435 (2009).
95. Jung, J.-I. & Edwards, D.D. X-ray photoelectron (XPS) and Diffuse Reflectance Infra Fourier Transformation (DRIFT) study of $Ba_{0.5}Sr_{0.5}Co_xFe_{1-x}O_{3-\delta}$ (BSCF: x=0-0.8) ceramics. *Journal of Solid State Chemistry* **184**, 2238 (2011).
96. Arnold, M., Xu, Q., Tichelaar, F.D. & Feldhoff, A. Local Charge Disproportion in a High-Performance Perovskite. *Chemistry Of Materials* **21**, 635-640 (2009).
97. Leo, A., Liu, S. & Costa, J.C.D.d. Development of mixed conducting membranes for clean coal energy delivery. *International Journal of Greenhouse Gas Control* **3**, 357 (2009).
98. Yi, J.X., Lein, H.L., Grande, T., Yakovlev, S. & Bouwmeester, H.J.M. High-temperature compressive creep behaviour of the perovskite-type oxide $Ba_{0.5}Sr_{0.5}Co_{0.8}Fe_{0.2}O_{3-\delta}$. *Solid State Ionics* **180**, 1564-1568 (2009).
99. Lipinska-Chwalek, M., Malzbender, J., Chanda, A., Baumann, S. & Steinbrech, R.W. Mechanical characterization of porous $Ba_{0.5}Sr_{0.5}Co_{0.8}Fe_{0.2}O_{3-\delta}$. *Journal of the European Ceramic Society* **31**, 2997 (2011).
100. Rutkowski, B., Malzbender, J., Beck, T., Steinbrech, R.W. & Singheiser, L. Creep behaviour of tubular $Ba_{0.5}Sr_{0.5}Co_{0.8}Fe_{0.2}O_{3-\delta}$ gas separation membranes. *Journal of the European Ceramic Society* **31**, 493 (2011).
101. Huang, B.X. et al. Anomalies in the thermomechanical behavior of $Ba_{0.5}Sr_{0.5}Co_{0.8}Fe_{0.2}O_{3-\delta}$ ceramic oxygen conductive membranes at intermediate temperatures. *Applied Physics Letters* **95** (2009).
102. Malzbender, J., Huang, B., Monch, J. & Steinbrech, R.W. A comparison of results obtained using different methods to assess the elastic properties of ceramic materials exemplified for $Ba_{0.5}Sr_{0.5}Co_{0.8}Fe_{0.2}O_{3-\delta}$. *Journal Of Materials Science* **45**, 1227-1230 (2010).
103. Huang, B.X., Malzbender, J., Steinbrech, R.W. & Singheiser, L. Discussion of the complex thermo-mechanical behavior of $Ba_{0.5}Sr_{0.5}Co_{0.8}Fe_{0.2}O_{3-\delta}$. *Journal of Membrane Science* **359**, 80 (2010).
104. Zhu, Q.S., Jin, T.A. & Wang, Y. Thermal expansion behavior and chemical compatibility of $Ba_xSr_{1-x}Co_{1-y}Fe_yO_{3-\delta}$ with 8YSZ and 20GDC. *Solid State Ionics* **177**, 1199-1204 (2006).

105. Kriegel, R., Kircheisen, R. & Topfer, J. Oxygen stoichiometry and expansion behavior of $Ba_{0.5}Sr_{0.5}Co_{0.8}Fe_{0.2}O_{3-\delta}$. *Solid State Ionics* **181**, 64-70 (2010).
106. Wang, H., Tablet, C., Yang, W. & Caro, J. In situ high temperature X-ray diffraction studies of mixed ionic and electronic conducting perovskite-type membranes. *Materials Letters* **59**, 3750 (2005).
107. Shannon, R.D. Revised Effective Ionic Radii and Systematic Studies of Interatomic Distances in Halides and Chaleogenides. *Acta Cryst* **A32**, 751-767 (1976).
108. BSI. in Part 2: Determination of density and porosity BS EN 623-2:1993.
109. in Vogel's Textbook of Quantitative Chemical Analysis 428-434 (Prentice Hall, 2000).
110. Gregg, S.J. & Sing, K.S.W. Adsorption, Surface Area and Porosity (Academic Press, 1982).
111. Brunauer, S., Emmett, P.H. & Teller, E. Adsorption of Gases in Multimolecular Layers. *Journal of the American Chemical Society* **60**, 309-319 (1938).
112. Rouquerol, J. et al. Recommendations for the characterization of porous solids. *Pure and Applied Chemistry* **66**, 1739-1758 (1994).
113. Klug, H.P. & Alexander, L.E. X-ray Diffraction Procedures for Polycrystalline and Amorphous Materials (John Wiley & Sons, New York, 1974).
114. http://pd.chem.ucl.ac.uk/pdnn/inst1/optics1.htm. (2013).
115. Langford, J.I. & Wilson, A.J.C. Scherrer after sixty years: A survey and some new results in the determination of crystallite size. *Journal of Applied Crystallography* **11**, 102-113 (1978).
116. Langford, J.I., Louer, D. & Scardi, P. Effect of a crystallite size distribution on X-ray diffraction line profiles and whole-powder-pattern fitting. *Journal Of Applied Crystallography* **33**, 964-974 (2000).
117. Egerton, R.F. Physical Principles of Electron Microscopy: An Introduction to TEM, SEM, and AEM (Springer Science, 2005).
118. Bearden, J.A. X-Ray Wavelengths. *Reviews of Modern Physics* **39**, 78-124 (1967).
119. Brouwer, P. Theory of XRF (PANalytical B.V., Almelo, 2010).
120. Elam, W.T., Shen, R.B., Scruggs, B. & Nicolosi, J. Accuracy of Standardless FP Analysis of Bulk and Thin Film Samples using a New Atomic Database. *Advances in X-ray Analysis* **47**, 104-109 (2004).
121. Macdonald, J.R. & Johnson, W.B. in Impedance Spectroscopy Theory, Experiment, and Applications
(eds. Barsoukov, E. & Macdonald, J.R.) p6 (Wiley Interscience, New Jersey, 2005).
122. Abram, E.J., Sinclair, D.C. & West, A.R. A Strategy for Analysis and Modelling of Impedance Spectroscopy Data of Electroceramics: Doped Lanthanum Gallate. *Journal Of Electroceramics* **10**, 165-177 (2003).

123. West, A., Sinclair, D. & Hirose, N. Characterization of Electrical Materials, Especially Ferroelectrics, by Impedance Spectroscopy. *Journal Of Electroceramics* **1**, 65-71 (1997).
124. Irvine, J.T.S., Sinclair, D.C. & West, A.R. Electroceramics: Characterization by Impedance Spectroscopy. *Advanced Materials* **2**, 132 (1990).
125. Briggs, D. in Surface Analysis by Auger and X-ray Photoelectron Spectroscopy (eds. Briggs, D. & Grant, J.T.) (IM publications & SurfaceSpectra Limited, Chichester, 2003).
126. Kelly, M.A. in Surface Analysis by Auger and X-ray Photoelectron Spectroscopy (eds. Briggs, D. & Grant, J.T.) (IM Publications & SurfaceSpectra Limited, Chichester, 2003).
127. Grant, J.T. in Surface Analysis by Auger and X-ray Photoelectron Spectroscopy (eds. Briggs, D. & Grant, J.T.) 869-874 (Im Publications & SurfaceSpectra Limited, Chichester, 2003).
128. www.casaxps.com. CasaXPS: Processing Software for XPS, AES, SIMS and More. (Accessed January 2012).
129. Tougaard, S. Background removal in x-ray photoelectron spectroscopy: Relative importance of intrinsic and extrinsic processes. *Physical Review B* **34**, 6779 (1986).
130. Shirley, D.A. High-Resolution X-Ray Photoemission Spectrum of the Valence Bands of Gold. *Physical Review B* **5**, 4709 (1972).
131. Moulder, J.F., Strickle, W.F., Sobol, P.E. & Bomben, K.D. Handbook of X-ray Photoelectron Spectroscopy (Perkin Elmer Corporation, Physical Electronics Division, Eden Prairie, MN, 1992).
132. Kak, A.C. & Slaney, M. Principles of Compurerized Tomographic Imaging (IEEE Press, New York, 1987).
133. Linke, W.F. Solubilities of Inorganic and Metal-Organic Compounds (American Chemical Society, 1958).
134. Mellor, J.W. A Comprehensive Treatise on Inorganic and Theoretical Chemistry (Longman Green & Co, 1923).
135. Mellor, J.W. A Comprehensive Treatise on Inorganic and Theoretical Chemistry (Longman Green & Co, 1923).
136. Yang, J., Liu, H., Martens, W.N. & Frost, R.L. Synthesis and Characterization of Cobalt Hydroxide, Cobalt Oxyhydroxide, and Cobalt Oxide Nanodiscs. *The Journal of Physical Chemistry C* **114**, 111-119 (2009).
137. Criado, J.M., Dianez, M.J., Macias, M. & Paradas, M.C. Crystalline structure and thermal stability of double strontium and barium carbonates. *Thermochimica Acta* **171**, 229-238 (1990).
138. Clearfield, A. Role of Ion Exchange In Solid-State Chemistry. *Chem Rev* **88**, 125-148 (1988).
139. Kingery, W.D., Bowen, H.K. & Uhlmann, D.R. Introduction to Ceramics (Wiley, New York, 1976).
140. Badwal, S.P.S. Zirconia-based solid electrolytes: microstructure, stability and ionic conductivity. *Solid State Ionics* **52**, 23-32 (1992).
141. Guo, Y. et al. Significant impact of the current collection material and method on the performance of $Ba_{0.5}Sr_{0.5}Co_{0.8}Fe_{0.2}O_{3-\delta}$

electrodes in solid oxide fuel cells. *J Power Sources* **196**, 5511-5519 (2011).

142. Yang, Z., Harvey, A., Infortuna, A. & Gauckler, L. Phase relations in the Ba–Sr–Co–Fe–O system at 1273 K in air. *J Appl Cryst* **42**, 153-160 (2009).
143. Ran, R., Guo, Y., Gao, D., Liu, S. & Shao, Z. Effect of foreign oxides on the phase structure, sintering and transport properties of $Ba_{0.5}Sr_{0.5}Co_{0.8}Fe_{0.2}O_{3-\delta}$ as ceramic membranes for oxygen separation. *Separation and Purification Technology* **81**, 384 (2011).
144. Vente, J.F., McIntosh, S., Haije, W.G. & Bouwmeester, H.J.M. Properties and performance of $Ba_xSr_{1-x}Co_{0.8}Fe_{0.2}O_{3-\delta}$ materials for oxygen transport membranes. *Journal Of Solid State Electrochemistry* **10**, 581-588 (2006).
145. Wang, H., Tablet, C., Feldhoff, A. & Caro, J. Investigation of phase structure, sintering, and permeability of perovskite-type $Ba_{0.5}Sr_{0.5}Co_{0.8}Fe_{0.2}O_{3-\delta}$ membranes. *Journal of Membrane Science* **262**, 20 (2005).
146. Ghadimi, A., Alaee, M.A., Behrouzifar, A., Asadi, A.A. & Mohammadi, T. Oxygen permeation of $Ba_xSr_{1-x}Co_{0.8}Fe_{0.2}O_{3-\delta}$ perovskite-type membrane: Experimental and modeling. *Desalination* **270**, 64 (2011).
147. Yang, Z. et al. Oxygen-Vacancy-Related Structural Phase Transition of $Ba_{0.8}Sr_{0.2}Co_{0.8}Fe_{0.2}O_{3-\delta}$. *Chemistry of Materials* **23**, 3169 (2011).
148. Zhao, L. et al. Electrochemical performance of novel cobalt-free oxide $Ba_{0.5}Sr_{0.5}Fe_{0.8}Cu_{0.2}O_{3-\delta}$ *J Power Sources* **195**, 1859-1861 (2010).
149. Girdauskaite, E. et al. Oxygen stoichiometry, unit cell volume, and thermodynamic quantities of perovskite-type oxides. *Journal Of Solid State Electrochemistry* **11**, 469-477 (2007).
150. Yang, J., Zhao, H., Liu, X., Shen, Y. & Xu, L. Bismuth doping effects on the structure, electrical conductivity and oxygen permeability of $Ba_{0.6}Sr_{0.4}Co_{0.7}Fe_{0.3}O_{3-\delta}$ ceramic membranes. *Int J Hydrogen Energy* **37**, 12694-12699 (2012).
151. Wackerl, J., Koppitz, T., Peck, D.-H., Woo, S.-K. & Markus, T. Correlation of thermal properties and electrical conductivity of $La_{0.7}Sr_{0.3}Cu_{0.2}Fe_{0.8}O_{3-\delta}$ material for solid oxide fuel cells. *Journal of Applied Electrochemistry* **39**, 1243-1249 (2009).
152. http://www.bruker.com/products/x-ray-diffraction-and-elemental-analysis/x-ray-diffraction/xrd-software/applications/xrd-software-applications/topas.html. (Accessed August 2013).
153. Zeng, P. et al. Re-evaluation of $Ba_{0.5}Sr_{0.5}Co_{0.8}Fe_{0.2}O_{3-\delta}$ perovskite as oxygen semi-permeable membrane. *Journal of Membrane Science* **291**, 148 (2007).
154. Ovenstone, J., Jung, J.-I., White, J.S., Edwards, D.D. & Misture, S.T. Phase stability of BSCF in low oxygen partial pressures. *Journal of Solid State Chemistry* **181**, 576-586 (2008).

155. Muller, P. et al. Decomposition pathway of cubic $Ba_{0.5}Sr_{0.5}Co_{0.8}Fe_{0.2}O_{3-\delta}$ between 700°C and 1000°C analyzed by electron microscopic techniques. *Solid State Ionics* **206**, 57 (2012).
156. http://www.dl.ac.uk/NCESS/xps/xps.htm. (Accessed August 2013).
157. Li, J.-G., Buìchel, R., Isobe, M., Mori, T. & Ishigaki, T. Cobalt-Doped TiO_2 Nanocrystallites: Radio-Frequency Thermal Plasma Processing, Phase Structure, and Magnetic Properties. *The Journal of Physical Chemistry C* **113**, 8009 (2009).
158. Batzill, M., Burst, J.M. & Diebold, U. Pure and cobalt-doped SnO_2(101) films grown by molecular beam epitaxy on Al_2O_3. *Thin Solid Films* **484**, 132 (2005).
159. Biesinger, M.C. et al. Resolving surface chemical states in XPS analysis of first row transition metals, oxides and hydroxides: Cr, Mn, Fe, Co and Ni. *Applied Surface Science* **257**, 2717 (2011).
160. Van Der Heide, P.A.W. Systematic x-ray photoelectron spectroscopic study of $La_{1-x}Sr_x$-based perovskite-type oxides. *Surface and Interface Analysis* **33**, 414 (2002).
161. Xu, Q., Chen, W. & Yuan, R. XPS Analysis of Ni and oxygen in single-sintered $SrTiO_3$ multifunction ceramic. *J Mater Sci Technol* **17**, 535-537 (2001).
162. Miller, D.J., Biesinger, M.C. & McIntyre, N.S. Interactions of CO_2 and CO at fractional atmosphere pressures with iron and iron oxide surfaces: one possible mechanism for surface contamination? *Surf Interface Anal* **33**, 299-305 (2002).
163. Bucher, E., Egger, A., Caraman, G.B. & Sitte, W. Stability of the SOFC Cathode Material (Ba,Sr)(Co,Fe)$O_{3-\delta}$ in CO_2-Containing Atmospheres. *Journal of The Electrochemical Society* **155**, B1218-B1224 (2008).
164. Yan, A. et al. A temperature programmed desorption investigation on the interaction of $Ba_{0.5}Sr_{0.5}Co_{0.8}Fe_{0.2}O_{3-\delta}$ perovskite oxides with CO_2 in the absence and presence of H_2O and O_2. *Applied Catalysis B: Environmental* **80**, 24-31 (2008).